ANALYSIS OF THE PETROLOGY AND GEOCHEMISTRY OF THE MAGMAS OF THE GALEMA RANGE IN THE SOMALIAN PLATEAU, ETHIOPIA: A PROBE OF LITHOSPHERIC PROCESSES OF THE NORTHERN EAST AFRICAN RIFT SYSTEM

By

Brandon Chiasera

A DISSERTATION

Submitted to
Michigan State University
in partial fulfillment of the requirements
for the degree of

Geological Sciences—Doctor of Philosophy

2020

ABSTRACT

ANALYSIS OF THE PETROLOGY AND GEOCHEMISTRY OF THE MAGMAS OF THE GALEMA RANGE IN THE SOMALIAN PLATEAU, ETHIOPIA: A PROBE OF LITHOSPHERIC PROCESSES OF THE NORTHERN EAST AFRICAN RIFT SYSTEM

By

Brandon Chiasera

As a continental rift evolves towards a mid ocean ridge, the continental lithosphere must rupture and extension must become accommodated exclusively by seafloor spreading. During this process, extensional strain is initially accommodated along the nascent rift margins, subsequently localizing to zones of focused magmatic intrusion. Asthenospheric conditions such as increased mantle potential temperature or presence of an upwelling, deep seated mantle anomaly may influence, or be responsible for, these extensional processes. While these processes are integral in the process of continental rifting, how they relate and influence each other remains an area of active scientific inquiry and debate. The Main Ethiopian Rift (MER) in East Africa is the ideal location to study extensional processes. We examine the Galema range, an area of focused magmatic activity along the eastern margin of the Central Main Ethiopian Rift, which is morphologically similar to areas of focused magmatism within the rift. To better understand the complex processes involved in continental rifting and how they are related, we present whole-rock, major and trace element data on 77 samples of the Galema range magmas, including isotopic geochemistry on 22 of these samples. We find that whole rock thermodynamic modeling and thermobarometric calculations on mineral-liquid pairs suggest that fractionation (and hence magma stalling depths) within the Galema range is polybaric (~7 and ~3 kbar). These results, when compared to zones of focused intrusion within the rift, indicate an incipient magmatic plumbing system. Trace element models of melt generation reveal melting conditions of 1418-

1450°C at 2.9-3.2 GPa. These conditions reveal that Ethiopian mantle T_P is elevated by ~68-100°C over ambient. In contrast, Si/Mg activity thermobarometry, which probes the point at which these magmas last re-equilibrated with the mantle, yielded broadly similar temperatures (1435-1474°C) but at lower pressures (2.1-2.6 ± 0.2 GPa). We interpret these results as evidence for magma stalling at a thermo-mechanical boundary to ascent, which we contend is the lithosphere-asthenosphere boundary (LAB). Isotopic analyses of the magmas of the Galema range indicate the presence of signatures of the Afar plume, Pan-African lithosphere, and depleted mantle. A subset of these isotopic analyses indicates the presence of a previously unknown, 4^{th} mantle end member, which we attribute to be a contribution from a recently created, and destroyed, sub-continental lithosphere beneath the eastern Ethiopian plateau. We contend that diking associated with the Galema range, which pre-dates magmatic belts within the rift; thermomechanically modified the lithosphere along this margin. The thermomechanical modification of the lithosphere mantle along this margin facilitated the subsequent development of within-rift magmatic chains. The implications of this are that off-rift magmatic activity may play an integral role in facilitating the development of rift architecture. We interpret contrasting results between two trace element modeling approaches as evidence for magma ponding subsequent to melt generation. While the continental lithosphere has thinned during extension, the lithosphere remains relatively thick late into the rifting process, despite the development of magmatic extension at crustal depths. The presence of an isotopic signature of a sub-continental lithospheric mantle indicates rapid creation and destruction of lithospheric material in processes attributed to the upwelling Afar plume. This process may be one way in which the lithosphere is thinned in the EARS, along with foundering and assimilation of material into the depleted asthenosphere.

I dedicate this work to my mother, Ann. This work would have never been started without you and your support. Furthermore, it would have never been finished had that support ever waivered. You never failed to push me in the right direction toward completion. I would also like to dedicate this work to the other half of my soul, Sonja. Your strength has always been something I aspire to and you have been like a shining beacon, guiding me toward my future. I would also like to dedicate this work to all the others who provided their unwavering support during my journey.

ACKNOWLEDGEMENTS

This work was supported by the National Aeronautics and Space Administration Planetary Geology and Geophysics Program (grant 10-PGG10-006), the Geological Society of America Student Research Grant, 2015, the Michigan State University Graduate Student Dissertation Continuation and Completion Fellowships, and the support of the Michigan State University Department of Earth and Environmental Sciences.

This work was made possible through the collaborative efforts of Guillaume Girard, Ian Bastow, Jasper Konter, Gezahegn Yirgu, Eric Grosfils, Dereje Ayalew, Paul Mohr, James R. Zimbelman, and Michael S. Ramsey. This work was also made possible with guidance from my esteemed committee members, Dr. Michael Velbel, Dr. Julie Libarkin, and Dr. David Long.

TABLE OF CONTENTS

LIST OF FIGURES

1. INTRODUCTION AND BACKGROUND

1.1 Introduction

As a continental rift evolves towards an oceanic spreading center, the mechanism of strain accommodation must transition from faulting and thinning of the lithosphere, to focused magmatic intrusion (Korme et al., 1997; Buck, 2004; Wolfenden et al., 2005; Buck, 2006; Casey et al., 2006; Corti, 2009; Rooney, 2010; Corti, 2012; Mazzarini et al., 2013b; Rooney et al., 2014a). Specifically, strain is thought to migrate from high angle border faults to zones of focused magmatic activity within the rift adjacent to the rift border faults (Ebinger and Casey, 2001b). These zones of focused magmatic intrusion must eventually migrate toward the rift axis as possible precursors to oceanic spreading centers (Ebinger, 2005). As rifting progresses, the continental lithosphere must thin, effectively to zero, for an oceanic spreading center to form and asthenospheric upwelling to occur. While elegant in its simplicity, observations from rifting environments show magmatic features that are unexplained by this model. Magmatism outside of the rift-border faults is frequently observed to be contemporaneous with episodes of both mechanical extension and focused magmatic intrusion within the rift (Abebe et al., 1998; Keranen and Klemperer, 2007). This magmatism occurs in areas of relatively thicker continental lithosphere and is contemporaneous with areas of magmatism that occur in areas of significantly thinned continental lithosphere (e.g., Nelson et al., 2019). Seemingly related to the rifting process, this magmatism is not adequately explained by the currently accepted models of continental rifting. One such area, the Galema Range, is located in the Main Ethiopian Rift (MER) area of the East African Rift System (EARS) (Mohr and Potter, 1976; Mohr, 1980; Woldegabriel et al., 1990). The East African Rift System has been recognized as an area of recent continental rifting activity which displays all the characteristics of a continental rifting

system, from initial fracturing and faulting of the crust, to nascent oceanic spreading (GeoPRISMS, 2013). The Galema range exists in an area adjacent to the MER with relatively thicker continental lithosphere on the rift shoulder (e.g., Maguire et al., 2006; Corti, 2009).

Here, we present a detailed geochemical study of the basalts that comprise the dikes of the Galema Range in order to assess their relationship to the continental rifting of the MER. When compared to studies of magmatic areas elsewhere in the MER, such as the Wonji Fault Belt (WFB) and Silti Debre-Zeyit Fault Zone (SDFZ), it may be ascertained whether there is any relationship in process to more recent, within-rift magmatic activity. Processes such as formation of magmatic plumbing systems in response to lithospheric stresses and magmatic accommodation of extensional strain will be probed and compared. If a relationship exists, it would suggest that the magmatic activity of the Galema Range is related to the magmatic activity within the rift. This relationship would suggest that the currently accepted models of continental rifting evolution must be re-evaluated as rift-related magmatic activity can occur outside of the rift itself.

We also present a detailed trace element analysis of the magmas of the Galema range. Through the examination and thermodynamic modeling of the trace element geochemical signature of the Galema magmas, we are able to obtain the extensive conditions of melt generation in the asthenosphere at the time that Galema was magmatically active. Parameters of asthenospheric conditions during melt generation such as pressure and mantle potential temperature give information about lithospheric thickness and the thermal state of the asthenosphere. Trace element geochemistry can also determine the source lithology that was melted to form the Galema magmas. These analyses reveal information about the structure of the lithosphere at the time of the activity of the Galema range and, when compared to the

lithospheric structure of more recent magmatism, how the lithosphere has been modified by continental rifting processes.

Radiometric $^{40}Ar/^{39}Ar$ method dating of the Galema range dikes will be presented here, revising previously obtained K-Ar dates (Mohr and Potter, 1976; Kennan et al., 1990), allowing for placing of the magmatic activity of the Galema range in temporal context within the evolution of the MER. Isotopic chemical analyses of the Galema range magmas will also be presented here. Determination of isotopic signatures such as $^{143}Nd/^{144}Nd$, $^{87}Sr/^{86}Sr$, $^{208}Pb/^{204}Pb$, $^{207}Pb/^{204}Pb$, $^{206}Pb/^{204}Pb$, ε_{Hf}, and ε_{Nd} allow for determination of the geochemical source reservoirs, and their mass fractions, that contributed to the source melt of the Galema range basalts. This allows an estimate of the proportions of contribution of the source reservoirs of the Afar plume, depleted mantle, African lithosphere, and sub-continental lithosphere present in the Galema melts. This gives indications of the lithospheric structure and plume influence during melt generation. Analysis of the lithospheric structure during the intrusion of the Galema magmas, when compared with the lithospheric structure of more recent magmatism, reveals information about how the lithosphere of the MER is modified, structurally and chemically, during continental rifting processes.

These analyses of the magmatism of the Galema range will indicate that the previous theories of continental rifting evolution need re-evaluation. Accommodation of extensional strain can occur through focused magmatic intrusion over a broader area within thicker lithosphere than previously hypothesized. Magmatic accommodation of strain can occur contemporaneously in areas with different lithospheric thickness. Magmatism induced by thermal input of an ascending mantle plume can modify and subsequently destroy lithospheric material, assisting in lithospheric thinning in addition to mechanical stretching. Thus, magmatism in a continental rift

can be induced by, and be the cause of, lithospheric thinning and adiabatic decompression melting. In addition to thermo-mechanical weakening of the lithosphere (e.g., Buck, 2006), our analyses of the Galema range indicates that focused magmatic intrusion plays additional roles in the rifting of a continent.

1.2 General continental rifting model and processes

1.2.1 Mechanical Rifting

The currently accepted model of evolution of a continental rift begins first with mechanical processes such as fracturing and faulting in response to the far-field extensional stresses which begin to thin the continental lithosphere (Ebinger, 2005). These far-field extensional stresses could be caused by processes such as: 1) divergent far-field plate motion such as subduction processes at opposing plate boundaries (slab pull), 2) asthenospheric upwelling causing extensional pressure and stress gradients on the lithosphere through uplift, or 3) asthenospheric convection inducing divergent lateral extensional stress on the overlying lithosphere (slab push) (Ebinger and Sleep, 1998). Fracturing and faulting of the crust accommodates lithospheric extensional strain and evolves in three stages, with a concomitant increase in magmatism (Wolfenden et al., 2005). Stage one of continental rift development begins with the formation of high angle border faults which run parallel to the developing rift axis. The initial location of these, and subsequent faults, may be related to pre-existing lithospheric structures (Ebinger, 2005). Stage two of development is characterized by faulting that progresses toward the rift axis and forms a segmented, hinged fault system that is doubly-flexed toward the rift axis and its margins, but still parallel to and offset from the rift axis (Wolfenden et al., 2005). Stage three of rift evolution is characterized by faulting and fracturing

along the axis of the rift (Wolfenden et al., 2005). These faults may originate as fractures at the surface of the crust and propagate downward ($\sigma 1$) to become normal faults as the tensile strength ($\sigma 3$) becomes equal to the tensile strength of the rock (Acocella et al., 2003).

The orientation and geographical location of these faults and fractures are often dictated by the local structure of the lithosphere. Lithospheric heterogeneities formed of previous geological processes, such as continental assembly, can cause weaknesses that can be exploited during subsequent episodes of continental deformation (e.g., Macgregor, 2015; Mazzarini et al., 2016; Purcell, 2018). Often, fractures and faults appear to have an orientations oblique to the trend of lithospheric weaknesses and the direction of extensional stress (Acocella and Korme, 2002; Korme et al., 2004; Mackenzie et al., 2005; Casey et al., 2006; Kendall et al., 2006; Corti, 2009; Agostini et al., 2011a; Agostini et al., 2011b; Autin et al., 2013; Corti et al., 2013; Philippon et al., 2015).

1.2.2 Magmatic Rifting

1.2.2.1 Melt Generation in Continental Rifts

1.2.2.1.1 Decreasing Pressure

Fundamentally, the process of continental rifting requires thinning of the lithosphere and intrusion of melt into the lithosphere (Buck, 2006). Thus, surface deformation occurs in the form of subsiding half-grabens and shallowing of the lithosphere-asthenosphere boundary (LAB) due to thermomechanical erosion (Spohn and Schubert, 1982; Davies, 1994; Wang et al., 2002; Corti et al., 2003; Corti et al., 2004; Ebinger, 2005; Wolfenden et al., 2005; Keranen et al., 2009; Rooney, 2010; Bastow and Keir, 2011; Corti, 2012; Maccaferri et al., 2014; Rooney et al., 2014a; Keir et al., 2015). Stretching and thinning of the lithosphere resulting from extensional forces alone is not sufficient to allow for the development of a fully mature continental rift

(Buck, 2006). The intrusion of melt into the lithosphere is required to thermomechanically modify it in such a way as to allow a continent to rift completely (Buck, 2006). As the base of the LAB ascends during continental rifting, adiabatic melting, through decompression of asthenospheric material, generates the melt that will intrude the lithosphere (Morton et al., 1979; Ebinger, 2005; Langmuir and Forsyth, 2007).

As the material is decompressed, its volume increases based on its isothermal compressibility, and by Le Châtelier's Principle, the equilibrium state of the system shifts toward one that favors the formation of the liquid phase over solid (Winter, 2001). As a material is decompressed below its equilibrium pressure ($\Delta G=0$), at constant temperature the liquid phase is preferred over the solid phase as the liquid phase is more stable (less ΔG) at lower pressures. The Clapeyron Equation dictates that to satisfy $\Delta G=0$, decrease in pressure of a material necessitates a decrease in $\Delta S(\sim T)$ of the material as its volume increases.

$$\frac{dP}{dT} = \frac{\Delta S}{\Delta V}$$

The Clapeyron Equation

However, if a material is incompressible, the ΔV will be minimal, regardless of the change in pressure. By the Clapeyron Equation it is possible that pressure on this incompressible material can be decreased without significant loss of heat through a change in volume. As asthenospheric material is solid and effectively incompressible, this mechanism allows for the possibility of hot volumes of material to be transported to shallower, cooler regimes of the asthenosphere. This leads to discussion of the mantle potential temperature (T_p).

The mantle potential temperature (T_p) is defined as the temperature (T) of a volume of magma if it were to ascend to shallower depths with no loss of heat by conduction to the surrounding asthenosphere, i.e. adiabatic (McKenzie and Bickle, 1988; Winter, 2001). The

difference in heat of this portion of magma as it ascends, without conductive heat loss to its surroundings, would thus be controlled by expansion of the material as determined by the Claperyon Equation. However, as asthenospheric material is solid prior to magma generation, it is effectively incompressible, and the loss of heat by expansion during ascent is 10-20 °C/GPa (0.3-0.6 °C/km) (Ahern et al., 1981; McKenzie and Bickle, 1988; Winter, 2001). This minimal change in temperature (ΔT) as a result of change in volume (ΔV) is not great enough to negate the difference in temperature of asthenospheric material that has ascended from depth with surrounding, shallow asthenosphere. Purely adiabatic processes are not plausible based on geologically possible rates of ascent (Winter, 2001). However, realistic rates of ascent can result in a heat loss of ~130 °C/GPa. (Winter, 2001), which is not a large enough ΔT to reduce the difference in temperature between the ascending and surrounding asthenosphere. Through these mechanisms, it is possible through plume ascent or mantle upwelling, to have a volume of asthenospheric material ascend and cross the geotherm along the adiabat (Winter, 2001). On cessation of its ascent at this new depth, the superheated material can introduce, through advection, higher temperatures to the surrounding asthenosphere and/or itself melt.

1.2.2.1.2 Increasing Temperature

Thermodynamic modeling of the magmatic products of the African-Arabian Large Igneous Province have shown that mantle T_p of the EARS was at its highest of ~170 °C above ambient (1350 °C ± 50) during the Oligocene (Rooney et al., 2012c). Source melt conditions of magmas from Djibouti have been modeled to estimate the mantle T_p anomaly at <10 Ma had decreased to a maximum of ~140 °C (Rooney et al., 2012c). Generally, younger magmas from areas across the MER have been modeled to have been generated at mantle T_p of ~1490 °C, less than those at Djibouti, but still elevated compared to ambient mantle T_p (Rooney et al., 2012c).

If the temperature of asthenospheric material is raised above the geothermal gradient for the depth at which they reside, melting and magma generation may occur. Le Châtelier's Principle dictates that the equilibrium point of a system will shift as a result of changes imposed on the system. In the case of an increase in temperature, the equilibrium point of the system will shift toward higher temperatures and favor formation of the liquid phase over the solid phase to maintain a minimal energy of the system ($\Delta G=0$)(Winter, 2001).

Increasing the temperature of the asthenosphere is not a straightforward process. The temperature of the asthenosphere increases with depth (geothermal gradient) reducing significant temperature variability for a given pressure. However, if asthenospheric material from greater depth and different thermal regime were to ascend, the temperature of shallow material would increase through conduction. Within the East African Rift System, the far-field extensional forces are generated through uplift as a result of impingement of the ascending Afar plume (Pik et al., 1999; Ebinger, 2005; Corti, 2009). The Afar plume is a broad thermal upwelling, ascending from the core-mantle boundary (Ritsema et al., 1999; Corti, 2009), which represents advection of a volume of superheated material into the cooler, upper mantle.

1.2.2.1.3 Variation of the Components of the System

The lithospheric component of magmas from the East African Rift System represents contributions to the melt from lithologies associated with the Sub Continental Lithospheric Mantle. The Sub Continental Lithospheric Mantle (SCLM) is a volume of depleted yet hydrated asthenospheric material underlying the lithosphere of continental plates (Winter, 2001). At the base of this volume of material is the lithosphere-asthenosphere boundary (LAB). The SCLM may have originated through the accumulation and density sorting of residuals from mantle plumes (Arndt et al., 2009). As melt has been extracted at some point during the formation of the

SCLM, it is depleted in CaO, Fe_2O_3, TiO_2, Na_2O and K_2O (Turner and Hawkesworth, 1995). Consequently, melts derived from the depleted peridotite of the SCLM will also display lower relative concentrations of these major element species.

Hydration of the SCLM may take place through one or more of several processes: During the dehydration of subducting slabs associated with continental assembly (Turner and Hawkesworth, 1995), by addition of small amounts of melt from the underlying asthenosphere (McKenzie, 1989; Turner and Hawkesworth, 1995), or by percolation of hydrous fluids ascending from asthenospheric upwelling (Pilet et al., 2011). Small degrees of partial melt at high pressure ahead of an ascending mantle plume or as the result of asthenospheric material upwelling during continental rifting thermochemically interact with lithospheric mantle material (Pilet et al., 2011). Thermochemical modification can generate both cryptic and modal metasomatism of peridotite while forming veins in the host material through the loss of heat to the host rock (Pilet et al., 2011). These veins of metasomatized material will then generate alkaline melts with subsequent melting (Pilet et al., 2011). Hydration by the addition of fluids has two effects: increasing the volatile content and enriching the trace element signature of the SCLM. Metasomatic reactions that occur within the SCLM effectively change the number and concentration of the components of the system, potentially changing the eutectics and/or solidus curves that dictate melting behavior.

In a multi-component system, the concentrations of the individual components dictate at what temperature a system will begin and complete melting. Empirically determined behaviors of the phases during melting define the liquidus of a phase diagram (Morse, 1980; Winter, 2001). Within a phase diagram of a complete solid solution, the concentrations of the individual components dictate at what temperature the system crosses the solidus, thereby determining the

melting point of the system. Within a eutectic system, the lowest temperature of melting is defined as an empirically defined eutectic point (Morse, 1980). If the temperature of a multi component system is increased, without changing pressure, the system must intersect the eutectic point at the onset of melting where temperature becomes invariant (by the Gibbs phase rule) until one of the components is completely melted (Winter, 2001). At this point, the temperature of the system may increase and melt the remaining components until the remainder of the components of the system is melted. The individual concentrations of the components determine which eutectic is first intersected (if more than one). The components that composed the system themselves determine where the eutectics lie within the phase diagram. Thus, the number and species of phases of a system determine at what temperature range over which the system will melt.

The addition of volatiles, such as H_2O or CO_2 to a volume of asthenosphere generally has the effect of lowering the temperature of its solidus (White and McKenzie, 1989; Winter, 2001). If water exists in the solid asthenosphere, it is incorporated into hydrous mineral phases and is of low concentration. CO_2 exists in the asthenosphere at high pressure as carbonate minerals (e.g., Wyllie, 1979; Morse, 1980; Winter, 2001; Dasgupta and Hirschmann, 2006). Le Châtelier's Principle states that if we are to add these volatiles to a melt generated from the asthenosphere, the effect is to make the new solution more stable with respect to the solid phase, thereby reducing its melting temperature (Morse, 1980; Winter, 2001). Primary magmas within the Main Ethiopian Rift have been estimated to contain ≤ 1 wt. % H_2O (Trua et al., 1999; Rooney et al., 2007; Rooney, 2010) and the modeling results that have been reported here have similar water content. As H_2O is determined to be a minor phase and the source melts of the EARS are

considered to be dry, water likely does not play a role in affecting the melting temperature of magmatic sources in the MER.

1.3 Magmatic Intrusion in Continental Rifts

Magmatic intrusion provides a necessary form of extensional strain accommodation as lithospheric yield strength is too great to be overcome strictly through mechanical faulting and fracturing (Buck, 2006; Bialas et al., 2010). As the lithosphere is thinned during extension, the asthenosphere rises and melts adiabatically providing the melt for magmatic diking (McKenzie and Bickle, 1988; Ebinger and Sleep, 1998; Ebinger and Casey, 2001b; Dugda, 2005; Ebinger, 2005; Yirgu et al., 2006; Corti, 2009; Bastow and Keir, 2011). Magmatic activity initiates during stage three of the currently accepted model of continental rifting and migrates toward the rift axis (Ebinger, 2005; Wolfenden et al., 2005). This magmatism may overprint the structures created during stage two and may exploit the fractures and faults as pathways for ascent (Korme et al., 1997; Casey et al., 2006; Rooney, 2010; Corti, 2012; Mazzarini et al., 2013b; Rooney et al., 2014a; Mazzarini et al., 2016). This suggests that magmatism becomes the dominant form of strain accommodation as large, normal border faults did not continue to form after stage one (Ebinger and Casey, 2001b).

Beginning as small dikes eroding the base of the lithosphere, the ascending magma thermo-mechanically modifies the lithosphere and allows for progressive diking to occur. This creates a feedback mechanism, causing focusing of the magmatic activity (Bialas et al., 2010; Bastow and Keir, 2011; Havlin et al., 2013; Daniels et al., 2014). As the lithosphere continues to deform and thin along the rift axis, magmatism shifts toward more focused activity along the axis due to increased magma flux created by adiabatic melting in the thinned areas (Morton et al.,

1979; Ebinger, 2005), or a change in topography at the base of the lithosphere due to the thinning, which channels melt material toward the axis (Corti, 2012; Keir et al., 2015).

The depth at which magmas stall on ascent is testable through the study of their major element geochemistry. The depth at which a magma stalls in the lithosphere, in part, controls the crystal phases that precipitate from that magma, thereby influencing the composition of the crystal phases and residual magma from which they fractionate (Green and Ringwood, 1967; O'Hara, 1968; Green, 1969; Thompson, 1972; Wilson, 1994). Thus, studies of major element geochemistry, dependent on fractionating crystal phases, give indications as to the depth of stalling of an ascending magma. In this way, areas of magmatic activity in a continental rift setting can be tested to determine whether they are a result of extensional stresses by characterization of their geochemistry.

In addition to where magma stalls on ascent in the lithosphere, the geographic location of magmatic zones is also dictated by processes related to continental rifting. Much in the same way that mechanical rifting features can exploit pre-existing lithospheric heterogeneities, magmatism can exploit these same weaknesses on ascent, or during lateral propagation, and appear at locations not predicted by the currently accepted models (Korme et al., 1997; Korme et al., 2004; Corti, 2009; Pallister et al., 2010; Keir et al., 2011; Corti, 2012; Rooney et al., 2014a; Mazzarini et al., 2016). Compounding this, magmatism may exist at off-axis locations where the lithosphere is the thinnest because of increased adiabatic melting and melt may even be channeled to these thinned locations along topography of the lithosphere-asthenosphere boundary (Kendall et al., 2005; Holtzman and Kendall, 2010; Corti, 2012; Rooney et al., 2014a; Keir et al., 2015). These interactions of an ascending magma with the structure of the lithosphere help determine where an area of focused magmatic intrusion will exist.

Magma may migrate away from the rift axis to a location outside of the rift-border faults (e.g., Pallister et al., 2010). The formation of half grabens during the mechanical rifting process may create blocks which exert a downward force due to gravity. As this happens, the melt that may have accumulated beneath the blocks due to adiabatic melting may be forced to migrate laterally and be intruded into the lithosphere at a location near to, or outside of the rift-border faults (Corti et al., 2004; Corti, 2012; Maccaferri et al., 2014).

The existence of contemporaneous mechanical and magmatic rifting related features that do not agree with the currently accepted models of continental rifting evolution suggest that these models are far too simplistic and must be reevaluated. Off-axis mechanical and magmatic features within the rift suggest that strain accommodation within the rift is more widely distributed than the models suggest and may even occur outside of the rift-border faults. The existence of rifting related features on one side of the rift axis suggests that symmetrical evolution of the rift, as predicted by the currently accepted models, may not occur. Contemporaneous events of faulting and magmatic intrusion associated with continental rifting processes suggest that there is not a straightforward progression from mechanical to magmatic accommodation of strain. These processes observed in continental rifting environments suggest that the process of migration of faulting and magmatism to the rift axis may not be as straightforward as predicted.

The East African Rift System (EARS) is a recently active continental rifting environment (Figure 1). Preserved within the EARS are all stages of continental rifting evolution, from initial fracturing and faulting of the crust to focused magmatic intrusion (GeoPRISMS, 2013). The EARS displays evidence of contemporaneous faulting and magmatism, in areas that display

variable lithospheric thicknesses. Thus, the EARS is the optimal location to study the evolution and progression of multiple stages continental rifting and how they are related to one another.

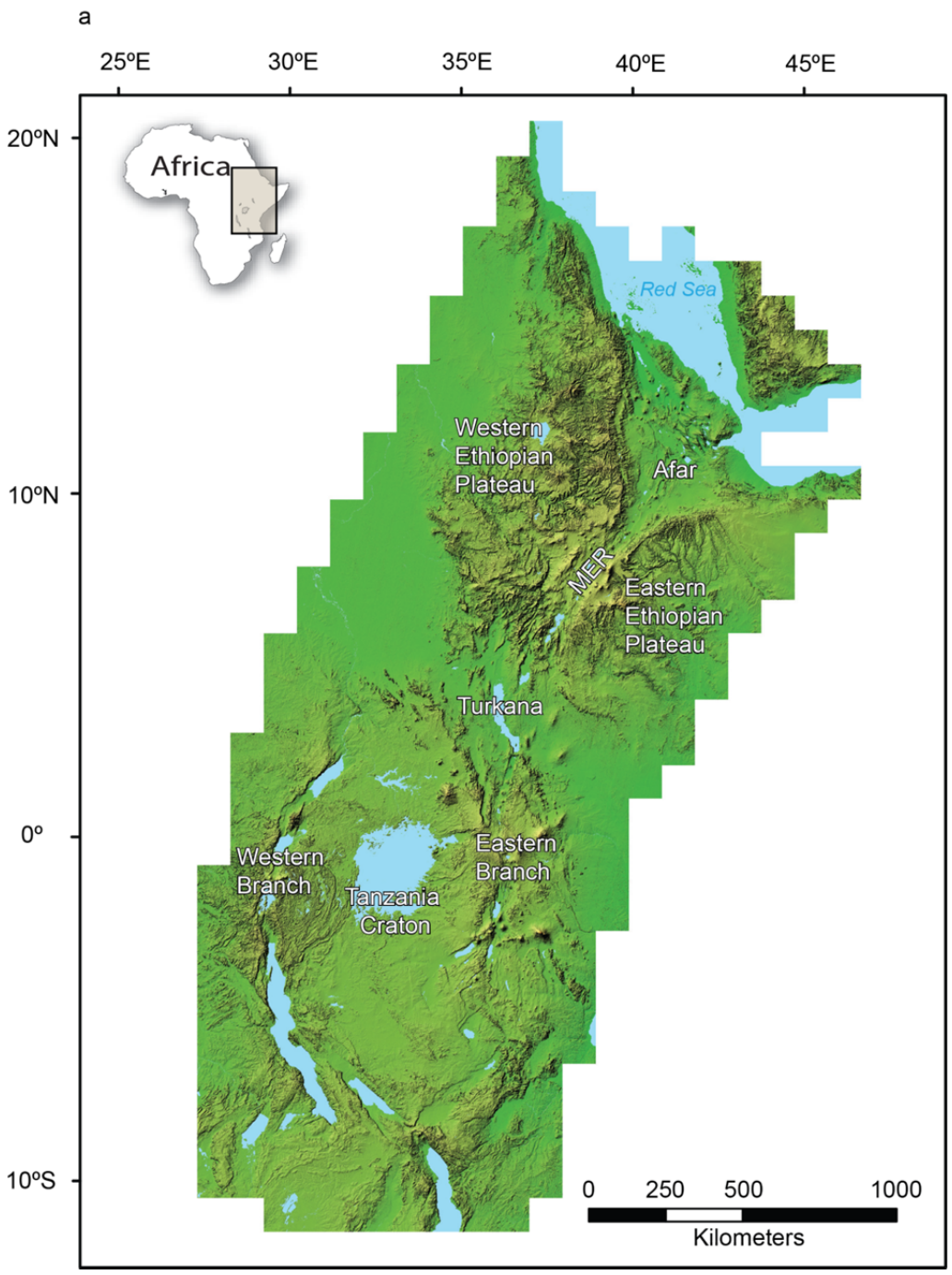

Figure 1.1.

Overview maps of a. the East African Rift System (EARS), b. the Main Ethiopian Rift (MER), and c.the Central Main Ethiopian Rift (CMER), indicating locations described in the text. NMER: Northern Main Ethiopian Rift, SMER: Southern Main Ethiopian Rift, YTVL: Yerer-

Figure 1.1. (cont'd.)

Tullu Wellel Volcanotectonic Lineament, BTSH: Boru Toru Structural High, WFB: Wonji Fault Belt, SDFZ: Silti-Debre Zeyit Fault Zone, AMZ: Akaki Magmatic Zone.

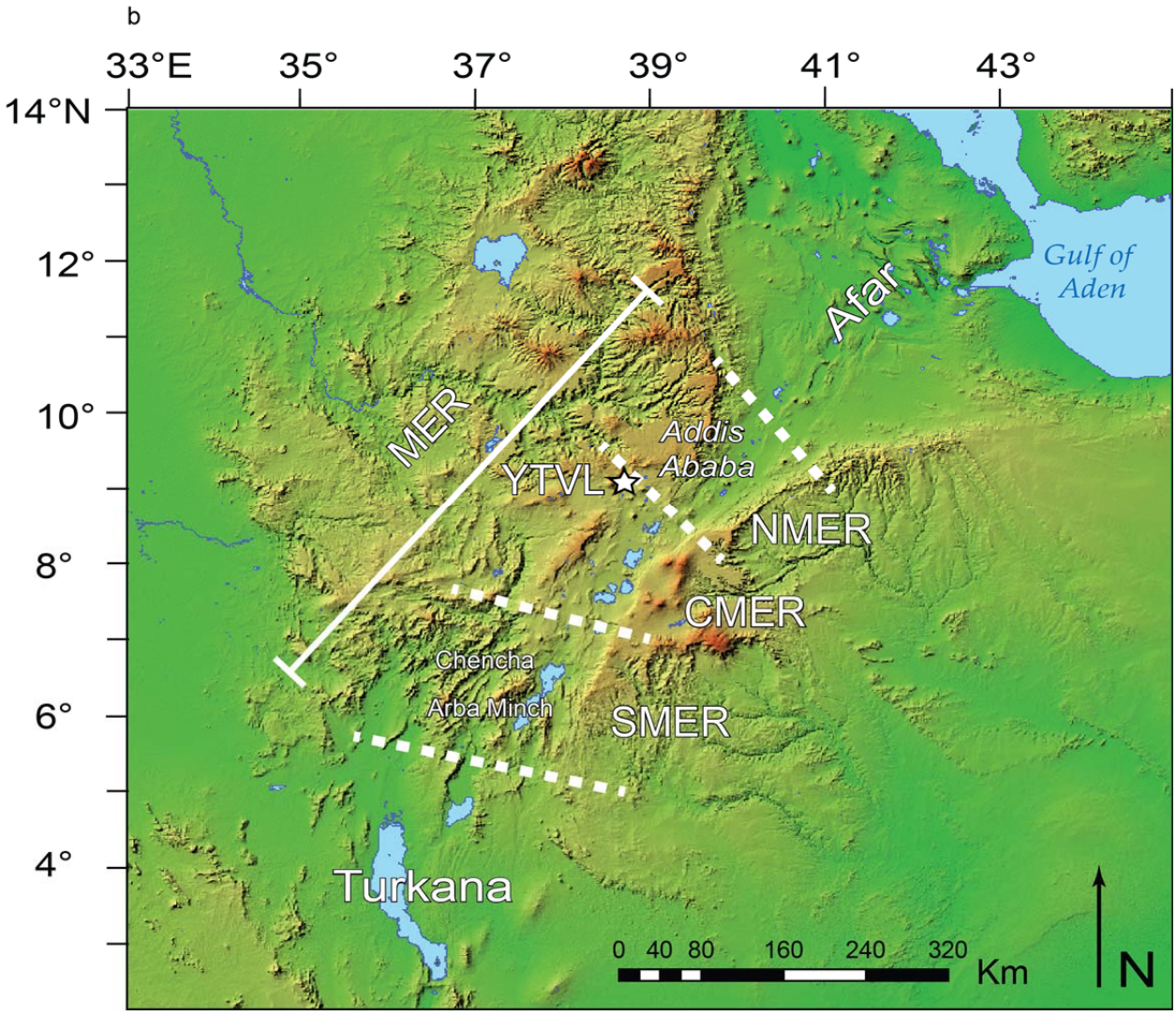

Figure 1.1. (cont'd.)

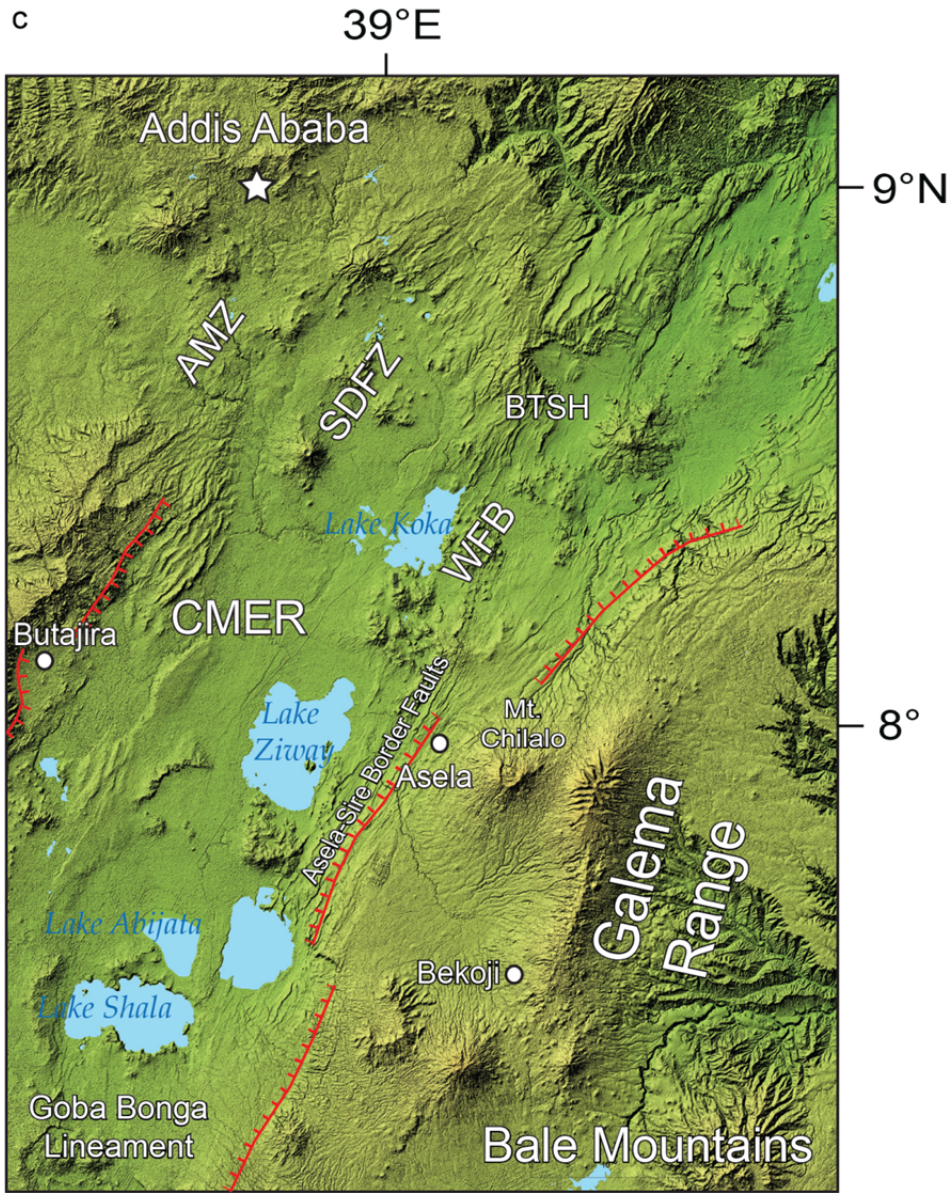

1.4 Geologic History of the EARS

1.4.1 Pre-Rift Tectonic and Magmatic Activity of the EARS

The East African Rift System (EARS) is a continental rifting zone that runs from Djibouti in the northern section of the rift to Mozambique in the southern section (Figure 1.1a). The entire progression of a continental rift system can be found in the EARS, from tectonic activity

associated with initial rifting that is characterized as fracturing and faulting of the crust, to the continent-ocean transition that is accompanied by significant magmatic activity (GeoPRISMS, 2013). These features are the result of the complex geological history of the African continent interacting with a large mantle plume impinging upon its base, creating the extensional stresses and magmatic activity necessary to form them.

The African continent was assembled during the Proterozoic collision of East and West Gondwana (Stern, 1994; Cutten, 2002). This collision created NNE-SSW trending suture zones within the Precambrian rock in Ethiopia and NW-SE trending shear zones (McWilliams, 1981; Stern, 1994; Abdelsalam and Stern, 1996; Maguire et al., 2006; Macgregor, 2015; Purcell, 2018). The collision also resulted in a Himalayan style orogenic belt which runs from Ethiopia south into Kenya that exposes ophiolite complexes (Abdelsalam and Stern, 1996). Island arcs and micro-continents may have also been accreted onto the continent as a result of this collision event (Korme et al., 2004; Dugda, 2005; Maguire et al., 2006). This continental assembly was followed by magmatic activity in the Eocene with basaltic volcanism in the broadly rifted zone in the Turkana basin of northern Kenya and southern Ethiopia at ~45 Ma (Ebinger et al., 1993b; George and Rogers, 2002; Corti, 2009; Rooney, 2017)(Figure 1.1a). These events were followed in the Oligocene by a major uplift event (Burke, 1996), possibly due to a rifting event in the Sudan. This extensional event generated N-S trending structural heterogeneities across the region (Mège et al., 2016; Purcell, 2018) as well as creating the structures responsible for the Yerer-Tullu Wellel Volcanotectonic Lineament (YTVL)(Figure 1.1b)(Keranen et al., 2004; Korme et al., 2004; Maguire et al., 2006; Trestrail et al., 2017). This sequence of continental assembly and previous rifting events leads to the existence of lithospheric structural heterogeneities which influence the evolution and activity of the most recent continental rifting process (Corti, 2009;

Macgregor, 2015). The uplift in the Oligocene was accompanied by the eruption of large scale flood basalts throughout the MER.

Large-scale flood basalt magmatism throughout the northern EARS during the Oligocene is attributed to the impingement of the Afar plume on the base of the lithosphere (Figure 1.2a) (Woldegabriel et al., 1990; Baker et al., 1996; Hofmann et al., 1997; Rochette et al., 1998; Pik et al., 1999; Kieffer, 2004; Mackenzie et al., 2005; Tommasini et al., 2005; Cornwell et al., 2006; Furman et al., 2006a; Yirgu et al., 2006; Corti, 2009; Rooney, 2017). The flood basalt activity, also known as the Oligocene trap phase, resulted in the deposition of a 1-2km thick series of basalts across the region (Figure 1.2a)(Rooney, 2017). Mafic material in the form of a ~8km thick layer was underplated to the base of the crust during the Oligocene as a result of the plume impingement and flood basalt volcanism (Deniel et al., 1994; Dugda, 2005; Mackenzie et al., 2005; Cornwell et al., 2006; Maguire et al., 2006; Daly et al., 2008; Bronner et al., 2011) and this underplated mafic material may also contribute to the crustal uplift (Cornwell et al., 2006; Maguire et al., 2006). The mafic underplating may have implications for the evolution of the rift over time, effectively creating a thicker lithosphere which is more resistant to rifting under the western plateau (Dugda, 2005; Mackenzie et al., 2005).

The flood basalts of the western plateau in Ethiopia have been attributed to the impact of the Afar plume at the base of the lithosphere. These basalts were erupted sometime after the impingement of the plume began (late Oligocene)(Figure 1.2a) (Pik et al., 1999; Kieffer, 2004; Corti, 2009; Rooney, 2017). Thermal input by the Afar plume elevated the mantle potential temperature above ambient to ~1500 °C (Rooney et al., 2012c; Rooney, 2017). The flood basalts are composed of tholeiitic to alkaline basalts with a bimodal chemical character based on Ti weight percent that gives a high Ti basalt (2.4-5 wt% TiO_2) and a low Ti basalt (1-2.6 wt% TiO_2)

(Pik et al., 1999; Kieffer, 2004). The majority of the source melts of the flood basalt groups are interpreted to be the result of contributions of the geochemical source reservoirs of the Afar plume, depleted mantle, and African lithosphere (Pik et al., 1999). Isotopic and trace element geochemical analyses of a subset of the flood basalts (HT2; Pik et al., 1999) on the western Ethiopian plateau indicate their source melts were formed by contributions from the geochemical reservoirs of the Afar plume, depleted mantle, African lithosphere, and metasomatized material (Beccaluva et al., 2009; Furman et al., 2016; Rooney et al., 2017). The presence of a metasomatized component in the source melts of this group of flood basalts indicates melting and destruction of the Sub-Continental Lithospheric Mantle (SCLM) that was created during the Pan-African continental assembly (Furman et al., 2016; Rooney et al., 2017). Immediately after the flood basalts were extruded, large, chemically similar shield volcanoes formed on the plateau signifying a decrease in extruded volume (Kieffer, 2004; Corti, 2009).

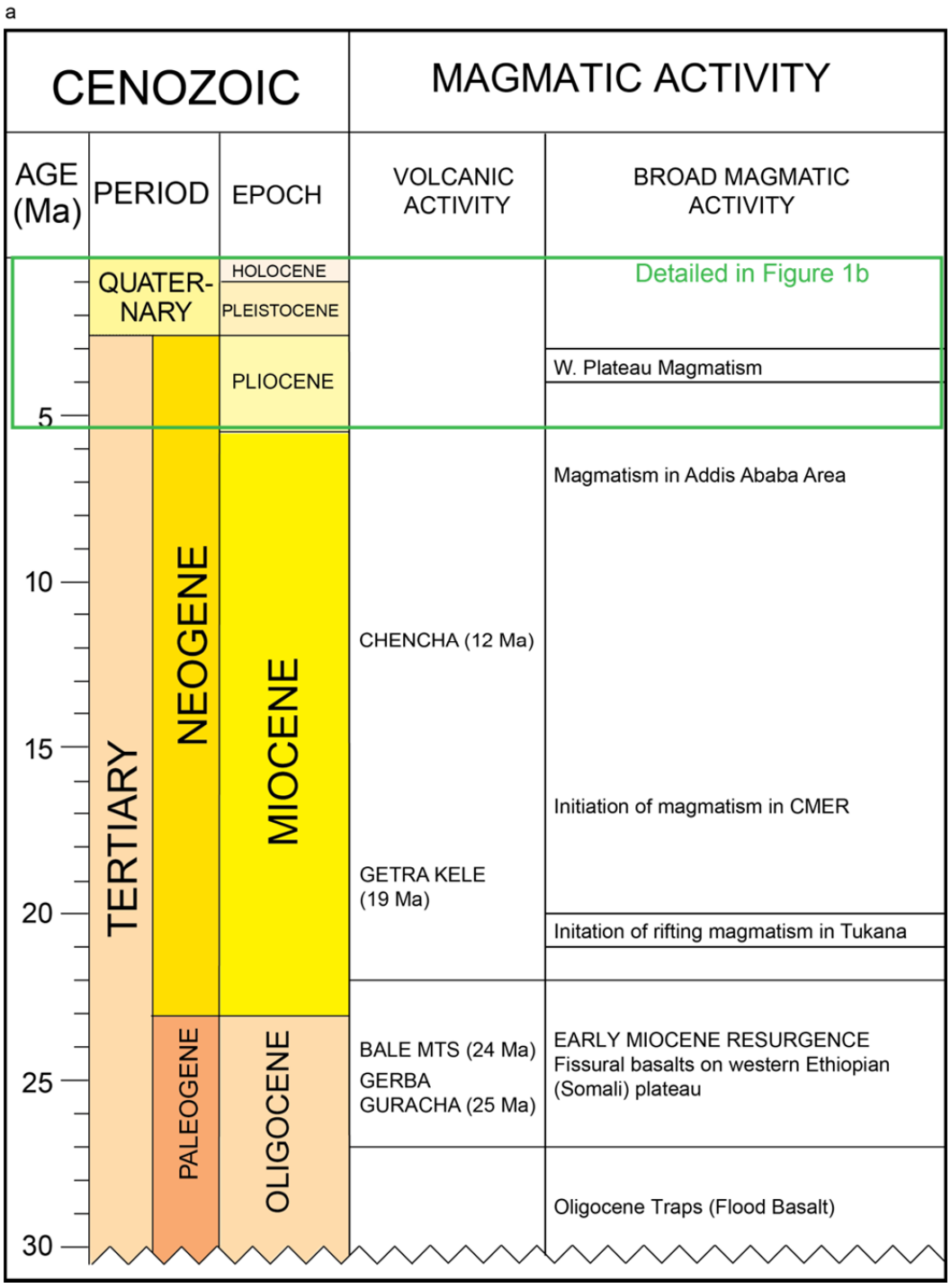

Figure 1.2.

Geochronometric age diagram of the magmatic activity of the Main Ethiopian Rift (MER) as detailed in the background section. CMER: Central Main Ethiopian Rift.

Figure 1.2. (cont'd.)

b

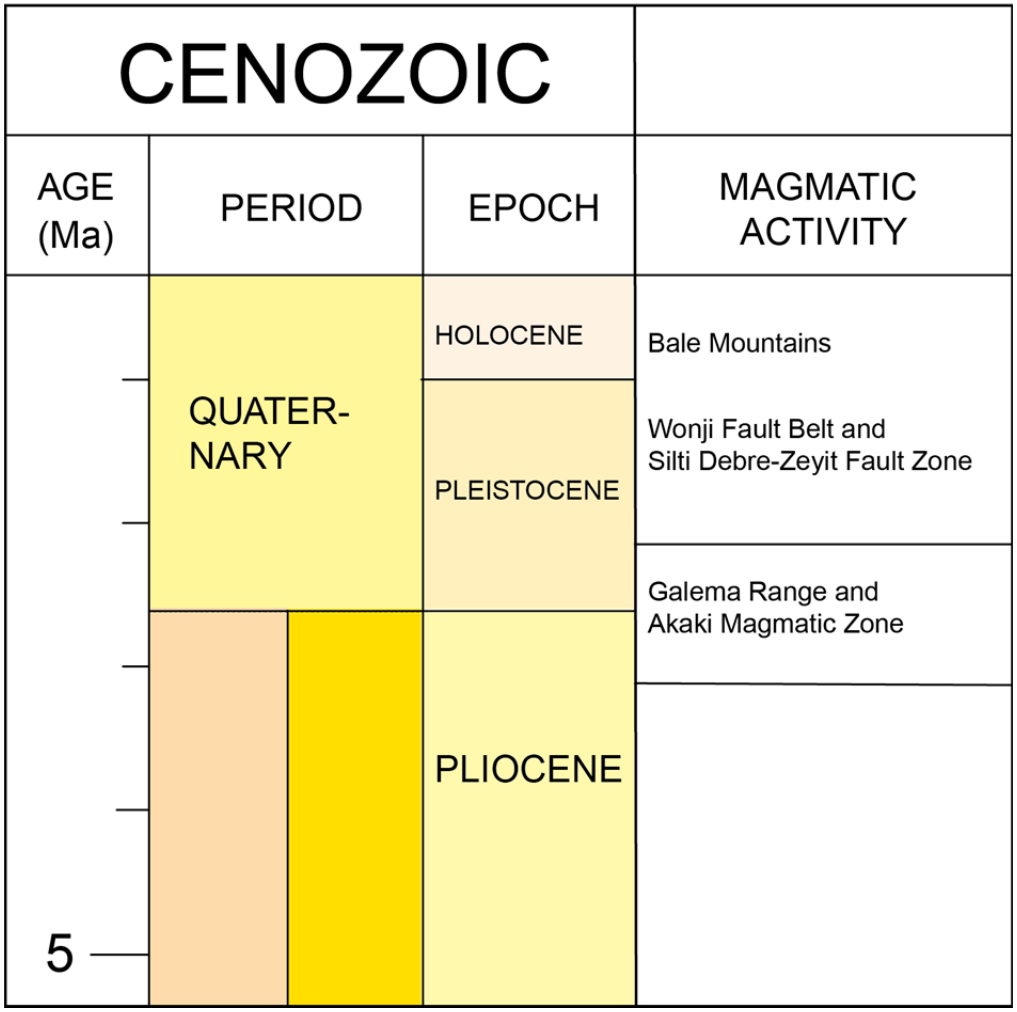

1.4.2 Afar

Magmatism in Afar began with the emplacement of dikes at 31-29 Ma (Figure 1.2a), contemporaneous with the emplacement of the flood basalts on the western rift, and has remained active to present day (Ferguson et al., 2013; Field et al., 2013; Rooney et al., 2013). The source melts of the mafic dikes in Afar show three end members; the Afar plume ("C" reservoir), depleted mantle (MORB) and the SCLM (Deniel et al., 1994; Rooney et al., 2012a; Rooney et al., 2013). Magmas from Erta Ale' have oxygen isotope signatures indicating

contamination by a hydrated oceanic crust in the melt perhaps indicating a contribution from the SCLM (Barrat et al., 1998b). These silicic magmas decreased in volume over time, suggesting that the effect of the plume was at first to provide heat and melt the SCLM. Afterward, the plume material itself melted (Deniel et al., 1994). Locations showing a complete sequence of magmatic products from basalt to rhyolite that were not erupted in order of increasing SiO_2 may indicate that the shift from silicic to basaltic magmatic activity in Afar is related to a dramatic change in magmatic plumbing systems, where the later basaltic magmas ascended with little time to fractionate (Field et al., 2013). These events were followed by dominantly silicic volcanism and the onset of rifting of the EARS in the Miocene (Rooney, 2017).

1.4.3 Miocene Magmatism and Rift Initiation of the EARS

In the early Miocene a resurgence of volcanism occurred throughout the region, with increased basaltic activity in Turkana and both shield volcanism and fissure fed basalts on the eastern and western Ethiopian plateaus (Figure 1.1a, b)(Figure 1.2a)(Rooney, 2017; Nelson et al., 2019). Subsequent magmatism largely localized to the developing MER and took the form of large silicic centers and smaller basaltic eruptions (Figure 1.1a)(Rooney et al., 2011).

Rifting initiated with the formation of a small rift basin in Afar at ~25 Ma (Figure 1.1a,b)(Figure 1.2a)(Bosworth et al., 2005). Contemporaneous with the activity in Afar is the magmatism of Gerba Guracha shield volcano on the western Ethiopian plateau at ~24-25 Ma (Figure 1.2a)(Rooney et al., 2014b; Rooney et al., 2017) and the Bale Mountains on the eastern Ethiopian plateau at ~ 24 Ma (Figure 1.1c) (Figure 1.2a)(Nelson et al., 2019). The magmatism of Gerba Guracha and the Miocene activity of the Bale Mountains indicate contributions to their melts from a HIMU-like ($\mu=^{238}U/^{204}U$; high $\mu = ^{206}Pb/^{204}Pb>20$) source component. This has been interpreted to be a similar process to melting of an ancient metasome that was created

during African continental assembly (Rooney et al., 2014b; Rooney et al., 2017; Nelson et al., 2019), similar to processes that occurred to form the High-Ti magma type (HT2) flood basalts (Furman et al., 2016).

At ~20-21Ma, rifting activity initiated in the Turkana area, south of the MER (Figure 1.1a,b)(Figure 1.2a) as a result of the plume impingement and associated extensional stresses (Morley, 1994; Bonini et al., 2005; Yirgu et al., 2006). This activity is described as faulting and fracturing of the crust as extension of the lithosphere began (Chorowicz, 2005). The magmatism within the Turkana area during this time was primarily basaltic in composition, and was generated as a result of an elevated mantle potential temperature of ~1513 °C (Rooney et al., 2012c; Rooney, 2017). Isotopic geochemistry of these Turkana area magmas indicates their source melts contain a contribution from a HIMU-like source reservoir (Furman et al., 2006b; Rooney, 2017). While the Afar plume was not impinging on the base of the lithosphere directly at Turkana, the initial expression of thinning and rifting is a result of pre-existing weaknesses in the lithosphere and crust (Bonini et al., 2005). Rifting subsequently migrated northward from Turkana, expressed by fracturing and faulting of the crust (Bonini et al., 2005).

1.4.4 Rift Evolution and Segmentation

Following the activity in the Afar and Turkana areas, rifting migrated and formed the Main Ethiopian Rift (MER), which is divided in the literature into multiple segments based on rift morphology, rift progression and tectonic and magmatic activity (Figure 1.1b)(e.g., Corti, 2009; Rooney, 2017). The three divisions of the Main Ethiopian Rift consist of the Northern, Central and Southern Main Ethiopian Rifts (NMER, CMER, SMER respectively) (Woldegabriel et al., 1990; Corti, 2009)(Figure 1.1b.). The NMER starts where the MER meets the Afar region (Figure 1.1b). There is no definite morphological change for this transition between segments

except for the broadening of the rift valley into Afar, or the pattern of faults at ~10°N that are interpreted to be the southern extension of the Red Sea rift (Wolfenden et al., 2004; Corti, 2009).

The trend of the MER is, in part, defined by the strike of faults produced during the continental rifting process, from the high angle border faults on the rift margins to the more recent faults within the rift. As discussed previously, faulting in the MER propagates downward ($\sigma1$) from the surface of the crust in response to extensional stresses ($\sigma3$) and the strike of the resultant faults ($\sigma2$) plays a role in defining the rift trend (Acocella et al., 2003). The current extension direction of the MER is roughly ESE-WNW (Ebinger and Casey, 2001b; Bonini et al., 2005; Casey et al., 2006; Corti, 2009; Keir et al., 2011). The orientation of the strike should be normal to the orientation extensional stress; however, analog models suggest that the strike of the fault is often the bisector of the angle between the plate motion vector and the strike of the rift trend normal to the plate motion vector (Corti et al., 2013). With this considered, the faults, and thereby the trend of the rift, should be mostly similar along the rift axis creating a nearly linear rift trend. The morphology of the MER as a whole shows that this is not the case and existing lithospheric heterogeneities or changes in extensional strain orientation are responsible for the non-linear morphology of the MER.

In the north, rifting proceeded south from the Afar area into the MER at ~11Ma to the latitude of the Yerer-Tullu Wellel Volcanotectonic Lineament (YTVL)(Figure 1.1b)(Wolfenden et al., 2004; Bonini et al., 2005; Furman, 2007; Keranen and Klemperer, 2007). At this location, the trend of the rift shifted westward to follow the trend of the YTVL, which is interpreted as being a series of pre-existing lithospheric weaknesses (Abebe et al., 1998; Keranen and Klemperer, 2007; Trestrail et al., 2017). Magmatism within the YTVL is interpreted to be a result of melt migration along the lithosphere-asthenosphere boundary (LAB) from locations

within the MER (Trestrail et al., 2017). The rifting in the YTVL was abandoned at about 6.6-3.5 Ma and continued southward into the CMER possibly as the result of a rotation in the stress field from N130° to N105° thereby making rifting in the YTVL less favorable (Keranen and Klemperer, 2007)

The NMER runs from the Afar region south to where it connects with the CMER at the Boru-Toru Structural High (BTSH) at ~7°N with a trend of about NE-SW (Figure 1.1b). South of the BTSH, the CMER border faults trend at ~N25°E-N35°E (Corti, 2009). Magmatic activity in the CMER began at ~17 Ma with eruptions of trachyte and basaltic lavas (Figure 1.2a)(Woldegabriel et al., 1990; Bonini et al., 2005). Following this was eruption of basaltic flows in the Addis Ababa area at ~7 Ma which decrease in age toward the rift (Figure 1.2a) (Morton et al., 1979), possibly illustrating the riftward progression of magmatic activity and strain accommodation. Volcanic activity on the western plateau is dated at ~4-3.3 Ma for volcanoes in E-W alignment associated with the YTVL (Figure 1.1a)(Figure 1.2a)(Morton et al., 1979; Woldegabriel et al., 1990). Volcanism then became concentrated into the Wonji Fault Belt (WFB) in the CMER at ~1.6 Ma, illustrating the abandonment of the rifting processes in the YTVL during the southward progression of the MER (Figure 1.1b)(Figure 1.2a)(Woldegabriel et al., 1990).

The CMER runs from the BTSH in the north, at the latitude of the YTVL, to the Goba Bonga lineament in the south (Figure 1.1c). The western margin of the CMER exists as a monocline between the western Ethiopian plateau and the rift floor (Morton et al., 1979; Woldegabriel et al., 1990). The eastern rift margin of the CMER is bounded by the ~5-8 Ma Asela-Sire border faults (Figure 1.1c)(Bonini et al., 2005; Abebe et al., 2010). These features generate an asymmetric cross section of the rift in the CMER. The magmatism of the CMER will

be discussed in detail in a later section. The CMER connects to the SMER in the south at the Goba Bonga lineament (Bonini et al., 2005)(Figure 1.1c).

In the SMER, the rift propagated northward from the Turkana area at ~23-25 Ma (Rooney, 2017) and border faults were initially formed with a trend of N5-20° (Figure 1.1b). The rift trend rotates eastward where it encounters the E-W trending Goba Bonga lineament to trend at N20-35° (Figure 1.1c)(Bonini et al., 2005; Corti, 2009; Corti et al., 2018). The Goba Bonga lineament is a rift-transverse structure, exhibiting E-W trending faults and magmatic features (Corti et al., 2018). This transverse structure may have inhibited the northward rifting progression from Turkana and is also attributed to the magmatism of the Bale Mountains (Figure 1.1c)(Corti et al., 2018). The magmatic activity in the SMER is less developed in comparison to the CMER and magmatic activity occurs over a broad area, illustrating that magmatic activity has not been focused as much as the CMER (Corti, 2009). The youngest expression of magmatic activity that migrated from the Turkana region, known as Getra Kele and Chencha, exists on the rift shoulders. These areas of magmatism have been dated at ~19 Ma and ~12 Ma, respectively (Figure 1.1b)(Figure 1.2a)(George et al., 1998; George and Rogers, 2002; Rooney, 2010). Geochemistry of these magmas indicates deep fractionation trends and poorly developed magmatic plumbing systems, though the source melt of Chencha is interpreted as being shallower. The WFB in the SMER shows fractionation depths similar to Chencha and the SDFZ on the western margin shows a deeper melting column, interpreted to be due to a thicker lithosphere in the area. The magmatic areas of the SMER illustrate how the depth of the lithosphere can vary across the rift as well as temporally, but exerts a first-order control on magmatism (Rooney, 2010).

Rifting then progressed southward once again until it joined with the stalled rifting from Turkana in the south (Figure 1.1a, b). At this point, the southward progressing rift activity may have overprinted and reactivated the initial rifting structures created earlier (Bonini et al., 2005). Rifting continued southward from Turkana where it bifurcates around the Tanzanian craton (Figure 1.1a)(Furman and Graham, 1999; Dugda, 2005; Corti, 2009). Rifting processes began in the western rift at ~12 Ma and the eastern rift at ~23 Ma (Figure 1.1a)(Kampunzu et al., 1986; Ebinger, 1989; Pasteels et al., 1989). The morphologies of the eastern and western rift lead to the general interpretation that they represent a less evolved stage of continental rifting.

1.4.5 Magmatism of the CMER

The Quaternary magmatic activity in the NMER is marked by the Wonji Fault Belt (WFB)(Figure 1.1c), a series of right stepping, en-echelon faults and dikes within the rift that run from Afar to the SMER, which are interpreted to be <1.8 Ma (Figure 1.2a)(Woldegabriel et al., 1990; Ebinger and Casey, 2001b; Acocella et al., 2003; Wolfenden et al., 2004; Bonini et al., 2005; Rooney et al., 2005; Casey et al., 2006; Kurz et al., 2007; Corti, 2009; Rooney et al., 2011). While there is some debate about the current activity of the EARS, recent InSAR measurements of volcanoes of the WFB display deformation, suggesting active, shallow magmatic processes (Biggs et al., 2011). The magmatic activity of the WFB displays bimodal chemistry with large, central silicic volcanoes and basaltic flows and aligned cinder cones (Woldegabriel et al., 1990; Ebinger and Casey, 2001b; Kurz et al., 2007).

The WFB marks the youngest rifting activity within the rift over the last 2 Ma. The trend of the WFB shows obliquity to the border faults that define the rift by upwards of ~20° (Figure 1.1c)(Ebinger and Casey, 2001b; Bonini et al., 2005). Features of the EARS such as the change in trend of the rift from north to south, the abandonment of the YTVL, and the obliquity of the

most recent in-rift faulting to the border faults, were at one time interpreted to be due to a rotation of the extensional stress field in the region (Korme et al., 1997; Keranen and Klemperer, 2007). However, a growing body of work suggests that pre-existing lithospheric structures such as the YTVL, BTSH, the Goba Bonga lineament, the Tanzanian craton, the suture zones created during continental assembly, and weaknesses formed as a result of the Cretaceous rifting event, all impart a first-order control on the orientation of fracturing and faulting of the lithosphere and its location during continental rifting, and there has been little to no rotation of the stress field in the MER (Rogers et al., 1998b; Acocella and Korme, 2002; Korme et al., 2004; Bonini et al., 2005; Dugda, 2005; Ebinger, 2005; Mackenzie et al., 2005; Casey et al., 2006; Maguire et al., 2006; Keranen and Klemperer, 2007; Agostini et al., 2011a; Agostini et al., 2011b; Keir et al., 2011; Corti, 2012; Autin et al., 2013; Corti et al., 2013). This interaction with lithospheric structures may also control the shape of the faults, creating sigmoid shaped faults as the fault tips interact with the previously emplaced border faults (Korme et al., 2004; Autin et al., 2013; Corti et al., 2013; Philippon et al., 2015), making interpretations of plate kinematics complicated at best. This illustrates that factors such as pre-existing lithospheric structures can influence development of the rift.

In conjunction with the WFB, another magmatic zone lies to the west in the CMER, known as the Silti-Debre Zeyit Fault Zone (SDFZ) (Figure 1.1c)(Figure 1.2a)(Mohr, 1962; Woldegabriel et al., 1990; Gasparon et al., 1993; Ebinger and Casey, 2001b; Acocella et al., 2003; Bonini et al., 2005; Rooney et al., 2005; Casey et al., 2006; Kurz et al., 2007; Rooney et al., 2007; Corti, 2009; Rooney et al., 2014b). The SDFZ is a linear chain of nested calderas, scoria cones and basaltic flows that run in a sub-parallel strike to the WFB from the BTSH in the

north into the SMER to the south (Woldegabriel et al., 1990; Rooney et al., 2005; Rooney et al., 2007).

The magmatic products of the SDFZ range from basalts to trachy-basalts while the magmatic products of the WFB display a bimodal chemistry of mafic dikes and flows and large silicic centers with rare intermediate products (Mohr, 1962; Woldegabriel et al., 1990). The SDFZ lavas in the CMER show chemical characteristics of being derived from melting of a peridotite source, with minor metasomatism, no crustal contamination signature and contain xenoliths that record a range of different depths (Rooney et al., 2005; Rooney et al., 2007; Rooney et al., 2011).

The WFB displays some similar characteristics to the SDFZ in the CMER in that there is no crustal contamination and only minor metasomatism. However, the fractionation depth of the WFB magmas has been interpreted to be <5km while the fractionation of the SDFZ magmas occurred at multiple depths, leading to the interpretation that the WFB has a more developed magmatic plumbing system (Rooney et al., 2007; Rooney, 2010). The depth of melting in the SDFZ has also been interpreted as being deeper than the WFB, supported by geophysical measurements in the area showing a shallow low velocity zone beneath the WFB (Bastow et al., 2008; Rooney et al., 2011). The presence of the shallow velocity zone beneath the off-axis WFB magmatism suggests that pre-existing lithospheric structures impart a first-order control over the location of magmatism and strain accommodation in continental rifting (Rooney et al., 2011). This pre-existing lithospheric structure has been interpreted as a shallowing of the lithosphere-asthenosphere boundary (LAB) under the WFB, asymmetric across the rift (Rooney et al., 2011). Geophysical studies, including seismic anisotropy, show that this steep LAB can channel melt

upwards and towards the WFB, inducing adiabatic melting (Holtzman and Kendall, 2010; Corti, 2012; Keir et al., 2015).

To the west of the SDFZ, on the rift shoulder, lies a lineation of scoria cones and lava flows known as the Akaki Magmatic Zone (AMZ)(Figure 1.1c)(Figure 1.2a)(Rooney et al., 2014a). Geochemical characteristics of the magmas of the AMZ show similarities to the SDFZ, including trace element enrichments and major element geochemistry indicating fractionation of clinopyroxene. Statistical analysis of the monogenetic vents of the AMZ shows a similar depth of magma reservoirs with respect to the SDFZ (Rooney et al., 2014a). Geophysical seismic analyses of the AMZ area shows elevated Vp/Vs ratios indicating intruded mafic material with a fluid phase. The proximity of the AMZ to the YTVL (Figure 1.1b, c), and the clustering analysis, suggest that it formed in a highly fractured crust, coincident with the formation of the pre-existing lithospheric structures of the YTVL. These pre-existing lithospheric weaknesses imparted a first-order control on the availability of magma in the area (Rooney et al., 2014a).

1.4.6 Rift Adjacent Magmatism

On the eastern Ethiopian plateau, a new pulse of magmatism occurred at the Bale Mountains at ~0.66-1.61Ma (Figure 1.1c)(Figure 1.2a)(Nelson et al., 2019). This episode of magmatism displays geochemical evidence of different source melt reservoirs than those which existed in the Miocene. These more recent magmas show evidence of the Afar plume, depleted mantle, and African lithosphere, similar to magmas from the more recent, within-rift WFB in the CMER (Nelson et al., 2019). As the HIMU-like signature of the Miocene magmas is no longer present, it is hypothesized that the ancient SCLM has been removed at the Bale Mountains since the Miocene (Nelson et al., 2019). This change in source melt chemistry at the Bale Mountains represents removal of an ancient, metasomatized SCLM through melting to form the intrusions

as the Bale Mountains. Within the rift, the focused magmatic intrusion of the WFB displays no HIMU-like signature in its source melt, indicating that there is a lack of a metasomatized SCLM within the rift of the CMER.

On the eastern plateau, outside of the rift-border faults that define the CMER, are a series of magmatic intrusions known as the Galema range (Mohr and Potter, 1976; Mohr, 1980; Woldegabriel et al., 1990)(Figure 1.1c). The Galema Range is an area of Cenozoic, rift-adjacent magmatism on the eastern Ethiopian plateau. Located at ~130km southeast of Addis Ababa, it exists to the east of the border faults that define the rift valley in the CMER (Figure 1.1c). Consisting of a series of right stepping, en-echelon mafic dikes trending at ~ 30°N and aligned, eroded scoria cones (Mohr and Potter, 1976; Mohr, 1980; Woldegabriel et al., 1990), the magmatic products of the dikes of the Galema Range have been previously described as being bimodal in silica content, composed of hawaiites (trachy-basalts) and comendites (rhyolites) (Mohr, 1980). K-Ar dating of samples of the Galema range have yielded dates of formation at ~2.1 to ~3.1 Ma (Figure 1.2a)(Mohr and Potter, 1976). The processes that resulted in the off-rift magmatic activity that formed the dikes of the Galema Range are not well constrained, but have been attributed to the possible existence of pre-existing lithospheric structures (Mohr and Potter, 1976; Corti, 2012). This area of focused magmatic intrusion, seemingly not in agreement with the currently accepted models of continental rifting in its location, will be the focus of this study.

Several models have been used to explain the occurrence of this rift-adjacent magmatic activity, each based on the assumption that the magma has migrated from a centrally located magma chamber to outside of the rift border faults. As described earlier, the magmatic activity of the YTVL resulted in magma interaction between the evolving rift and a Pre-Cambrian lineament. Extension along this lineament (and associated magmatism) was abandoned after the

local stress field rotated, resulting in rift migration to a different (and most recent) trend (Abebe et al., 1998; Keranen and Klemperer, 2007).

Magmatic activity outside of the rift in other areas may also be explained through modeling magmatic exploitation of pre-existing lithospheric heterogeneities. In one such model, the magma follows pathways formed by pre-existing lithospheric heterogeneities laterally from a location within the rift itself to be emplaced and erupt in an off-rift location (Corti, 2012). This model has been expanded upon to include the mechanisms necessary to force magma migration laterally, based on vertical forces induced from the weight of the blocks formed in the grabens within the rift (Corti et al., 2003; Corti et al., 2004; Maccaferri et al., 2014).

The documented occurrence of the 2009 Harrat Lunayyir seismic crisis was attributed to magma intrusion into the Saudi Arabian crust, creating the observed seismic activity. As this orientation of this seismic activity was between the orientation of the rift axis and the direction of extensional stress, the laterally intruded dikes were interpreted to be derived from the centrally located magma chamber located along the rift axis (Pallister et al., 2010).

Regardless of the mechanisms responsible for the emplacement of off-axis or off-rift magmatic activity, their existence, if related to the rifting processes, proves that focused magmatism does not occur in a symmetrical morphology across the rift as the current models of continental rifting predict. As magmatism accommodates an increasing amount of extensional strain as a rift evolves, these magmatic areas also suggest that extensional strain is accommodated over a much broader area than the currently accepted models state. Thus, while aspects of the current model of rift evolution may prove to be correct, a reevaluation of this model is needed to account for these off-rift and off-axis areas of focused magmatism.

1.5 Melt generation and sources

The melt associated with focused magmatic intrusions may be due, in part, to adiabatic melting as the asthenosphere rises in response to crustal thinning (Ebinger, 2005; Bastow and Keir, 2011; Keir et al., 2013). However, in addition to this adiabatically derived melt, the interaction of the Afar plume with the base of the lithosphere generates a considerable portion of magmatism within the EARS. The Afar plume is characterized through seismic imaging of large thermal upwelling from the core-mantle boundary to the base of the African lithosphere (Ritsema et al., 1999; Montelli et al., 2004; Montelli et al., 2006). While there is some debate as to the morphology of the plume, seismic imaging shows upper mantle low velocity anomalies which are related to the Afar plume (Bastow et al., 2005; Benoit et al., 2006a; Benoit et al., 2006b; Bastow et al., 2008; Garnero and McNamara, 2008). Upper mantle temperatures in Afar have been estimated at being ~140°C above ambient mantle temperatures (Rooney et al., 2012c; Ferguson et al., 2013; Armitage et al., 2015). Geochemical studies of the magmatic material intruded into the lithosphere create a chemical fingerprint of the plume that is impinging upon the base of the African lithosphere. Evidence of this chemical fingerprint in magmas of the EARS give indications as to the contribution of the Afar plume as a component of the source melt.

The composition of the Afar plume was initially categorized to be of a HIMU composition based on an initial value of $^{206}Pb/^{204}Pb$ >20 from samples from the Gulf of Aden (Schilling et al., 1992). This has since been revised through $^{206}Pb/^{204}Pb$ geochemistry to be of "C" reservoir based on a larger sample set and new value of ~19.6 (Rooney et al., 2012a; Giordano et al., 2014; Rooney et al., 2014b). This interpretation is supported by ε_{Nd} vs. ε_{Hf} data and $^{3}He/^{4}He$<15 R_A values from the same suite of samples (Rooney et al., 2012a).

The composition of the basalts from the EARS suggests that they are not generated from a melt of "C" reservoir alone and some other source melt materials must be incorporated (Schilling et al., 1992; Furman, 1995; Furman and Graham, 1999; Tommasini et al., 2005; Furman, 2007; Rooney et al., 2012a; Giordano et al., 2014). Trace element geochemical trends of the basalts of the EARS show at least three end members of compositions of the melted source material; the Afar plume, the depleted mantle (DM) and the African lithosphere (Hart et al., 1989; Schilling et al., 1992; Rooney et al., 2012a).

The depleted mantle component of the magmas of the EARS is defined as having lower $^{207}Pb/^{204}Pb$ values, similar to MORB (Schilling et al., 1992; Rooney et al., 2012a). The compositions of magmas from the EARS plot in an array between the accepted values of $^{207}Pb/^{204}Pb$ for both the "C" reservoir and the DM; indicating that they must be a mixture between the two sources (Schilling et al., 1992; Rooney et al., 2012a).

The values of ε_{Nd} for magmas of the EARS support the two end member array of "C" reservoir and DM, however, when plotted with these two sources, an indication is given of a third end member component. A plot of ε_{Nd} data shows an array between these two sources and the composition of the African lithosphere (Rooney et al., 2012a). Previously, based on $^{207}Pb/^{204}Pb$ vs. $^{208}Pb/^{204}Pb$ data plots, this component was interpreted to be some hybridized mixture of depleted mantle material (Schilling et al., 1992). This hybrid source is formed when African lithospheric material founders, and mixes into the DM prior to melt generation and rift related magmatism (Schilling et al., 1992; Rooney et al., 2012a). This hybrid material then mixes with Afar plume material to form the three component source melt observed in many EARS magmas.

Some magmas of the EARS contain a chemical signature of a metasomatic component in their source melts. This signature is evident in a negative K and positive Ti in primitive mantle normalized trace element plots (Rooney, 2017). This component may be an indication of a metasomatized sub-continental lithospheric mantle that has been melted and incorporated into the source melts of these magmas (Furman et al., 2016; Rooney et al., 2017; Nelson et al., 2019). The SCLM material may have been the cause of the previous interpretations of the composition of the Afar plume as HIMU reservoir (Schilling et al., 1992; Rooney et al., 2012a).

Other geochemical analyses suggest that African crustal material is incorporated into the melt. African continental crust is inferred as being an end member in the source melt of the basalts based on negative Zr/Nb trends with enrichment in Ba, K, Rb and Th (Hart et al., 1989; Tommasini et al., 2005). This crustal component was assimilated into the melt when either deeper mafic melt ponded at the base of the crust on ascent (Tommasini et al., 2005) or during fractional crystallization and assimilation processes within the continental crust (Hart et al., 1989).

The history of rifting processes of the EARS indicates a complicated interplay between the lithosphere of the African continent, magmatism, and the Afar plume. Previous hypotheses regarding the evolution and progression of continental rifting processes of the EARS have proven to be too simplistic with regard to this complexity. The previous hypotheses ignore the presence of rift-adjacent magmatism in their explanation of rifting evolution. However, as the geologic history of the EARS shows that some areas of rift-adjacent magmatism seem intimately linked to the rifting processes, they must be included in explanations of how continental rifting occurs. In some cases, investigations of rift-adjacent magmatism may provide valuable details

about continental rifting processes as they can occur during a transitional state of continental rifting, after rift initiation, but before continental breakup.

2. MAGMATICALLY ASSISTED OFF-RIFT EXTENSION – THE CASE FOR BROADLY DISTRIBUTED STRAIN ACCOMMODATION

2.1 Introduction

As a continental rift progresses towards an oceanic spreading center, the mechanism of strain accommodation must transition from faulting and thinning of the lithosphere, to focused magmatic intrusion (Korme et al., 1997; Buck, 2004; Wolfenden et al., 2005; Buck, 2006; Casey et al., 2006; Corti, 2009; Rooney, 2010; Corti, 2012; Mazzarini et al., 2013b; Rooney et al., 2014a). Specifically, strain is thought to migrate from high angle border faults to zones of focused magmatic activity within the rift that are adjacent to the rift border faults (Ebinger and Casey, 2001a). Though the specific mechanisms remain controversial, these zones of focused magmatic intrusion must eventually migrate toward the rift axis as possible precursors to oceanic spreading centers (Ebinger, 2005). While elegant in its simplicity, observations from rifting environments reveal magmatic features that are unexplained by this model. For example, magmatism outside of the rift proper is frequently observed to be contemporaneous with episodes of both mechanical extension and focused magmatic intrusion within the rift (Abebe et al., 1998; Keranen and Klemperer, 2008). Seemingly related to the rifting process, this magmatism is not adequately explained by the currently accepted models of continental rifting.

The East African Rift System (EARS) preserves within it a broad range of rifting morphologies from incipient rifting in the south to the transition from continental to oceanic crust in the north (Gregory et al., 1896; Woldegabriel et al., 1990; Ebinger and Casey, 2001a; Ebinger, 2005; Corti, 2009). The existing models of strain accommodation within continental

Chiasera, B., Rooney, T.O., Girard, G., Yirgu, G., Grosfils, E., Ayalew, D., Mohr, P., Zimbelman, J.R. and Ramsey, M.S.(2018) Magmatically assisted off-rift extension—The case for broadly distributed strain accommodation Geosphere, v. 14, p. 1544-1563.

rifting settings were borne of studies of the EARS. As studies of this system progressed, the initial models of rift-centered strain accommodation have evolved into models where the extensional strain is accommodated both by the rift border faults and the magmatic belts within them (Ebinger, 2005; Wolfenden et al., 2005). The amount and of extensional strain that is accommodated by the rift border faults and magmatic belts, and the timing of this accommodation, remain controversial (e.g. Bilham et al., 1999; Bendick et al., 2006; Casey et al., 2006; Pizzi et al., 2006; Agostini et al., 2011a; Molin and Corti, 2015). The Main Ethiopian Rift, located directly south of Afar, is a transitional region whereby strain is accommodated both by rift border faults and focused magmatic intrusion (Ebinger and Casey, 2001a; Casey et al., 2006; Pizzi et al., 2006; Corti, 2009)(Figure 2.1a). Within the Main Ethiopian Rift, recent magmatic activity has been focused along linear belts known as the Silti Debre-Zeyit Fault Zone (SDFZ) and the Wonji Fault Belt (WFB) (Mohr, 1962; Morton et al., 1979; Woldegabriel et al., 1990; Ebinger and Casey, 2001a; Acocella et al., 2003; Wolfenden et al., 2004; Bonini et al., 2005; Rooney et al., 2005; Casey et al., 2006; Kurz et al., 2007; Rooney et al., 2007; Corti, 2009; Rooney et al., 2014a)(Figure 2.1b). While much attention has been given to the magmatic activity along these linear belts within the rift proper (Rooney et al., 2007; Rooney, 2010; Rooney et al., 2011; Rooney et al., 2014a; Medynski et al., 2015), there is a growing realization that magmatic activity associated with rifting is more diffuse (e.g., Abebe et al., 1998; Meshesha and Shinjo, 2007; Rooney et al., 2016; Trestrail et al., 2016).

Here we undertake a petrographic and geochemical analysis of an area of focused magmatic intrusion on the South-Eastern Ethiopian plateau, which is interpreted to be contemporaneous with rift development but occurs outside of the Ethiopian Rift valley (Mohr and Potter, 1976;

Chiasera, B., Rooney, T.O., Girard, G., Yirgu, G., Grosfils, E., Ayalew, D., Mohr, P., Zimbelman, J.R. and Ramsey, M.S.(2018) Magmatically assisted off-rift extension—The case for broadly distributed strain accommodation Geosphere, v. 14, p. 1544-1563.

Kennan et al., 1990). The Galema range is a NNE trending series of en-echelon dikes, lavas and eroded cinder cones, located approximately 35 km east of the Asela-Sire Border Fault (Figure 2.1c). We focus upon constraining the magmatic plumbing system of the Galema range through the use of geochemical and petrographic analyses, offering insight into the architecture of the magmatic plumbing system in which the magma ascended and the depths of crystal phase fractionation. The depths at which a magma commonly stalls on ascent are, in part, determined by the extensional stresses acting on the lithosphere at the time, and these volumes at depth represent presumed zones of magmatic strain accommodation (Corti et al., 2003). In this manner, a profile of the lithospheric strain at an off-rift location may be constructed. Our results demonstrate that the Galema range accommodated extensional strain after the initial formation of the border faults that define the rift, but before the inception of zones of focused magmatic intrusion within the rift (i.e. WFB, SDFZ). This suggests that strain accommodation by focused magmatic intrusion can occur over a broad area in continental extension settings. Furthermore, the emplacement of the Galema range also shows that migration of focused magmatic activity toward the rift axis is not always a straightforward progression as some models of continental rifting evolution assert.

2.2 Background

2.2.1 Cenozoic Magmatic Evolution Of The African-Arabian Large Igneous Province

Cenozoic magmatic activity in East Africa commenced in the Eocene with basaltic volcanism in the broadly rifted zone in the Turkana area of northern Kenya and southern Ethiopia at ~45 Ma (Ebinger et al., 1993b; George and Rogers, 2002; Corti, 2009)(Figure 2.1a). Large scale

Chiasera, B., Rooney, T.O., Girard, G., Yirgu, G., Grosfils, E., Ayalew, D., Mohr, P., Zimbelman, J.R. and Ramsey, M.S.(2018) Magmatically assisted off-rift extension—The case for broadly distributed strain accommodation Geosphere, v. 14, p. 1544-1563.

flood basalts were emplaced during the Oligocene as a result of the impingement of the Afar plume (Baker et al., 1996; Hofmann et al., 1997; Rochette et al., 1998; Pik et al., 1999; Kieffer, 2004). In the early Miocene a resurgence of volcanism occurred throughout the region, with increased basaltic activity in Turkana and both shield volcanism and fissure fed basalts on the Ethiopian plateau (Rooney, 2017). Subsequent magmatism is largely localized to the developing MER and took the form of large silicic centers and smaller basaltic eruptions (Rooney et al., 2011).

2.2.2 Development of the MER

The MER runs from Afar in north-eastern Ethiopia to Turkana in Kenya, and changes from a ~NE-SW trend in the north to a ~N-S trend in the south. The MER is divided into three sectors: the Northern Main Ethiopian Rift (NMER), the Central Main Ethiopian Rift (CMER) and the Southern Main Ethiopian Rift (SMER) (Woldegabriel et al., 1990; Corti, 2009)(Figure 2.1a). These sectors evolved at different times and into a non-linear trend (Woldegabriel et al., 1990; Wolfenden et al., 2004; Bonini et al., 2005; Keranen and Klemperer, 2008; Corti, 2009; Abebe et al., 2010; Balestrieri et al., 2016).

The CMER is bounded by the Boru-Toru Structural High (BTSH) and the Goba-Bonga structural lineament (Bonini et al., 2005)(Figure 2.1a.). The main border fault in this area of the CMER, known as the Asela-Sire border fault, is a segmented system of high-angle, normal faults (>60°) that define the MER. These trend at approximately N30°E-N40°E in this, separating the CMER from the south-eastern Ethiopian plateau (Woldegabriel et al., 1990; Boccaletti et al., 1998; Abebe et al., 2010), and are mid-Miocene (Ebinger and Casey, 2001a), no older than ~8 Ma (Woldegabriel et al., 1990; Bonini et al., 2005; Abebe et al., 2010).

2.2.3 Methods of Extensional Strain Accommodation in the CMER

The Asela-Sire border faults formed during the southward propagation of rifting from Afar. (Bonini et al., 2005; Abebe et al., 2007; Keranen and Klemperer, 2008). The N-S trend of the Asela-Sire border faults led to the interpretation that the orientation of extensional stress had rotated to roughly E-W from the previous NW-SE direction (Boccaletti et al., 1998; Bonini et al., 2005). It should be noted that this difference in trend has been attributed, not to rotation of the stress field, but to the interference of pre-existing lithospheric weaknesses interacting with an extensional stress field oblique to the trend of the rift (Corti, 2008; Agostini et al., 2011b; Corti et al., 2013). Post-dating the initiation of the Asela-Sire border faults, the magmatic activity within the CMER was focused on the Quaternary Wonji Fault Belt (WFB) and the Silti-Debre Zeyit Fault Zone (SDFZ) (Mohr, 1962; Woldegabriel et al., 1990; Rooney et al., 2014a)(Figure 2.1b). While the WFB accommodates some of the extensional strain in the CMER, the Asela Sire rift border faults also currently continue to accommodate a portion of this strain (Pizzi et al., 2006; Corti, 2009; Agostini et al., 2011a). However, the amount of extensional strain accommodated by the rift-border faults and the timing of this strain accommodation by both mechanisms remains controversial.

Analysis of the river network patterns in the CMER indicates that a portion of the extensional strain is accommodated by the Asela-Sire border faults (Molin and Corti, 2015). GPS velocities show that the recent extension rate across the MER is approximately 4.0 ± 0.9 mm/yr., accommodated by both mechanical stretching and faulting of the lithosphere as well as aseismic dike injection (Bendick et al., 2006).

Chiasera, B., Rooney, T.O., Girard, G., Yirgu, G., Grosfils, E., Ayalew, D., Mohr, P., Zimbelman, J.R. and Ramsey, M.S.(2018) Magmatically assisted off-rift extension—The case for broadly distributed strain accommodation Geosphere, v. 14, p. 1544-1563.

Structural analysis of the CMER indicates that the Aslea-Sire border faults have recently accommodated extensional strain - as recorded by fault-slip data recorded across the rift (Agostini et al., 2011a). This analysis also indicates that extensional strain accommodation of the WFB, via faulting of the crust, is subordinate to that accommodated at the eastern rift-border fault. However, forces exerted by the magma overpressure of an intruding dike can reduce the amount of observable slip along nearby faults (Rubin and Pollard, 1988). The compressive force exerted by the intruding dike in the direction of σ_3, as a result of the buoyancy of an ascending magma, can change the local stress field in the host rock by increasing compression to each side of the dike and reducing compression above (Rubin and Pollard, 1988). One consequence of this is that pre-existing faults that are located adjacent to the intruding dike (i.e. those not generated by intrusion of the dike) can become locked (Rubin and Pollard, 1988). Exploitation of pre-existing faults by magmatic intrusion on ascent adds volume to the host rock, accommodating extensional strain (Rubin and Pollard, 1988). In areas experiencing both faulting and intrusion (such as the WFB), the total amount of deformation is partitioned between fault-slip and volumetric increase, but the observable amount of fault-slip appears to be reduced, complicating estimates of amount of strain accommodation by faulting.

2.2.4 Magmatic Strain Accommodation During The Plio-Quaternary

2.2.4.1 Wonji Fault Belt And Silti Debre-Zeyit Fault Zone

The Wonji Fault Belt (WFB), located near the eastern rift margin and subparallel to the rift axis in the CMER, is described as a series of right stepping, en-echelon faults and dikes within the rift, which are interpreted to be <1.8 Ma (Woldegabriel et al., 1990; Ebinger and Casey, 2001a; Wolfenden et al., 2004). The volcanism of the WFB is described as being bimodal in

nature with silicic volcanism, sometimes forming large calderas, and basaltic volcanism forming lava flows and scoria cones (Mohr, 1967; Mohr et al., 1980; Rooney et al., 2005; Kurz et al., 2007).

Located toward the western rift margin, the SDFZ is characterized as a linear chain of nested calderas, scoria cones, and basaltic flows with associated silicic centers also oriented subparallel to the rift axis (Woldegabriel et al., 1990; Gasparon et al., 1993; Rooney et al., 2005; Rooney et al., 2007; Rooney et al., 2011).

The locations of both the WFB and SDFZ along the rift margins may be due to the existence of pre-existing lithospheric weaknesses within the MER. When a low obliquity extensional stress field is applied to these weaknesses, the result is formation of boundary faults oblique to the extension direction, followed by formation of internal faults nearly perpendicular to the direction of extension (Corti, 2008; Agostini et al., 2009; Agostini et al., 2011b). Analog modeling of stress direction oblique to pre-existing lithospheric weakness suggests that the WFB in the CMER represents an intermediate stage of rift development (Agostini et al., 2011b).

2.2.4.2 The Galema Range

We focus on the Galema range, an area of Pliocene, rift-adjacent magmatism on the south-eastern Ethiopian plateau (Figure 2.1c). Located ~130 km southeast of Addis Ababa, it occurs to the east of the border faults that define the rift valley in the CMER (Figure 2.1c). Morphologically, the Galema range displays striking similarities to magmatic features located within the rift valley of the MER. For example, the Galema range consists of a series of right stepping, en-echelon mafic dikes trending at ~ 10-20°N and aligned, eroded scoria cones (Mohr and Potter, 1976; Mohr, 1980; Woldegabriel et al., 1990), similar to the WFB. The Galema range

Chiasera, B., Rooney, T.O., Girard, G., Yirgu, G., Grosfils, E., Ayalew, D., Mohr, P., Zimbelman, J.R. and Ramsey, M.S.(2018) Magmatically assisted off-rift extension—The case for broadly distributed strain accommodation Geosphere, v. 14, p. 1544-1563.

extends from the volcanic center in the north known as Gara Badda to the volcanic center in the south known as Gara Enkulo (Figure 2.1c). The dikes, which constitute the range, span a distance of ~70 km, and are arranged in a dextral, en-echelon formation within a ~7 km wide fissure system (Mohr and Potter, 1976). Maars and cinder cones exist between the two volcanic centers, along with the ~4.5 m thick dikes that gradually disappear at the latitude of Gara Enkulo (Mohr and Potter, 1976). The Galema range rises to an elevation ~1000 m above the south-eastern Ethiopian plateau and is comprised of the magmatic pile erupted from the dikes and silicic centers (Mohr and Potter, 1976). Evidence of this volcanism can be found in the volcanic edifices that appear within the Galema range. Volcanic edifices within the WFB are dominantly of two varieties: cinder cones and large silicic centers. The Galema range preserves within it volcanic necks of silicic composition, which are the exposed magmatic plumbing system of large silicic centers (Figure 2.2). Moreover, the scoria cones found within the WFB are rooted by dikes; the exposed dikes evident in the Galema range are parallel to the magmatic plumbing system of these scoria cones. Field work has revealed eroded scoria cones in the southern portion of the study area (Mohr and Potter, 1976).

Chiasera, B., Rooney, T.O., Girard, G., Yirgu, G., Grosfils, E., Ayalew, D., Mohr, P., Zimbelman, J.R. and Ramsey, M.S.(2018) Magmatically assisted off-rift extension—The case for broadly distributed strain accommodation Geosphere, v. 14, p. 1544-1563.

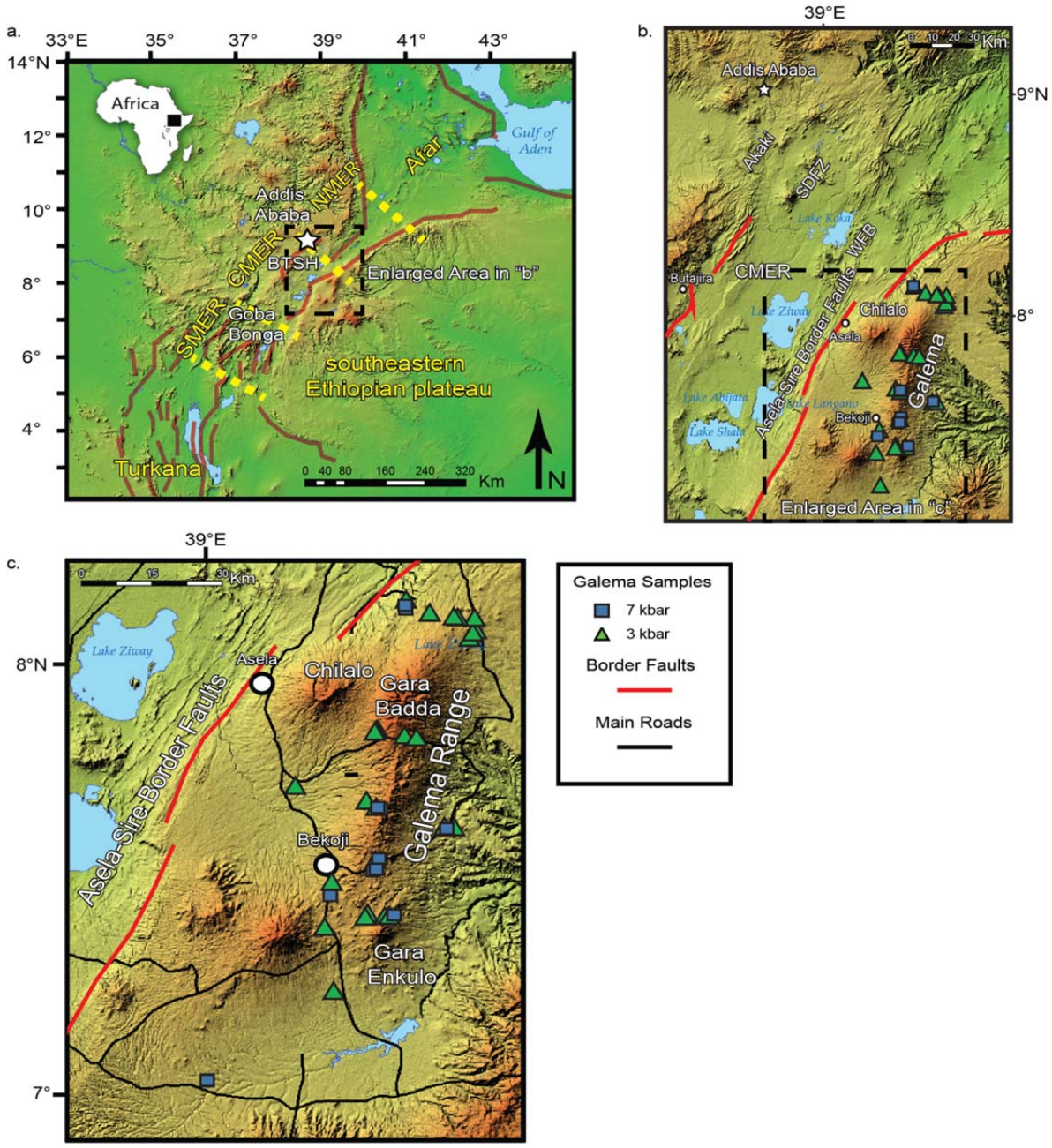

Figure 2.1.

(A) Map of the Main Ethiopian Rift (MER) section of the East African Rift System (EARS) showing Afar, the Northern Main Ethiopian Rift (NMER), Central Main Ethiopian Rift (CMER),

Chiasera, B., Rooney, T.O., Girard, G., Yirgu, G., Grosfils, E., Ayalew, D., Mohr, P., Zimbelman, J.R. and Ramsey, M.S.(2018) Magmatically assisted off-rift extension—The case for broadly distributed strain accommodation Geosphere, v. 14, p. 1544-1563.

Figure 2.1. (cont'd.)

and Southern Main Ethiopian Rift(SMER). Also shown is the Boru-Toru structural high (BTSH). (B) Map of the Central Main Ethiopian Rift (CMER) showing location of the Wonji Fault Belt (WFB), Silti-Debre Zeyit Fault Zone (SDFZ), and the Akaki magmatic zone. (C) Enlarged portion of the Central Main Ethiopian Rift (CMER) showing the location of the Galema range and samples used in this study. Samples are color coded to indicate their inferred depths of fractionation derived from thermodynamic MELTS modeling (see text for details).

Chiasera, B., Rooney, T.O., Girard, G., Yirgu, G., Grosfils, E., Ayalew, D., Mohr, P., Zimbelman, J.R. and Ramsey, M.S.(2018) Magmatically assisted off-rift extension—The case for broadly distributed strain accommodation Geosphere, v. 14, p. 1544-1563.

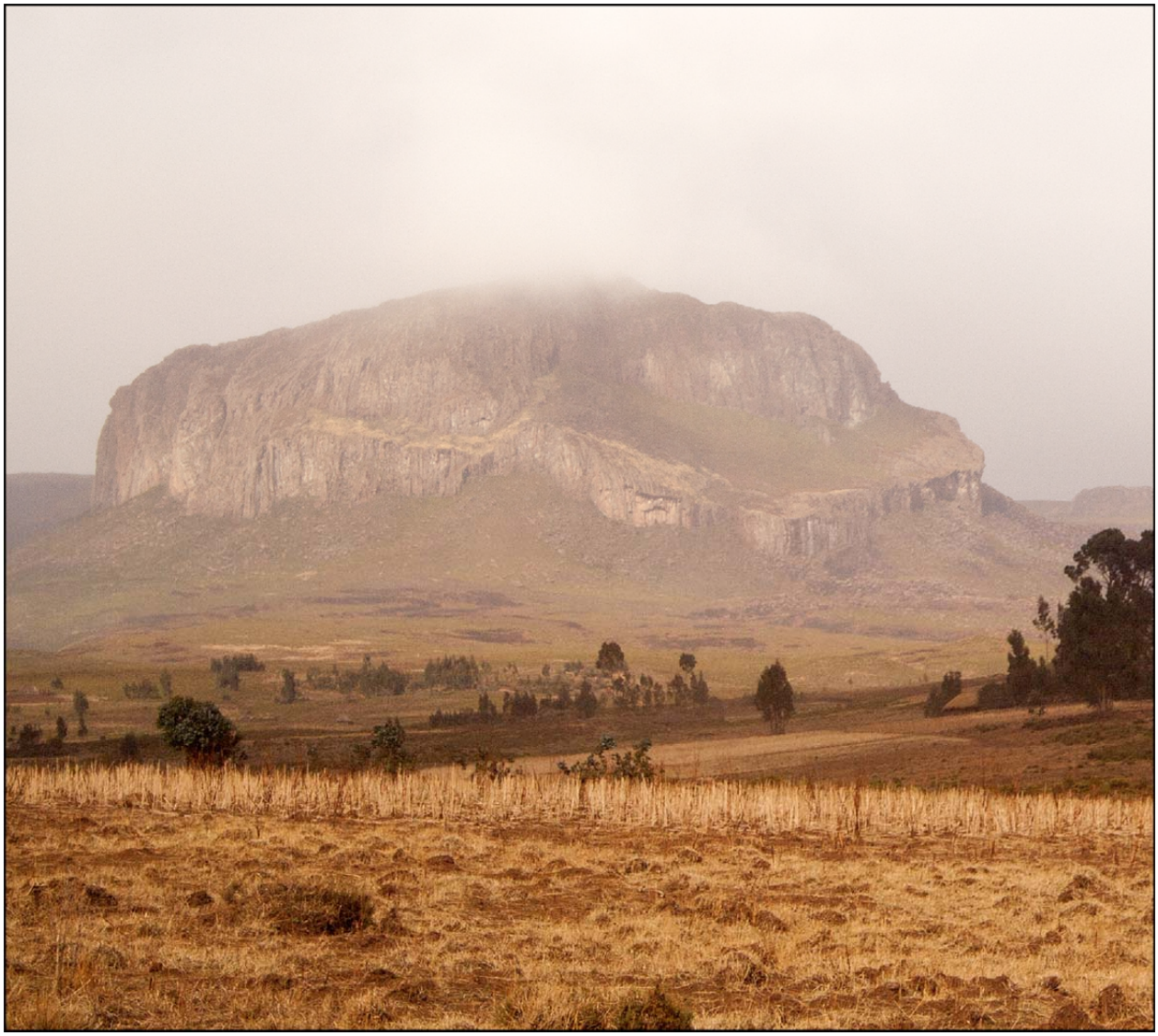

Figure 2.2.

Photograph of a silicic center in the Galema range, which is evidence of the volcanic activity responsible for the relief of the range before erosion. Photo courtesy of T.O. Rooney.

While the magmatic features of the Galema range and the WFB display striking morphological similarities, the direct evidence of the existence of faulting of the Galema range is

less apparent than that of the WFB. This may indicate that while both areas have accommodated extensional strain, the amount of strain accommodated by faulting in the Galema range may be less profound. Indirect evidence, however, suggests that faults existed prior to the onset of magmatic intrusion. Recent work has highlighted the influence of pre-existing faults and fractures within the lithosphere on the morphology of dike swarms and volcanic fields (Le Corvec et al., 2013; Mazzarini et al., 2016). These studies indicate that in areas of relatively thicker crust, alignments of dikes and monogenetic vents (i.e. scoria cones) are parallel to the trend of pre-existing lithospheric fractures and faults (Mazzarini et al., 2016). Thus, the alignment of dikes and scoria cones of the Galema range, in the area of thicker crust (see section 5.5) of the eastern Ethiopian plateau, suggest that the ascending mafic dikes exploited pre-existing lithospheric faults and fractures. As the ascending dikes are captured by the pre-existing faults (Le Corvec et al., 2013), evidence of the existence of these faults may be obscured as they are cut by the intruding magma (Rubin and Pollard, 1988).

Glaciation during the middle to late Pleistocene, eroded the up to 2000m thick magma pile and exposed the dikes that had fed the cinder cones of the Galema range (Mohr and Potter, 1976). Taken together, it is evident that the magmatic plumbing systems of both silicic and mafic edifices are exposed within the Galema range. It is important to note that such erosion would have removed all faulting induced above propagating dikes, as mentioned earlier. The implication of such erosion would be the preservation of a magmatic plumbing system, broadly similar to that beneath the modern WFB, but devoid of clear evidence of faulting.

K-Ar dating of samples of the Galema range have yielded dates of formation at ~2.1 to ~3.1 Ma (Mohr and Potter, 1976) and 1.97 ± 0.02 Ma (Kennan et al., 1990). The existence of off-rift

Chiasera, B., Rooney, T.O., Girard, G., Yirgu, G., Grosfils, E., Ayalew, D., Mohr, P., Zimbelman, J.R. and Ramsey, M.S.(2018) Magmatically assisted off-rift extension—The case for broadly distributed strain accommodation Geosphere, v. 14, p. 1544-1563.

zones of focused intrusion such as the Galema range are not well constrained within the current rifting framework, but have been attributed to the possible existence of pre-existing lithospheric structures (Mohr and Potter, 1976; Corti, 2012).

2.3 Methods

2.3.1 Whole Rock Geochemical Analysis

A field excursion in 2008 recovered 77 samples from dikes, basaltic flows, scoria cones and silicic centers of the Galema range. These samples were cut to minimize alteration due to weathering before being further cut into ~30 g billets. After polishing to remove saw marks and cleaning in an ultrasonic bath of deionized water, the billets were crushed in a steel jaw crusher and then powdered in a Bico ceramic disk mill. The powders were then fused with a lithium tetraborate ($Li_2B_4O_7$) flux into glass discs following procedures detailed elsewhere (e.g. Rooney et al., 2012). Major element oxide abundances and loss on ignition values were determined via X-Ray fluorescence analysis on a Bruker S4 PIONEER instrument at Michigan State University (Table 1)(Supplementary Tables).

2.3.2 In-Situ LA-ICP-MS Mineral Analysis

Analyses of clinopyroxene and plagioclase mineral phases were performed on a representative subset of samples ranging primitive to evolved compositions, on the basis of their bulk rock MgO content, using in-situ spot analyses by Laser-Ablation Inductively Coupled Plasma Mass Spectrometry (LA-ICP-MS) following protocols developed together with other studies (Rooney et al., 2016; Trestrail et al., 2016). Standard petrographic thin sections were loaded into a 15 x 15 cm two-volume HelEx sample cell, integral to a Teledyne Photon

Chiasera, B., Rooney, T.O., Girard, G., Yirgu, G., Grosfils, E., Ayalew, D., Mohr, P., Zimbelman, J.R. and Ramsey, M.S.(2018) Magmatically assisted off-rift extension—The case for broadly distributed strain accommodation Geosphere, v. 14, p. 1544-1563.

Machines Analyte G2 193 nm excimer laser ablation system at Michigan State University. Multiple spots of 110 μm diameter in individual crystals were ablated for 30 s with a laser repetition rate of 10 Hz at a fluence of 4.1 J/cm^2. A gas blank was collected after each sample for ~ 20 s and gas blank intensities were subtracted from ablation intensities. The ablated material was transferred to a Thermo Scientific ICAP Q quadrupole ICP-MS in a flux of 0.75 L/min of high purity He carrier gas for analysis. The ICP-MS was tuned for highest intensities, low oxide production rate (ThO/Th < 0.7%) and low double-charged cation formation rate (Ba^{2+}/Ba < 1.5%) by performing a surface scans of NIST SRM 612 glass standard, while signal stability was subsequently tested over a 3-minute surface scan of NIST SRM 612. Data were calibrated using 20 natural and synthetic geological standards (Supplementary Tables) mounted on the same sample tray together with the samples. These were analyzed sequentially without opening the sample chamber and interrupting automation. Data were collected using the ICP-MS in kinetic energy discrimination (KED) mode in which the ionized material circulates through a collision cell fluxed with He, reducing isobaric interferences with oxide and argide compounds, enhancing detection limits of light mass isotopes including major elements and lowering their signal intensities, allowing for their quantification at a precision and accuracy similar to trace elements (Supplementary Tables). Data were drift corrected using surface scans of well-characterized fused rock powder standards (JB-1a and BHVO-1) analyzed approximately every hour during analysis at 10μm/s and other ablation parameters identical to those described above. Replicated analyses of JB-1a and BHVO-1 analyzed as unknowns by surface scans analyses achieved ±5% accuracy and day-averaged reproducibility of 5% (1σ) or better (Supplementary Tables). The raw sum of all major element oxides with Fe expressed as FeO was calculated for each mineral

Chiasera, B., Rooney, T.O., Girard, G., Yirgu, G., Grosfils, E., Ayalew, D., Mohr, P., Zimbelman, J.R. and Ramsey, M.S.(2018) Magmatically assisted off-rift extension—The case for broadly distributed strain accommodation Geosphere, v. 14, p. 1544-1563.

analysis, in order to normalize all major and trace element compositions to 100 wt. % oxides. Practically, 100 wt. % oxides was our internal standard for all mineral analyses, such assumption is reasonable for all stoichiometrically anhydrous minerals. If necessary, certain laser ablation signals were then filtered to remove certain sections of ablation sequences exhibiting evidence of micro-crystal inclusions and or alteration. Reproducibility of the in-situ spot analyses was assessed separately by performing ten 30-second ablations on each of the basalt glass standards GSD-1G and BCR-2G for major and trace elements using analytical conditions identical to those above; on these homogeneous glass materials, reproducibility is also generally of 5% (1σ) or better (Supplementary Tables).

2.4 Results

2.4.1 Petrography

In hand sample, the mafic specimens collected from the Galema range can be described as massive, non-vesicular basalts with sparse, 1-5mm scale plagioclase crystals. A subset of samples is scoriaceous with visible plagioclase crystals at the 1-5mm scale. As a whole, the samples show little to no evidence of alteration or magma mingling at hand sample scale.

In thin section, a majority of the samples collected from the Galema range exhibit crystal phases dominated by plagioclase and a lesser abundance of samples display olivine as the primary crystal phase. A subset of samples include clinopyroxene crystals as part of the phenocryst population (Figure 2.3). These crystal phases rarely display resorption or skeletal textures, and most appear to be in equilibrium with the ground mass while none display evidence of zoning (Figure 2.4)(Supplementary Tables). All samples are observed to contain plagioclase laths within

Chiasera, B., Rooney, T.O., Girard, G., Yirgu, G., Grosfils, E., Ayalew, D., Mohr, P., Zimbelman, J.R. and Ramsey, M.S.(2018) Magmatically assisted off-rift extension—The case for broadly distributed strain accommodation Geosphere, v. 14, p. 1544-1563.

a cryptocrystalline to aphanitic groundmass. Opaque Fe-Ti oxide crystals also occur as a fractionating phase in all samples in plane polarized light. Anhedral olivine crystals occur as part of the mineral assemblage in varying abundances in samples with > ~2.5 wt. % MgO, appearing as the primary mineral phase in samples with > ~9.0 wt. % MgO, though often altered to iddingsite (Figures 2.4, 2.5). Anhedral to subhedral clinopyroxene crystals occur as part of the phenocryst assemblage in samples with between ~7.0 wt. % and ~8.0 wt. % MgO (Figures 2.4, 2.5). Plagioclase crystals are present within the range of ~1.3 to ~9.6 MgO wt. %. It is the primary mineral phase in samples from ~1.0 to ~4.5 MgO wt. % and occurs in varying abundance with olivine between ~4.5 to 9.6 wt. % MgO (Figure 2.3).Within the Galema range, the temporal relationship between the silicic centers and mafic dikes is not well constrained and we therefore focus on the mafic samples in an effort to characterize their magmatic plumbing systems. Samples with > ~59 wt.% SiO_2 (< ~1.4 wt.% MgO), as determined by X-Ray fluorescence analysis, were not included considered further.

Chiasera, B., Rooney, T.O., Girard, G., Yirgu, G., Grosfils, E., Ayalew, D., Mohr, P., Zimbelman, J.R. and Ramsey, M.S.(2018) Magmatically assisted off-rift extension—The case for broadly distributed strain accommodation Geosphere, v. 14, p. 1544-1563.

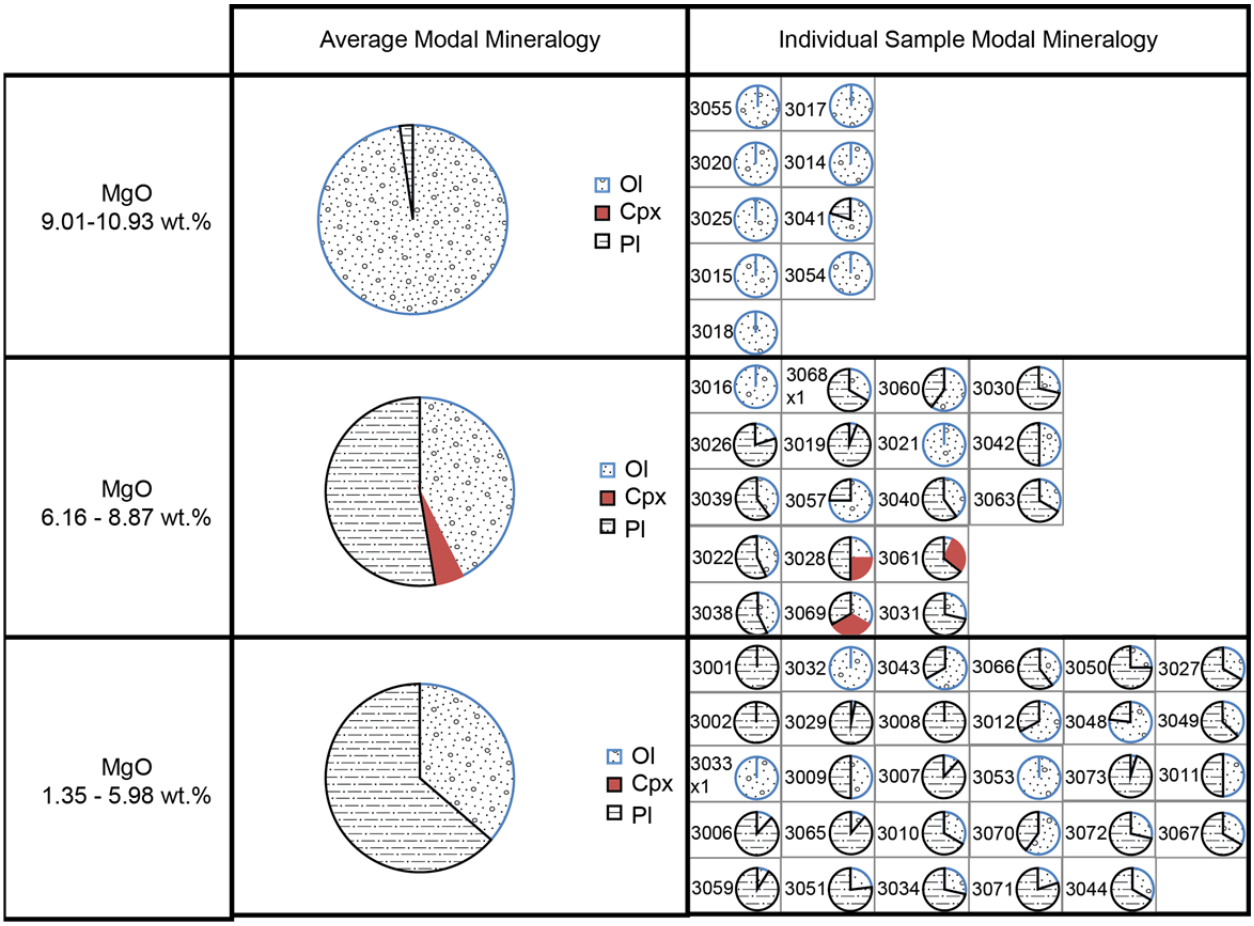

Figure 2.3.

Chart showing the crystal phase distribution of samples from the Galema range. Divisions are based on the dominant crystal phase observed and reported in MgO wt. %. Individual samples which are components of the larger divisions are also presented. Relative crystal phase abundances were normalized based on the observed phenocrysts. Groundmass or vesicle abundance are not included.

Chiasera, B., Rooney, T.O., Girard, G., Yirgu, G., Grosfils, E., Ayalew, D., Mohr, P., Zimbelman, J.R. and Ramsey, M.S.(2018) Magmatically assisted off-rift extension—The case for broadly distributed strain accommodation Geosphere, v. 14, p. 1544-1563.

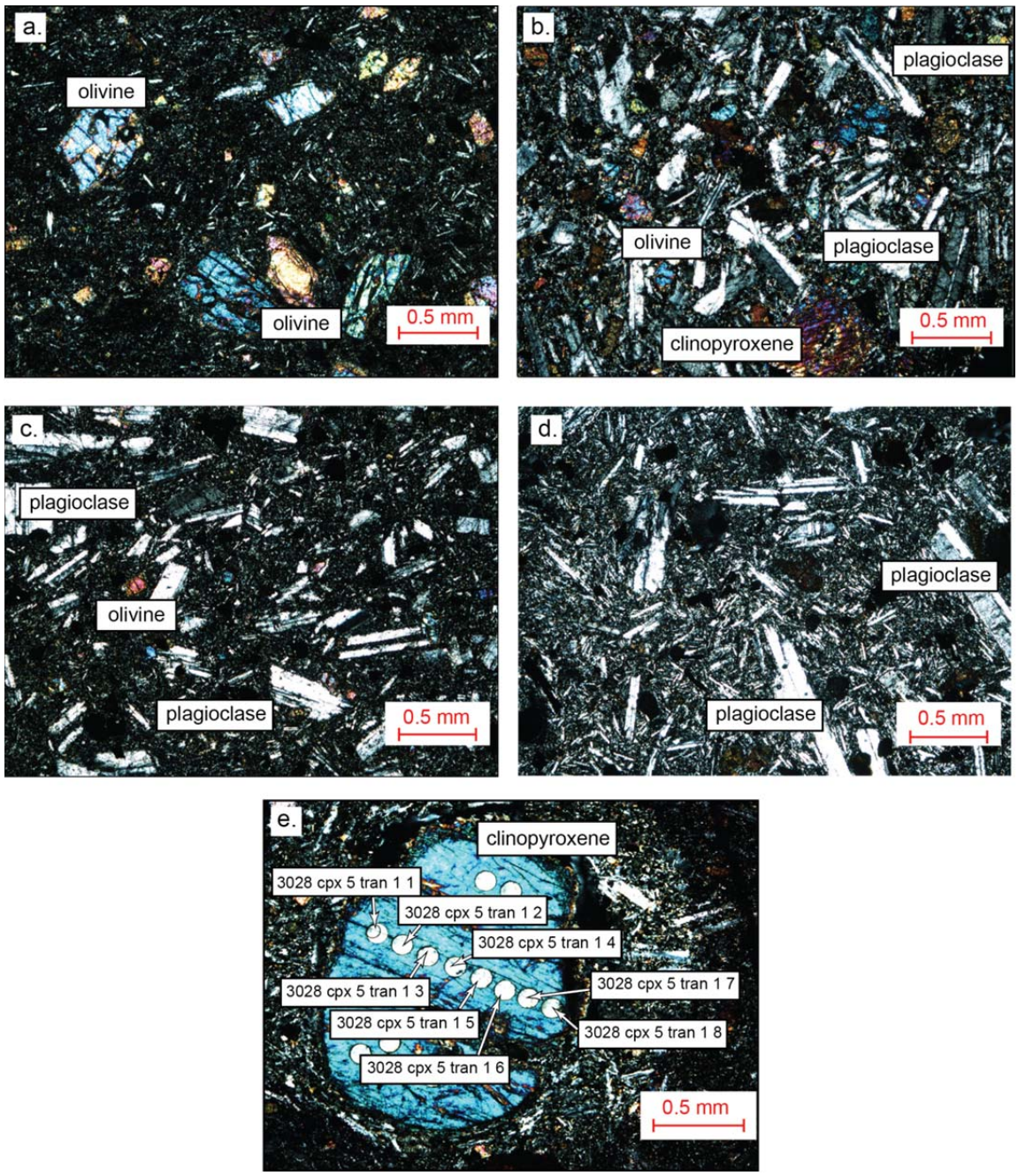

Figure 2.4.

Photomicrographs showing the crystal phases of samples from the Galema range including olivine, clinopyroxene and plagioclase phenocrysts. a. Sample 3015 (10.21 wt. %

Chiasera, B., Rooney, T.O., Girard, G., Yirgu, G., Grosfils, E., Ayalew, D., Mohr, P., Zimbelman, J.R. and Ramsey, M.S.(2018) Magmatically assisted off-rift extension—The case for broadly distributed strain accommodation Geosphere, v. 14, p. 1544-1563.

Figure 2.4. (cont'd.)

MgO) b. Sample 3061 (7.94 wt. % MgO) c. Sample 3072 (4.86 wt. % MgO) d. Sample 3029 (3.28 wt. % MgO) e. Clinopyroxene 5 from sample 3028 (7.15 wt. % MgO). Circular impressions are locations where some of the LA-ICP-MS analyses were performed. Labels indicate individual analyses of a transect, corresponding to data in Supplementary Tables.

2.4.2 Major Element Geochemistry

On the basis of the Total Alkali Silica (TAS) diagram (LeMaitre, 2002), our samples from the Galema range plot in an array from picro-basalt to rhyolite (Figure 2.5). The magmatic products of the Galema range have been described previously as bimodal in silica content, composed of hawaiites (trachy-basalts) and comendites (rhyolites)(Mohr, 1980). There is a noticeable lack of samples with SiO_2 content between ~59 wt. % to ~68 wt. % (Supplementary Material)(Figure 2.5). This lack of such sample compositions, also known as the Daly Gap, is described in many locations in the EARS (Baker, 1987; Trua et al., 1999; Peccerillo et al., 2003; Rooney et al., 2012b). This gap has been interpreted as a function of differential tapping of magma chambers at depth (Peccerillo et al., 2007), and more recently as the result of a magma mush where more silicic material has evolved and removed from the magma chamber to fractionate and shallower levels (Trua et al., 1999; Rooney et al., 2012b).

Chiasera, B., Rooney, T.O., Girard, G., Yirgu, G., Grosfils, E., Ayalew, D., Mohr, P., Zimbelman, J.R. and Ramsey, M.S.(2018) Magmatically assisted off-rift extension—The case for broadly distributed strain accommodation Geosphere, v. 14, p. 1544-1563.

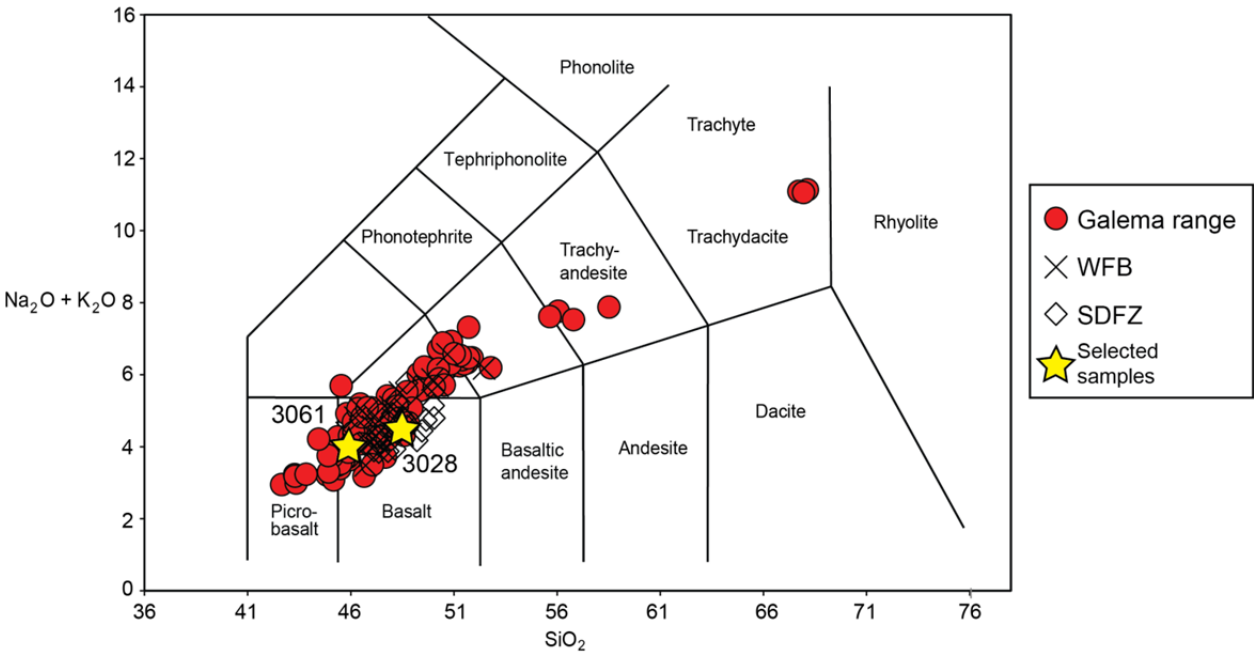

Figure 2.5.

Total Alkali Silica (TAS) (After LeMaitre (2002)) diagram showing the Galema range samples used in this study. Note the prominent lack of samples between ~59 and ~67 wt.% SiO_2. See text for details.

Variation diagrams of the major element geochemistry of samples with > ~1.4 wt.% MgO show trends consistent with fractional crystallization of olivine, plagioclase, pyroxene and Fe-Ti oxides occurring over the course of magmatic evolution (Figure 2.6). In samples with > ~9 wt. % MgO content, the relatively flat trend of Fe_2O_3 and TiO_2 vs. MgO is consistent with crystallization of olivine. Crystallization of pyroxene occurs in the compositional range of ~6 to ~9 wt.% MgO as indicated by the decreasing trend of CaO/Al_2O_3 vs. MgO. Below ~5 wt.% MgO, formation of Fe-Ti oxides is indicated by a break in slope of Fe_2O_3 and TiO_2 vs. MgO

Chiasera, B., Rooney, T.O., Girard, G., Yirgu, G., Grosfils, E., Ayalew, D., Mohr, P., Zimbelman, J.R. and Ramsey, M.S.(2018) Magmatically assisted off-rift extension—The case for broadly distributed strain accommodation Geosphere, v. 14, p. 1544-1563.

(Figure 2.6). Below ~6 wt.% MgO, plagioclase is the primary fractionating phase as indicated by the slope of the CaO/Al_2O_3 vs. MgO variation diagram.

Chiasera, B., Rooney, T.O., Girard, G., Yirgu, G., Grosfils, E., Ayalew, D., Mohr, P., Zimbelman, J.R. and Ramsey, M.S.(2018) Magmatically assisted off-rift extension—The case for broadly distributed strain accommodation Geosphere, v. 14, p. 1544-1563.

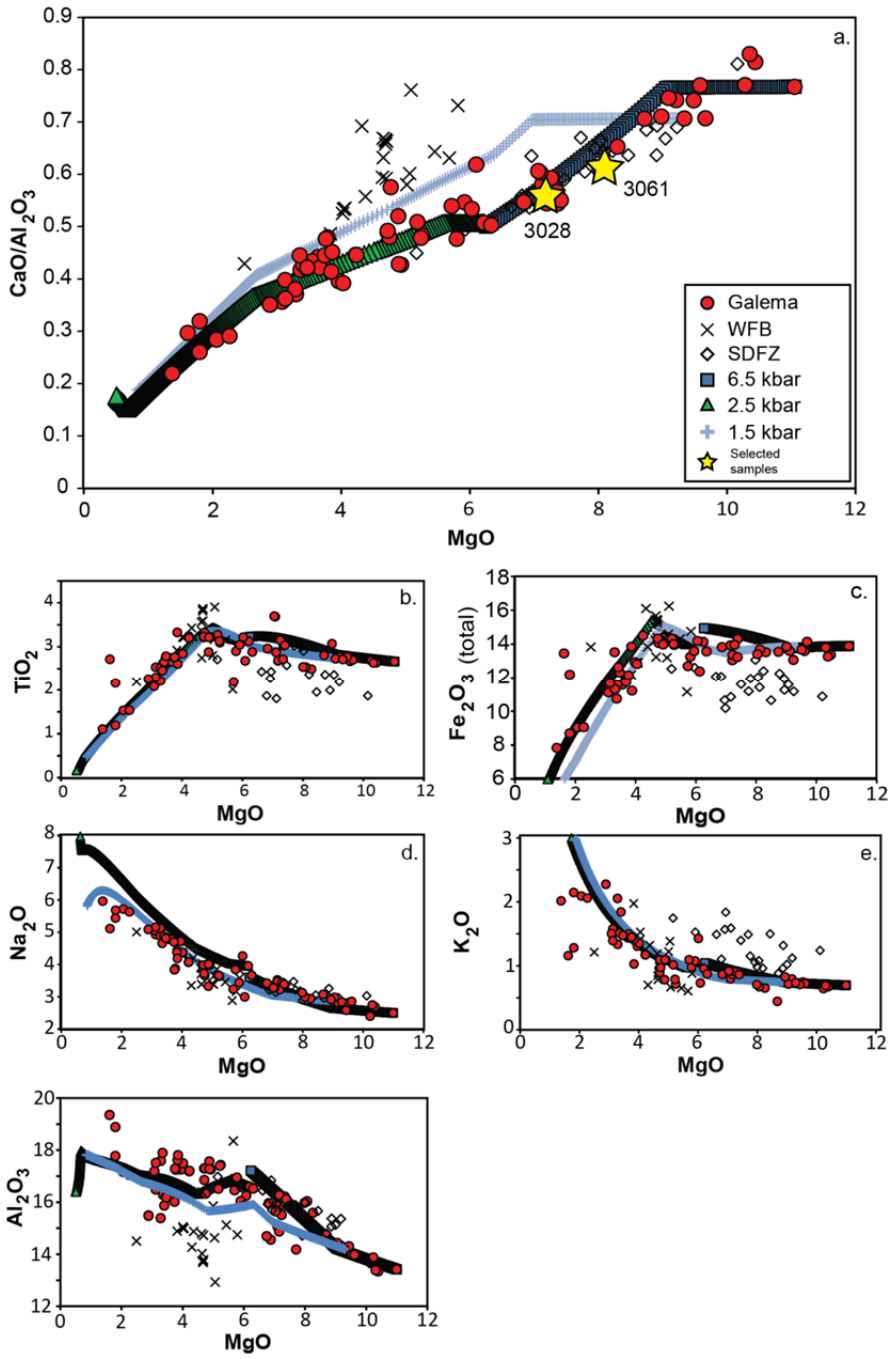

Figure 2.6.

a-e. Major element variation diagram. Included are data from the Silti-Debre Zeyit Fault Zone (SDFZ)(Rooney et al., 2005), the Wonji Fault Belt (WFB)(Rooney et al., 2007), and this study.

Chiasera, B., Rooney, T.O., Girard, G., Yirgu, G., Grosfils, E., Ayalew, D., Mohr, P., Zimbelman, J.R. and Ramsey, M.S.(2018) Magmatically assisted off-rift extension—The case for broadly distributed strain accommodation Geosphere, v. 14, p. 1544-1563.

Figure 2.6. (cont'd.)

The patterns observed are consistent with fractionation of the observed mineral assemblages including olivine, plagioclase feldspar and clinopyroxene. Results of MELTS modeling have been plotted with two trends showing the polybaric architecture of the magma plumbing system of the Galema range. Two MELTS models were applied to fully resolve the chemistry of the Galema basalts. The first MELTS model utilized the conditions of constant pressure of 7 kbar, 1 wt.% H_2O, and fO_2 value of 0 QFM with temperature decreasing continuously from 1350 C˚ and starting composition of Sample 3014, MgO wt.% = 11.00. This model only resolved the chemistry of the Galema basalts above ~6.1 wt.% MgO. To resolve the more evolved chemistries of the Galema basalts, a second model was applied utilizing a starting composition of Sample 3016 (MgO wt.% = 6.2) with a constant pressure of 3 kbar, 0.5 wt.% H_2O, fO_2 at QFM and continuous decreasing temperature from 1200 ˚C. (Stars indicate whole-rock geochemistry of samples chosen for thermobarometric calculations.).

2.4.3 Mineral Chemistry

Results of in-situ LA-ICP-MS analysis on the crystal phases of samples selected for crystal availability from each of the pressure regimes determined in section 5.2.1 (3028, 3029, 3061, 3068 and 3072) reveal compositions confirming the observations in thin section of the presence of plagioclase and pyroxene phases (Supplementary Tables). Multiple analyses of each crystal were performed and data were averaged across each crystal as no significant core-to-rim zoning was observed (Supplementary Tables)(Figure 2.4e). The size of the laser spot created an averaging effect of the crystal chemistry in each analysis, obscuring any chemical evidence of

Chiasera, B., Rooney, T.O., Girard, G., Yirgu, G., Grosfils, E., Ayalew, D., Mohr, P., Zimbelman, J.R. and Ramsey, M.S.(2018) Magmatically assisted off-rift extension—The case for broadly distributed strain accommodation Geosphere, v. 14, p. 1544-1563.

fine zoning for each crystal. After filtering the samples that showed clear signs of inclusion and or alteration, the crystal chemistry of each spot in an individual transect was analyzed for evidence of chemical zoning and the standard deviation for each transect was calculated (Supplementary Tables)(Figure 2.4e). These data were averaged to determine the average crystal chemistry. The averaging calculations allow for a more representative composition of the clinopyroxene phenocrysts in equilibrium with the melt, facilitating thermobarometric calculations.

Labradorite occurs as the most abundant plagioclase phase in samples 3029 (3.28 wt.% MgO) (An_{52-54}), 3061 (7.94 wt.% MgO)(An_{63-65}) and 3072 (4.86 wt.% MgO)(An_{51-56}). Bytownite occurs as the most abundant plagioclase phase of sample 3068 (7.02 wt.% MgO)(An_{71-78}) (Supplementary Tables)(Figure 2.7a). The clinopyroxene phase of samples 3061 and 3028 (7.15 wt.% MgO) are classified as augite with Wo_{38-40}, Fs_{9-15} and Wo_{38-42}, Fs_{11-16} respectively (Supplementary Tables)(Figure 2.7b).

Chiasera, B., Rooney, T.O., Girard, G., Yirgu, G., Grosfils, E., Ayalew, D., Mohr, P., Zimbelman, J.R. and Ramsey, M.S.(2018) Magmatically assisted off-rift extension—The case for broadly distributed strain accommodation Geosphere, v. 14, p. 1544-1563.

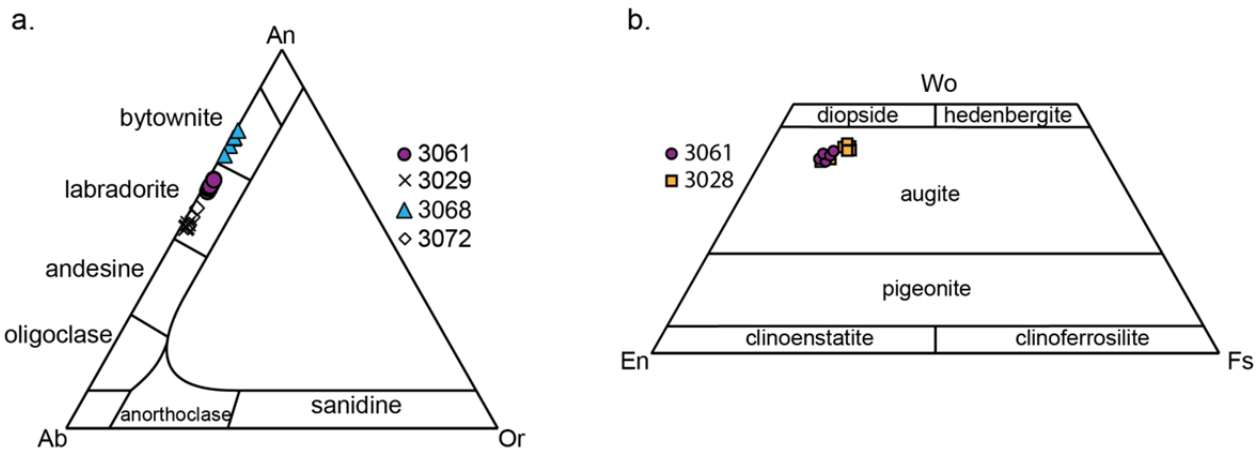

Figure 2.7.

Classification of plagioclase (a.) and clinopyroxene (b.) phenocrysts from the samples in this study determined through the use of in-situ LA-ICP-MS analysis. See text for sample selection criteria and methods

To determine whether the crystal phases are in equilibrium with the ground mass, and to choose suitable candidates for thermobarometric calculations, the in-situ analyses were used in combination with the whole-rock XRF analyses to calculate partition coefficient (K_D) values between crystal with melt. In sample 3061, K_D $(Fe\text{-}Mg)^{cpx\text{-}liq} = 0.27 \pm 0.02$ while in sample 3028 $K_D = 0.29 \pm 0.01$ These values are, well within the K_D $(Fe\text{-}Mg)^{cpx\text{-}liq}$ values of 0.29 ± 0.08 proposed by Putirka (2008), suggesting that the crystals are in equilibrium with melt.

Crystal assemblages from the analyzed samples reveal no discernable pattern with regard to sample location on the Galema range. Small groupings of samples with similar crystal assemblages are present; however, these small groups lie in close proximity (<5 km) to samples

Chiasera, B., Rooney, T.O., Girard, G., Yirgu, G., Grosfils, E., Ayalew, D., Mohr, P., Zimbelman, J.R. and Ramsey, M.S.(2018) Magmatically assisted off-rift extension—The case for broadly distributed strain accommodation Geosphere, v. 14, p. 1544-1563.

with a dissimilar assemblage. It is unclear if this is an artifact of sample availability or perhaps magmatic processes at such scale.

2.5 Discussion

2.5.1 Extensional Strain Accommodation by Zones of Focused Magmatic Intrusion

To first order, dikes are emplaced perpendicular to the orientation of the least compressive stress (σ_3)(Rubin and Pollard, 1988; Rubin, 1990; Parsons and Thompson, 1991; Rubin, 1992). In rifting environments, the orientation of the least compressive stress is in the direction of the extensional strain imposed on the lithosphere. If this intruded magma is sourced from a location other than the host rock (i.e. not a result of partial melting of the crust), and is allowed to remain in the host rock through magma cooling and dike freezing, the result is an increase of the volume of the host rock (Parsons and Thompson, 1991). In this way, magmatic intrusion accommodates extensional strain. The rapid emplacement of dikes can accommodate up to millennia worth of accumulated strain within the host rock (Parsons and Thompson, 1991). The depth where magma stalls on ascent and forms magma chambers coincides with depths where lithospheric strain accommodation occurs. Locations where magma is emplaced perpendicular to the direction of least principle compressive stress (σ_3), such as areas experiencing lithospheric extension, indicate areas where the crust may accommodate extensional strain aseismically (Corti et al., 2003). Thus, an estimate of the architecture of a magmatic plumbing system and the depths at which magma accumulates can constrain where and how strain is accommodated in the lithosphere in areas of extensional tectonics.

Chiasera, B., Rooney, T.O., Girard, G., Yirgu, G., Grosfils, E., Ayalew, D., Mohr, P., Zimbelman, J.R. and Ramsey, M.S.(2018) Magmatically assisted off-rift extension—The case for broadly distributed strain accommodation Geosphere, v. 14, p. 1544-1563.

The stalling of a magma on ascent is testable through the study of its major element geochemistry (e.g., Trua et al., 1999; Peccerillo et al., 2003; Rooney, 2010). The depth at which a magma stalls in the lithosphere, in part, controls the phases that form from that magma, thereby influencing the composition of the phase and residual magma from which the phase fractionates (Green and Ringwood, 1967; O'Hara, 1968; Green, 1969; Thompson, 1972; Wilson, 1994). Previous studies within the region have shown that deeper dike stalling depths resulted in greater stability of clinopyroxene, in contrast to shallower conditions where olivine and plagioclase dominate the fractionating assemblages, illustrating the use of major element geochemical analysis in the interpretation of the architecture of a magmatic plumbing system (Trua et al., 1999; Peccerillo et al., 2003; Rooney et al., 2005; Rooney et al., 2007).

2.5.2 Characterization of the Mafic Magmatic Plumbing System of the Galema Range

2.5.2.1 MELTS Modeling

To constrain the depths of magma stalling of the Galema range, and thereby establish where extensional strain is being accommodated in the lithosphere, thermodynamic modeling of the crystal fractionation sequence was performed using Excel-MELTS (Ghiorso and Sack, 1995; Asimow and Ghiorso, 1998; Gualda and Ghiorso, 2015). An initial composition for modeling was chosen as the most primitive sample from our data suite (Sample 3014, MgO wt.% = 11.00)(Figure 2.6). Multiple models were run utilizing this initial composition with varying pressures (10 kbar – 2 kbar), water contents (0%-5%) and fO_2 (QFM ±1). Utilizing a constant pressure of 7 kbar, 1 wt.% H_2O, and fO_2 value of QFM with temperature decreasing continuously from 1350 ˚C, the modeled evolution of this initial composition was found to fit the observed data above ~6.1 wt.% MgO in major element variation diagrams (Figure 2.6). At 7

Chiasera, B., Rooney, T.O., Girard, G., Yirgu, G., Grosfils, E., Ayalew, D., Mohr, P., Zimbelman, J.R. and Ramsey, M.S.(2018) Magmatically assisted off-rift extension—The case for broadly distributed strain accommodation Geosphere, v. 14, p. 1544-1563.

kbar, the MELTS model predicts minor olivine to begin fractionating at 1307 °C (10.98 wt.% MgO). The dominant fractionating crystal phase of the model at this pressure is clinopyroxene, which begins fractionating at 1250 °C (9.01 wt.% MgO) and continues to where the model deviates from the data at ~6.1 wt.% MgO (Supplementary tables). Below ~6.1 wt.% MgO the model with these initial conditions deviates significantly from the observed data when plotted in major element variation diagrams. To resolve this deviation from the observed data, a second model was created, utilizing a starting composition of ~6 wt% MgO (i.e., sample 3016, MgO wt.% = 6.20)(Figure 2.6). At a constant pressure of 3 kbar, 0.5 wt.% H_2O, fO_2 at QFM and continuous decreasing temperature from 1200 ˚C, the results of the model fit the observed data with a compositional range of ~1.3 to ~6.1 wt.% MgO (Figure 2.6). The 3 kbar model predicts that olivine will begin fractionating at 1181 °C (6.21 wt.% MgO). At 1158 °C (5.62 wt.% MgO) the MELTS model predicts the dominant fractionating crystal phase to be plagioclase, which continues fractionating through the end of the model. Minor amounts of spinel will begin fractionating at 1133 °C (4.53 wt.% MgO). Minor clinopyroxene does fractionate in the model at this pressure, but plagioclase is clearly fractionating in greater proportion (Supplementary tables).

The results of the MELTS model agree with the variation diagrams and petrography of the Galema basalts. The 7 kbar model predicts the primary crystalizing phase to be olivine at 10.98 wt.% MgO while the variation diagrams show that olivine is the primary crystalizing phase above ~9 wt. % MgO (Figure 2.6). This is in agreement with the petrography of samples in that compositional range (Figure 2.3). The MELTS model predicts that clinopyroxene should fractionate at 9.01 wt.% MgO at 7 kbar, in agreement with the slope of the CaO/Al_2O_3 vs. MgO

Chiasera, B., Rooney, T.O., Girard, G., Yirgu, G., Grosfils, E., Ayalew, D., Mohr, P., Zimbelman, J.R. and Ramsey, M.S.(2018) Magmatically assisted off-rift extension—The case for broadly distributed strain accommodation Geosphere, v. 14, p. 1544-1563.

variation diagram in that compositional range (Figure 2.6). A subset of samples from compositional range of ~7 to ~8 wt.% MgO also displays clinopyroxene as a member of the phenocryst population (Figure 2.3). The 3 kbar MELTS model predicts that the primary fractionating crystal phase to be plagioclase at ~5.62 wt. % MgO, which is in agreement with the CaO/Al_2O_3 vs. MgO variation diagram in that compositional range (Figure 2.6). The petrography of samples from this compositional range also shows plagioclase as the dominant crystal phase (Figure 2.3). The 3 kbar MELTS model predicts spinel fractionating at 4.53 wt.% MgO, consistent with the Fe_2O_3 vs. MgO variation diagram (Figure 2.6) and the occurrence of oxide phases in the petrography (Figure 2.3).

Spinel and plagioclase exist in the petrography of the basalts of the Galema range for compositions above ~5.62 wt.% MgO, which is not accounted for in the deeper MELTS model (Figure 2.6). The presence of these phases may be the result of the shallower fractionation, subsequent to the initial stages where clinopyroxene was dominant at greater depths.

The results of these thermodynamic models are thus consistent with the existence of a polybaric fractionation system, which is centered at 25 and 11km depth (Figure 2.8). The modeled pressures of fractionation, when correlated with the suite of samples analyzed, show no discernable correlation with their locations on the Galema range (Figure 2.1c).

Chiasera, B., Rooney, T.O., Girard, G., Yirgu, G., Grosfils, E., Ayalew, D., Mohr, P., Zimbelman, J.R. and Ramsey, M.S.(2018) Magmatically assisted off-rift extension—The case for broadly distributed strain accommodation Geosphere, v. 14, p. 1544-1563.

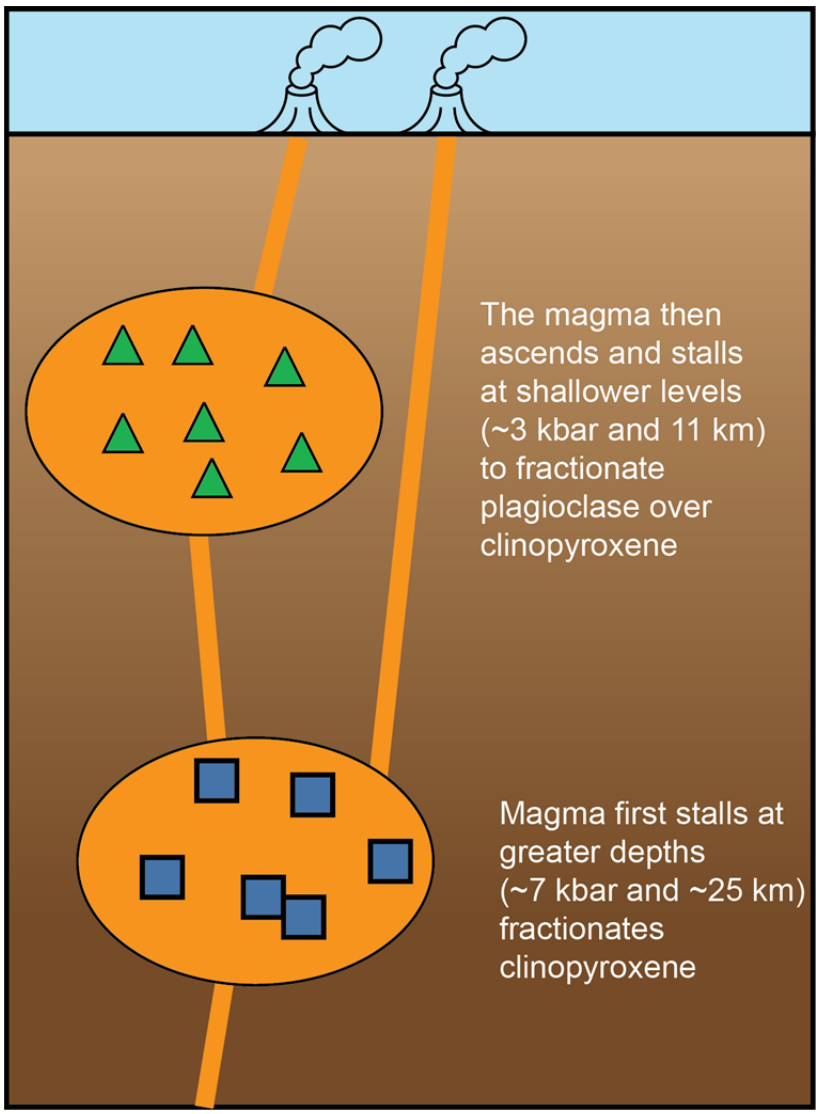

Figure 2.8.

Cartoon depicting the magma plumbing system of the Galema range as indicated by our analysis. Figure not to scale.

2.5.2.2 Thermobarometry

To ascertain the pressures of fractional crystallization, and to validate the Excel-MELTS model of magmatic evolution, the in-situ geochemical analysis of the crystal phases of the

Chiasera, B., Rooney, T.O., Girard, G., Yirgu, G., Grosfils, E., Ayalew, D., Mohr, P., Zimbelman, J.R. and Ramsey, M.S.(2018) Magmatically assisted off-rift extension—The case for broadly distributed strain accommodation Geosphere, v. 14, p. 1544-1563.

Galema range was applied to clinopyroxene-melt thermobarometry calculations (Nimis, 1995). The samples were chosen based upon the MgO compositional range and the availability of analytically-suitable clinopyroxene crystals. Liquid compositions for the selected samples were estimated using the whole rock geochemical data for sample 3028 (60% Groundmass) and 3061 (25% Groundmass) following the methodology of (Putirka et al., 2003; Putirka, 2008; Bédard, 2014). The water content (0.1-1 wt.%) for the magmas in the thermobarometry calculations were estimated based on the H_2O compositions determined in the MELTS modeling. The thermobarometric calculations determined that samples 3061 and 3028 fractionated at pressures of 6.7 to 8.6 kbar (24.4km to 31.3km depth)(Figure 2.9). These calculations are within ±2.0 kbar of the pressures determined in the MELTS models (Figure 2.6).

Chiasera, B., Rooney, T.O., Girard, G., Yirgu, G., Grosfils, E., Ayalew, D., Mohr, P., Zimbelman, J.R. and Ramsey, M.S.(2018) Magmatically assisted off-rift extension—The case for broadly distributed strain accommodation Geosphere, v. 14, p. 1544-1563.

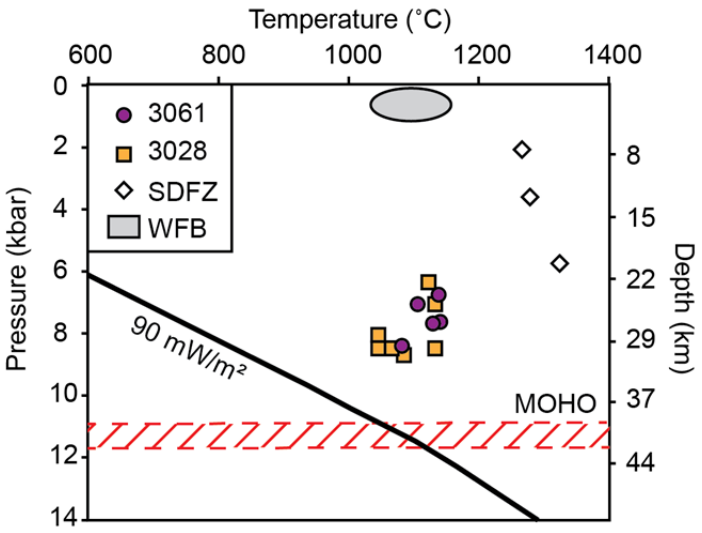

Figure 2.9.

Pressure-temperature chart of clinopyroxene-liquid thermobarometric calculations indicating that Galema magmas fractionated at greater pressure and depth than rift axial and rift marginal magmas. Pressure calculations based on Nimis (1995) and temperature calculations based on Nimis and Taylor (2000). Additional data from Rooney et al. (2005) and Rooney et al. (2007). Moho depth estimates from Keranen et al. (2009). Geotherm estimate from Hasterok and Chapman (2011).

While plagioclase mineral data were collected (Supplementary tables), these data were not used in thermobarometric calculations. Plagioclase-liquid thermobarometers have large errors associated with their pressure estimates, with some as high as ±3 kbar (Putirka, 2008). These estimates were not useful for our analysis of the magmatic plumbing system of the Galema range.

Chiasera, B., Rooney, T.O., Girard, G., Yirgu, G., Grosfils, E., Ayalew, D., Mohr, P., Zimbelman, J.R. and Ramsey, M.S.(2018) Magmatically assisted off-rift extension—The case for broadly distributed strain accommodation Geosphere, v. 14, p. 1544-1563.

2.5.3 Geophysical Constraints

Geophysical observations of the lithosphere of the MER show regions of higher P-wave velocities (V_p) in the crust at 10 km beneath the surface expressions of the WFB, SDFZ, and the Galema range (Keranen et al., 2004; Rooney et al., 2014a)(Figure 2.10a). This higher V_p indicates the existence of higher density material, which is consistent with a considerable volume of solidified, mafic material, interpreted to be gabbroic in composition that was intruded into the lithosphere (e.g, Mahatsente et al., 1999; Keranen et al., 2004). The differences in magnitude of V_p between the Galema range, WFB, and the SDFZ, may be due to differences in the volume of higher density material stored in the lithosphere between each location. This depth at which higher V_p occurs beneath the Galema range is consistent with the results of our MELTS modeling and thermobarometric calculations. This correlation may be evidence of cooled mafic material at these depths, resulting from stalled magmatic intrusion similar to processes observed in the WFB and SDFZ (Keranen et al., 2004; Rooney et al., 2005). Residual gravity measurements are entirely consistent with the seismic velocity anomalies. Specifically, the gravity data show a distinct negative residual gravity across the entire rift. Outside the rift there is typically no significant anomaly, with the exception of the Galema range on the eastern plateau. The anomaly beneath the Galema range has been previously interpreted to be the result of silicic flows (Mahatsente et al., 1999), however this interpretation was not based upon field data. The magnitude of this gravity anomaly is related to the amount and density of material within the crust and does not offer a unique solution to the observations.

Chiasera, B., Rooney, T.O., Girard, G., Yirgu, G., Grosfils, E., Ayalew, D., Mohr, P., Zimbelman, J.R. and Ramsey, M.S.(2018) Magmatically assisted off-rift extension—The case for broadly distributed strain accommodation Geosphere, v. 14, p. 1544-1563.

2.5.4 Extensional Strain Accommodation by Focused Magmatic Intrusion within the MER

Recent activity in Afar indicates that extensional strain is accommoded by focused magmatic intrusion within polybaric magmatic plumbing systems. Bimodal chemistry of magmatic products within the Dabbahu magmatic segment in Afar has been attributed to polybaric fractionation resulting from multiple depths of magma storage, which is also in agreement with geophysical studies (Ayele et al., 2009; Belachew et al., 2011; Field et al., 2012; Wright et al., 2012; Hammond, 2014). Zones of focused magmatic intrusion are also found in the MER in the WFB and SDFZ. Geophysical measurements show a volume of dense, intruded material within the lithosphere at the SDFZ (Keranen et al., 2004). Geochemical analysis of the magmatic products of the SDFZ indicate that the magmas were derived from sub-lithospheric depths (Rooney et al., 2005). The intruded material was introduced into the crust adding volume to the lithosphere at the SDFZ, indicating that the magmatism of the SDFZ represents accommodation of strain through focused magmatic intrusion.

Similarly, the WFB in the CMER plausibly represents an area of extensional strain accommodation by focused magmatic intrusion. Intruded material beneath the WFB, which added volume to the lithosphere, has been observed in geophysical measurements (e.g. Keranen et al., 2004; Rooney et al., 2007; Bastow et al., 2008; Biggs et al., 2011; Keir et al., 2011; Kim et al., 2012; Keir et al., 2015). Seismic anisotropy indicates the structure of these intrusions to be vertical dikes aligned in the orientation perpendicular to the extensional stress field affecting the MER (Keir et al., 2005; Kendall et al., 2006). These dikes are not derived from partial melting of the lithosphere, again requiring added volume to the crust (Rooney et al., 2007; Rooney et al., 2011). The WFB thus represents an area of magmatic strain accommodation.

Chiasera, B., Rooney, T.O., Girard, G., Yirgu, G., Grosfils, E., Ayalew, D., Mohr, P., Zimbelman, J.R. and Ramsey, M.S.(2018) Magmatically assisted off-rift extension—The case for broadly distributed strain accommodation Geosphere, v. 14, p. 1544-1563.

As noted previously, the Galema range displays a similar morphology to the Quaternary zones of focused intrusion within the MER. The morphological similarities between the Galema range and areas of focused magmatism within the rift (e.g., dikes aligned perpendicular to the σ_3 induced by the extensional stress field) suggest that the Galema range also magmatically accommodated strain, but intriguingly, exists outside the rift proper.

The polybaric fractionation system of the Galema range is also consistent with the architecture of the magma plumbing system of the WFB. Thermodynamic modeling, petrographic modeling and thermobarometric calculations have shown that the WFB consists of a polybaric fractionation system at deep crustal levels before magma ascends to consistently shallow levels within the crust (Trua et al., 1999; Rooney et al., 2005; Rooney et al., 2007; Rooney et al., 2011). The magmas of the WFB have been interpreted, through clinopyroxene thermobarometry, as having crystallization pressures of 0.1 kbar to 5.0 kbar (Rooney et al., 2007) - a narrower and shallower range of fractionation depths than the magmas of the Galema range.

The thermobarometric calculations of the Galema range indicate greater pressures of magma stalling and fractionation in comparison to those found at the WFB. These pressures are more consistent with those determined from analyses of the SDFZ. The SDFZ displays geochemical evidence of increased fractionation of clinopyroxene over plagioclase in its magmas, suggesting deeper levels of fractionation than at the WFB (e.g., Green and Ringwood, 1967; Rooney et al., 2005; Rooney et al., 2007). Similarly, thermobarometric estimates derived from host lavas within the SDFZ indicate fractionation pressures over a range from 2.0 kbar to 5.6 kbar (Rooney et al., 2005). This increased depth of magma stalling for the less mature magmatic plumbing system of

Chiasera, B., Rooney, T.O., Girard, G., Yirgu, G., Grosfils, E., Ayalew, D., Mohr, P., Zimbelman, J.R. and Ramsey, M.S.(2018) Magmatically assisted off-rift extension—The case for broadly distributed strain accommodation Geosphere, v. 14, p. 1544-1563.

the SDFZ, is more similar to the Galema range. These observation indicate a greater similarity in magmatic processes between the Galema range and the SDFZ in comparison to the WFB.

2.5.5 Factors Controlling The Depth Of Magmatic Stalling In Extensional Settings

Thermal modification of the base of the lithosphere allows for magma to intrude and begin fluxing into the affected areas (Havlin et al., 2013). This thermal modification allows for subsequent dikes to intrude further before freezing, broadly modifying the lithosphere in such a way as to allow diking and magma ascent to proceed (Bialas et al., 2010; Bastow and Keir, 2011; Havlin et al., 2013; Daniels et al., 2014). Once in the lithosphere, the depth at which a magma may stall is controlled by how the buoyancy forces of the magma interact with density contrasts of the lithosphere (Menand, 2011).

Buoyancy forces affecting a dike within the lithosphere depend on the availability and amount of magma generated (Parsons and Thompson, 1991). Buoyant magma will ascend to levels within the lithosphere where density differences are equal to the magma overpressure, which is generated by the buoyancy forces (Rubin, 1990). However, in a persistent rift zone, the constant extensional stress in the lithosphere is large enough to offset the stress state that results from lithospheric density differences (Rubin, 1990). If the extensional stress field increases during dike ascension, but magma flux remains constant, the magma overpressure is essentially cancelled and the dike is trapped at depth. Extension reduces the horizontal stress perpendicular to the rift zone (σ_3), allowing dikes to increase in width, but decreases their chance for ascent when the extensional stress field returns to normal (Rubin, 1990). If magma flux and resultant magma overpressure increased after such an event, the dike would again be allowed to ascend, but in a wider, more well developed conduit.

Chiasera, B., Rooney, T.O., Girard, G., Yirgu, G., Grosfils, E., Ayalew, D., Mohr, P., Zimbelman, J.R. and Ramsey, M.S.(2018) Magmatically assisted off-rift extension—The case for broadly distributed strain accommodation Geosphere, v. 14, p. 1544-1563.

Magma flux into the lithosphere determines the development of a rift magmatic plumbing system. Greater available magma volume is necessary to form larger dikes, which may traverse the crust to shallow levels (Rooney et al., 2014). A reduced magma flux into the lithosphere would create a more complex magmatic plumbing system as smaller dikes would have difficulty ascending directly to the surface due to reduced thermal weakening of the lithosphere (Buck, 2004; Bialas et al., 2010; Havlin et al., 2013). The less mature magmatic plumbing system of the Galema range, in comparison to the WFB, may be due to an overall decreased magma flux into the lithosphere resulting from both the average extent and rate of lithospheric stretching and thinning. This reduced magma flux would also inhibit the ascension of any dikes trapped at depth due to a temporary increase in the local stress field.

2.5.6 Lithospheric Extension And Magma Generation

As the lithosphere thins, the underlying asthenosphere must ascend to compensate partially for this reduced thickness, generating an increasing melt (Langmuir and Forsyth, 2007). Increased extension rate also increases the amount of adiabatic melting of the asthenosphere and can therefore increase magma flux into the lithosphere (Langmuir and Forsyth, 2007).

With progressive lithospheric thinning, the depth of melting of the asthenosphere shallows as the lithospheric cap is reduced and adiabatic melting can occur at decreased depth (Wang et al., 2002; Rooney, 2010). Stretching of the lithosphere manifests as an overall thinning of the plate, resulting in a shallowing of both lithosphere-asthenosphere boundary (LAB) and the Moho. Active source seismic studies within the MER show a Moho depth of ~32-36 km, but beneath the relatively less stretched south-eastern Ethiopian plateau, upon which the Galema range lies, the Moho is at a depth of ~42-46 km (Keranen et al., 2009; Rooney et al., 2014a)(Figure 2.10b).

Chiasera, B., Rooney, T.O., Girard, G., Yirgu, G., Grosfils, E., Ayalew, D., Mohr, P., Zimbelman, J.R. and Ramsey, M.S.(2018) Magmatically assisted off-rift extension—The case for broadly distributed strain accommodation Geosphere, v. 14, p. 1544-1563.

Given this increased Moho depth, we anticipate a deeper melting column beneath the Galema range (which is controlled by the depth of the LAB).

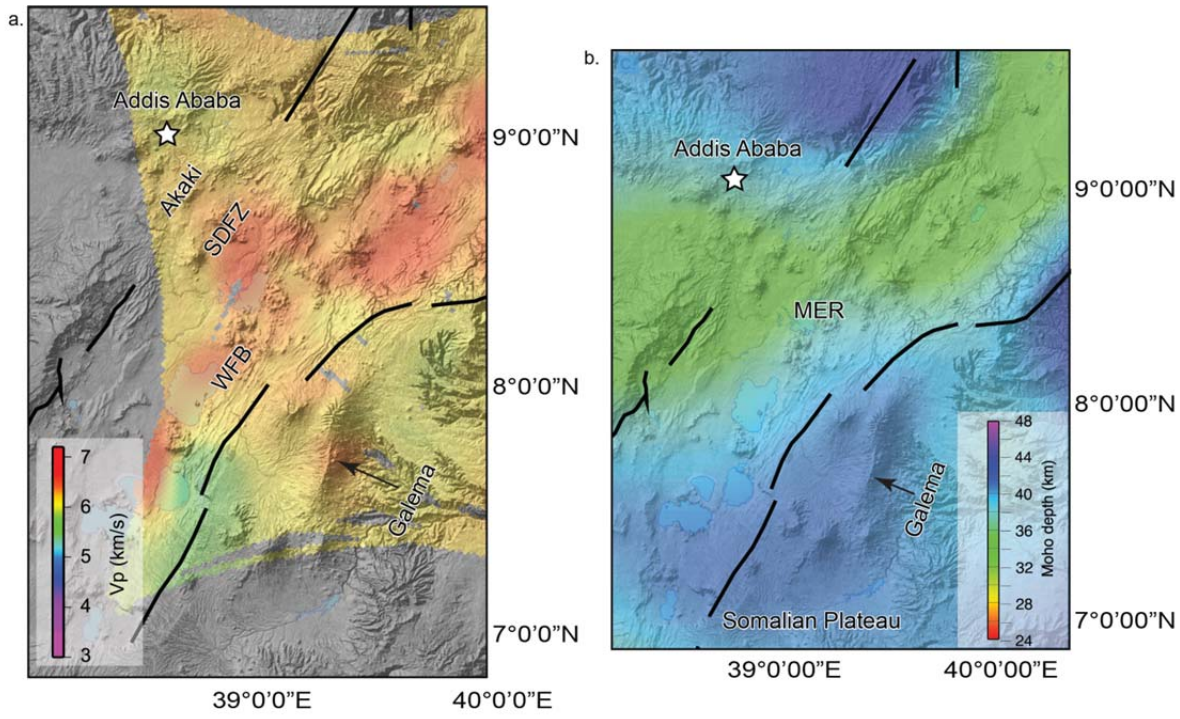

Figure 2.10.

a. Depth slice at 10 km for V_p in the Central Main Ethiopian Rift (CMER), indicating higher velocities beneath the Galema range, consistent with the presence of solidified mafic material with greater density at depth. Modified from Keranen et al. (2004) and Rooney et al. (2014a). b. Moho depth in the Central Main Ethiopian Rift (CMER), indicating a region of deeper Moho beneath location of the Galema range on the south-eastern Ethiopian plateau in comparison to Moho depth of areas of focused magmatic activity within the rift valley. The deeper Moho beneath the plateau is an indication of less lithospheric stretching and thinning. Modified from Keranen et al. (2009) and Rooney et al. (2014a).

Chiasera, B., Rooney, T.O., Girard, G., Yirgu, G., Grosfils, E., Ayalew, D., Mohr, P., Zimbelman, J.R. and Ramsey, M.S.(2018) Magmatically assisted off-rift extension—The case for broadly distributed strain accommodation Geosphere, v. 14, p. 1544-1563.

An examination of the melting depth of the magmas of the Galema range reveals depths greater than those at the WFB. Variation of SiO_2 vs. FeO^* for Galema range lavas (corrected for olivine fractionation using the PRIMELT3 MEGA modeling suite (Herzberg and Asimow, 2015)) exhibits a distinct grouping displaying higher FeO^* content than experimentally derived melts of fertile mantle peridotite at a pressure of ~25-30 kbar (Baker and Stolper, 1994; Kushiro, 1996; Furman et al., 2006a)(Figure 2.11). The grouping of the Galema range lavas at high FeO* also exceeds lavas from the adjacent MER, e.g. the WFB and Akaki (Rooney et al., 2007; Rooney et al., 2014a) and suggests a source melt for the Galema basalts at pressures greater than ~30 kbar (~110 km depth), deeper than the interpreted melting depths of the WFB and Akaki (~73 km depth)(Figure 2.11a). Compositions from the Galema range do not plot along the same trend as other areas of focused magmatic activity within the MER on an olivine-plagioclase-quartz ternary diagram. While the compositions of the other areas of focused magmatic activity (WFB, SDFZ, and Akai) plot along experimentally derived boundary curves for the 3-phase saturated liquid at 30 kbar (Walker et al., 1979; Hirose and Kushiro, 1993), Galema range compositions plot in a region that may indicate a higher melting pressure (Figure 2.11b). We suggest that the source melt of the Galema range was generated beneath thicker lithosphere in comparison to melts within the MER.

Chiasera, B., Rooney, T.O., Girard, G., Yirgu, G., Grosfils, E., Ayalew, D., Mohr, P., Zimbelman, J.R. and Ramsey, M.S.(2018) Magmatically assisted off-rift extension—The case for broadly distributed strain accommodation Geosphere, v. 14, p. 1544-1563.

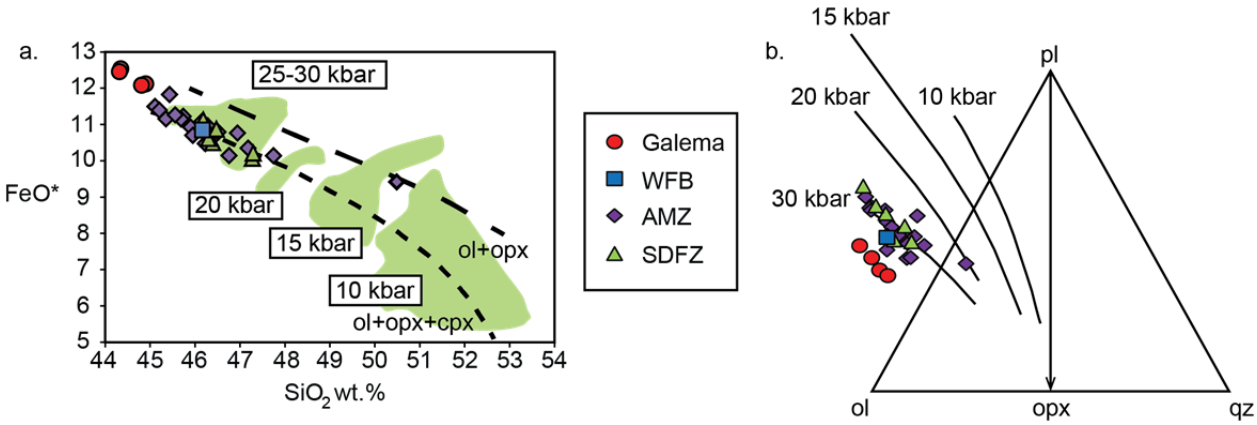

Figure 2.11.

a. FeO vs. SiO diagram, after Furman et al. (2006a) and Baker and Stolper (1994) suggesting that the source melt of the material of the Galema range was generated at ~30 kbar pressure. Iron content for samples was converted to FeO total and corrected to primary composition using PRIMELT3MEGA (Herzberg and Asimow, 2015) to obtain FeO*. Only samples with Mg# > 62 were used. Additional sample data from Rooney et al. (2005); Furman et al. (2006a); Rooney et al. (2014a). b. Olivine-plagioclase-quartz ternary diagram, along with boundary curves plotted experimentally for the 3-phase saturated liquids at different pressures (after Walker et al., 1979; Hirose and Kushiro, 1993) showing that samples from the Galema range plot away from the 30 kbar pressure line, indicating greater pressure of melt generation. Samples were corrected to primary composition using PRIMELT3MEGA (Herzberg and Asimow, 2015) before computation of components. Only samples with Mg# > 62 were used. Additional sample data from Rooney et al. (2005); Furman et al. (2006a); Rooney et al. (2014a).*

Chiasera, B., Rooney, T.O., Girard, G., Yirgu, G., Grosfils, E., Ayalew, D., Mohr, P., Zimbelman, J.R. and Ramsey, M.S.(2018) Magmatically assisted off-rift extension—The case for broadly distributed strain accommodation Geosphere, v. 14, p. 1544-1563.

2.5.7 Model For The Development Of Extension Along The Asela-Sire Border Faults.

2.5.7.1 Formation Of The Asela-Sire Border Faults

Rifting initially manifests as faulting and progresses towards the development of connected half grabens (Ebinger, 2005). The classic continental rift shape of a down-thrown valley floor and steep, high-angle border faults develops and progressive faulting becomes more focused within the rift valley (Corti et al., 2004; Wolfenden et al., 2005; Corti, 2012; Maccaferri et al., 2014). These faults have accommodated strain since their formation, though it is difficult to ascertain if this accommodation of strain was of a constant magnitude throughout their history.

2.5.7.2 Melt Generation, Migration And Initiation Of Magmatic Intrusion At The Galema Range

Thinning of the lithosphere occurs in response to the extensional forces induced during continental rifting. Recent estimates indicate within the MER, both the crust and lithosphere are thinned beneath the rift valley (Keranen et al., 2009; Bastow and Keir, 2011; Rooney et al., 2014a; Keir et al., 2015). This thinning of the lithosphere results in decompression and consequent melting of the underlying asthenosphere, generating the melt necessary for continental rifting processes to occur (McKenzie and Bickle, 1988; Ebinger and Sleep, 1998; Ebinger and Casey, 2001a; Ebinger, 2005; Langmuir and Forsyth, 2007). As magma began to intrude at the base of the lithosphere, perpendicular to the σ_3 generated by the regional extensional stress, the thermal gradient rose, broadly modifying the lithosphere in such a way as to allow diking and magma ascent to proceed (Bialas et al., 2010; Bastow and Keir, 2011; Havlin et al., 2013; Daniels et al., 2014).

Chiasera, B., Rooney, T.O., Girard, G., Yirgu, G., Grosfils, E., Ayalew, D., Mohr, P., Zimbelman, J.R. and Ramsey, M.S.(2018) Magmatically assisted off-rift extension—The case for broadly distributed strain accommodation Geosphere, v. 14, p. 1544-1563.

Following the generation of melt beneath the rift margin, subsidence of the half grabens forced magma laterally along the base of the crust, to outside of the border faults (Corti et al., 2003; Corti et al., 2004; Maccaferri et al., 2014). As this melt was relocated to beneath the southeastern Ethiopian plateau, it raised the thermal gradient and assisted in the thermomechanical modification of the lithosphere at that location (Bialas et al., 2010; Bastow and Keir, 2011; Havlin et al., 2013; Daniels et al., 2014)(Figure 2.12) This modification facilitated subsequent magmatic intrusion, which ascended to form the Galema range. Additionally, the thermal modification induced by magmatic intrusion would have the effect of reducing lithospheric strength to a degree that would make strain accommodation by faulting unfavorable within the extensional stress field (Buck, 2004). Thus, activity of the nearby Asela-Sire border fault would have ceased or been reduced during these events. The local stress field and presence of pre-existing lithospheric heterogeneities within the crust, at the time of the formation of the Galema range, dictated the pathways of ascent and determined the location and morphology of the range (Mazzarini et al., 2013b; Rooney et al., 2014a). Magmatic intrusion through pre-existing lithospheric weaknesses will still result in extensional strain accommodation through the addition of volume to the crust if the intruded material remains within the host rock and is not sourced from the host rock itself.

Chiasera, B., Rooney, T.O., Girard, G., Yirgu, G., Grosfils, E., Ayalew, D., Mohr, P., Zimbelman, J.R. and Ramsey, M.S.(2018) Magmatically assisted off-rift extension—The case for broadly distributed strain accommodation Geosphere, v. 14, p. 1544-1563.

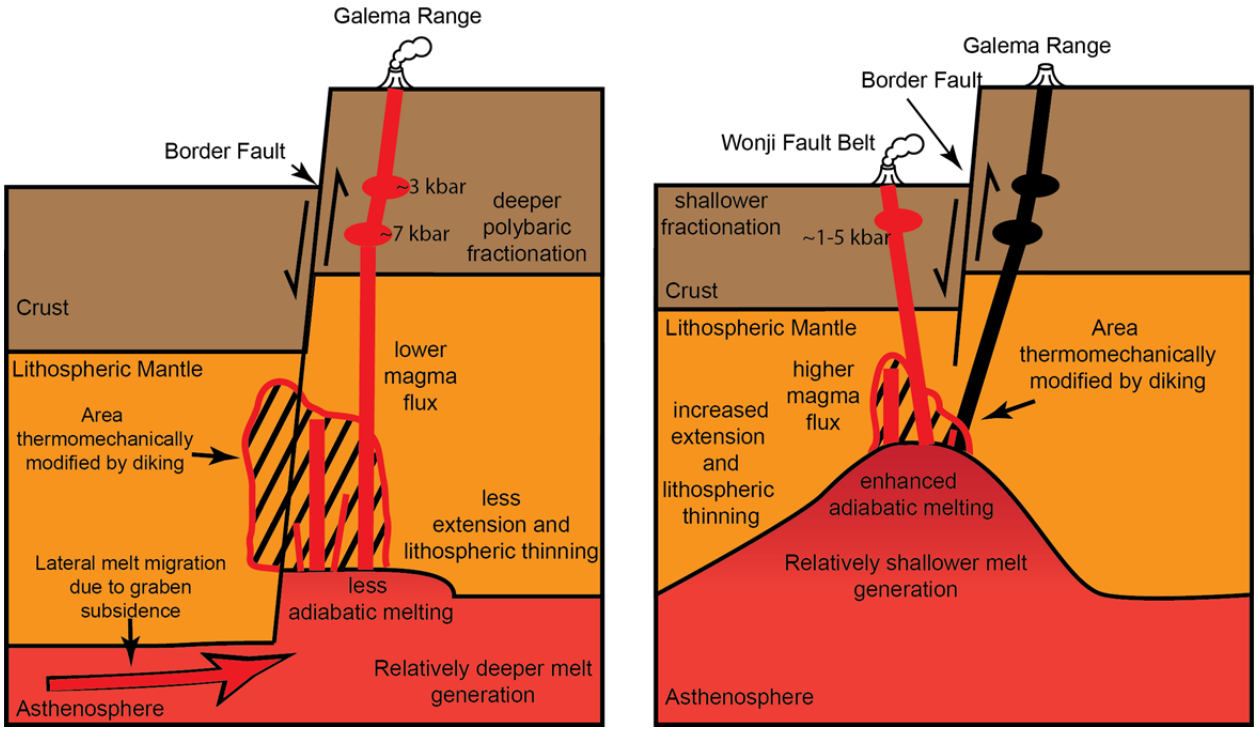

Figure 2.12.

Cartoon showing the hypothesized formation of the Galema range and subsequent formation of the WFB on the eastern rift margin. Initial activity of the Galema range generated thermomechanical modification of the lithosphere resulting from vertical diking and ascending magma. This area of modified lithosphere facilitated the ascent of the magma that would form the Wonji Fault Belt. Following this, a reduction or pause in the extension resulted in less magma available to flux into the lithosphere. This reduction in magma supply reduced the magma overpressure necessary for dike ascension and caused a cessation of magmatism at the Galema range. Continued extension progressively thinned the lithosphere within the rift, generating a greater adiabatic melt fraction from shallower depths. This increased melt resulted in an increased magma flux into the lithosphere, allowing for the development of a more well-

Chiasera, B., Rooney, T.O., Girard, G., Yirgu, G., Grosfils, E., Ayalew, D., Mohr, P., Zimbelman, J.R. and Ramsey, M.S.(2018) Magmatically assisted off-rift extension—The case for broadly distributed strain accommodation Geosphere, v. 14, p. 1544-1563.

Figure 2.12. (cont'd.)

developed magma plumbing system at the younger WFB. This more well-developed magma plumbing system allowed for the WFB to become the dominant location of magmatic strain accommodation within the rift as a result of the thermomechanical modification of the earlier diking beneath the Galema range. Figure not to scale.

2.5.7.3 Cessation of Magmatism in the Galema Range

After the formation of the Galema range, magmatism in this off-rift location ceased due to several possible processes related to either continued extension or reduced magma supply or both. A temporary reduction in the extension rate would lead to a reduction in adiabatic melting of the asthenosphere, limiting the amount of magma available to flux into the lithosphere. This reduced magma supply would have the effect of decreasing the magma overpressure in ascending dikes, allowing them to become trapped at depths where this pressure equals the density-controlled stress within the surrounding lithosphere. If extension and resultant magma production continued to be diminished for a long enough period, the dikes that had previously ascended into the lithosphere would freeze, effectively ending magmatic activity.

As the lithosphere continued to deform and thin along the rift axis, magmatism shifted toward more focused activity along the axis due to increased magma flux created by adiabatic melting in the newly thinned areas (Morton et al., 1979; Ebinger, 2005). Magmatism may also shift location due to a change in the topography at the base of the lithosphere (as a result of progressive thinning), which channels melt material toward the axis (Corti, 2012; Keir et al., 2015). While the shift in magmatic activity toward the rift axis may be due to a change in

topography at the base of the lithosphere, we modify this model to include magmatic intrusion of the Galema range dikes, and the consequent unavoidable thermomechanical modification of the lithosphere (Buck, 2004; Bialas et al., 2010; Bastow and Keir, 2011; Havlin et al., 2013; Daniels et al., 2014).

2.5.7.4 Initiation of Magmatism of the WFB

Lithospheric thinning associated with continued extension generated an increased melt fraction at shallower depths (McKenzie and Bickle, 1988; Langmuir and Forsyth, 2007). The magma generated during this more advanced state of extension intruded the lithosphere at the same broad location, which was thermomechanically modified by the previous activity of the Galema range.

The greater melt fraction increased the magma flux into the lithosphere, allowing for the formation of larger dikes. These larger dikes would be able to more easily ascend to the surface, forming more well developed magmatic plumbing system with shallower levels of fractionation, as observed at the WFB (Rooney et al., 2014a)(Figure 2.12). Greater melt production would allow for an increase in the amount of magmatic material erupted, increasing surface topography and simultaneously reducing the extensional stress at the bottom of the lithospheric plate through magma injection. This dynamic allows magma to ascend to shallower levels before stalling (Behn et al., 2006).

As a continental rift evolves, magmatism is influenced less by pre-existing lithospheric structures and more by the lithospheric strain profile due to the thermal modification of the lithosphere (Isola et al., 2014; Robertson et al., 2016). Magmatism became the dominant form of strain accommodation in the WFB as a result of the enhancement of the magmatic plumbing

Chiasera, B., Rooney, T.O., Girard, G., Yirgu, G., Grosfils, E., Ayalew, D., Mohr, P., Zimbelman, J.R. and Ramsey, M.S.(2018) Magmatically assisted off-rift extension—The case for broadly distributed strain accommodation Geosphere, v. 14, p. 1544-1563.

system assisted by, among other processes, the earlier focused magmatism of the Galema range. Furthermore, this suggests that magmatic strain accommodation does not linearly migrate toward the rift axis during rift evolution, and may in fact be more distributed and episodic.

2.5.7.5 Broader Impacts

During the early stages of continental rifting, extensional strain is accommodated through faulting and stretching of the lithosphere, resulting in the formation of the high angle border faults that will define the rift. Following this, magmatic intrusion begins to accommodate extensional strain, which should migrate and focus along the rift axis (Wolfenden et al., 2005). Recent work has suggested that strain accommodation in the Afar region via focused magmatic intrusion did not occur until very recently and that prior to this, the only expression of magmatic activity was the emplacement of large-scale flood basalts (Stab et al., 2015). These areas of focused magmatic intrusion may represent the organization of magmatic strain accommodation organizing into axial segments (Medynski et al., 2015). The Galema range may represent an intermediate stage of continental rifting, occurring after the formation of the rift border faults but before the organization of axial magmatic segments. This intermediate stage is characterized by pulsed accommodation of extensional strain by focused magmatic intrusion outside the rift proper, and accommodation of extensional strain by faulting and stretching of the lithosphere during periods between magmatic intrusions.

2.6 Conclusions

The Galema range, which is located on the south-eastern Ethiopian plateau adjacent to the rift margin, is a zone of focused dike intrusion that displays morphological similarities to zones

Chiasera, B., Rooney, T.O., Girard, G., Yirgu, G., Grosfils, E., Ayalew, D., Mohr, P., Zimbelman, J.R. and Ramsey, M.S.(2018) Magmatically assisted off-rift extension—The case for broadly distributed strain accommodation Geosphere, v. 14, p. 1544-1563.

of focused magmatic intrusion within the Main Ethiopian Rift. Our results demonstrate that the depths of stalling of the mafic magmas of the Galema range are deeper than those at the WFB, consistent with a less developed magma plumbing system for the Galema range. We find that magma generation beneath the Galema range occurs at greater depths than beneath the WFB, indicating that the lithosphere had undergone relatively less extension in comparison to the modern rift. On the basis of these observations, and existing geodynamic constraints, we propose the following model explaining the origin of off-axis zones of focused intrusion: 1. the initial development of rift-border faults controlled the migration of melt into the lithospheric mantle. The transit of the melt through the crust was controlled, in part, by the establishment of a horizontal axis of least compressive stress during graben formation and thereby facilitating rift adjacent volcanism, 2. with continued rift evolution, the transit of melt through the lithospheric mantle occurred along the same pathways established during the earlier rift-adjacent volcanism enhancing magmatism along one rift margin. However, variations in the amount of magma production and resultant magma overpressure in ascending dikes may have allowed for the eruption of within-rift zones of focused intrusion

We propose that the Galema range represents an intermediate stage of continental rift evolution, occurring after the formation of the rift border faults but before the formation of axial magmatic segments. In this hybrid rifting model, strain is accommodated by oscillations between both the rift-border faults and areas of focused magmatic intrusion. However, the amount of strain partitioned between each mechanism and the timing are not yet resolved. These findings have implications for the initial development of zones of focused magmatic intrusion within rifts. In particular, this work demonstrates that it is possible to have multiple periods of extension

Chiasera, B., Rooney, T.O., Girard, G., Yirgu, G., Grosfils, E., Ayalew, D., Mohr, P., Zimbelman, J.R. and Ramsey, M.S.(2018) Magmatically assisted off-rift extension—The case for broadly distributed strain accommodation Geosphere, v. 14, p. 1544-1563.

being accommodated through focused magmatic intrusion or displacement of faults along a single margin. These observations will need to be incorporated into ongoing debates about the timing of initiation of magma-facilitated extension (Wolfenden et al., 2005; Stab et al., 2015).

Chiasera, B., Rooney, T.O., Girard, G., Yirgu, G., Grosfils, E., Ayalew, D., Mohr, P., Zimbelman, J.R. and Ramsey, M.S.(2018) Magmatically assisted off-rift extension—The case for broadly distributed strain accommodation Geosphere, v. 14, p. 1544-1563.

3. GEOCHEMICALLY CONSTRAINING THE DEPTH OF THE LITHOSPHERE-ASTHENOSPHERE BOUNDARY IN THE CENTRAL MAIN ETHIOPIAN RIFT SYSTEM

3.1 Introduction

When continents rift apart, the continental lithosphere ultimately thins to rupture prior to the onset of seafloor spreading. The rate and timing of lithospheric thinning has important implications for magma generation: rapid thinning can result in voluminous decompression melting of the mantle, but if thinning rates are slow, melting will be suppressed as the mantle cools to the surface by conduction (e.g., Bown and White, 1995). Mantle potential temperature (T_P) also plays an important role in governing rift-related melting (White and McKenzie, 1989), but is not easily constrained at the rifted margins where theoretical models and/or analysis of the deeply-buried geological record are our only means of gleaning information concerning rift development (e.g., Eagles et al., 2015).

The Main Ethiopian Rift (MER) provides an excellent opportunity to address these issues, since it exposes subaerially the final stages of continental breakup above an anomalously slow-wavespeed mantle (Ritsema et al., 1999; Benoit et al., 2006a; Benoit et al., 2006b; Bastow et al., 2008). Stretching factors estimated from crustal thickness in the Ethiopian rift are lower than would be predicted by traditional rifting models (e.g., McKenzie, 1978) because considerable extension has been accommodated by dike intrusion (e.g., Mackenzie et al., 2005; Cornwell et al., 2006; Stuart et al., 2006). Whether or not crustal stretching factors are a sensible proxy for plate stretching factors, however, can only be determined by assessment of plate thickness.

Measurement of the depth to the LAB constrains plate thickness. This measure provides insights into plate stretching, but this boundary is notoriously difficult to constrain (e.g., Eaton et al., 2009). LAB depth has been explored seismically in the MER by wide-angle seismic profiling (e.g., Maguire et al., 2006), joint inversion of surface waves and P-to-S receiver functions (Dugda et al., 2007), modeling of seismic anisotropy (Bastow et al., 2010), and receiver functions (e.g., Rychert et al., 2012).

Receiver function analysis seeks to identify P-to-S or S-to-P converted energy from velocity discontinuities beneath a seismograph station. Such techniques thus work well when the velocity gradient is steep, but cannot necessarily identify features if the velocities vary gradationally (Eaton et al., 2009; Gallacher and Bastow, 2012). Surface wave studies cannot resolve sharp boundaries, but estimate lithosphere-asthenosphere boundary (LAB) depth through the use of velocity contour proxies (e.g., the 1.7% fast velocity contour: e.g. Darbyshire and Eaton, 2010). These results are useful but imprecise. In locations lacking a sharp Moho, such as Ethiopia (e.g., Dugda et al., 2007; Bastow et al., 2010), melt intrusion into the lithospheric mantle likely results in a gradational LAB (e.g., Bastow et al., 2010); thus, alternative methods are required to resolve the depth at which rigid lithosphere gives way to convecting asthenosphere. Given that magma generation and ascent mechanisms within a continental rift are sensitive to plate thickness (e.g., McKenzie and Bickle, 1988; White and McKenzie, 1989; Ebinger and Sleep, 1998; Ebinger and Casey, 2001a; Wang et al., 2002; Ebinger, 2005; Rooney et al., 2011), geochemical studies of rift magmas can provide additional data concerning the behavior of the continental lithosphere and how it has thinned over time.

Geochemical techniques that provide estimates of the shallowing of the LAB and degree of thinning of the lithosphere have previously been applied in the MER (Rooney et al., 2005;

Furman et al., 2006a; Ayalew and Gibson, 2009; Rooney, 2010; Ferguson et al., 2013; Chiasera et al., 2018). The chemistry of a magma may preserve the pressure and temperature characteristics of the magma during its ascent from the asthenosphere. Thermodynamic modeling of the chemical evolution of a magma and comparison to melting studies can give an estimate of the depths at which melt was generated. Thermobarometric estimates of crystal phase fractionation indicate the depths at which a magma last encountered a barrier to ascent allowing it to re-equilibrate with the surrounding asthenosphere (e.g., at the LAB).

We examine the Galema range, an area of focused magmatism emplaced parallel to the eastern margin of the Central MER (Figure 1.1). We present whole-rock trace element data on 77 samples of magmatic products of the Galema range. We demonstrate for the first time, through a combination of thermodynamic modeling techniques, that the melts were generated at relatively high pressures and temperatures (2.9-3.2 GPa, ~103-114 km depth, 1418-1450°C) but stalled and re-equilibrated below a still-thick (78-89km) lithosphere. Our work thus has important implications for our understanding of plate thinning during rifting.

3.2 Background

3.2.1 Cenozoic Magmatic Evolution of the African-Arabian Large Igneous Province

Cenozoic magmatic activity in East Africa commenced in the Eocene with a pulse of flood basalt magmatism in the broadly-rifted zone of the Turkana Depression (northern Kenya) and throughout southern Ethiopia (Ebinger et al., 1993a; George et al., 1998; Furman et al., 2006b). Subsequent magmatic activity during the Oligocene migrated northward with eruption of flood basalts across Ethiopia as a result of the impingement of the Afar plume (Baker et al., 1996; Hofmann et al., 1997; Rochette et al., 1998; Pik et al., 1999; Kieffer, 2004). Miocene volcanism

occurred broadly throughout the region, with shield building and fissure-fed basalts on the Ethiopian Plateau and increased basaltic activity in Turkana (e.g., Rooney, 2017).

Subsequent volcanic activity took the form of smaller basaltic eruptions, and the formation of large silicic centers that localized to the developing MER (Rooney et al., 2011). Plio-Quaternary magmatism occurred on the margins of the Central MER (CMER), and is best represented by the Akaki Magmatic Zone along the western margin (Rooney et al., 2014a), and the en-echelon mafic dikes of the Galema range along the eastern margin (Mohr and Potter, 1976; Mohr, 1980) (Figure 1.1c). Magmatism focused within the MER during the Quaternary into the Wonji Fault Belt (WFB) and Silti-Debre Zeyit Fault Zone (SDFZ), a series of en-echelon dikes, lava flows, scoria cones, and associated silicic centers (Mohr, 1967; Mohr, 1980; Woldegabriel et al., 1990; Rooney et al., 2005; Kurz et al., 2007) (Figure 1.1c).

3.2.2 The Galema Range

The Galema range, located on the eastern Ethiopian plateau in the CMER (Figure 1.1c), is an area of focused magmatic intrusion. Magmatic activity in the Galema Range manifests as en-echelon mafic dikes, aligned scoria cones, and associated silicic centers (Mohr and Potter, 1976; Mohr, 1980; Chiasera et al., 2018). Geochronological estimates place magmatism of the Galema range within the Pliocene, dating from 2.1 to 3.1 Ma (Mohr and Potter, 1976; Kennan et al., 1990). While it is located on the rift shoulder, the Galema range has been linked to the same extensional stresses that have formed other extensional features of the CMER such as the WFB and SDFZ (Figure 1.1c)(Chiasera et al., 2018).

3.3 Methods

A field excursion in 2008 recovered 77 samples from dikes, basaltic flows, scoria cones and silicic centers of the Galema range and surrounding areas (Figure 3.1c). As the magmatic locations such as Gademsa and Boseti are considered to be part of the larger WFB within the rift (e.g., Mohr, 1967), magmatic features such as Chilalo, Mt. Bada, and the Galema range may be part of a larger magmatic system on the eastern Ethiopian plateau (e.g., Mazzarini et al., 2013a; Mazzarini et al., 2013b). These nearby areas of magmatic activity would have been generated within the same conditions as those of the Galema range, such as mantle potential temperature and melt generation depth. After these samples were cut to minimize alteration due to weathering, they were further cut into ~30 g billets, then polished to remove saw marks and cleaned in an ultrasonic bath of deionized water before being crushed in a steel jaw crusher and powdered in a Bico ceramic disk mill. The powders were then fused into glass discs with a lithium tetraborate ($Li_2B_4O_7$) flux following procedures detailed elsewhere (e.g., Rooney et al., 2012b). Major element oxide abundances and loss on ignition values were determined by X-Ray fluorescence analysis on a Bruker S4 PIONEER instrument at Michigan State University (Supplemental Material). The discs were then analyzed in triplicate for trace elements using a Photon Machines G2 excimer laser coupled to a Thermo iCap ICP-MS following procedures detailed elsewhere (Rooney et al., 2015; Rooney et al., 2018).

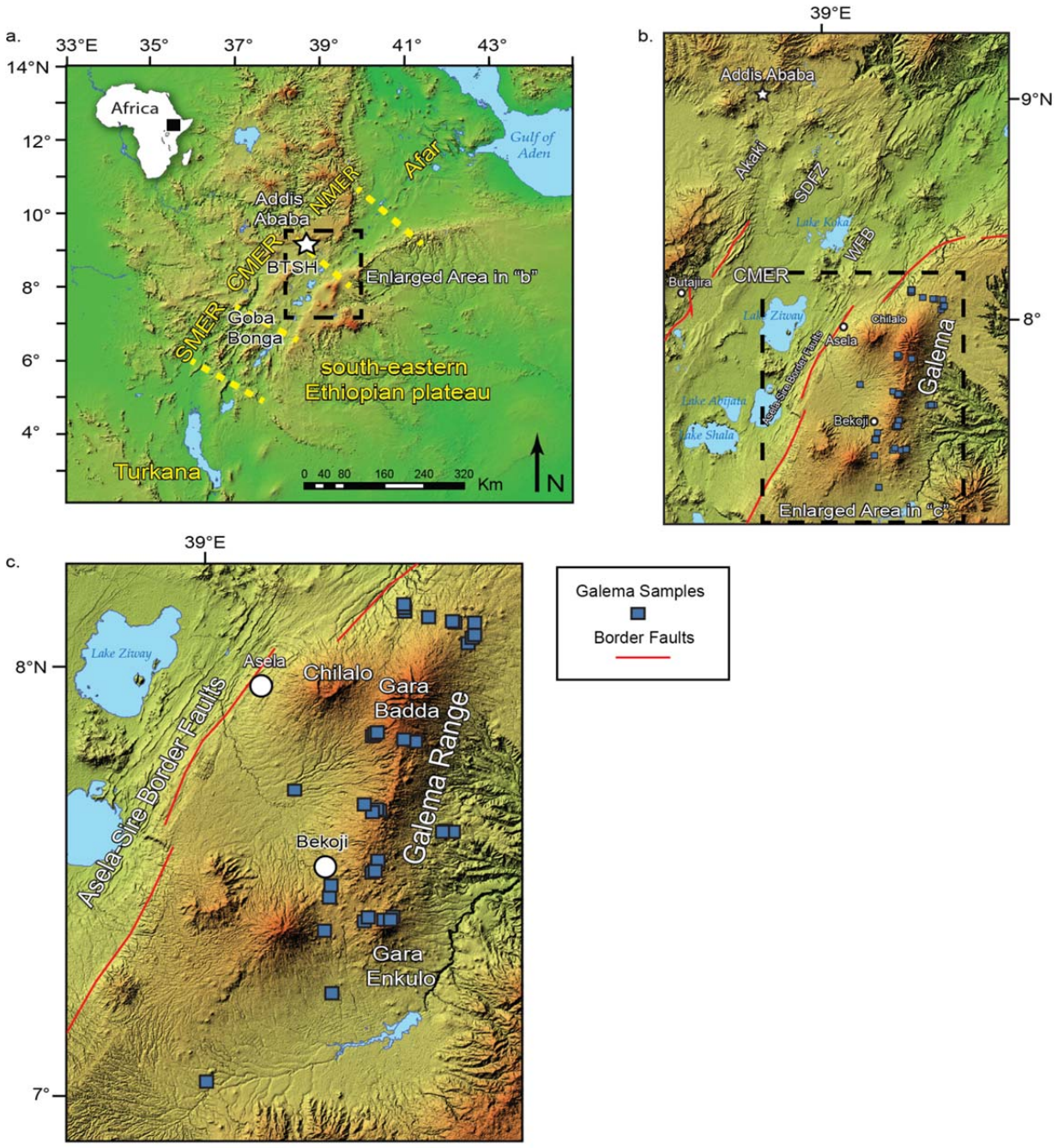

Figure 3.1.

a. Tectonic setting of the Main Ethiopian Rift (MER) within the East African Rift System (EARS). Northern Main Ethiopian Rift (NMER), Central Main Ethiopian Rift (CMER) and Southern Main Ethiopian Rift (SMER). Dashed line delineates (b). b. The Central Main Ethiopian Rift (CMER).

Figure 3.1. (cont'd.)

WFB: Wonji Fault Belt; SDFZ: Silti-Debre Zeyit Fault Zone; AMZ: Akaki Magmatic Zone; YTVL: Yerer-Tullu Wellel Volcanotectonic Lineament. Dashed line delineates (c). c. Enlarged portion of the CMER showing the location of the Galema range and samples used in this study.

3.4 Results

Major element geochemistry of the Galema range volcanics reveals compositions that range from picrobasalt to rhyolite (Chiasera et al., 2018). Major element chemical analysis, sample petrography and clinopyroxene geochemistry have been examined in previous work (Chiasera et al., 2018) and will not be covered in this contribution. CIPW norm calculations reveal that the more primitive magmas (i.e. >6 wt. % MgO) of the Galema range are silica undersaturated and nephelene-normative. To minimize variance associated with fractionation, we concentrate our further analyses on samples with >3 wt. % MgO.

3.4.1 Trace Element Geochemistry

Trace element geochemistry of samples with >6 wt. % MgO display two distinct groupings when plotted on a primitive mantle normalized spider diagram (Figure 3.2). The first group displays an enrichment in the most incompatible trace elements with a negative K anomaly and positive Ti anomaly (Figure 3.2a). The second group, exhibited by most samples from the Galema range, displays a general enrichment over primitive mantle in the most incompatible trace elements with a positive Ba anomaly, negative Th-U anomaly and positive Nb-Ta anomaly (Figure 3.2b).

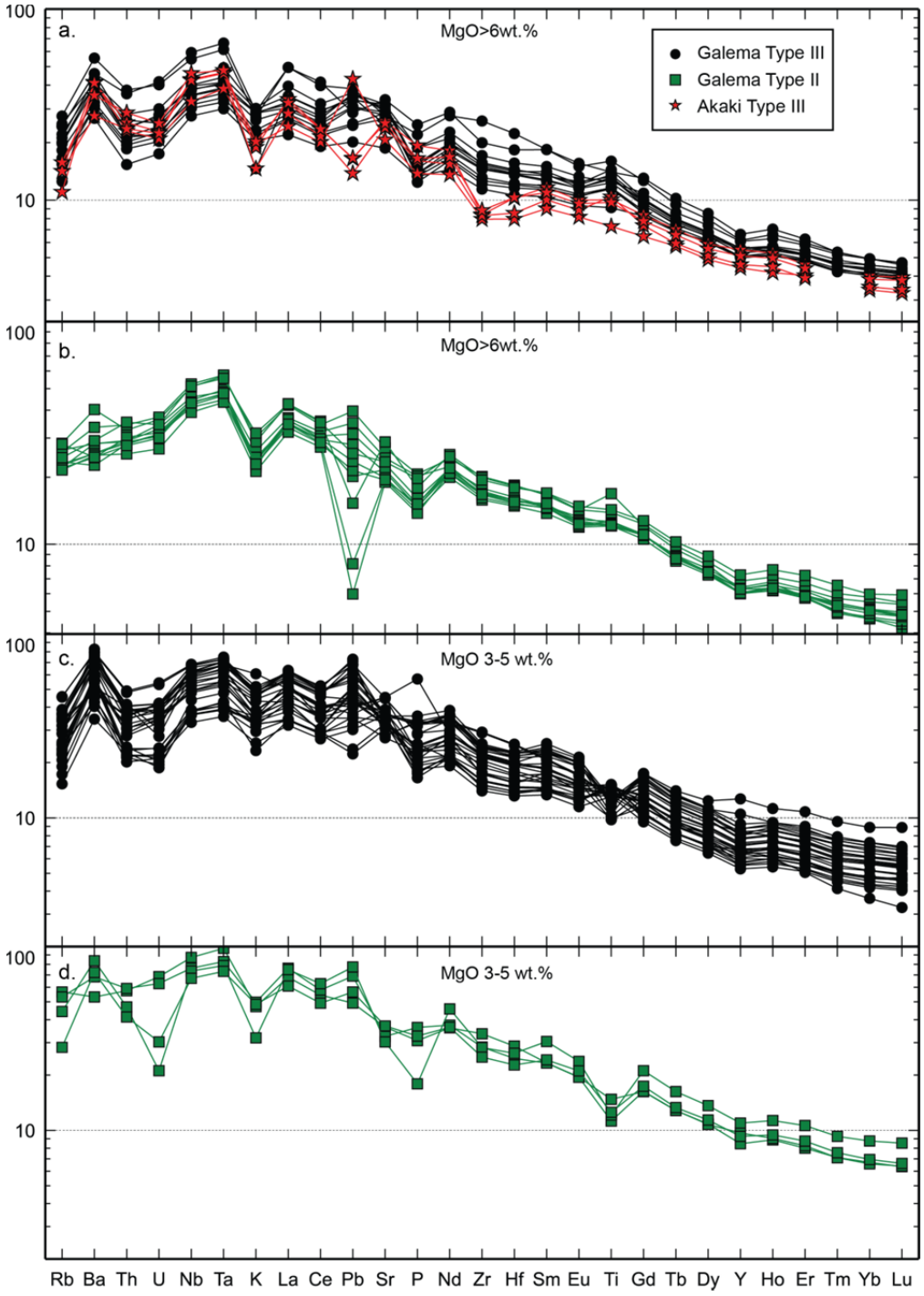

Figure 3.2.

Primitive mantle (Sun and McDonough, 1989) normalized trace element diagrams for Galema Range and AMZ samples with greater than 6 wt.% MgO (a,b) and 3-6 wt.% MgO (c,d). AMZ data are from Rooney et al. (2014a).

Trace element geochemical patterns of samples with <6 wt.% MgO display similar trends to the more mafic samples in that they are strongly enriched in the most incompatible elements and display a negative K anomaly for the first group (Figure 3.2c) and negative Th-U anomaly and positive Nb-Ta anomaly for the second group (Figure 3.2d). Variations between the trace element patterns of the more evolved and primitive samples are consistent with fractionation of typical mineral phases during magma evolution (e.g., Ti variation due to fractionation of magnetite).

An additional plot of samples from the Akaki magmatic zone (AMZ) magmas with similar MgO concentrations (Rooney et al., 2014a) reveals a similar trace element pattern to the second group of Galema samples (Figure 3.2a). Akaki samples also show broad similarities in trace element vs. MgO wt.% plots (Rb, Nb, Zr, Yb, Eu, La) with those of the Galema range (Figure 3.3). There is some minor variance in the Ba vs. MgO wt.% and Sr vs. MgO wt.% data, with Akaki displaying a slight enrichment in the more primitive samples (Figure 3.3).

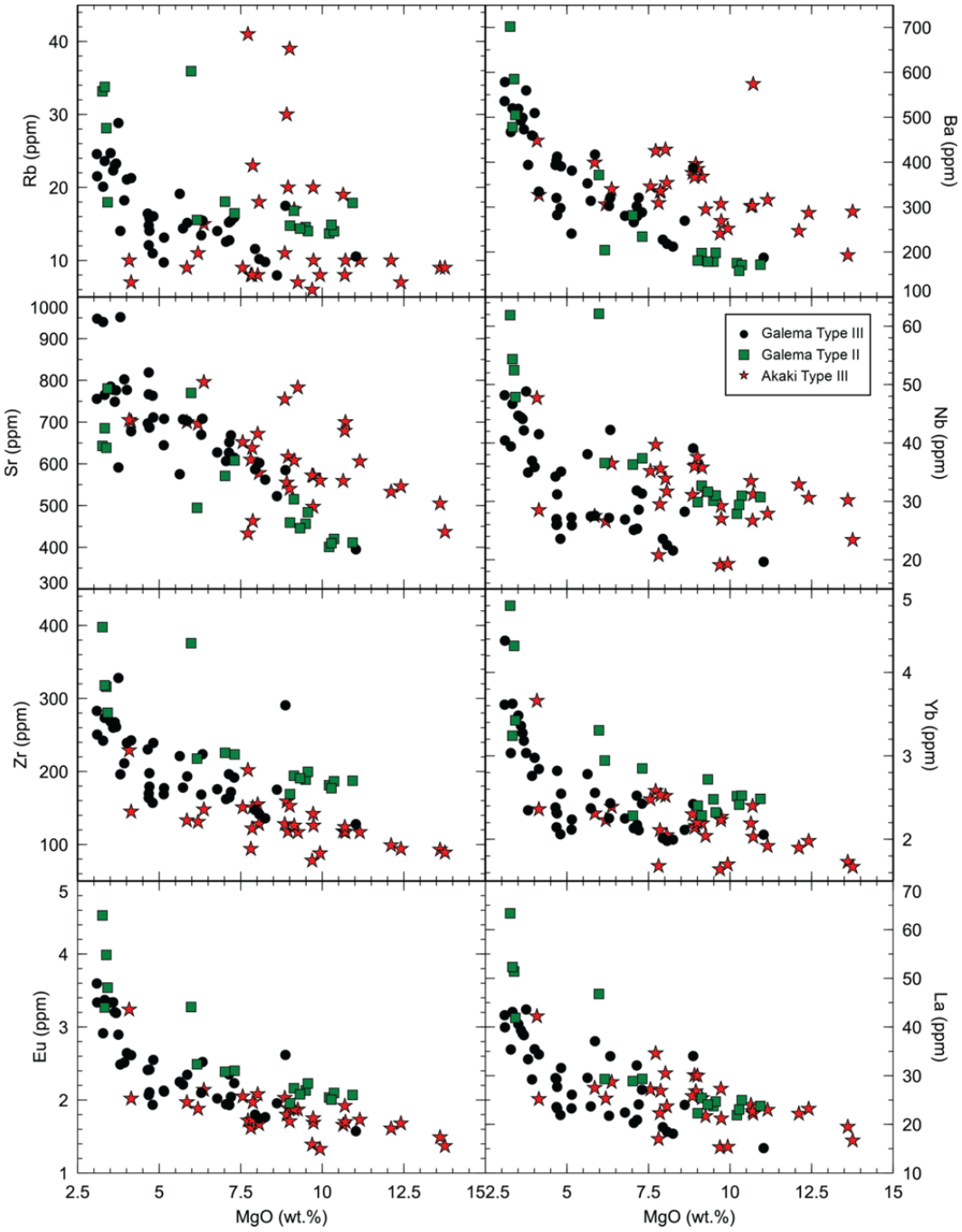

Figure 3.3.

Bivariate plot for samples from the Galema Range and AMZ for samples with >3 wt.% MgO. Symbols are the same as Figure 2. AMZ data are from Rooney et al. (2014a).

Primitive mantle diagrams of the first group of magmas from the Galema range display characteristics similar to those identified as basanites from the Miocene volcano - Gerba Guracha on the eastern Ethiopian plateau (Figure 3.2b,d) (Rooney et al., 2017). Specifically, both magma suites display primitive mantle-normalized trace element patterns of elevated Nb and Ta, but lack the strong positive Ba anomaly common in many Ethiopian basalts (Rooney, 2017). Examination of the geochemistry of the basanites from Gerba Guracha have led to the interpretation that they were the result of melts derived from a mixture of asthenospheric and metasomatized lithospheric mantle sources (Rooney et al., 2017). We presume a similar origin for the Galema Range lavas that display parallel geochemical characteristics. Determination of the melting conditions of the metasomatic-influenced magmas of the Galema range is complicated by the potentially diverse range of lithologies that may have contributed to their origin; existing thermo-barometric models typically presume standard peridotite source lithologies, creating significant complexity for any forward or inverse models of melt generation for this magma type (Rooney, 2019).

Primitive mantle-normalized diagrams of the second group of magmas of the Galema range displays characteristics similar to those identified in the Type III group of magmas of the East African Rift (Figure 3.2a,c) (Rooney, 2017). This trace element geochemistry pattern is widely distributed in Cenozoic magmas, and is found in locales across East Africa (Rooney et al., 2014a). These magmas formed from a mixture of the Afar plume, depleted upper mantle and a lithospheric component (Rooney et al., 2013; Rooney et al., 2014a). Mafic samples of the AMZ (> 6 wt.% MgO) (Rooney et al., 2014a) also display similar trace element geochemistry to the Type III magmas of the EARS (Figure 3.2a). Type III magmas in the MER have been interpreted as melts derived from an upper mantle peridotite (Rooney, 2017) and provide an opportunity to

constrain the conditions of melt generation. To determine melting conditions of the magmas of the Galema range, only primitive samples with >6 wt.% MgO were considered for modeling.

The magmatic sources of the AMZ have been determined through trace element geochemical modeling to be a mixture of Afar plume, depleted mantle and Pan-African lithosphere lithologies (Rooney et al., 2014a; Rooney, 2019). As the contemporaneous AMZ lies on the conjugate rift margin from the Galema range, and its trace element geochemistry shows striking similarities to Galema range samples (Figure 3.2), it is a logical assumption that magmatic processes in the two areas may have been similar. Thus, we use the previous interpretations of the AMZ melting parameters as a comparison to our determinations of those of the Galema range.

3.5 Discussion

The trace element geochemistry of Galema range primitive magmas suggests that the source of parental melts was a mixture of Afar plume, depleted mantle and a lithospheric component. The T_P of Group III East African magmas is elevated (Rooney et al., 2012c), likely due to the African Superplume. Here we explore the utility of the magma generation and evolution as probes of the rifting process, specifically the extent to which the lithosphere has been thinned.

3.5.1 Modeling

Geochemical and thermodynamic models may be used to explore the parameter space of asthenospheric melting within the CMER. Models that employ the use of major element geochemistry effectively probe the conditions under which a magma last equilibrated with the asthenosphere (Herzberg and O'Hara, 2002; Lee et al., 2009; Kimura and Kawabata, 2014; Kimura and Ariskin, 2014). Models that determine the evolution of trace element geochemistry of a magma reveal information about conditions of initial magma generation (McKenzie and

O'Nions, 1991; Kimura and Kawabata, 2014). To constrain conditions under which magmas were generated and up to the point where they intruded the lithosphere on ascent, we have thus used several models to determine mantle T_P, depth of melting, and melt lithology for the Galema range magmas.

3.5.1.1 Mantle Potential Temperature and Conditions of Melt Equilibration

To determine whether the mantle T_P was sufficiently elevated to generate the Galema range magmas, the SiO_2 activity thermobarometer of Lee et al. (2009) was employed. SiO_2 is buffered at given temperatures and pressures by the mineralogy of the system, and is not greatly affected by source composition (Lee et al., 2009). This thermobarometer requires that a magma be corrected to primary compositions. Primary compositions thus should be unaffected by crystal phase fractionation during magmatic evolution and are equivalent to the composition of the magma when it was last in equilibrium with the mantle (Lee et al., 2009). The Galema range basalts display modal abundances of both olivine and plagioclase in the more primitive samples (Chiasera et al., 2018), indicating that both phases must be corrected for to achieve primary melt compositions. As the model of Lee et al. (2009) only corrects to primary compositions for olivine fractionation, the Galema basalts compositions were first back-corrected to primary melt composition for both plagioclase and olivine fractionation using the reverse fractional crystallization component of the Petrolog v.3.1.1.3 modeling suite (Danyushevsky and Plechov, 2011), following the methodology described in El-Rus and Rooney (2017)(Supplemental Material). Initial pressure (0.7 GPa) and fO_2 values (QFM + 0.16) for the back-correction calculations were taken from Chiasera et al. (2018). Samples 3030, 3031, 3042, 3061, 3063 and 3077 (Supplemental Material) were chosen from the Group III Galema magmas based on minimal modal abundance of plagioclase (Chiasera et al., 2018), which yielded successfully-

corrected primary melt compositions (Supplemental Material). These back-corrected compositions were then used as thermobarometer inputs, effectively bypassing the built-in back-correction procedure for the Lee et al., (2009) model. Akaki samples 2001, 2004, 2006 and 2029 (Supplemental Material) were also chosen for the same thermobarometric calculations based on MgO concentration and lack of plagioclase phenocrysts. The Akaki samples did not require correction to primary compositions on the basis of plagioclase fractionation, and thus the built-in olivine correction of Lee et al. (2009) was used.

After correcting to primary melt compositions, the results of the thermobarometry calculations for the Galema samples indicate temperatures of 1435-1471°C and pressures of 2.1-2.6 ± 0.2 GPa. (Supplemental Material). The results of the thermobarometry calculations for the Akaki samples similarly indicate a temperature range of 1416-1452°C and pressure range of 2.1-2.5 ± 0.2 GPa. (Supplemental Material).

The following conversion for pressure (p) to depth (h) was utilized,

$$p(h) = \rho g h$$

in which $p(h)$=pressure in Pa, ρ= density (2800 kg/m^3; Dziewonski and Anderson, 1981), g=gravitational acceleration (9.81 m/s^2), and h=depth in meters.

The approximate depth range for the Galema range samples is 76 - 95 ± 7 km. The approximate range of depths for the Akaki samples is 76 - 91 ± 7 km. Models that employ major element geochemistry are useful in the determination of equilibrium conditions of a magma (Herzberg and O'Hara, 2002; Lee et al., 2009; Kimura and Kawabata, 2014; Kimura and Ariskin, 2014). As such, these results reflect depths at which the Galema magmas last equilibrated with the asthenosphere, prior to intrusion into the lithosphere (Lee et al., 2009).

The back-corrected chemical values of the Galema range basalts were also applied to the major element, MgO-T thermobarometer of the Hydrous Adiabatic Melting Model Simulator version 1 (HAMMS1)(Kimura and Kawabata, 2014). The temperature, pressure and melt fraction values from the MgO-T thermobarometer in HAMMS1 are estimates of the conditions of final equilibration of the melt with mantle (Kimura and Kawabata, 2014). The results of the HAMMS1 model indicate a temperature range of 1430-1474° C, a pressure range of 2.2-2.6 GPa, and a melt fraction (F%) range of 9-11% for the Galema range basalts (Supplemental Material). The approximate range of equivalent depths of these pressures is 80-95 km. (Figure 3.5). For the AMZ samples, the major element, MgO-T thermobarometer of HAMMS1 indicates a temperature range of 1400-1434°C, a pressure range of 2.3-2.5 GPa, and a melt fraction range of 4-6% (Supplemental Material). The approximate range of equivalent depths for these pressures is 84-91 km. (Figure 3.5).

3.5.1.2 Conditions of Melt Generation

Trace element geochemical models help constrain the initial conditions of melt generation, as the concentrations of incompatible elements are greatly influenced by melting conditions within asthenospheric material (McKenzie and O'Nions, 1991; Kimura and Kawabata, 2014). To determine the temperatures and pressures of melt generation for the Galema range basalts, the HAMMS1 model of Kimura and Kawabata (2014) was used. HAMMS1 estimates the temperature, pressure, water content, melt fraction and contamination percentage of a magma through iterative forward modeling of melt composition(s). The primary method of estimation is based on fitting predicted concentrations of trace elements, after application of intensive variables to melting calculations, with those of the measured magma. As trace elements are particularly sensitive to processes of melting (McKenzie and O'Nions, 1991; Anderson, 2007;

Kimura and Kawabata, 2014), this modeling methodology is useful in determining the primary intensive parameters of melting of a magma. However, as HAMMS1 employs a forward modeling approach, prior knowledge of the initial source lithology and chemistry is necessary.

As noted previously, most Galema range basalts follow a pattern of a Type III magma (Rooney, 2017), which is the result of a mixing of three source reservoirs: depleted upper mantle, Afar plume, and a lithospheric component (sub-continental lithospheric mantle)(Rooney, 2017). This interpretation is based upon the isotope geochemistry of lavas in the region, which have shown in multi-isotope space that magmas in Afar and the MER comprise a mixture of Afar plume, depleted mantle, and Pan-African lithosphere (Rooney et al., 2012a; Alene et al., 2017; Feyissa et al., 2017). The relative concentrations of these components in the source of magmas from the CMER have been estimated as ~80% depleted upper mantle, ~20% Afar plume, and small amounts of a lithospheric component (Rooney et al., 2014a). This lithospheric component was likely a portion of the lower sub-continental lithospheric mantle (SCLM) that foundered (e.g., Bédard, 2006; Van Wijk et al., 2008; Lee et al., 2011) and mixed into the depleted upper mantle as a result of thermal/chemical erosion by the Afar plume (Rooney et al., 2012a; Furman et al., 2016). Thus, we have chosen an 80:20 (DM:PM) mixture (Sun and McDonough, 1989; Workman and Hart, 2005; Rooney et al., 2014a) as our starting melt lithology for the HAMMS1 calculations (Supplemental Material). To account for the lithospheric component of Rooney et al. (2017) and Rooney et al. (2012a), we have chosen a composition equal to an experimental analysis of melting of a clinopyroxenite-hornblendite (Pilet et al., 2008) (Supplemental Material). As we have determined that there is little to no crustal contamination of the Galema samples, the chemistry of crustal material built-in to HAMMS1 as a contaminant was not used. Instead, the lithospheric composition was entered into HAMMS1 in place of the built-in

chemistry of crustal material in order to vary its concentration during processing. For continuity of process, we used the same Galema Type III and Akaki samples were used as for the Lee et al. (2009) thermobarometer discussed above (Supplemental Material).

Within the HAMMS1 model, the temperature, pressure, H_2O content and contamination percentage were all varied systematically within specified ranges (Temperature: 1300-1500°C, Pressure: 3.5-2.0 GPa., H_2O: 0-1 wt.%, lithospheric component: 0-5%) to achieve an acceptable match between the trace element concentrations of the modeled melt and the Galema range basalt chemistry. In addition to the trace element calculations, melting pressures and temperatures determined from MgO melt thermometry (Herzberg and O'Hara, 2002; Kimura and Ariskin, 2014) and melt fraction (f %) for a peridotite source are also calculated within HAMMS1 for the selected samples (Kimura and Kawabata, 2014).

The conditions of the HAMMS1 calculations that best matched the trace element distribution of the observed data for the magmas of the Galema range are: 1418-1450°C at a pressure range of 2.9-3.2 GPa, under anhydrous conditions, and with lithospheric component additions of 0.5-1.1% (Figure 3.4a)(Supplemental Material). The input conditions that best fit the observed data for the AMZ samples have a similar temperature and pressure range 1430-1438°C; 3.0-3.1 GPa, with lithospheric component additions of 0.8-1.5% (Figure 3.4b)(Supplemental Material). This translates to melt generation depth ranges of 106-116km for the Galema range, and 109-113km for the Akaki samples (Figure 3.5).

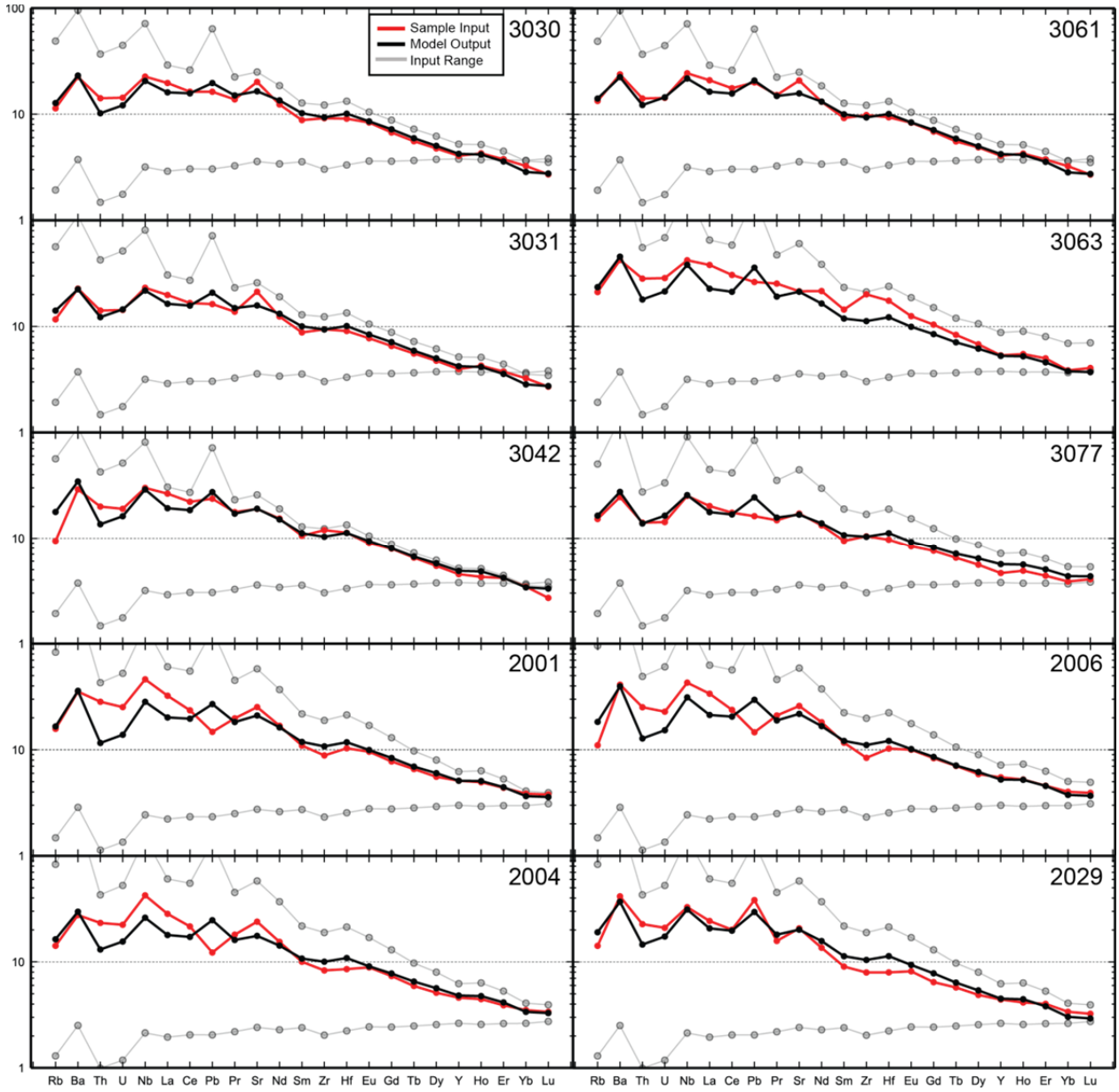

Figure 3.4.

Trace element spider diagrams showing selected samples input into to the HAMMS modeling suite (Kimura and Kawabata, 2014) for selected Galema range and AMZ samples. See text for discussion on source chemistry and mantle conditions used. AMZ data from Rooney et al. (2014a). Light grey plots represent model outputs for the end member values of the range of

Figure 3.4. (cont'd.)

initial conditions described in the main text (1500C°, 2GPa, 1% lithosphere for the enriched plot and 1411C°, 3GPa, 1% lithosphere for the depleted plot).

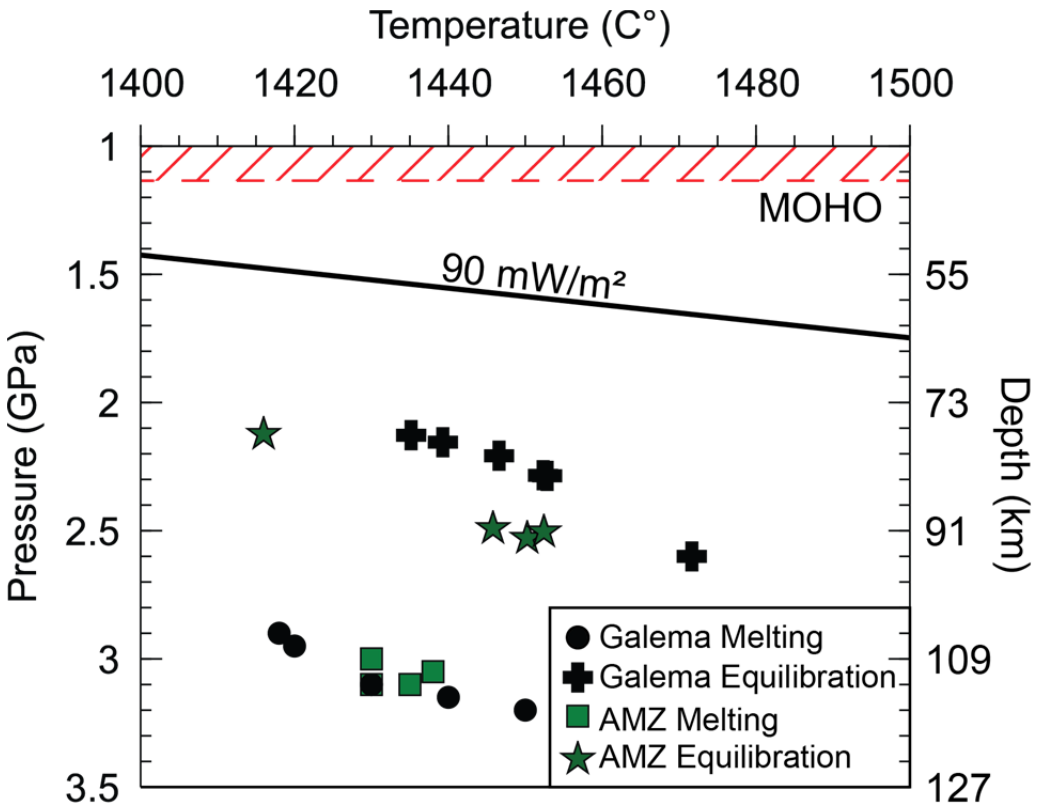

Figure 3.5.

Pressure temperature chart of melting and asthenospheric equilibration of the Galema range and AMZ Type III magmas. Temperature and pressure estimates from our thermodynamic, trace element modeling (HAMMS1)(Kimura and Kawabata, 2014) and major element, olivine thermobarometry (Lee et al., 2009). Moho depth estimates from Keranen et al. (2009). Geotherm estimate from Hasterok and Chapman (2011).

3.5.2 Model Discussion

3.5.2.1 Mantle Potential Temperature

The results of the SiO_2 thermobarometry indicate that the mantle (T_P) during the final equilibration with the mantle of the Galema range magmas was 1435-1471°C. The results of the HAMMS1 modeling indicate T_P of the initial melting of the magmas of the Galema range to have a similar range of 1418-1450°C. The temperatures derived from the major element thermobarometry of HAMMS1 indicate a temperature range of melt equilibrium for the magmas of the Galema range of 1430-1474°C, displaying remarkable coherence with the independently-derived temperatures of the SiO_2 thermobarometry and trace element modeling.

These estimates of the T_P of the mantle during the formation of the Galema magmas corroborate other estimates in the region. Magmatic volume estimations from the Virunga province indicate $T_P \approx 1430$°C for the southern EARS (Rogers et al., 1998a). Beccaluva et al. (2009) used the petrogenetic modeling techniques of Albarede (1992) to determine that T_P=1200-1500°C for Ethiopian flood basalts on the northwestern Ethiopian plateau. Thermodynamic calculations (PRIMELT-2; Herzberg and Asimow, 2008) performed on a large dataset of <10 Ma lavas from the MER have shown that mantle T_P of the EARS was at its highest, ~170°C above ambient (1350°C ± 50), during the Oligocene (Rooney et al., 2012c). Source melt conditions of magmas from Djibouti have been modeled to estimate the maximum mantle T_P anomaly at <10 Ma had decreased to ~140°C (Rooney et al., 2012c). The SiO_2 thermobarometer of Lee et al. (2009) has previously been applied to magmas from Afar, resulting in a T_P range of 1472-1489°C (Ferguson et al., 2013). REE inversion modeling (McKenzie and O'Nions, 1991) was also applied to these Afar magmas, resulting in a T_P estimate of 1450°C (Ferguson et al., 2013).

These previously determined T_P values are in the same range as the results of our thermobarometry calculations. However, use of individual techniques only, such as trace element thermodynamic modeling or major element thermobarometry, provides information about one aspect of the melt generation and ascent processes. Despite the application of these individual techniques to assess T_P, a common theme has emerged: the mantle T_P of East Africa is elevated above that of ambient upper mantle (Rooney et al., 2012c).

3.5.2.2 Melting Pressures

Fundamentally, the process of continental rifting requires thinning of the lithosphere and intrusion of melt into the lithosphere (Buck, 2006). As the base of the lithosphere-asthenosphere boundary (LAB) ascends during continental rifting, adiabatic melting generates melt that will intrude the lithosphere (Morton et al., 1979; McKenzie and Bickle, 1988). Thinning of the lithosphere and shallowing of the LAB may occur due to thermomechanical erosion (Spohn and Schubert, 1982; Davies, 1994; Wang et al., 2002).

Our SiO_2 thermobarometry calculations show the magmas of the Galema range re-equilibrated with asthenosphere at pressures of 2.1-2.6 ± 0.2 GPa (~76-95 km depth). The results of the major element thermobarometry estimates from HAMMS1 suggest similar pressure-temperature conditions: 2.2-2.6 GPa (80-95 km depth). The HAMMS1 trace element modeling results suggest melt generation pressures for the Galema range to be 2.9-3.2 GPa (106-116 km depth).

This range of depths and temperatures is consistent with other estimates of the melt generation depth and ponding of magmas in the region, despite the diverse array of techniques being applied. Iron concentrations of magmas that have been corrected to primitive compositions (FeO*) suggest that the depth of melt ponding (and subsequent melt re-equlibration) within the

MER to be in the range of 53-105 km (Rooney et al., 2005; Furman et al., 2006a). The same technique was also used to estimate a depth of melt residence for the Galema range basalts of ~110 km (Chiasera et al., 2018). The SiO_2 thermobarometer of Lee et al. (2009) has previously been applied to magmas from Afar, resulting in a magma re-equilibration depth estimate of ~83-94 km (Ferguson et al., 2013).

REE inversion modeling (McKenzie and O'Nions, 1991) was applied to Afar magmas, resulting in a depth estimate of the melting column to be 80-95 km (Ferguson et al., 2013). These estimates of the depth of the melting column in Afar, combined with estimates of extension rates, have led to the interpretation that the lithosphere in the area is 60-80 km thick (Ferguson et al., 2013). REE inversion modeling (McKenzie and O'Nions, 1991) of Quaternary magma chemistry from the NMER has estimated a melting depth range of 53-100 km with the shallower depth interpreted as the base of the lithosphere (Ayalew and Gibson, 2009; Rooney, 2010).

The variance in estimates of melt pressures and temperatures may arise from the methodology used, which effectively probe two different processes: melt generation, and melt equilibration within the asthenosphere. Estimates of melting depth that are based on trace element geochemistry reveal information pertaining to the initial depth of melt generation (McKenzie and O'Nions, 1991; Kimura and Kawabata, 2014). Depth estimates based on major element geochemistry, however, reveal the pressures at which the melt last equilibrated (e.g. stalled) within the asthenosphere, before intrusion into the lithosphere (Herzberg and O'Hara, 2002; Lee et al., 2009; Kimura and Kawabata, 2014; Kimura and Ariskin, 2014). While these estimates of the depth of melt generation in the EARS broadly agree with the results of our analyses of the melting conditions of the magmas of the Galema range, there exists natural

variation in the systems that were studied. Lithospheric thickness varies within the MER (e.g., Rooney, 2010), with the thinnest lithosphere in Afar (Ferguson et al., 2013).

We have demonstrated a consistent difference exists between the depth of melt generation (106-116 km) and depth of re-equilibration (~76-95 km) for the Galema Range. We have also demonstrated a similar deviation for the depth of melt generation (109-113 km) and melt re-equilibration (~76-91 km) for the AMZ. Given the conceptual model of melt generation at depth, ascent of this melt towards the LAB, and ponding of the melt at the base of the lithosphere, we may provide insights into the operation and location of these processes.

3.5.3 Geophysical Constraints on Continental Rifting Processes

The results of our modeling of Galema range magma source melting conditions show an anomalously high mantle T_P (+~68-100°C) and a melt stalling/re-equilibration depth of ~80 km, interpreted as the lithosphere-asthenosphere boundary. Next, we explore how this hypothesis fits with the existing geophysical literature.

3.5.3.1 The temperature of the Ethiopian mantle

Although it has been suggested by some authors that the Ethiopian mantle is thermochemically "normal" (e.g., Rychert et al., 2012), with magmatism the result of passive decompression melting in response to extension (e.g., Rychert et al., 2012; Hammond et al., 2013), a consensus has generally emerged amongst the seismological community that the Ethiopian mantle is characterized by markedly deep-seated (e.g., Benoit et al., 2006a; Benoit et al., 2006b; Chang and Van der Lee, 2011) slow wavespeeds (e.g., Bastow et al., 2008; Bastow et al., 2010; Gallacher et al., 2016). The Ethiopian upper mantle is seismically amongst the slowest worldwide (Bastow, 2012). Our observations of relatively deep mantle melting at elevated T_P

below Ethiopia corroborate these studies, and emphasize the requirement for both elevated temperatures and mantle melting to explain the seismic observations.

3.5.3.2 The Ethiopian LAB

The highest resolution images of Ethiopian lithospheric seismic structure are the wide-angle seismic profiles that emerged from the Ethiopia Afar Geoscientific Lithospheric Experiment (Mackenzie et al., 2005; Maguire et al., 2006). Unfortunately, they do not penetrate the entire lithosphere; instead their resolution terminates at a 55-60 km-deep mantle reflector – the 'L' reflector. Our inferred ~80 km estimate for LAB depth corroborates the conclusion of Maguire et al. (2006) that the L-reflector is not the LAB but a mid-lithosphere discontinuity.

S-to-P receiver function studies in Ethiopia differ in their claims concerning the LAB below Galema: Rychert et al. (2012) suggest that no mantle lithosphere remains, but more recent analysis by Lavayssière et al. (2018) places the LAB at 80-100 km depth. A more coherent picture of LAB depth for Galema emerges from the surface wave literature: Dugda et al. (2007) suggest 60-80 km, while Bastow et al. (2010) suggest the MER lithosphere is characterized by anisotropic elongate melt inclusions to ~75 km depth. Both results are closely matched by the findings of our study.

The P-wave velocity model of Bastow et al. (2008) reveals slow upper mantle wavespeeds to depths of ~100km beneath the Galema range (Figure 3.6). Body-wave travel-time tomography does a poor job of constraining the depths of anomalies, but the apparent termination of low-wavespeeds below Galema, as shown here, is consistent with our hypothesis that ~80km-thick lithosphere was heated during Pliocene magmatism. Notably, the amplitudes of the slow-wavespeed anomalies below Galema are markedly lower than below the MER to the west. Thus, while the Galema lithospheric mantle remains warm, it is likely now melt-free, at

least in comparison to the MER. This thermal modification of the SCLM beneath Galema on the eastern Ethiopian plateau may have influenced the location of the later magmatism of the WFB (Chiasera et al., 2018).

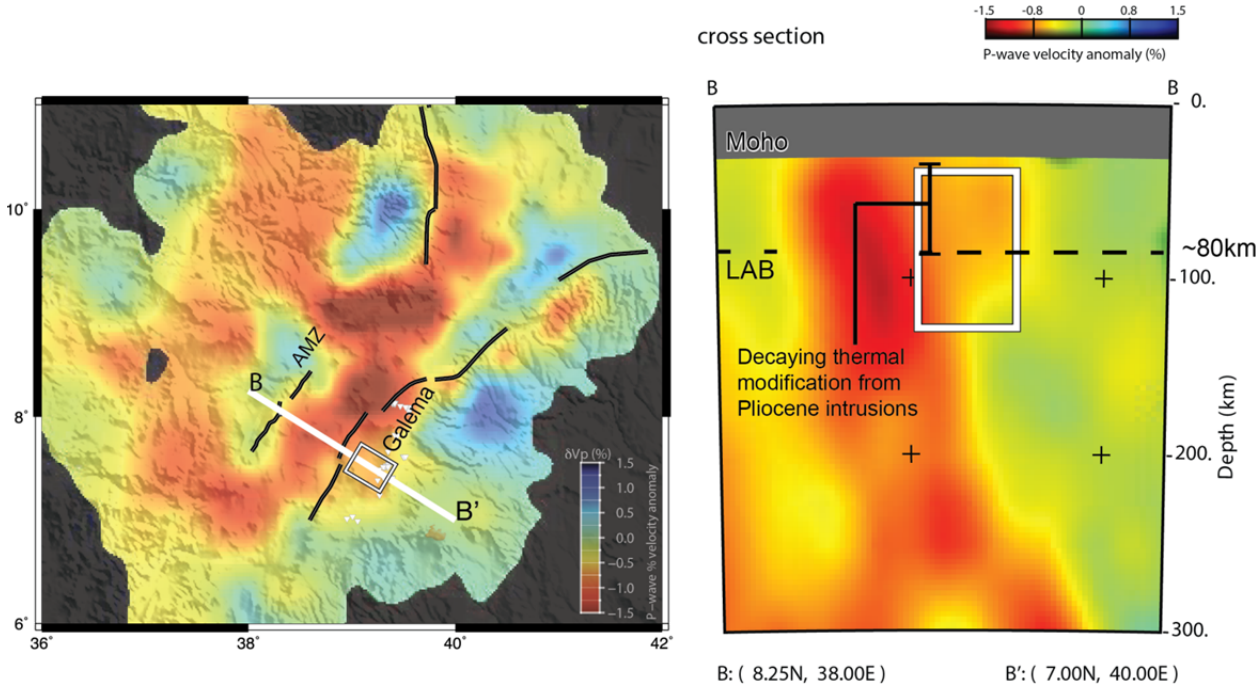

Figure 3.6.

75km depth-slice through the P-wave velocity model of (Bastow et al., 2008) and associated cross section (B-B') for orthogonal transect across the Galema range.

3.5.4 Lithospheric stretching and adiabatic decompression melting during formation of the Galema range

Although we cannot precisely know the pre-rift depth of the LAB below the Galema range, our present-day estimate of 80 km allows us to draw some conclusions concerning plate stretching factors (β) (McKenzie, 1978). Globally, Proterozoic lithosphere is ~100km thick (e.g., Djomani et al., 2001), similar to the thickness indicated by surface waves for undeformed portions of the Nubian and Somali plates to the west and east of the MER respectively (e.g.,

Fishwick and Bastow, 2011). The implication of these observations is that β=1.25 beneath the Galema range, remarkably similar to the β=1.3 estimate derived by Maguire et al. (2006) from wide-angle seismic study of the Ethiopian crust. These results indicate that at least in the MER, crustal stretching factors are a good proxy for plate stretching factors, consistent with the view that magma intrusion has accommodated considerable MER extension at both crustal (e.g., Keranen et al., 2004; Mackenzie et al., 2005; Cornwell et al., 2006; Maguire et al., 2006; Rooney et al., 2007) and lithospheric depths (e.g., Bastow et al., 2010).

Our new constraints on stretching factors in the vicinity of the MER have implications for melt generation by plate stretching and decompression of the ambient upper mantle. Assuming (i) a plate stretching model for decompression of the ambient upper mantle, (ii) a composition of fertile peridotite, and (iii) ambient mantle temperatures (1350°C), the calculated depth to the LAB beneath the Galema range (~80km) is close to the region where melt may be generated (Herzberg and O'Hara, 2002). However, since our data and modeling suggest that melt is generated at even greater depths than the LAB, such a model is inconsistent with our observations and interpretations. Rifting models that account for the finite rate of plate thinning in response to plate stretching (e.g., Bown and White, 1995) demonstrate that in rifting cases where the strain-rate is low, such as the MER (~6mm/yr; e.g., Bilham et al., 1999), the lithosphere will be strongly affected by conductive cooling to the surface. Such conductive cooling suppresses both plate thinning and decompression melting, even where the ambient upper mantle exhibits elevated mantle potential temperature. It therefore follows that simplistic plate stretching models are inappropriate for estimating stretching factors, calculating melt generation, and generally describing extensional processes within the MER. A robust conclusion of our work, however, is that plate thinning alone cannot generate the Type III magmas erupted

in the Galema range: elevated mantle potential temperatures associated with the Afar plume are also necessary.

The presence of a mantle thermal anomaly in the East African upper mantle has implications for lithospheric stability. In particular, the presence of fusible lithologies within the lithospheric mantle (e.g., amphibole and phlogopite-bearing metasomes) can result in melt generation upon minor thermobaric destabilization of the lithospheric mantle (Rooney et al., 2014b; Rooney et al., 2017). In the Virunga province of the Western Branch of the East African Rift, the abundant occurrence of metasome-derived magmas has been explained in terms of conductive heating of the lithospheric mantle by a plume located in the underlying convecting mantle (Rogers et al., 1998a). The occurrence of the magmas affected by metasomatic processes (Rooney et al., 2017) within the suite of lavas erupted within the Galema range indicates a parallel process - the lavas contain melt derived from metasomatized lithospheric mantle. The presence of magmas affected by metasomatism indicates a steeper thermal gradient across the lithosphere, caused either by increased thermal input to the SCLM, and/or thermal-mechanical thinning of the lithosphere. The presence of these lavas is further evidence for the continued existence of relatively thick lithospheric mantle adjacent the MER. The persistence of relatively thick lithosphere in the relatively advanced stages of rifting in Ethiopia has important implications for melt production during the final stages of continental breakup. Specifically, thinning of the continental lithosphere prior to the onset of seafloor spreading will occur at a faster rate than if it had been achieved at a constant rate since the onset of rifting. The resulting pulse in decompression melting would thus be expected to erupt over the continent-ocean transition, potentially forming so-called seaward-dipping reflector sequences, as is being

observed today in the Afar Depression in the Red Sea rift (e.g., Bastow and Keir, 2011; Bastow et al., 2018).

3.6 Conclusions

Geochemical analysis of magmas from the Galema range indicates they comprise a mixture of lithologies representing the Afar plume, ambient upper mantle, and metasomatized SCLM. The melts of the Galema range were generated as a result of an increased T_p of ~1450°C (~100°C above ambient mantle), related to thermal input from the ascending Afar plume. Our thermodynamic modeling and thermobarometric calculations indicate that the melts of the Galema range ascended from their depth of generation at ~110 km to stall at ~80km depth where they partially re-equilibrated at the base of the LAB.

P-wave tomographic models reveal a low velocity body of material beneath the Galema range at ~80-100km depth. We interpret this as the thermally-perturbed SCLM, resulting from thermal input by the intrusion of the Galema magmas on ascent. The depths of the lower bound for this thermal perturbation are consistent with the results of our modeling, with the shallow depth indicating the location of the LAB.

We present the following model based on existing constraints and our combined geochemical and geophysical results: (1) existing isotopic constraints (Rooney et al., 2012a) and our new trace element modeling require that, prior to the commencement of magmatic activity within the modern MER, lithospheric material foundered and mixed with the ambient asthenosphere; (2) increased mantle T_P, as a result of the impingement of the Afar plume, generated melts of both the plume and hybrid ambient upper mantle that mixed to form Type III magmas; (3) these magmas ascended and stalled at the LAB beneath each margin, allowing for

partial re-equilibration with the surrounding mantle (Figure 3.7a); (4) as these magmas intruded the lithosphere, they perturbed the thermal state, raising the temperature of the SCLM on the rift margins (Figure 3.7a); (5) thermobaric destabilization of the lithospheric mantle during this process generated magmas affected by melting of amphibole-bearing metasomes. The thermal modification of the SCLM by magma intrusion associated with the Galema range and the AMZ on the western margin, may have influenced the location of the younger WFB and SDFZ (Chiasera et al., 2018); and, (6) the subsequent focused magmatic intrusion along the SDFZ and WFB became the dominant areas of magmatic strain accommodation within the rift border faults (Figure 3.7b). These younger magmatic intrusions heated the SCLM beneath the rift axis (Figure 3.7b).

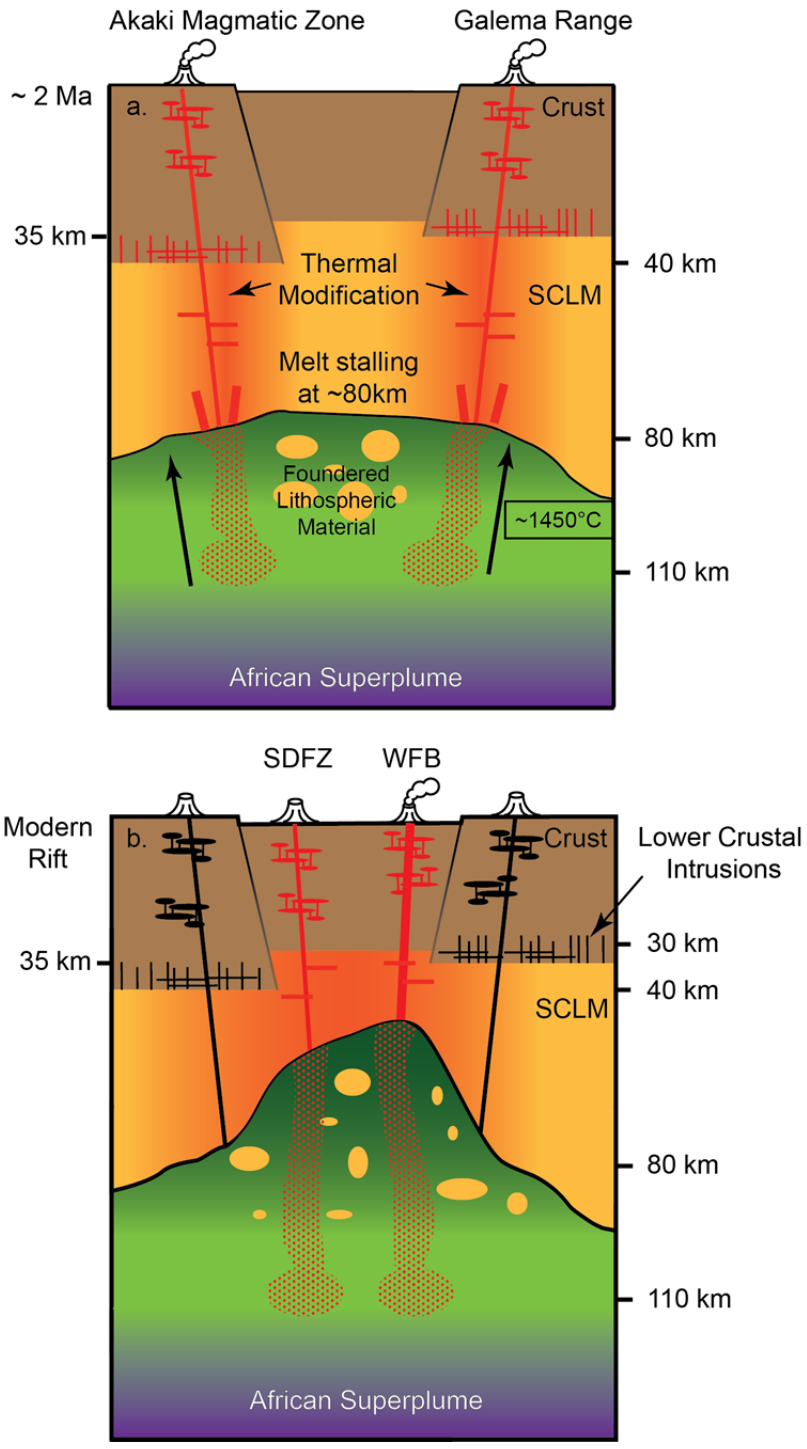

Figure 3.7.

Cartoon showing the hypothesized generation of the source melt of the magmas of the Galema range. a) Neoproterozoic, sub-continental lithospheric mantle foundered from the base

Figure 3.7. (cont'd.)

of the lithosphere and mixed into the upper mantle. The ascending Afar plume increased the mantle T_P to1418-1474°C, inducing melting conditions and mixing with the depleted mantle/SCLM hybrid. The melting column exists within a range of ~3.2-2.1 GPa (~117-77km depth) with the top interpreted as the thermomechanical barrier of the LAB. After which, the magma intruded the lithosphere and ascended within a polybaric magma plumbing system (Chiasera et al., 2018) to form the mafic dikes of the Galema range. b) The thermal modification of the SCLM, as evidenced by geophysical models, may have influenced the final location of the focused magmatism at the WFB (Chiasera et al., 2018).

Our key results are that the ambient upper mantle beneath the Galema range has an elevated T_P (~100°C), and that the lithosphere remains relatively thick, despite the magmatic extension underway at crustal depths.

4. ISOTOPIC SOURCE CHEMISTRY OF THE MAGMAS OF THE GALEMA RANGE; EVIDENCE OF A RECENTLY GENERATED SUB-CONTINENTAL LITHOSPHERIC MANTLE IN THE EAST AFRICAN RIFT SYSTEM

4.1 Introduction

The rifting of a continent occurs as the result of extensional stresses acting upon the continental lithosphere. The generation of these extensional stresses may be induced through impingement by an ascending mantle plume at the base of the lithosphere, resulting in uplift of the continent (e.g., Ebinger, 2005). Continental rifting must progress from initial faulting and fracturing of the crust to magmatic intrusion. This transition from extensional strain accommodation from faulting and thinning to focused magmatic intrusion is not well understood. While it is generally assumed that the transition to accommodation by focused magmatic intrusion is a progressive one, we show here that the transition may be more complex, with earlier phases of magmatic strain accommodation on the rift shoulder.

During phases when focused magmatic intrusion is active, extensional deformation within the plate must vary with depth. At shallower levels, diking clearly accommodates extension. However, at deeper levels, our data show the destabilization and destruction of the lithospheric mantle during these phases of focused intrusion. This not only implies that accommodation of extensional strain through focused magmatic intrusion can occur within thicker lithosphere, but that focused magmatic intrusion itself may contribute to lithospheric thinning.

The Main Ethiopian Rift (MER) is a recently active continental rift that displays a combination of rifting processes, from fracturing and faulting of the lithosphere to magmatically

accommodated extension. The MER preserves evidence of a range of lithospheric thicknesses, modified by the rifting process and impact of the Afar plume (e.g., Rooney, 2010; Ferguson et al., 2013). Thus, areas of magmatism within the MER are ideal settings to study how a mantle plume interacts with the lithosphere at a transitional stage of continental rifting, after initiation and prior to oceanic spreading. Much attention has been paid to the more recent magmatism within the MER border faults at locations where the lithosphere that has been thinned by extensional processes (e.g., Furman et al., 2006a; Rooney et al., 2012a). However, there is a growing realization that magmatism associated with rifting processes is older and more broadly distributed to areas outside of the rift that have thicker lithosphere (Chiasera et al., 2018). Studies of the impact of the Afar plume have been performed on flood basalt magmatism that occurred within a relatively thick lithosphere (e.g., Pik et al., 1999); however, these flood basalts occurred before the formation of the MER. There is little information available on the impacts of the Afar plume on areas of focused magmatic intrusion that occurred in thick lithosphere after the formation of the MER.

The Galema Range is an area of focused magmatism intruded into the eastern Ethiopian plateau, adjacent to the Central MER (Mohr and Potter, 1976; Mohr, 1980). The basalts of the Galema Range represent a magma generated by influence of the Afar plume in an area of relatively thicker lithosphere, before the most recent magmatism within the rift (Figure 4.1)(Mohr and Potter, 1976; Mohr, 1980; Kennan et al., 1990; Chiasera et al., 2018). We present isotopic geochemical data on 22 samples of magmatic products of the Galema Range. We demonstrate that some Galema Range magmas display evidence of Afar plume material in their source melts, mixed with a hybridized melt of depleted mantle and Pan-African lithosphere. Other Galema Range magmas display an additional fourth end member, which we contend is

evidence of a sub-continental lithospheric mantle that was recently generated by the Afar plume, prior to the onset of melting. This work demonstrates the evolution of geochemical reservoir compositions over the last ~2 Ma in the Central Main Ethiopian Rift. The presence of a signature of a plume-derived, metasomatic component indicates ongoing destruction of the SCLM. We also present here $^{40}Ar/^{39}Ar$ dates for the basalts of the Galema Range of 2.01 to 2.56 Ma, reaffirming previous dates obtained from K-Ar dating, placing the Galema magmatism to before that of the Wonji Fault Belt within the rift, and after the formation of the adjacent Asela-Sire border faults. This indicates that extensional strain accommodation through focused magmatic intrusion can occur prior to that which occurs within the rift proper. This magmatic strain accommodation can also occur over a broad area, to locations outside of the rift-border faults.

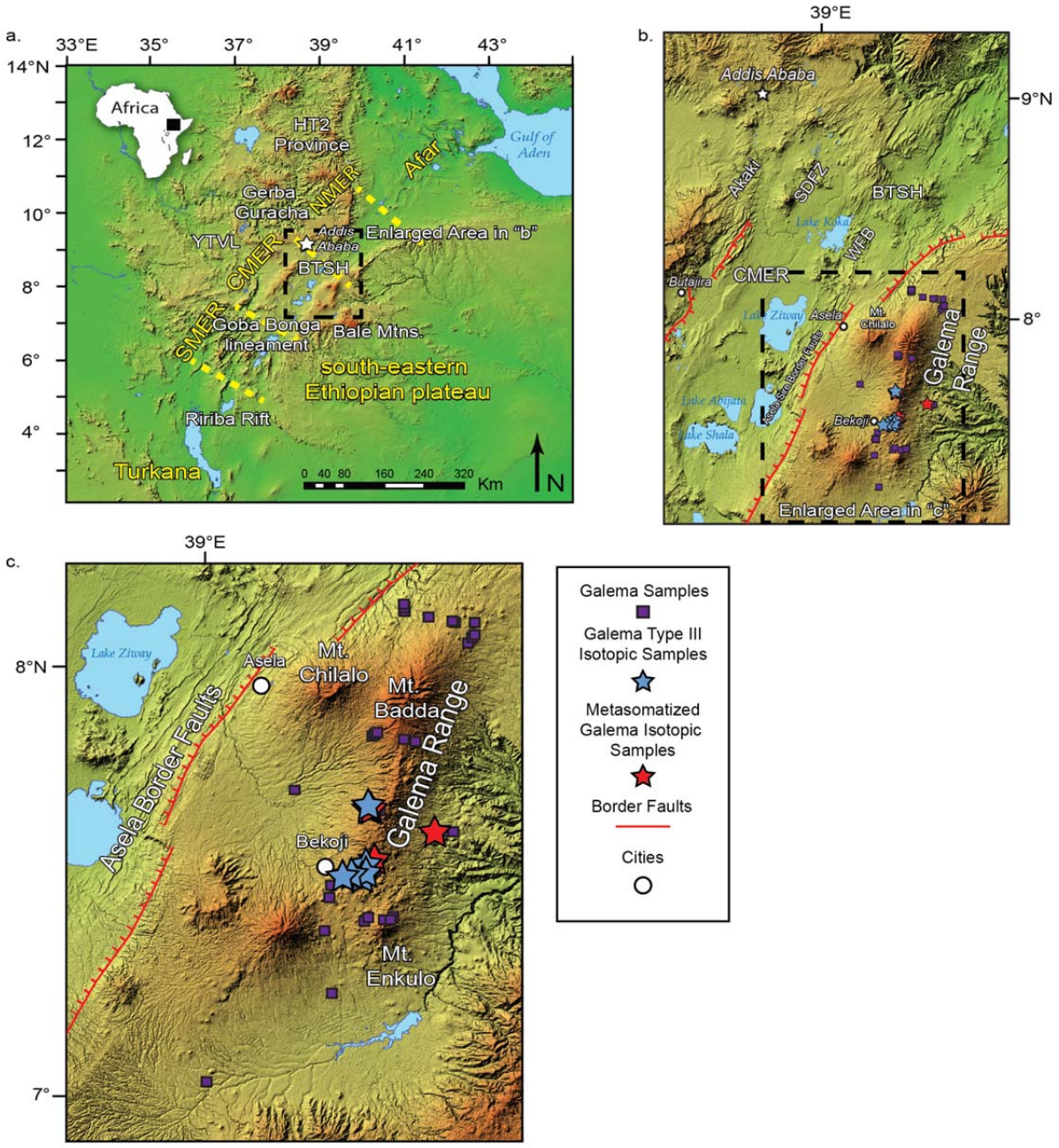

Figure 4.1.

a. Tectonic setting of the Main Ethiopian Rift (MER) within the East African Rift System (EARS). Northern Main Ethiopian Rift (NMER), Central Main Ethiopian Rift (CMER) and Southern Main Ethiopian Rift (SMER). Dashed line delineates (b). b. The Central Main Ethiopian Rift (CMER). WFB: Wonji Fault Belt; SDFZ: Silti-Debre Zeyit Fault Zone; YTVL:

Figure 4.1. (cont'd.)

Yerer-Tullu Wellel Volcanotectonic Lineament; BTSH: Boru-Toru Structural High. Dashed line delineates (c). c. Enlarged portion of the CMER showing the location of the Galema Range and samples used in this study. Location of other Galema samples from (Chiasera et al., 2018).

4.2 Background

4.2.1 Cenozoic Magmatic Evolution of the African-Arabian Large Igneous Province

A pulse of flood basalt magmatism in the Eocene marked the commencement of East African Cenozoic magmatic activity in the broadly-rifted zone of the Turkana Depression (northern Kenya) and southern Ethiopia (Ebinger et al., 1993a; George et al., 1998; Furman et al., 2006b). During the Oligocene, magmatic activity migrated northward with the eruption of flood basalts on the eastern Ethiopian plateau (Baker et al., 1996; Hofmann et al., 1997; Rochette et al., 1998; Pik et al., 1999; Kieffer, 2004). Shield building and fissure-fed basaltic magmatism occurred during the Miocene throughout East Africa (e.g., Rooney, 2017; Nelson et al., 2019).

Volcanic activity subsequently generated large silicic centers and smaller basaltic eruptions that localized to the developing MER (Rooney et al., 2011). Magmatism along the margins of the Central MER (CMER) occurred during the Plio-Quaternary, represented by the Akaki Magmatic Zone along the western margin (Figure 4.1b)(Rooney et al., 2014a), the Bale mountains on the eastern Ethiopian plateau (Figure 4.1a)(Nelson et al., 2019), and the Galema Range along the eastern margin (Mohr and Potter, 1976; Mohr, 1980; Chiasera et al., 2018) (Figure 4.1b,c). Quaternary magmatism focused within the MER in the form of series of en-echelon dikes, lava flows, scoria cones and associated silicic centers of the Wonji Fault Belt (WFB) and Silti-Debre Zeyit Fault Zone (SDFZ) (Mohr, 1967; Mohr, 1980; Woldegabriel et al., 1990; Rooney et al.,

2005; Kurz et al., 2007; Rooney et al., 2007; Rooney, 2010; Rooney et al., 2011; Rooney et al., 2012a) (Figure 4.1b).

Magmatism of the East African Rift System, and the extensional forces causing the rifting, have been attributed to the impingement of an upwelling of hot (140°C above ambient mantle; Rooney et al., 2012b), enriched mantle material (i.e. Afar plume) at the base of the African lithosphere (Schilling et al., 1992; Deniel et al., 1994; Nyblade and Robinson, 1994; Ebinger and Sleep, 1998; Pik et al., 1999; Furman, 2007; Rooney et al., 2012a; Rooney et al., 2012c). Evidence of contribution of the Afar plume to the magmatic geochemical reservoirs the EARS can be found in the isotopic geochemistry of the magmas generated as a result of rifting. Initially, the mantle reservoir for the Afar plume was identified as having the isotopic signature of the HIMU reservoir ($^{206}Pb/^{204}Pb>20$)(Schilling et al., 1992; Deniel et al., 1994). However, subsequent analyses of EARS basalts now indicate that the HIMU signature is the result of overprinting on the isotopic chemistry of the reservoir by melting of metasomatized, sub-continental lithospheric mantle (SCLM) material and that the Afar plume is of a "C" reservoir composition ($^{206}Pb/^{204}Pb \cong 19.6$)(Rooney et al., 2012a; Giordano et al., 2014; Rooney et al., 2014b; Furman et al., 2016). The absence of a HIMU signature is evident in the ε_{Hf} vs ε_{Nd} plot (Figure 4.2f) where the isotopic signatures of more recent within-rift magmas of the WFB and SDFZ fall above the mantle array and away from the signature of HIMU, which is below the array (Rooney et al., 2012a). Most magmas within the EARS do not display an isotopic signature purely of the Afar plume, indicating that there must be mixing of additional geochemical reservoirs into their source melts.

Generally, the magmas of the East African Rift System preserve within them isotopic evidence of the Afar plume, an upper mantle component (depleted mantle), and a crustal or

lithospheric component in varying fractions (Schilling et al., 1992; Deniel et al., 1994; Barrat et al., 1998a; Pik et al., 1999; Trua et al., 1999; Rogers et al., 2000; Peccerillo et al., 2003; Furman et al., 2006a; Rooney et al., 2012a; Rooney et al., 2014b). Values of $^{206}Pb/^{204}Pb$ of EARS basalts are more similar to the less radiogenic value of depleted mantle (i.e. MORB) of $^{206}Pb/^{204}Pb \cong$ 17.5 identified from the Indian Ocean than they are of values from the Afar plume value of $^{206}Pb/^{204}Pb \cong 19.6$, (Schilling et al., 1992; Rooney et al., 2012a; Rooney, 2017). This depletion, relative to the Afar plume signature, indicates that depleted mantle must be one of the mantle reservoirs that comprise the source melts of the EARS basalts. Values of $^{207}Pb/^{204}Pb$ and $^{208}Pb/^{204}Pb$ of EARS basalts further indicate that their source melts cannot simply be a binary mixture of the Afar plume and depleted mantle source reservoirs and must contain a third reservoir (Schilling et al., 1992). This third geochemical reservoir has been identified as being Pan-African lithosphere with similar $^{206}Pb/^{204}Pb$ values to the depleted mantle, but with more radiogenic values of $^{207}Pb/^{204}Pb$ and $^{208}Pb/^{204}Pb$ vs. $^{206}Pb/^{204}Pb$ (Schilling et al., 1992; Rooney et al., 2012a). The presence of Pan-African lithosphere as a geochemical reservoir in EARS magmas has been attributed to the foundering and mixing of lithospheric material into the depleted upper mantle, generating a hybrid reservoir, which then mixed with Afar plume material (Schilling et al., 1992; Rooney et al., 2012a; Furman et al., 2016).

4.2.2 The Galema Range

Located on the eastern Ethiopian plateau in the CMER (Figure 4.1b,c), the Galema Range is an area of right stepping, en-echelon mafic dikes trending at ~ 10-20°N and aligned, eroded scoria cones (Mohr and Potter, 1976; Mohr, 1980; Woldegabriel et al., 1990). The Galema Range extends from the volcanic center of Mt. Bada to the north, to the volcanic center of Mt Enkulo to the south, with maars and cinder cones existing between the two volcanic centers

(Figure 4.1c). The ~4.5 m thick dikes constituting the Galema Range span a length of ~70 km, and occupy a ~7 km wide fissure system. The dikes gradually disappear at the latitude of Mt. Enkulo (Mohr and Potter, 1976). The Galema Range was built to an elevation ~1000m above the south-eastern Ethiopian plateau by the magmatic pile erupted from the dikes and silicic centers (Mohr and Potter, 1976). Volcanic edifices within the WFB are dominantly of two varieties: cinder cones and large silicic centers.

Geochronological estimates have placed the of the age of the magmatism of the Galema Range within the Pliocene, from 2.1 to 3.1 Ma (Mohr and Potter, 1976; Kennan et al., 1990). This age post-dates the formation of the Asela-Sire border faults in the CMER, which have been dated at ~5-8 Ma (Bonini et al., 2005; Abebe et al., 2010), and pre-dates the within-rift magmatism of the WFB and SDFZ at ~1.8-1.28 Ma (Woldegabriel et al., 1990; Chernet et al., 1998; Wolfenden et al., 2004; Abebe et al., 2005; Rooney et al., 2005). The Galema Range has been linked to the extensional stresses that resulted in magmatism at the WFB and SDFZ, though it is older and located on the rift shoulder (Figure 4.1b)(Chiasera et al., 2018).

4.3 Methods

A field excursion in 2008 recovered 77 samples from dikes, basaltic flows, scoria cones and silicic centers of the Galema Range and surrounding areas (Figure 4.1b,c). 22 of these samples (Supplemental material) were chosen to represent the most primitive compositions (i.e. least affected by crystal phase fractionation) based on the occurrence of phenocrysts in hand sample and thin section, as well as lack of vesicles. A subset of 17 of these samples was selected for isotopic analysis (Figure 4.1c)(Supplemental material). The samples were cut to minimize alteration due to weathering and further cut into ~30 g billets. After being then polished to

remove saw marks, these samples were cleaned in an ultrasonic bath of deionized water before being crushed in a steel jaw crusher and powdered in a Bico ceramic disk mill. Aliquots of these powders were then processed following the procedures of Konter and Storm (2014) and Finlayson et al. (2018). After removal of any existing alteration products, single dissolutions of these powders were prepared using the techniques outlined in Koppers et al. (2003) at the Center for Earth and Environmental Isotope Research (CEEIR) of the University of Texas at El Paso (UTEP). Following the methods of Konter and Storm (2014), separations were performed by passing the dissolutions through Eichrom Sr-resin, TRU-resin and Ln-resin at the CEEIR at UTEP. The entire sample aliquot was passed through the Sr-resin column, collecting both the Sr and Pb fraction. Pre-cleaned Sr-resin (250 µl resin bed; 100-150 mesh) was washed with 6M HCl and H_2O. Prior to loading the sample, the resin in conditioned with 3M HNO_3. The sample was dissolved in 3M HNO_3 before loading into the exchange column. Nd and the matrix were collected by washing the loaded resin with 3M HNO_3, which was reserved for further separation. Sr was extracted from the resin by washing with H_2O. Pb was extracted from the same resin by washing with 6M HCl. To improve purity, the Sr elution was passed through the Sr-resin a second time. The Pb fraction was cleaned with AG1-x8 resin and HBr-HCl chemistry following Hanan and Schilling (1989). The reserved Nd fraction was treated with ascorbic acid to reduce all Fe^{3+} to Fe^{2+} before passing through a chromatographic column loaded with TRU resin (Horwitz et al., 1993; Pin and Zalduegui, 1997). Ion exchange columns loaded with Eichrom TODGA resin were used to separate Hf from the dissolutions following the procedures detailed in (Connelly et al., 2006)

The remaining subset of 5 samples (Supplemental material) were crushed in a ceramic plate chipper and picked to remove phenocrysts prior to $^{40}Ar/^{39}Ar$ method dating at the University of

Nevada Las Vegas. These samples were wrapped in Al foil and stacked in 6 mm (inner diameter) sealed fused silica tubes. Individual packets averaged 2 mm thick and neutron fluence monitors (FC-2, Fish Canyon Tuff sanidine) were placed every 5-10 mm along the tube. Synthetic K-glass and optical grade CaF_2 were included in the irradiation packages to monitor neutron induced argon interferences from K and Ca. Loaded tubes were packed in an Al container for irradiation. Samples irradiated at the U. S. Geological Survey TRIGA Reactor, Denver, CO were in-core for 7 hours in the 1 MW TRIGA type reactor. Correction factors for interfering neutron reactions on K and Ca were determined by repeated analysis of K-glass and CaF_2 fragments. Measured $(^{40}Ar/^{39}Ar)_K$ values were 7.14 (± 4.18%) x 10^{-2}. Ca correction factors were $(^{36}Ar/^{37}Ar)_{Ca}$ = 2.59 (± 1.17%) x 10^{-4} and $(^{39}Ar/^{37}Ar)_{Ca}$ = 8.26 (± 0.53) x 10^{-4}. J factors were determined by fusion of 5-6 individual crystals of neutron fluence monitors which gave reproducibility's of 0.09% to 0.12% at each standard position. Variation in neutron fluence along the 100 mm length of the irradiation tubes was <4%. Matlab curve fit was used to determine J and uncertainty in J at each standard position. No significant neutron fluence gradients were present within individual packets of crystals as indicated by the excellent reproducibility of the single crystal fluence monitor fusions.

Irradiated FC-2 sanidine standards together with CaF_2 and K-glass fragments were placed in a Cu sample tray in a high vacuum extraction line and were fused using a 20 W CO_2 laser. Sample viewing during laser fusion was by a video camera system and positioning was by a motorized sample stage. Samples analyzed by the furnace step heating method used a double vacuum resistance furnace similar to the Staudacher et al. (1978) design. Reactive gases were removed by three GP-50 SAES getters prior to being admitted to a MAP 215-50 mass spectrometer by expansion. The relative volumes of the extraction line and mass spectrometer

allowed 80% of the gas to be admitted to the mass spectrometer for laser fusion analyses and 76% for furnace heating analyses. Peak intensities were measured using a Balzers electron multiplier by peak hopping through seven cycles; initial peak heights were determined by linear regression to the time of gas admission. Mass spectrometer discrimination and sensitivity were monitored by repeated analysis of atmospheric argon aliquots from an on-line pipette system. Measured $^{40}Ar/^{36}Ar$ ratios were 291.85 ± 0.08% during this work; thus a discrimination correction of 1.0125 (4 AMU) was applied to measured isotope ratios. The sensitivity of the mass spectrometer was ~6 x 10^{-17} mol mV^{-1} with the multiplier operated at a gain of 36 over the Faraday. Line blanks averaged 3.10 mV for mass 40 and 0.01 mV for mass 36 for laser fusion analyses and 18.34 mV for mass 40 and 0.06 mV for mass 36 for furnace heating analyses. Discrimination, sensitivity, and blanks were relatively constant over the period of data collection. Computer automated operation of the sample stage, laser, extraction line and mass spectrometer as well as final data reduction and age calculations were done using LabSPEC software written by B. Idleman (Lehigh University). An age of 28.02 Ma (Renne et al., 1998) was used for the Fish Canyon Tuff sanidine fluence monitor in calculating ages for samples.

For $^{40}Ar/^{39}Ar$ analyses a plateau segment consists of three or more contiguous gas fractions having analytically indistinguishable ages (i.e. all plateau steps overlap in age at ± 2σ analytical error) and comprising a significant portion of the total gas released (typically >50%). Total gas (integrated) ages are calculated by weighting by the amount of ^{39}Ar released, whereas plateau ages are weighted by the inverse of the variance. For each sample inverse isochron diagrams are examined to check for the effects of excess argon. Reliable isochrons are based on the MSWD criteria of Wendt and Carl (1991) and, as for plateaus, must comprise contiguous steps and a

significant fraction of the total gas released. All analytical data are reported at the confidence level of 1σ (standard deviation).

4.4 Results

4.4.1 Radiometric Dating Results

$^{40}Ar/^{39}Ar$ method dating performed on the five samples from the Galema Range indicates an age of eruption ranging from 2.01 to 2.56 Ma. Sample 3007 resulted in a total gas age of 2.01 ± 0.02 Ma with a plateau age of 1.97 ± 0.02 Ma. Analysis of samples 3024 resulted in a total gas age of 2.29 ± 0.02 Ma, 3034 resulted in a total gas age of 2.01 ± 0.02 Ma, 3043 resulted in a total gas age of 2.14 ± 0.01 Ma, and 3065 resulted in a total gas age of 2.56 ± 0.02 Ma, all with no plateau ages (Figure 4.3)(Supplemental material).

4.4.2 Isotopic Results

The Galema Range samples can be divided into two groups based on their trace element concentrations (Chapter 3). Samples 3022, 3026, 3027, 3028, 3030, 3057, 3060, and 3061 are classified as Type III magmas based on their pattern of primitive mantle normalized trace element concentrations (Supplemental material)(Rooney, 2017). Samples 3014, 3015, 3016, 3017, 3018, 3021, 3025, 3054, and 3055 are classified as Galema samples affected by metasomatized source material (Supplemental material). The subdivision of the metasomatic Galema Samples was determined based on their primitive mantle normalized trace element diagrams (Chapter 3). This group displays an enrichment in the most incompatible trace elements with a negative K anomaly and positive Ti anomaly (Chapter 3). The subdivision of the metasomatized Galema samples display primitive mantle normalized trace element patterns similar to that of the Type II magmas of Rooney (2017).

$^{87}Sr/^{86}Sr$ isotopic values for both the Type III and metasomatic samples center at 0.703698 (Figure 4.2)(Supplemental Material). $^{143}Nd/^{144}Nd$ values for the Type III and metasomatic samples center at 0.5128 (Figure 4.2)(Supplemental material). $^{176}Hf/^{177}Hf$ values for the Type III Galema samples center at 0.2829, lower than the value for metasomatic Galema samples of 0.2831 (Figure 4.2)(Supplemental material). Galema Type III samples display isotopic ratios of $^{208}Pb/^{204}Pb$ ranging from 38.44 to 38.55, $^{207}Pb/^{204}Pb$ ranging from 15.55 to 15.57, and $^{206}Pb/^{204}Pb$ ranging from 18.42 to 18.63 (Figure 4.2)(Supplemental material). The isotopic Pb ratios of the metasomatic Galema samples are generally more radiogenic with some overlap. Metasomatic Galema samples display a range of $^{208}Pb/^{204}Pb$ from 38.40 to 39.12, $^{207}Pb/^{204}Pb$ from 15.57 to 15.58, and $^{206}Pb/^{204}Pb$ from 18.41 to 19.26. The primary differences between the two groups are that the metasomatic Galema samples consistently display more radiogenic values of $^{206}Pb/^{204}Pb$, $^{208}Pb/^{204}Pb$, $^{143}Nd/^{144}Nd$, and ε_{Nd} than those of the Type III Galema samples (Figure 4.2)(Supplemental material).

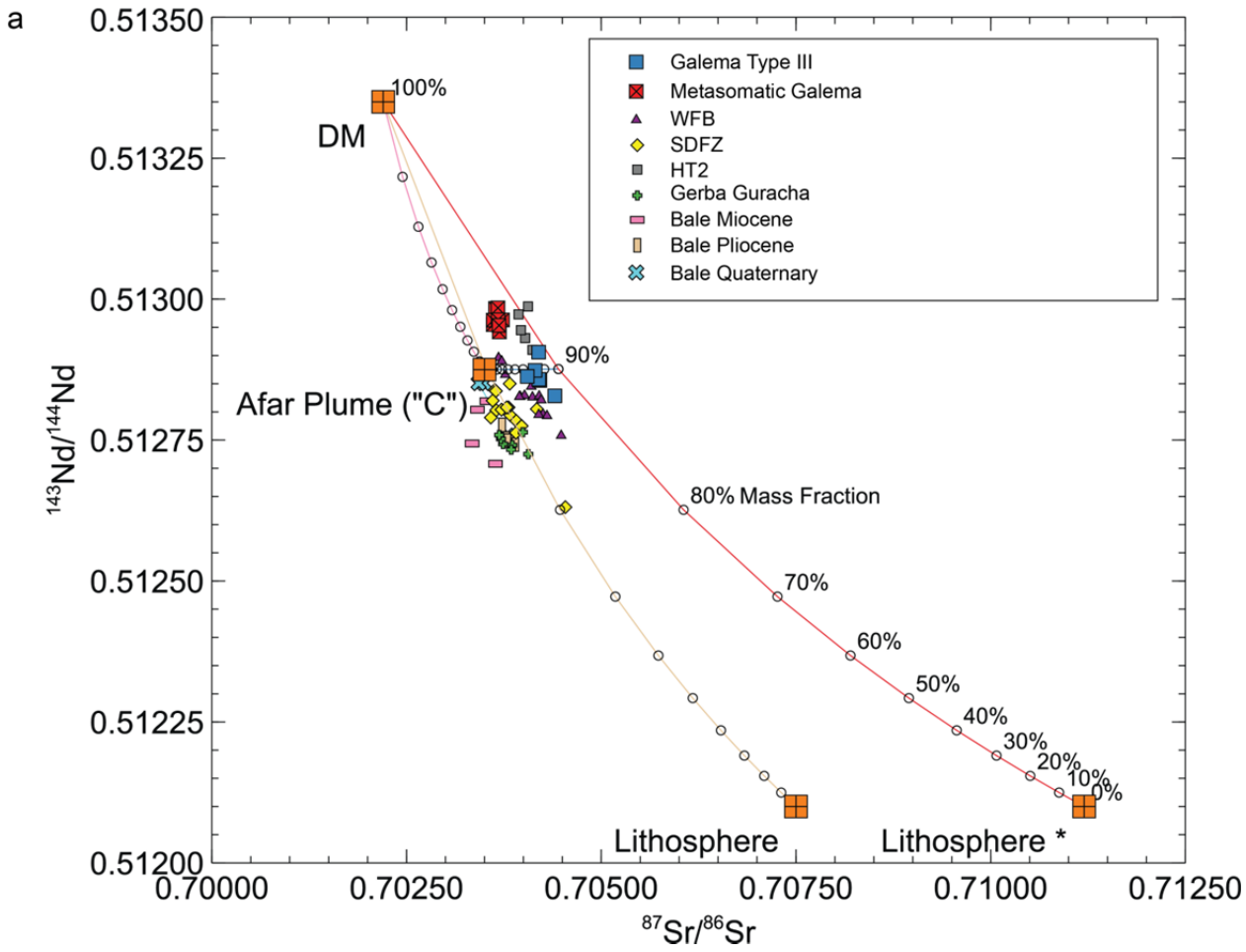

Figure 4.2.

Plots of isotopic geochemistry of samples from the Galema Range basalts and other areas of magmatism in the MER. See text for subdivisions. End member compositions of Afar plume, Depleted Mantle (DM) and Pan-African lithosphere (lithosphere) from Schilling et al., (1992), Rooney et al. (2012), and Rooney et al., (2013). See text for details. Wonji Fault Belt (WFB) and Silti Debre-Zeyit Fault Zone (SDFZ) data from Rooney et al., (2012a). HT2 data from Pik et al., (1999). Gerba Guracha data from Rooney et al., (2014b). Bale Mountains data from Nelson et al.,(2019). Also plotted are hyperbolic mixing lines and mass fractions (f b) between end members as described in the text. Lithosphere represents revised composition of Pan-African lithosphere as discussed in the text.*

Figure 4.2. (cont'd.)

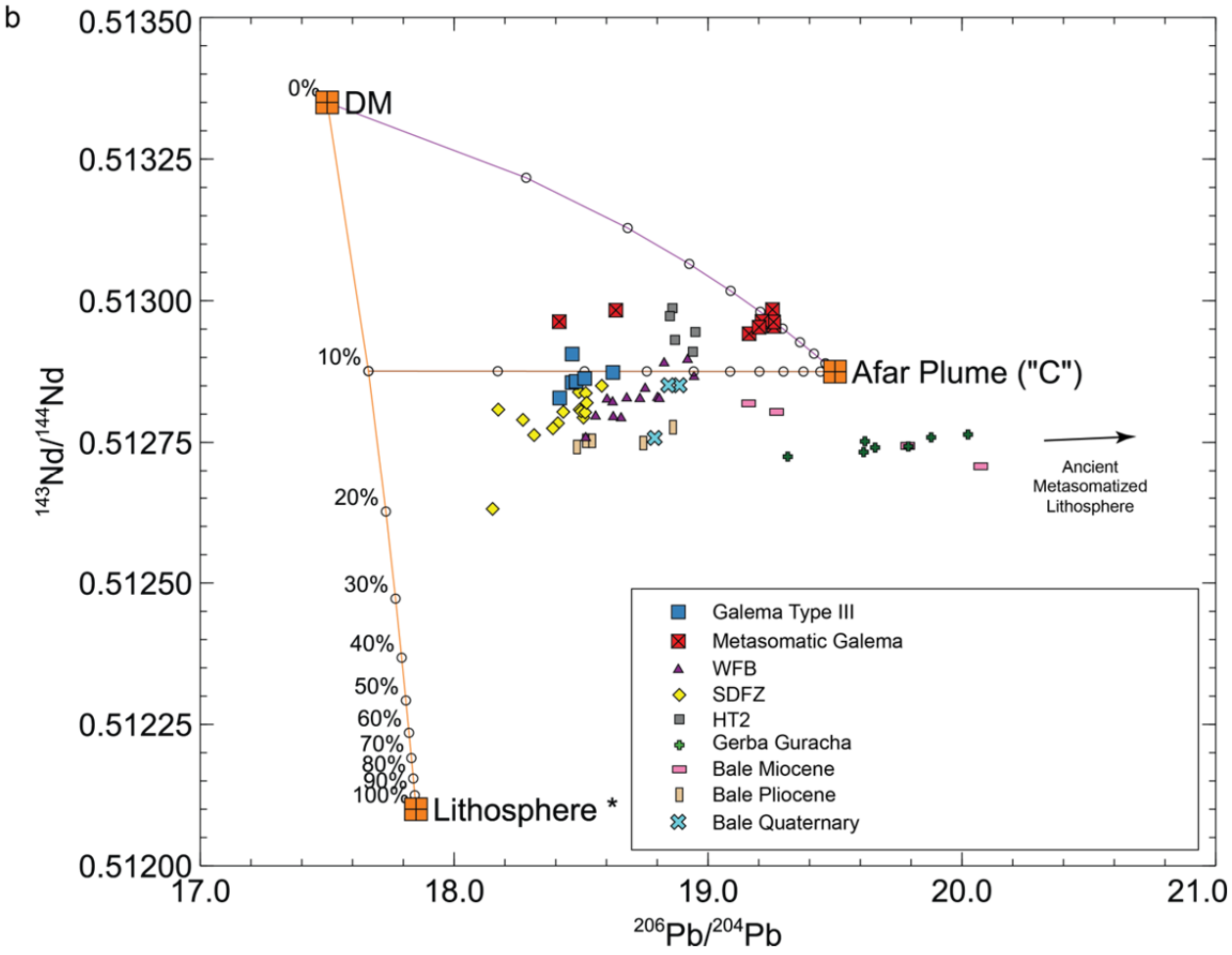

Figure 4.2. (cont'd.)

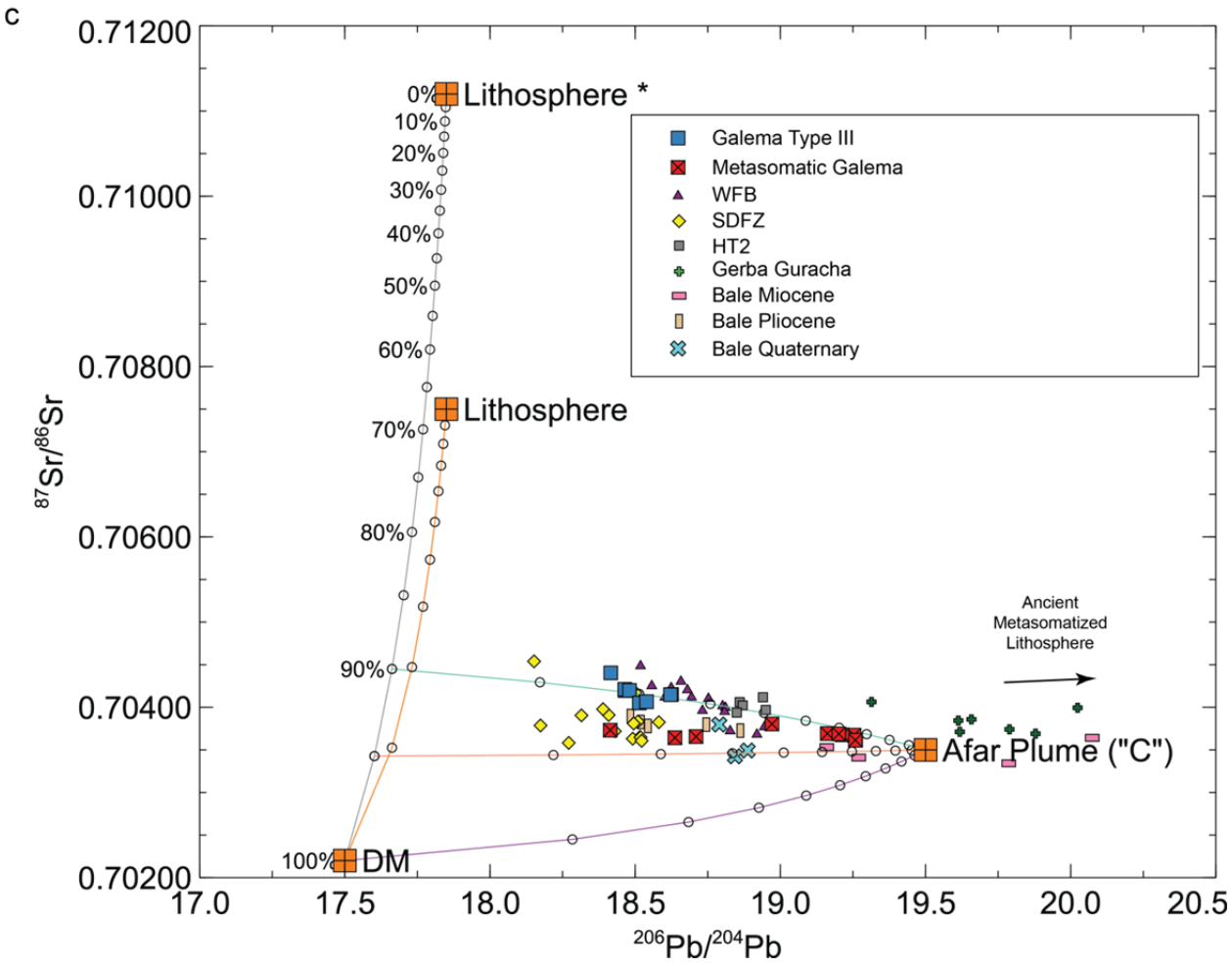

Figure 4.2. (cont'd.)

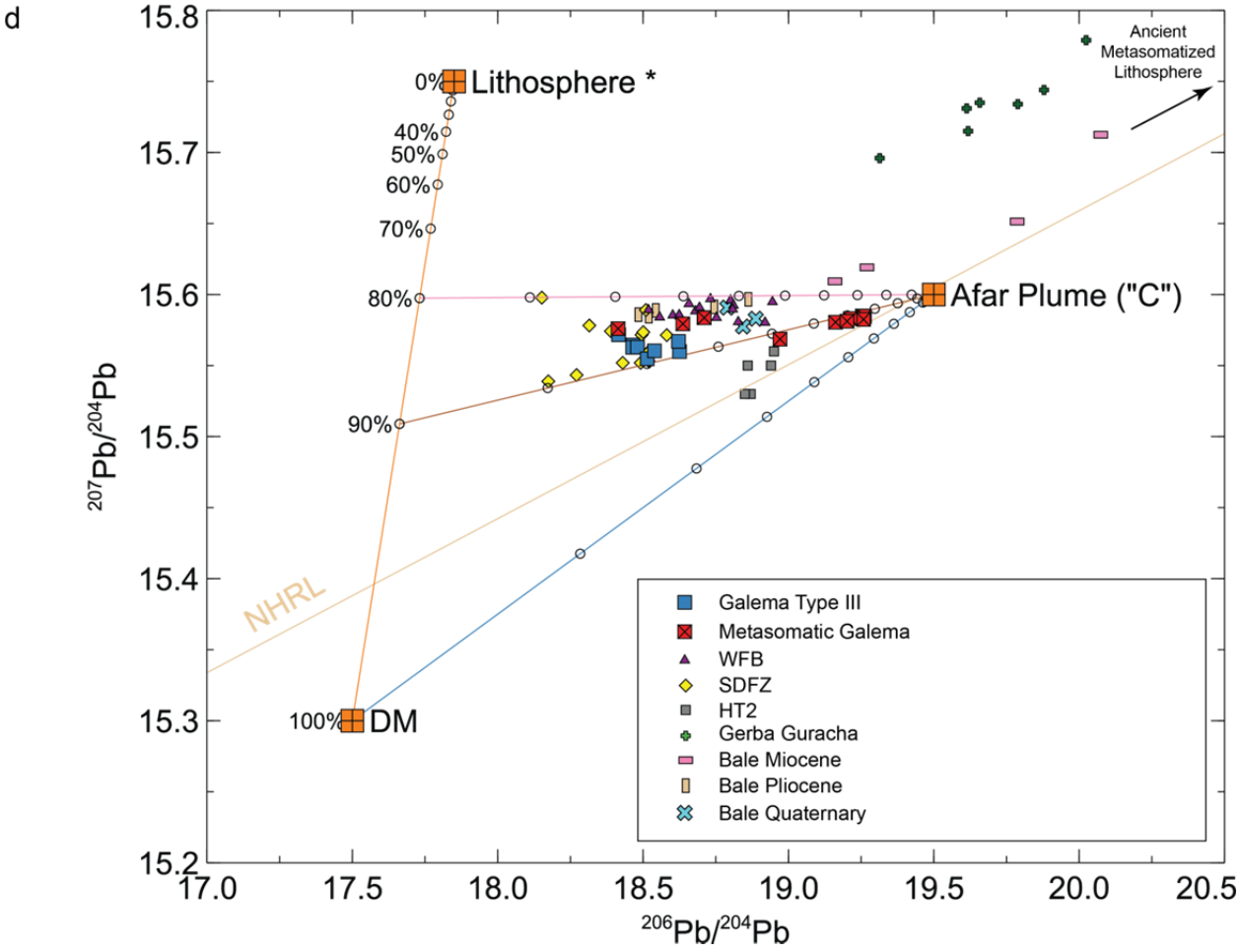

Figure 4.2. (cont'd.)

e

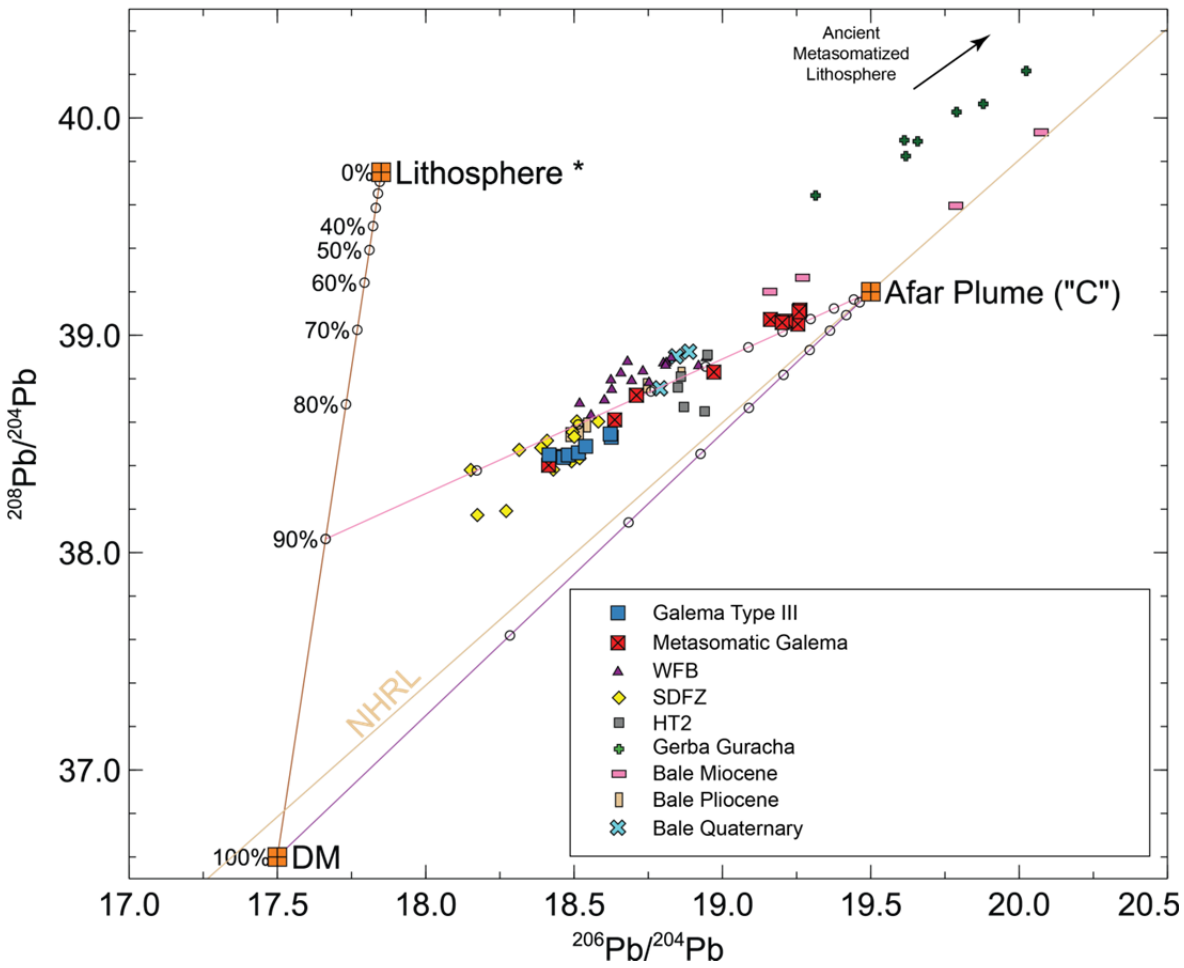

Figure 4.2. (cont'd.)

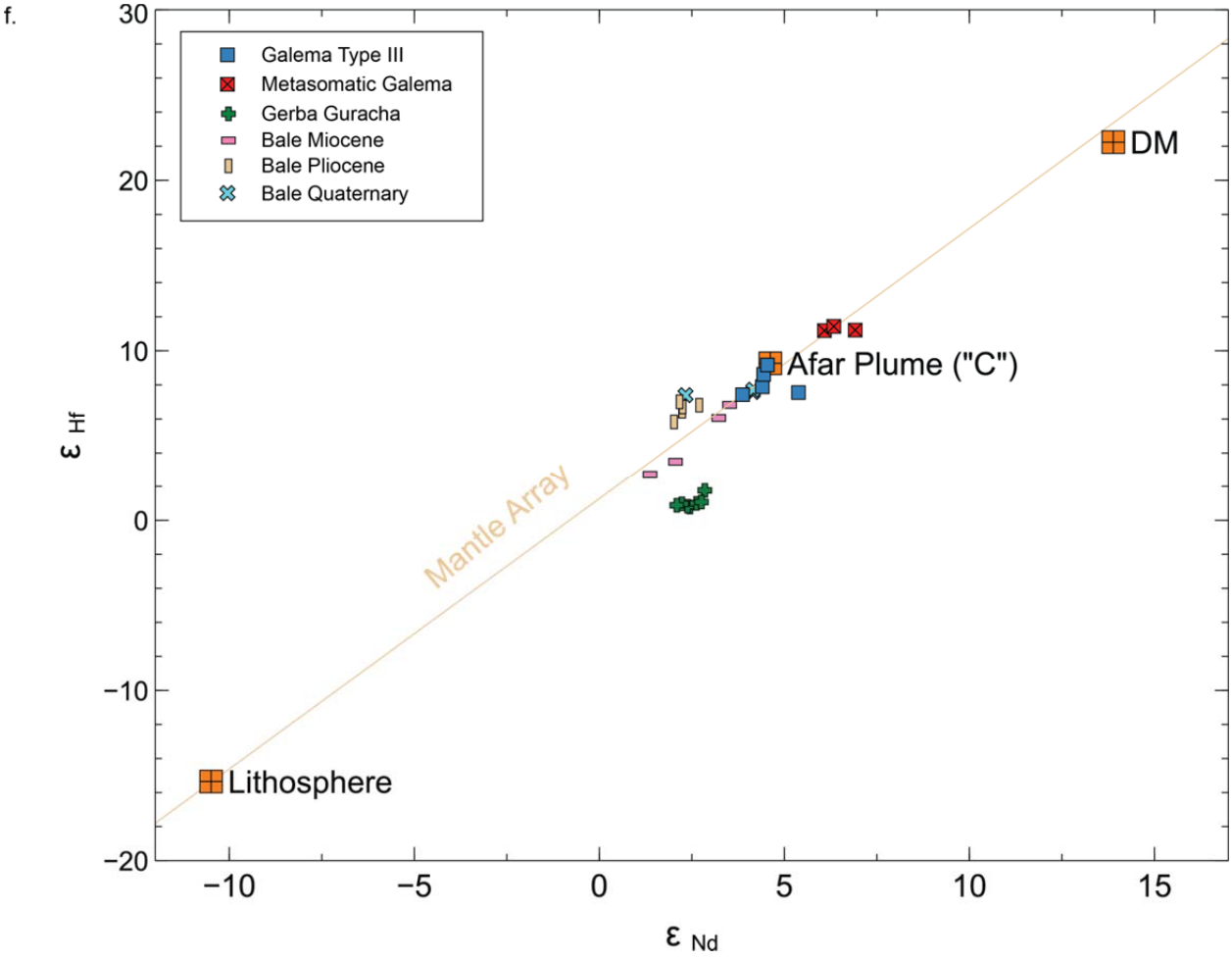

4.5 Discussion

4.5.1 Evidence of Metasomatism

A subgroup of the Galema Range samples shows evidence of metasomatism within their source melts as evidenced by their primitive mantle normalized trace element diagrams. Other magmas from the MER have been identified as having a metasomatic source component, such as the basanites from the Miocene Gerba Guracha volcano (Rooney et al., 2017), and the Oligocene HT2 flood basalts on the eastern Ethiopian plateau (Pik et al., 1999; Rooney, 2017). Primitive mantle normalized trace element diagrams from these locations display a Type II pattern, with

elevated Nb and Ta, but lack the strong positive Ba anomaly common in many Ethiopian basalts (Rooney, 2017). The basanites from Gerba Guracha have been interpreted to be the products of melts derived from a mixture of asthenospheric melts, and melts generated from metasomatized lithospheric geochemical reservoirs that were created during Pan-African assembly (Rooney et al., 2017). The HT2 magmas have been interpreted to be the result of mixing of the Afar plume with a hybrid mantle reservoir that is composed of depleted mantle and metasomatized SCLM material that had been generated as a result of the impact of the Afar plume (Furman et al., 2016; Rooney, 2017). Though they lack the Type II magma signature evident in the Gerba Guracha and HT2 magmas, the metasomatic Galema magmas display a negative K anomaly. This may indicate influence of an amphibole bearing metasome in the metasomatic Galema magmas (Rooney et al., 2014b). This indicates that the metasomatic Galema magmas may be the product of mixing of Afar plume material with a hybrid source that is composed of depleted mantle and metasomatized SCLM. This process is similar to that which generated the magmas of Gerba Guracha (Rooney et al., 2017) and the HT2 basalts (Furman et al., 2016).

4.5.2 Timing of the Galema Range Magmatism

The results of the $^{40}Ar/^{39}Ar$ method dating (2.01 to 2.56 Ma) of the Galema Range coincide with previous results of the K-Ar method dating (2.1 to 3.1 Ma) (Mohr and Potter, 1976; Kennan et al., 1990). These results reaffirm that the focused magmatic intrusion of the Galema Range is Pliocene in age, pre-dating the magmatism of the SDFZ (<1.28 Ma) and WFB (<1.8 Ma) within the rift of the CMER (Woldegabriel et al., 1990; Chernet et al., 1998; Wolfenden et al., 2004; Abebe et al., 2005; Rooney et al., 2005). This revised age estimate also places the focused magmatic intrusion of the Galema Range after the formation of the border faults that define the Main Ethiopian Rift in the CMER, which developed at ~5-8 Ma (Bonini et al., 2005; Abebe et

al., 2010). As the focused magmatic intrusion of the Galema Range must have accommodated extensional strain resulting from lithospheric stretching on the rift margin (Chiasera et al., 2018), and it is dated after the initial formation of the Asela-Sire border faults, there must have been partitioning of strain between the border faulting and magmatic intrusion within the CMER at ~2Ma (Chiasera et al., 2018). Most recently, extensional strain accommodation on the eastern margin of the CMER has been partitioned between the Asela-Sire border faults and the within-rift, WFB (Figure 4.1b,c)(Mohr, 1962; Woldegabriel et al., 1990; Bendick et al., 2006; Pizzi et al., 2006; Agostini et al., 2011a; Rooney et al., 2014a; Molin and Corti, 2015; Chiasera et al., 2018). As the Galema Range lies within an area of thicker lithosphere on the eastern Ethiopian plateau (Chapter 3), the timing of rifting activity within the CMER indicates that not only can magmatic strain accommodation occur within an area of relatively thick lithosphere, but that the lithosphere must have thinned (by ~37 km) relatively rapidly from the time of the activity at the Galema Range to that of the WFB and SDFZ (~1 Ma). The mechanisms of this rapid thinning and modification of the lithosphere are not well understood in the EARS. Thus, we examine the relationship of the Galema Range to the structure of the lithosphere and how it may be modified over a protracted time scale.

4.5.3 Tectonic Relationship of the Galema Range Magmas

The Galema Range lies on the eastern Ethiopian plateau, bounded by cross-rift structures in the north by the Yerer-Tullu Wellel Volcanotectonic Lineament (YTVL) and in the south by the Goba Bonga lineament (Figure 4.1)(Abebe et al., 1998; Bonini et al., 2005; Keranen and Klemperer, 2008; Corti et al., 2018). The YTVL is a Precambrian, E-W trending lithospheric heterogeneity, transverse to the MER, that was reactivated in the Miocene (~12 Ma) (Abebe et al., 1998; Trestrail et al., 2017). Defining the transition between the Northern MER (NMER) and

the CMER, the YTVL influenced the progression of rifting processes during the development of the MER (Keranen and Klemperer, 2008). The crustal deformation within the YTVL during rifting extends to the lithospheric mantle, with evidence of channelized melt flow through the SCLM on the western Ethiopian plateau as recently as <1 Ma (Trestrail et al., 2017). The deep crustal structures of the YTVL most likely extend into the MER, represented by the Boru-Toru Structural High (BTSH), which is interpreted to be pre-existing lithospheric weaknesses, forming a transfer zone during rift propagation between the NMER and CMER (Bonini et al., 2005).

The Goba Bonga lineament is a Pliocene aged, structural high within the CMER, representing an E-W trending, pre-existing structural lineament that separates the CMER from the Southern Main Ethiopian Rift to the south (Bonini et al., 2005; Corti et al., 2018). Magmatism on the eastern Ethiopian plateau at the Bale Mountains has been identified that is associated with the E-W trending structures of the Goba Bonga lineaments; however, the Galema Range is unrelated, and is identified as being associated with pre-existing, N-S trending lithospheric heterogeneities (Corti et al., 2018). The Galema Range most likely exists in its location on the eastern plateau due to exploitation of pre-existing N-S lithospheric heterogeneities by ascending magma (Mohr and Potter, 1976; Corti, 2012; Mazzarini et al., 2016; Chiasera et al., 2018). These N-S lithospheric heterogeneities may be related to N-S trending magmatic linear features further to the east, on the eastern Ethiopian plateau, that were generated by extensional lithospheric stresses (Mège et al., 2016; Purcell, 2018). These heterogeneities, and the overall trend of the MER, may be the result of fabric created during the Pan-African continental assembly of the Mozambique belts and the Arabian-Nubian Shield (Purcell, 2018). The N-S trending heterogeneities at the Galema Range, however, may terminate at, or because of, the E-W trending structures of the BTSH and the Goba Bonga lineament,

determining the northern and southern bounds of the Galema Range. Thus, much like modern magmatism within the rift, the Galema Range is bounded by these existing structural features.

The Galema Range may have been abandoned due to migration of magmatic strain accommodation toward the rift axis (Chiasera et al., 2018), similar to processes that occurred in the Southern Main Ethiopian Rift (SMER). Magmatism within the SMER has been interpreted to have initiated as rifting progressed northward from the Lake Turkana area during the Pliocene (~5 Ma)(Bonini et al., 2005). This initiation of rifting in the SMER resulted from reactivation of Oligocene to Mid-Miocene rift structures (Macgregor, 2015). Structures formed in the Turkana depression during a subsequent stage of mid to late Miocene rifting are thought to represent eastward migration of rifting activity (Macgregor, 2015) into the Turkana basin and Chew Bahir basin during the Plio-Pleistocene. The failed Ririba rift, in the broadly rifted zone of southern Ethiopia, east of the Chew Bahir basin, is hypothesized to be the result of extension progressing southward from Ethiopia that initiated magmatism at ~3.7 Ma (Corti et al., 2019). Magmatism of the Ririba rift ceased ~1.5 Ma afterward, placing its abandonment at ~2.2 Ma as magmatism shifted toward the rift axis within the Lake Turkana basin (Corti et al., 2019). The Ririba rift then reactivated with new magmatism at ~0.13-0.16 Ma (Corti et al., 2019), coinciding with the more recent magmatic activity of the WFB and SDFZ (Woldegabriel et al., 1990; Chernet et al., 1998; Wolfenden et al., 2004; Abebe et al., 2005; Rooney et al., 2005). As the Ririba rift and Galema Range lie along the same ~N-S trend and are contemporaneous in age of activity, they may represent a continuation of magmatic strain accommodation from the CMER into Turkana during the Pliocene. Their abandonment may represent contemporaneous migration of magmatic strain accommodation toward the rift axis throughout the MER.

The Galema Range exists in an area of thicker lithosphere on the eastern Ethiopian plateau. Its exact location, length, and trend have been dictated by previously existing lithospheric structures, generated by regional extensional stresses acting on the lithosphere. It is these lithospheric heterogeneities that may have initially allowed the Galema Range to magmatically accommodate strain within the thicker lithosphere of the eastern Ethiopian plateau. To examine how the lithosphere can thin rapidly during the time of the activity of the Galema Range to that of the WFB, we must examine how strain is magmatically accommodated within the rift proper in areas of relatively thinner lithosphere.

4.5.4 The WFB and Magmatic Strain Accommodation

Over the last ~2 Ma, extensional strain has been accommodated on the eastern margin of the CMER by the Galema Range, Asela-Sire border faults, and the WFB. The WFB is the most recent expression of magmatic accommodation of extensional strain in the CMER. Lithospheric extension processes and their impacts determine, in part, the elements of an area of focused magmatic intrusion, such as depth of melting (e.g., Langmuir and Forsyth, 2007; Havlin et al., 2013; Chiasera et al., 2018). The depth of melting of the Galema Range is deeper (~110 km; Chapter 3) when compared to the WFB (~73 km; Rooney et al., 2007). These differences in the magmatic activity between the Galema Range and the WFB may be due to further progression of rifting processes, allowing for thinning of the lithosphere and increase in melt generation over a relatively short time (Chiasera et al., 2018). While the areas of magmatic intrusion of the Galema Range and WFB appear relatively similar with regard to magmatic accommodation of strain within in the lithosphere (Chiasera et al., 2018), it is unknown whether these similarities extend to their geochemical reservoirs. The increased lithospheric thickness of the Galema Range, in comparison to the WFB, should indicate greater crustal assimilation of the Galema magmas.

Analysis of the geochemical reservoirs of the Galema Range source melts will assist in determining crustal and lithospheric material contributions. Determinations of contributions of these reservoirs can shed light on how lithospheric structure and the effects of the Afar plume have changed during rift evolution. Similarities between these geochemical reservoir contributions between the Galema Range and WFB would indicate similar magmatic processes, and by extension, similar lithospheric structure. To examine these, we must compare the isotopic geochemistry and interpretations of the geochemical reservoirs of the Galema Range to that of the WFB.

4.5.5 Analysis of Source Melt Signatures of Magmas of the Galema Range

The isotopic signatures of the Galema Range samples plot within ternary isotopic spaces defined by the isotopic compositions of their geochemical reservoirs. These isotopic spaces exist within plots of $^{143}Nd/^{144}Nd$ vs. $^{206}Pb/^{204}Pb$, $^{87}Sr/^{86}Sr$ vs. $^{206}Pb/^{204}Pb$, $^{207}Pb/^{204}Pb$ vs. $^{206}Pb/^{204}Pb$, and $^{208}Pb/^{204}Pb$ vs. $^{206}Pb/^{204}Pb$ (Figure 4.2). The plots of $^{87}Sr/^{86}Sr$ vs. $^{143}Nd/^{144}Nd$ and ε_{Hf} vs ε_{Nd} indicate the isotopic chemistry of the Galema samples lies along, or just off of, a mixing line between these end members (Figure 4.2a). The geochemical reservoir end members that define these ternary spaces and mixing lines of these plots are the Afar plume, Depleted mantle (DM), and Pan-African lithosphere (lithosphere), and were chosen based on previous approximations of the geochemical reservoirs of EARS basalts (Hart et al., 1989; Schilling et al., 1992; Deniel et al., 1994; Pik et al., 1999; Trua et al., 1999; Peccerillo et al., 2003; Furman et al., 2006a; Rooney et al., 2012a; Rooney et al., 2013; Rooney et al., 2014a; Rooney et al., 2014b; Furman et al., 2016; Rooney, 2017).

When plotted, the isotopic approximations determined from previous works for the Afar plume, depleted mantle, and Pan-African lithosphere define ternary spaces, within which

compositions representing mixtures of these end member should lie (Figure 4.2). Approximations of the isotopic chemistry and elemental abundances used in plotting and modeling are listed in the Supplementary material. Approximations used for the isotopic chemistry of the Afar plume, depleted mantle and Pan-African lithosphere are from Schilling et al., 1992 and Rooney et al., 2012a. The ε_{Hf} and ε_{Nd} values used for the Afar plume, depleted mantle and Pan-African lithosphere are from Rooney et al. (2013).

Initial interpretations of the plots of the three mantle end members within the Galema Range samples provide tentative information on the contributions of the end members to the isotopic signatures of the Galema magmas. In a plot of $^{143}Nd/^{144}Nd$ vs. $^{206}Pb/^{204}Pb$, the Type III Galema magmas plot in a tight grouping, between the three end members (Afar plume, DM, and Lithosphere), while the metasomatic Galema samples appear to form an array from the Type III magmas toward the Afar plume end member (Figure 4.2b). This distribution is generally repeated in plots of $^{87}Sr/^{86}Sr$ vs. $^{206}Pb/^{204}Pb$, $^{207}Pb/^{204}Pb$ vs. $^{206}Pb/^{204}Pb$, and $^{208}Pb/^{204}Pb$ vs. $^{206}Pb/^{204}Pb$ (Figures 4.2c, 4.2d, 4.2e), indicating that the Galema Type III and metasomatic samples are the result of mixing of the three end members, with a greater contribution of the Afar plume to the metasomatic samples. In a plot ε_{Hf} vs ε_{Nd} (Figure 4.2f), both the Galema Type III and metasomatic samples lie along the mantle array with the Type III samples overlapping the signature of the Afar plume and the metasomatic samples lying closer to the DM end member. Within a plot of $^{87}Sr/^{86}Sr$ vs. $^{143}Nd/^{144}Nd$, the three mantle end members appear to form a mixing line rather than a ternary space (Figure 4.2a). Both the Galema Type III and metasomatic samples lie off this line, toward more radiogenic values of $^{87}Sr/^{86}Sr$ and/or $^{143}Nd/^{144}Nd$, indicating they are not the result of mixing of the chosen isotopic chemistry of these end

members, or there is an unknown fourth end member in this isotopic space. These initial interpretations will be explored further in the following sections.

4.5.6 Comparison of the Galema Magmas to Other Areas of Magmatism in the CMER

4.5.6.1 Galema Type III Magmas

Comparisons of the Galema Range isotopic geochemistry with other areas of focused magmatic intrusion with similar trace element distributions (Type III) in the region reveal broad similarities with regard to contributions from the Afar plume, depleted mantle, and Pan-African lithosphere end members. However, noticeable differences may be the result of variable contributions from these three mantle end members at different locations and/or ages.

In the plot of $^{143}Nd/^{144}Nd$ vs. $^{206}Pb/^{204}Pb$ (Figure 4.2b), the Type III Galema magmas lie in a group close to isotopic values of samples from Silti Debre-Zeyit Fault Zone (Figure 4.1b) (Rooney et al., 2012a), but with slightly more radiogenic $^{143}Nd/^{144}Nd$ values, suggesting a greater contribution of the depleted mantle end member to the older Galema Range. Also in this plot, the Galema Range Type III samples lie at similar compositions to samples from the Quaternary WFB (Rooney et al., 2012a), but with more radiogenic $^{143}Nd/^{144}Nd$ and less radiogenic $^{206}Pb/^{204}Pb$ than the WFB (Figure 4.2b). This suggests that the Galema Range magmas may have a higher contribution from the depleted mantle, but a lower contribution from the Afar plume than the WFB magmas. Additionally, this plot indicates that the Galema Type III magmas plot in a similar location to those of Pliocene and Quaternary magmas of the Bale Mountains (Nelson et al., 2019), but with more radiogenic $^{143}Nd/^{144}Nd$ and less radiogenic $^{206}Pb/^{204}Pb$ than the Bale Mountains magmas (Figure 4.2b). This suggests that the Galema Range magmas contain a higher contribution from the depleted mantle and Pan-African lithosphere. In the plot of $^{87}Sr/^{86}Sr$ vs. $^{206}Pb/^{204}Pb$, the same patterns are generally observed (Figure 4.2c).

However, the Galema Type III magmas lie at similar $^{87}Sr/^{86}Sr$ values to those of the WFB and Bale Mountains, suggesting that the WFB and Bale Mountains magmas may have a higher contribution from the Afar plume, but similar a contribution from the depleted mantle to the Galema Type III magmas. In the plots of $^{207}Pb/^{204}Pb$ vs. $^{206}Pb/^{204}Pb$ and $^{208}Pb/^{204}Pb$ vs. $^{206}Pb/^{204}Pb$ (Figures 4.2d, 4.2e), the Galema Type III magmas exist at similar isotopic values to the SDFZ magmas, suggesting similar contributions from the three end members to their isotopic signatures. The WFB and Bale Mountains magmas plot at more radiogenic values of $^{207}Pb/^{204}Pb$, $^{208}Pb/^{204}Pb$, and $^{206}Pb/^{204}Pb$ than the Galema Type III magmas. This again suggests a lesser contribution from the depleted mantle and a greater contribution from the Afar plume to the WFB and Bale Mountains magmas than the Galema magmas.

These comparisons indicate that the source melt of the Galema Type III magmas contains similar geochemical reservoirs with similar contributions to magmas of the WFB and Quaternary Bale Mountains. These similarities indicate that the source melt generation processes, and the available geochemical reservoirs at these locations during their respective times of activity, are also similar. The metasomatic Galema samples, however, do not show these same similarities with the WFB and more recent Bale Mountains magmas and will be explored further to understand their respective source melt generation processes.

4.5.6.2 Galema Metasomatic Magmas

The metasomatic Galema samples reveal some similarities to other areas of magmatism on the plateaus flanking the MER that exhibit similar trace element patterns. Some differences may indicate differing contributions from the three geochemical reservoirs, issues with approximation of the isotopic values of the end members, or the presence of an unknown fourth end member.

In the plot of $^{143}Nd/^{144}Nd$ vs. $^{206}Pb/^{204}Pb$ (Figure 4.2b), the metasomatic Galema magmas plot at similar values to those of the Oligocene HT2 flood basalt lavas of the MER (Figure 4.2b)(Pik et al., 1999), but occur over a greater range of $^{206}Pb/^{204}Pb$. This suggests that the metasomatic Galema magmas contain a greater variation in contribution of the Afar plume end member than those of the HT2 magmas. When plotted with the metasomatic Galema samples, samples from Gerba Guracha (Rooney et al., 2014b), and the Miocene Bale mountains (Nelson et al., 2019) plot at lower $^{143}Nd/^{144}Nd$ values but much more radiogenic values of $^{206}Pb/^{204}Pb$ (Figure 4.2b). The $^{206}Pb/^{204}Pb$ values of the Gerba Guracha and Miocene Bale Mountains magmas lie outside of the ternary space defined by the end member isotopic chemistry, perhaps indicating contribution from an unknown fourth end member not plotted here. These patterns are repeated in a plot of $^{87}Sr/^{86}Sr$ vs. $^{206}Pb/^{204}Pb$ (Figure 4.2c); however, the $^{87}Sr/^{86}Sr$ values of the metasomatic Galema samples and Gerba Guracha and Miocene Bale Mountains samples appear to be similar. In the plot of $^{207}Pb/^{204}Pb$ vs. $^{206}Pb/^{204}Pb$ (Figure 4.2d), the metasomatic Galema samples plot at more radiogenic values of $^{207}Pb/^{204}Pb$ than the HT2 magmas with a greater range of $^{206}Pb/^{204}Pb$ values, initially indicating that the metasomatic Galema samples were composed of a greater contribution from the Afar plume and Pan-African lithosphere. In this plot, the Gerba Guracha and Miocene Bale Mountains samples lie outside of the ternary space defined by the end members with values enriched in both $^{207}Pb/^{204}Pb$ and $^{206}Pb/^{204}Pb$ compared to the metasomatic Galema samples. In the $^{208}Pb/^{204}Pb$ vs. $^{206}Pb/^{204}Pb$ plot, the metasomatic Galema samples form an array with the HT2 samples, indicating similar values for $^{208}Pb/^{204}Pb$ and $^{206}Pb/^{204}Pb$ and similar interpretations of the contributions of the end members as in the other isotopic plots. The Gerba Guracha and Miocene Bale Mountains samples once again plot at more radiogenic $^{208}Pb/^{204}Pb$ and $^{206}Pb/^{204}Pb$ values, lying outside of the ternary space defined by the end

members. In the plot of ε_{Hf} vs ε_{Nd}, the metasomatic Galema samples lie on the line of the mantle array between the Afar plume and DM end members, while age corrected values for Gerba Guracha lie below the mantle array between the Afar plume and lithosphere end members (Figure 4.2f). While the Galema Range, Gerba Guracha, and Miocene Bale Mountains samples display evidence of an unknown fourth end member, the data trends indicate that this 4th end member is not similar for these locations, and that there may be evidence in these plots of more than one additional end member. These initial results suggest that the metasomatic Galema samples do not display evidence of an ancient metasome as recorded in the isotopic signature of the Gerba Guracha and Miocene Bale Mountains magmas. The nature and origin of this fourth end member for the Galema Range samples will be explored further in the following sections.

As these are initial assessments of the isotopic chemistry of the Galema Range magmas and how they relate to the end member chemistry, we must employ mathematical models to estimate more specific mass fractions of the contributions of the end member isotopic chemistry to the Galema samples.

4.5.7 Definition of Hyperbolic Mixing Equations Used in Pseudo-Binary Mixing

To characterize the contributions of the multiple end members that define the ternary spaces to the isotopic chemistry of the Galema samples, we employ a pseudo-binary mixing technique based on mixing equations derived from the lever rule (Hanan et al., 1986; Schilling et al., 1992; Hanan and Schilling, 1997; Douglass and Schilling, 2000; Hanan et al., 2000; Rooney et al., 2012a).

By application of the lever rule, the fraction f_b of component b of the binary mixing of two components, a and b, is defined as:

$$f_b = \frac{x_m - x_a}{x_b - x_a} = \frac{y_m - y_a}{y_b - y_a}$$

(Eq. 1)

Where: x_i is the concentration of element x in component i

y_i is the concentration of element y in component i

m is the mixture

Application of this equation to the isotopic ratio $(x)_m$ for mixing of two components, *a* and *b*, gives:

$$(x)_m = \frac{f_b {}^{\alpha}x_b + [1 - f_b]{}^{\alpha}x_a}{f_b {}^{\beta}x_b + [1 - f_b]{}^{\beta}x_a}$$

(Eq. 2)

Where: ${}^{\alpha}x_i$ is the concentration of isotope α of element x in component i

Specific application of this equation to the isotopic ratio of $\frac{^{87}Sr}{^{86}Sr}$ for mixing of two components, *a* and *b*, gives:

$$\left(\frac{^{87}Sr}{^{86}Sr}\right)_m = \frac{f_b {}^{87}Sr_b + [1 - f_b]{}^{87}Sr_a}{f_b {}^{86}Sr_b + [1 - f_b]{}^{86}Sr_a}$$

(Eq. 3)

Substitution of $\left(\frac{^{87}Sr}{^{86}Sr}\right)[^{86}Sr]$ for $[^{87}Sr]$ for *a* and *b*, and assuming $[^{86}Sr] \cong [Sr]_{total}$, gives the following equation:

$$\left(\frac{^{87}Sr}{^{86}Sr}\right)_m = \frac{f_b Sr_b \left(\frac{^{87}Sr}{^{86}Sr}\right)_b + [1 - f_b]Sr_a \left(\frac{^{87}Sr}{^{86}Sr}\right)_a}{f_b Sr_b + [1 - f_b]Sr_a}$$

(Eq. 4)

Where: f_b is fraction of component b

$[Sr]_a$ is total Sr concentration of component a

$\left(\frac{^{87}Sr}{^{86}Sr}\right)_a$ is $\frac{^{87}Sr}{^{86}Sr}$ of component a

Application of this to the $\frac{^{143}Nd}{^{144}Nd}$ isotopic system gives:

$$\left(\frac{^{143}Nd}{^{144}Nd}\right)_m = \frac{f_b Nd_b \left(\frac{^{143}Nd}{^{144}Nd}\right)_b + [1 - f_b] Nd_a \left(\frac{^{143}Nd}{^{144}Nd}\right)_a}{f_b Nd_b + [1 - f_b] Nd_a}$$

(Eq. 5)

Where: f_b is fraction of component b

Nd_a is total Nd concentration of component a

$\left(\frac{^{143}Nd}{^{144}Nd}\right)_a$ is $\frac{^{143}Nd}{^{144}Nd}$ of component a

Rearranging the $\left(\frac{^{87}Sr}{^{86}Sr}\right)_m$ equation for f_b gives:

$$f_b = \frac{Sr_a \left[\left(\frac{^{87}Sr}{^{86}Sr}\right)_a - \left(\frac{^{87}Sr}{^{86}Sr}\right)_m\right]}{\left(\frac{^{87}Sr}{^{86}Sr}\right)_m [Sr_b - Sr_a] - Sr_b \left(\frac{^{87}Sr}{^{86}Sr}\right)_b - Sr_a \left(\frac{^{87}Sr}{^{86}Sr}\right)_a}$$

(Eq. 6)

Which is then substituted into the $\left(\frac{^{143}Nd}{^{144}Nd}\right)_m$ equation to define the hyperbolic mixing curve between components *a* and *b* in $\frac{^{87}Sr}{^{86}Sr}$ and $\frac{^{143}Nd}{^{144}Nd}$ space. Substitution and simplification of this equation gives:

$$\left(\frac{^{143}Nd}{^{144}Nd}\right)_m = \frac{Sr_a Nd_b \left(\frac{^{143}Nd}{^{144}Nd}\right)_b \left[\left(\frac{^{87}Sr}{^{86}Sr}\right)_a - \left(\frac{^{87}Sr}{^{86}Sr}\right)_m\right] + Sr_b Nd_a \left(\frac{^{143}Nd}{^{144}Nd}\right)_a \left[\left(\frac{^{87}Sr}{^{86}Sr}\right)_m - \left(\frac{^{87}Sr}{^{86}Sr}\right)_b\right]}{Sr_a Nd_b \left[\left(\frac{^{87}Sr}{^{86}Sr}\right)_a - \left(\frac{^{87}Sr}{^{86}Sr}\right)_m\right] + Sr_b Nd_a \left[\left(\frac{^{87}Sr}{^{86}Sr}\right)_m - \left(\frac{^{87}Sr}{^{86}Sr}\right)_b\right]}$$

(Eq. 7)

Rewritten in generic terms gives us the equation:

$$(y)_m = \frac{x_a y_b (y)_b [(x)_a - (x)_m] + x_b y_a (y)_a [(x)_m - (x)_b]}{x_a y_b [(x)_a - (x)_m] + x_b y_a [(x)_m - (x)_b]}$$

(Eq. 8)

Where: x_i = concentration of x component of end member *i*

y_i = concentration of y component of end member *i*

$(x)_i$ = isotopic ratio of x component of end member *i*

$(y)_i$ = isotopic ratio of y component of end member *i*

4.5.8 Application of Hyperbolic Mixing Equations to Pseudo Binary Mixing

The equation that defines the hyperbolic mixing line (Eq. 8) was applied to the compositions for depleted mantle and African lithosphere (Pik et al., 1999; Workman and Hart, 2005; Rooney et al., 2012a; Rooney et al., 2013). Once this hyperbolic mixing relationship was established, the isotopic ratio compositions and elemental concentrations were determined from (Eq. 4) for end member fractions (f_b) from 0.1 to 0.9. The elemental concentrations and isotopic ratios for each end member fraction (f_b) were used as a synthetic source to mix with the elemental concentrations (Meshesha and Shinjo, 2010; Rooney et al., 2012a; Rooney et al., 2013) and isotopic ratios (Rooney et al., 2012a; Rooney et al., 2013) determined for the Afar plume. Implementing (Eq. 6) and (Eq. 4) with these end member values determined the pseudo-binary mixing relationship between depleted mantle, African lithosphere, and Afar plume for each of

the isotopic ratios utilized to evaluate the reservoir mixing relationships ($\frac{^{143}Nd}{^{144}Nd}$, $\frac{^{87}Sr}{^{86}Sr}$, $\frac{^{176}Hf}{^{177}Hf}$, $\frac{^{206}Pb}{^{204}Pb}$, $\frac{^{207}Pb}{^{204}Pb}$, $\frac{^{208}Pb}{^{204}Pb}$).

4.5.9 Pseudo-binary mixing results

4.5.9.1 Galema Type III magmas

The results of application of the pseudo-binary mixing equations for all isotopic systems are shown in Figure 2 and listed in the Supplemental Material. For the Type III Galema samples, the pseudo-binary mixing curves applied to the $^{143}Nd/^{144}Nd$ vs. $^{206}Pb/^{204}Pb$ system indicate a ~20% contribution from the Afar plume (Figure 4.2b). The mixing curve between the depleted mantle (DM) and Pan-African lithosphere (lithosphere) intersect the pseudo-binary curve at a ratio of ~90% DM and ~10% lithosphere. Renormalizing these values gives an approximation of ~20% Afar Plume, ~72% DM, and ~8% lithosphere for the Type III magmas. For the $^{87}Sr/^{86}Sr$ vs. $^{206}Pb/^{204}Pb$ system, the Type III magmas are centered at the ratios of ~20% Afar Plume, ~64% DM, and ~16% lithosphere, after renormalization (Figure 4.2c). The Galema Type III samples lie remarkably close to the ratios of ~20% Afar Plume, ~72% DM, and ~8% lithosphere for both the $^{207}Pb/^{204}Pb$ vs. $^{206}Pb/^{204}Pb$ (Figure 2d) and $^{208}Pb/^{204}Pb$ vs. $^{206}Pb/^{204}Pb$ (Figure 4.2e) systems.

The isotopic contributions from the end members of ~20% Afar Plume, ~64% DM, and ~16% lithosphere for the Type III Galema samples are similar to estimates of source magma chemistry for Type III Galema Range magmas determined through utilization of trace element concentrations. Trace element, thermodynamic modeling of the source melt conditions of the Type III Galema magmas has determined the geochemical reservoirs were comprised of 80% DM, 20% Afar plume and a trace amount (≅1%) of lithospheric material (Chapter 3). The Galema samples appear to plot at similar isotopic values to both the WFB and SDFZ (Figures 4.2a-4.2e), indicating similar contributions of the end members to the magmas of the three

different locations. Isotopic chemistry of both the WFB and SDFZ have been interpreted to be the result of contributions from the Afar plume and a hybrid mixture of depleted mantle with Pan-African lithosphere (Rooney et al., 2012a). Results of previous application of the pseudo-binary mixing equations to magmas throughout the MER agree with our estimates of end member mass fractions of the Galema Range. These previous applications have estimated mass fractions of the three mantle end members to be 10-43% Afar plume, 49-80% depleted mantle, and 6-17% Pan-African lithosphere (Rooney et al., 2012a).

As the Galema Type III samples lie outside of the ternary space defined by the end members of Afar plume, DM and lithosphere for the $^{87}Sr/^{86}Sr$ vs. $^{143}Nd/^{144}Nd$ system (Figure 4.2a), it is not possible in this case to determine the contributions of the three end members using this method with this system. This may indicate that the approximations used for the isotopic ratios or elemental concentrations of one or more of the end members are not appropriate with regard to either Sr or Nd for the Galema samples. Considering the results of application of the pseudo-binary mixing curve to the other isotopic systems, all but the $^{87}Sr/^{86}Sr$ vs. $^{206}Pb/^{204}Pb$ system (Figure 4.2c) indicate ratios of ~20% Afar Plume, ~72% DM, and ~8% lithosphere, indicating that the issue must lie in the values of $^{87}Sr/^{86}Sr$ for one or more of the end members used or that their chemical composition has been affected by fractionation processes. A plot of the isotopic chemistry Galema Type III sample *vs* MgO indicates that there are no fractionation effects on any of the isotopic systems (Figure 4.3). Therefore, the issue with $^{87}Sr/^{86}Sr$ must lie with one or more of the isotopic approximations of $^{87}Sr/^{86}Sr$ initially plotted for one or more of the end members.

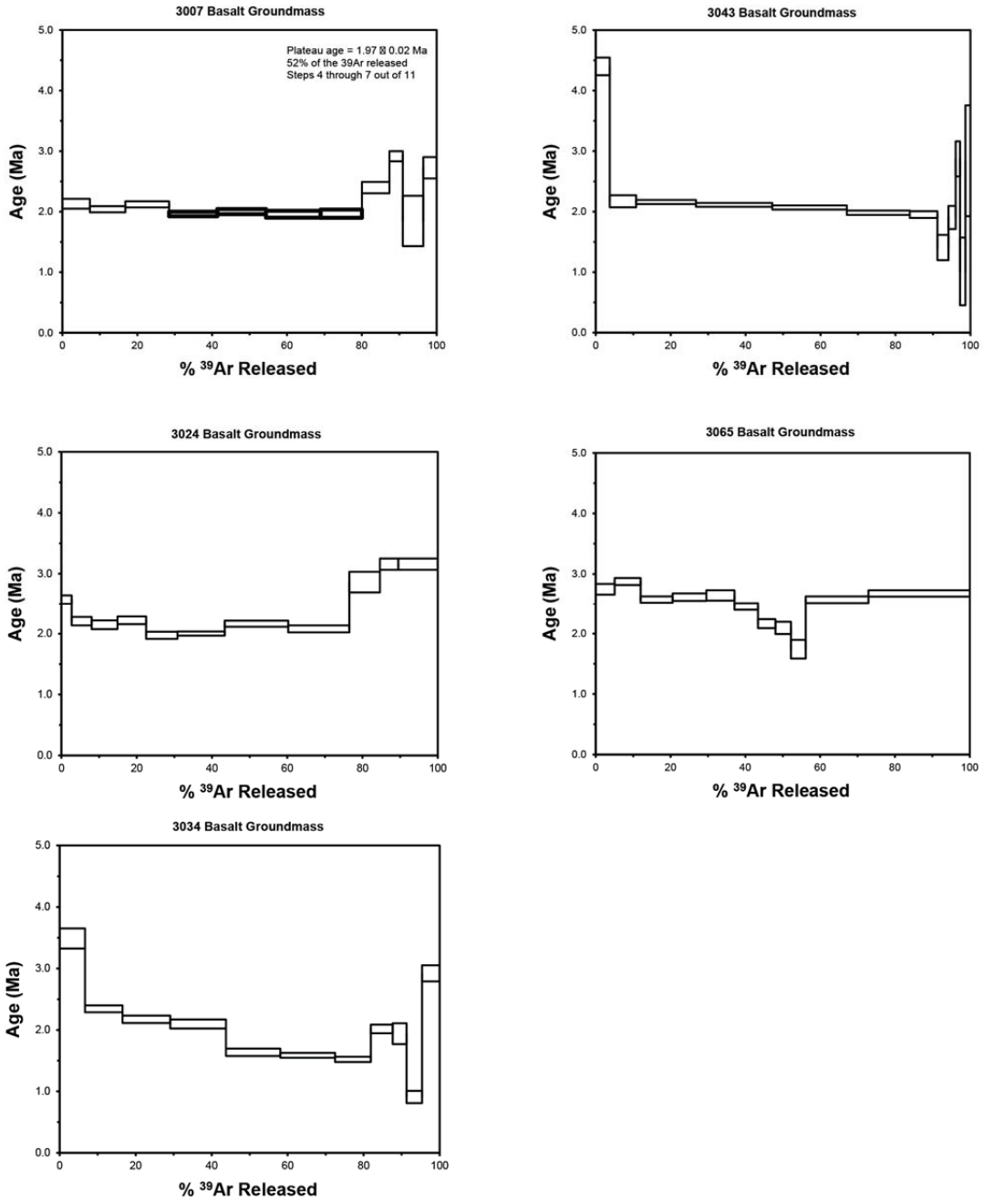

Figure 4.3.

Results of $^{40}Ar/^{39}Ar$ method dating for samples of the Galema Range indicating an eruptive age range of 2.01-2.51 Ma.

4.5.9.2 Metasomatic Galema magmas

When applied to the metasomatic Galema samples, the pseudo-binary mixing equations show a more variable role in the contributions of the three end members than the Type III samples. In the $^{143}Nd/^{144}Nd$ vs. $^{206}Pb/^{204}Pb$, $^{207}Pb/^{204}Pb$ vs. $^{206}Pb/^{204}Pb$, $^{87}Sr/^{86}Sr$ vs. $^{206}Pb/^{204}Pb$, and $^{208}Pb/^{204}Pb$ systems, the metasomatic Galema samples range in end member contributions from ~20% Afar plume, ~27% DM, and ~0% lithosphere, to ~60% Afar plume, ~76% DM, and 12% lithosphere (Figure 4.2)(Supplemental Material).

The variability in the end member contributions for the metasomatic Galema samples, and the mismatch in end member contributions across the various isotopic systems, suggests that while some are similar in their isotopic content to the Galema Type III magmas, some display an influence from a fourth end member. Following the array that is formed with the Type III and metasomatic Galema samples, this fourth end member appears to have an isotopic chemistry that is close to that of the Afar plume, but with higher $^{143}Nd/^{144}Nd$, and lower $^{207}Pb/^{204}Pb$ and $^{208}Pb/^{204}Pb$ than the fourth end member of the Gerba Guracha samples. To clarify further discussion, we refer to the fourth end member of the Galema Range as the G4 end member from here onward. The G4 end member may have mixed with magma similar in composition to that of the Galema Type III samples to generate the chemical signature of the metasomatic samples, effectively shifting them toward the isotopic signature of the Afar plume. Being of similar isotopic composition to the Afar plume, this G4 end member may have been generated from processes associated with the Afar plume itself. We hypothesize that this G4 end member represents a contribution from melting of metasomatized, sub-continental lithospheric mantle (SCLM).

The Gerba Guracha samples plotting in Figure 4.2 display evidence of an end member with more radiogenic Pb isotopic values than the Afar plume end member. These more radiogenic Pb values approach that of HIMU ($^{206}Pb/^{204}Pb$ >20) (Zindler and Hart, 1986; Rooney et al., 2012a). These more radiogenic values have been attributed to the melting of amphibole rich veins in a metasomatized sub-continental lithospheric mantle (SCLM) that was created during the Pan-African Assembly, generating a HIMU like signature (Rooney et al., 2014b; Nelson et al., 2019). This HIMU like component is reflected in the ε_{Hf} vs ε_{Nd} plot, where age corrected Gerba Guracha samples lie below the mantle array, toward the composition of HIMU (Figure 4.2f). This indicates that, while the metasomatic Galema samples may contain contributions of a metasomatized SCLM, the metasome is of distinctly different isotopic chemistry than that which contributed to the Gerba Guracha magmas. As an ancient metasome is interpreted to have contributed to the Miocene Bale Mountains magmas (Nelson et al., 2019), similar to processes that occurred at Gerba Guracha, their magmas would appear similar to those of the Galema Range in indications of metasomatic contribution. However, the isotopic signatures of the Miocene Bale Mountains magmas would indicate that this metasomatic contribution is of different composition than that which contributed to the magmas of the Galema Range.

Isotopic analyses of samples from Yemen suggest that their geochemical reservoirs show contribution from a upper mantle compositions that has been recently metasomatized by the ascending Afar plume (Baker et al., 1997; Baker et al., 1998). This metsomatization process would preserve much of the isotopic signature of the Afar plume, generating an end member that is similar, but not identical. This end member would most likely lie outside of the ternary space defined by the end members in the plots here, toward more radiogenic Pb isotopic values. This recently created metasome is most likely the G4 component evident in the metasomatic Galema

samples as it would be of different composition than the ancient, HIMU-like metasome that is evident in the Gerba Guracha and Miocene Bale Mountains samples (e.g., Nelson et al., 2019).

The metasomatic Galema samples display similar isotopic compositions, and therefore end member mass fractions, to samples from the HT2 magmas (Figures 4.2a-4.2e). The HT2 magmas have been previously interpreted to be comprised of Afar plume material mixed with a lithospheric signature, which has been identified as crustal in nature (Pik et al., 1999). These basalts have also been interpreted to be a result of interactions of the Afar plume with the lithospheric mantle, in which the ascending plume metasomatized the lithospheric mantle which was subsequently melted to form the source melt of the HT2 magmas (Beccaluva et al., 2009; Furman et al., 2016; Rooney, 2017).

We hypothesize that the G4 end member of the Galema Range is metasomatized sub-continental material, recently generated by the ascending Afar plume. If this metasome was Pan-African in origin, its isotopic composition would more closely resemble that of the metasomatic, HIMU-like end member identified for samples from Gerba Guracha and the Miocene Bale Mountains. The Afar plume had metasomatized the lithospheric mantle beneath the eastern Ethiopian plateau, similar to processes that have occurred in Yemen (Baker et al., 1997; Baker et al., 1998) and the quaternary magmatism of the Bale mountains (Nelson et al., 2019). Melting of this metasomatic material was incorporated into some of the Galema melts, generating the four component mixture of Afar plume, depleted mantle, Pan-African lithosphere, and G4. This process is similar to processes that occurred with melting of Pan-African metasomes in Gerba Guracha, Miocene Bale Mountains, and the HT2 magmas (Furman et al., 2016; Rooney et al., 2017; Nelson et al., 2019), but with a recently created metasome that is different in composition, similar to processes that occurred in the quaternary Bale mountains (Nelson et al., 2019). This

enrichment of the SCLM, and subsequent melting, represents a process of destruction and removal of the SCLM beneath the eastern Ethiopian plateau at ~2Ma. The Type III Galema magmas either did not incorporate any of this melted metasomatized material into their melts, or were able to ascend through areas of the SCLM that had not been metasomatized by the Afar plume. This allowed the Type III magmas to develop an isotopic signature closer to that of the WFB and SDFZ that do not display evidence of a metasomatized SCLM component. By the time of the activity of the WFB and SDFZ, the SCLM had been almost or completely removed, generating a three end member isotopic signature, and displaying evidence of lithospheric thinning due to removal of the SCLM in the CMER.

As with the Galema Type III samples, the metasomatized Galema samples lie outside of the mixing line defined by the Afar plume, DM , and lithosphere in the $^{87}Sr/^{86}Sr$ vs. $^{143}Nd/^{144}Nd$ system (Figure 4.2a). This plot further highlights the issue previously identified with the approximation of the $^{87}Sr/^{86}Sr$ content of the Pan-African lithosphere that was used and will be explored further in the following sections.

4.5.10 Simultaneous Solution of Isotopic Mixing Equations

To address the previously described issue with the $^{87}Sr/^{86}Sr$ value for the lithospheric end member, and to further explore the contributions of the various end members to the source melts of the Galema Range, we explore the application of equations designed to determine the weighted average of contributing end members to a multi-component mixture (Douglass and Schilling, 2000; Rooney et al., 2012a).

For a multi-component mixture, the isotopic composition is the weighted average of the contributing end member components defined by:

$$R_m = \frac{\sum C_i \omega_i R_i}{\sum C_i \omega_i}$$

(Eq. 9)

And the closure condition:

$$\sum \omega_i = 1$$

(Eq. 10)

Where: R_m is the isotopic ratio of the measured sample

C_i is the elemental concentration in end member i

R_i is the isotopic ratio in end member i

ω_i is the mass fraction of end member i in system

If all end member isotopic compositions (R_i) and isotopic concentrations (C_i) are known, Eq. 9 gives a series of three equations for a ternary mixing system. With the closure condition (Eq. 10), this series of equations is fully solvable (Rooney et al., 2012a).

For a ternary mixing system with end members a, b and c, application of Eq. 9 gives:

$$R_{mi} = \frac{R_{ai}C_{ai}\omega_a + R_{bi}C_{bi}\omega_b + R_{ci}C_{ci}\omega_c}{C_{ai}\omega_a + C_{bi}\omega_b + C_{ci}\omega_c}$$

(Eq. 11)

And application of Eq. 10 gives:

$$\omega_a + \omega_b + \omega_c = 1$$

(Eq. 12)

Where: i is the isotopic system

Rewriting Eq. 11 gives:

$$0 = (R_{ai}C_{ai} - R_{mi}C_{ai})\omega_a + (R_{bi}C_{bi} - R_{mi}C_{bi})\omega_b + (R_{ci}C_{ci} - R_{mi}C_{ci})\omega_c$$

(Eq. 13)

For a three end member system, Eq.13 and the closure equation (Eq. 12) can thus be written in matrix array form for solution of simultaneous equations:

$$\begin{bmatrix}0\\0\\1\end{bmatrix} = \begin{bmatrix}(R_{a1}C_{a1} - R_{m1}C_{a1}) & (R_{b1}C_{b1} - R_{m1}C_{b1}) & (R_{c1}C_{c1} - R_{m1}C_{c1})\\(R_{a2}C_{b2} - R_{m2}C_{a2}) & (R_{b2}C_{b2} - R_{m2}C_{b2}) & (R_{c2}C_{c2} - R_{m2}C_{c2})\\1 & 1 & 1\end{bmatrix}\begin{bmatrix}\omega_a\\\omega_b\\\omega_c\end{bmatrix}$$

(Eq. 14)

Inversion and premultiplication of the coefficient matrix to each side of the equation gives:

$$\begin{bmatrix}(R_{a1}C_{a1} - R_{m1}C_{a1}) & (R_{b1}C_{b1} - R_{m1}C_{b1}) & (R_{c1}C_{c1} - R_{m1}C_{c1})\\(R_{a2}C_{b2} - R_{m2}C_{a2}) & (R_{b2}C_{b2} - R_{m2}C_{b2}) & (R_{c2}C_{c2} - R_{m2}C_{c2})\\1 & 1 & 1\end{bmatrix}^{-1}\begin{bmatrix}0\\0\\1\end{bmatrix} = \begin{bmatrix}\omega_a\\\omega_b\\\omega_c\end{bmatrix}$$

(Eq. 15)

4.5.11 Determination of Weighted Averages of Contributing End Members

4.5.11.1 Galema Type III Magmas

Application of the simultaneous equations for determination of the weighted averages of contributing end members applied to the Galema Type III magmas for the $^{143}Nd/^{144}Nd$ vs $^{206}Pb/^{204}Pb$, $^{207}Pb/^{204}Pb$ vs. $^{206}Pb/^{204}Pb$, and $^{208}Pb/^{204}Pb$ vs. $^{206}Pb/^{204}Pb$ systems revealed a range of end member mass fractions of 16-25% Afar plume, 66-77% DM, and 5-12% Pan-African lithosphere. For the $^{87}Sr/^{86}Sr$ vs. $^{206}Pb/^{204}Pb$ system, application of the equations determined a range from 22-30% Afar Plume, 55-62% DM, and 14-19% Pan-African lithosphere. Full results listed in the Supplementary Material. Application of the simultaneous mixing equations to the $^{87}Sr/^{86}Sr$ vs. $^{143}Nd/^{144}Nd$ revealed unrealistic negative mass fractions, highlighting the previously mentioned issue of sample compositions outside of the ternary isotopic space defined by the chemical signatures of the end members.

4.5.12 Model Verification

To test the self-consistency of the system of equations to determine the weighted average of end member contributions, alternate isotope pairs were plotted in correlation diagrams (Rooney et al., 2012a)(Figure 4). For the plots of $^{208}Pb/^{204}Pb$ - $^{206}Pb/^{204}Pb$ vs $^{207}Pb/^{204}Pb$ - $^{206}Pb/^{204}Pb$ and $^{143}Nd/^{144}Nd$ - $^{206}Pb/^{204}Pb$ vs $^{207}Pb/^{204}Pb$ - $^{206}Pb/^{204}Pb$ the slopes of end member proportions range from 1.0473 to 1.145 with a range of R^2 values from 0.99 to 0.9985 (Figure 4.4a, b)(Supplemental Material). The plot of $^{87}Sr/^{86}Sr$- $^{206}Pb/^{204}Pb$ vs $^{207}Pb/^{204}Pb$ - $^{206}Pb/^{204}Pb$ displays inconsistent values with the other plots with a slope of 0.9721 and an R^2 value of 0.988 (Figure 4.4c). This large deviation from the other plots indicates that the model is not robust and does not account for all of the isotopic variability. On closer inspection of the isotopic pairs of this plot, it is apparent that the values for the lithosphere dataset are shifted from the linear fit line, affecting its slope and R^2 value. This issue is related to the previously identified problem affecting both the application of the pseudo-binary mixing equations and simultaneous mixing equations to the $^{87}Sr/^{86}Sr$ vs. $^{143}Nd/^{144}Nd$ isotopic system. As the isotopic data of the Galema Type III samples lies outside of the ternary isotopic space defined by the chemical signature of the end members, we had hypothesized that the chosen approximation of $^{87}Sr/^{86}Sr$ for one or more of the end members was potentially incorrect. The problems identified with the model validation indicate that this issue most likely lies with the approximation of $^{87}Sr/^{86}Sr$ used for the lithospheric end member.

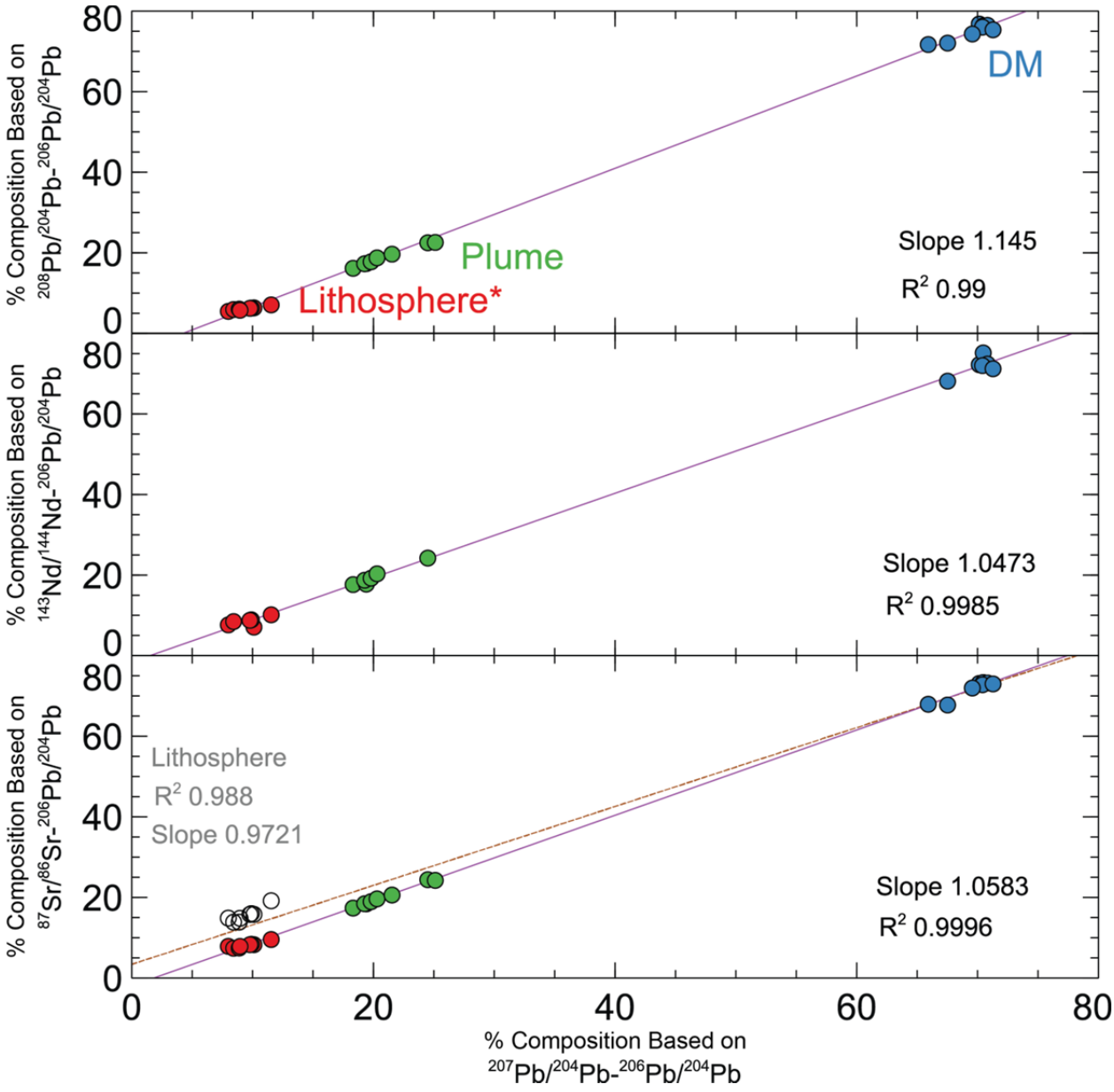

Figure 4.4.

Validation plots for simultaneous mixing equation solutions, including the validation of the solution utilizing the revised composition of the Pan-African lithosphere. See text for details. Abbreviations are the same as for Figure 4.2.

4.5.13 Estimation of the isotopic composition of the Pan-African Lithosphere

Isotopic data on the composition of the Pan-African lithosphere in the MER are sparse. Statistically speaking, isotopic compositions of the Pan-African lithosphere are most likely non-homogenous throughout the region. During Pan-African assembly, multiple blocks, with varying chemical compositions, accreted to form the continent. The western Ethiopian plateau, on which the Galema Range is located, may represent one of these blocks (Keranen and Klemperer, 2008), with a chemically distinct lithosphere from other areas in the MER. We have thus chosen to re-estimate the $^{87}Sr/^{86}Sr$ value of the lithospheric end member to provide more realistic results for the pseudo-binary and simultaneous equation mixing models. The least possible modification of the $^{87}Sr/^{86}Sr$ to align the model with the other isotopic systems is to change from the 0.7075 value of Rooney et al. (2012a) to a value of 0.7112 (lithosphere*)(Supplemental Material).

4.5.12 Analysis of Possible Crustal Contamination

The elevated value of 0.7112 for $^{87}Sr/^{86}Sr$ in the lithospheric end member may indicate that there has been crustal assimilation during the ascent of the Galema Type III magmas. The crustal contamination indicators of La/Nb and Ce/Pb show no significant evidence for crustal assimilation (Rooney et al., 2005; Rooney et al., 2007; Rooney et al., 2012a; Rooney et al., 2018)(Figure 4.5). To further examine the possibility of crustal contamination, we used the elemental ratios of K/P and Ti/Yb for the Type III Galema samples. The Type III samples contain K/P values > 2.3476 and Ti/Yb values > 6344.6 (Supplemental Data). Values of K/P <6.5 and Ti/Yb >6000 rule out significant crustal contamination (Leeman and Hawkesworth, 1986; Van Calsteren et al., 1986; Hart et al., 1989; Rooney et al., 2012a). Plots of $^{87}Sr/^{86}Sr$ and $^{143}Nd/^{144}Nd$ vs K/P and Ti/Yb (Figure 4.6) show no discernable trend in $^{143}Nd/^{144}Nd$ vs K/P or Ti/Yb and a minor increase in $^{87}Sr/^{86}Sr$ vs K/P and Ti/Yb (Δ0.00016). Within the lithosphere, Sr

is the most variable and thus, this variance is more likely an indication of an increase in K within the lithosphere. Combined with the invariance in $^{143}Nd/^{144}Nd$ of the Type III samples and the other analyses, we conclude that there was no significant crustal contamination of the Type III Galema Range samples.

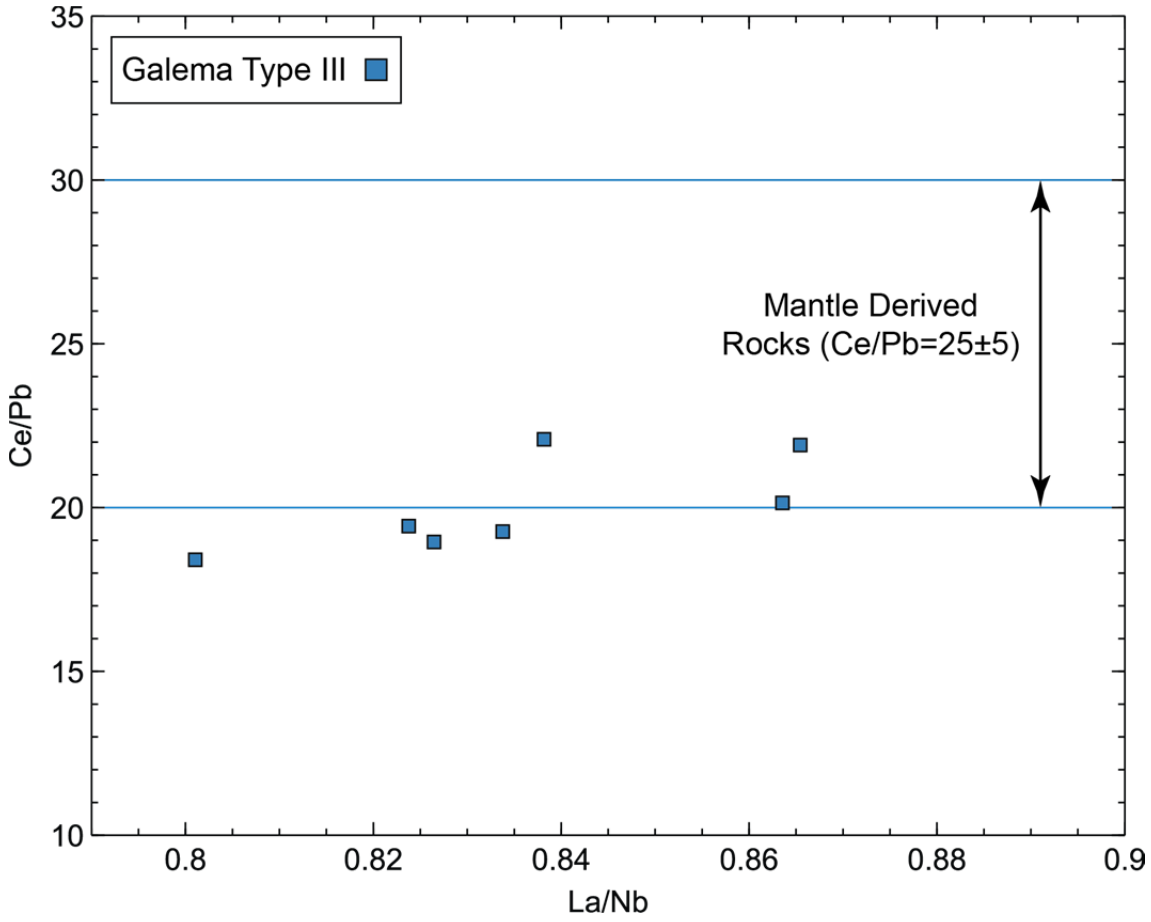

Figure 4.5.

Galema Type III samples plotted on Ce/Pb vs. La/Nb diagram indicating little to no crustal assimilation. The value range of mantle derived rocks of 25 ±5 from Hofmann et al., 1986.

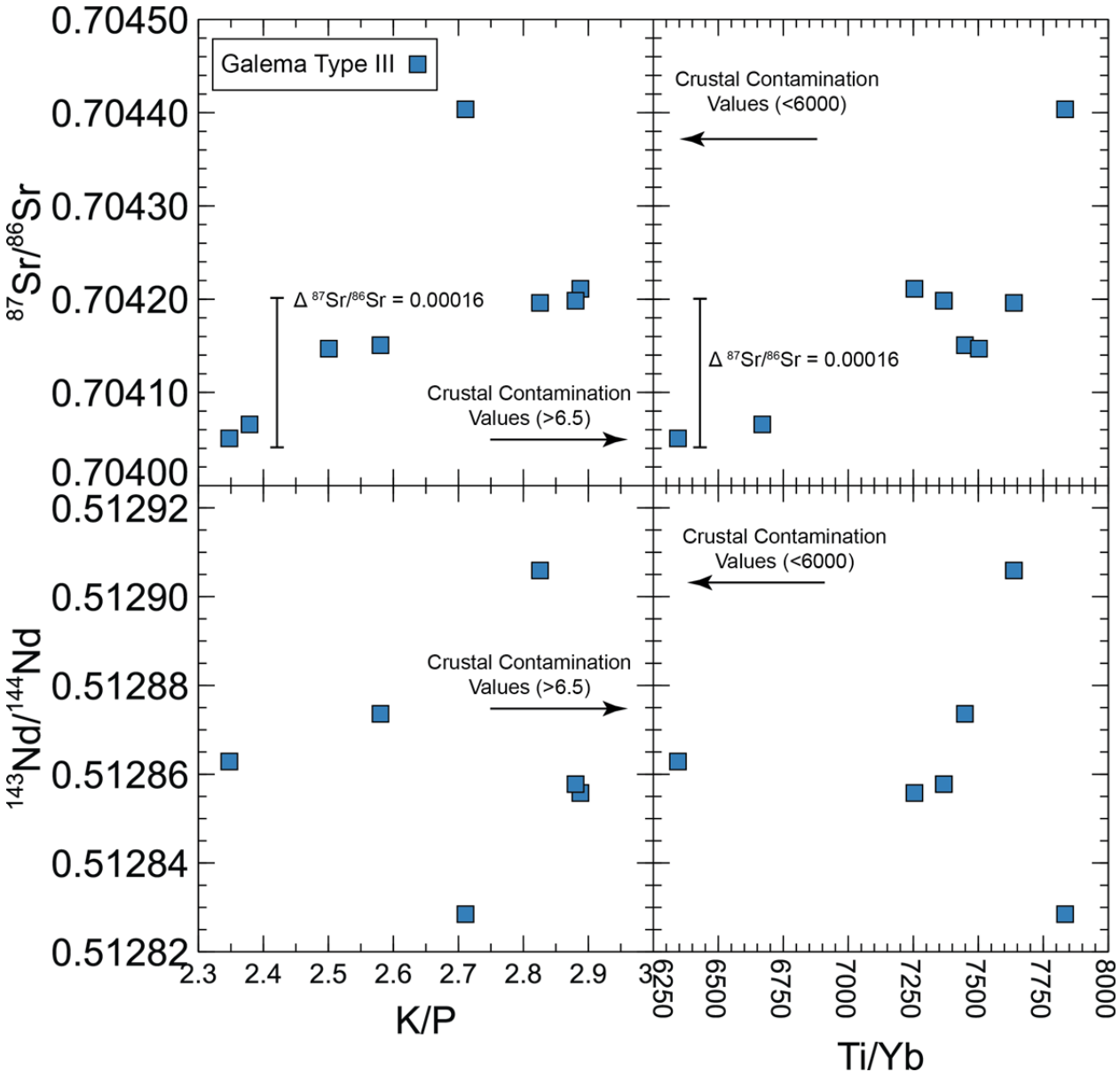

Figure 4.6.

Plot of $^{87}Sr/^{86}Sr$ and $^{143}Nd/^{144}Nd$ vs. K/P and Ti/Yb of the Galema Type III samples following Hart et al., 1989. Values of K/P <6.5 and Ti/Yb >6000 rule out significant crustal contamination for the Galema Type III samples. Minor variation (Δ0.00016) in $^{87}Sr/^{86}Sr$ vs. K/P indicates the slight positive trend is a result of an increase in K within the heterogeneous lithosphere and not a result of crustal contamination.

4.5.13 Re-Evaluation of the Isotopic Mixing Models

The modified composition of the Pan-African lithosphere (Supplemental Material) was re-applied to the simultaneous mixing equations. The mass fractions of Afar plume, DM, and lithosphere were not affected for the $^{143}Nd/^{144}Nd$ vs $^{206}Pb/^{204}Pb$, $^{207}Pb/^{204}Pb$ vs. $^{206}Pb/^{204}Pb$, or $^{208}Pb/^{204}Pb$ vs. $^{206}Pb/^{204}Pb$ systems. Reapplication of the simultaneous mixing equations to the $^{87}Sr/^{86}Sr$ vs. $^{206}Pb/^{204}Pb$ system determined a new range from 17% Afar Plume, 68% DM, and 7% lithosphere to 24% Afar Plume, 73% DM, and 10% lithosphere (Supplemental Material). Reapplication of the model verification to the plot of $^{87}Sr/^{86}Sr$ - $^{206}Pb/^{204}Pb$ vs $^{207}Pb/^{204}Pb$ - $^{206}Pb/^{204}Pb$ displays values consistent with the other plots with a slope of 1.0583 and an R^2 value of 0.9996 (Figure 4.4c). These values are now consistent with the other plots indicating a robust model that accounts for all of the isotopic variability (Rooney et al., 2012a).

In addition to this, the new estimate of the $^{87}Sr/^{86}Sr$ value of the Pan-African lithosphere (lithosphere*) now generates a ternary isotopic space between the three end members in the $^{87}Sr/^{86}Sr$ vs. $^{143}Nd/^{144}Nd$ isotopic system (Figure 4.2a). The isotopic compositions of the Type III Galema samples now lie within this ternary space, allowing for a realistic solution when the simultaneous mixing equations are applied to the system. For the $^{87}Sr/^{86}Sr$ vs. $^{143}Nd/^{144}Nd$ system, application of the equations determined a range from 5% Afar Plume, 56% DM, and 7% lithosphere* to 37% Afar Plume, 87% DM, and 9% lithosphere* (Supplemental Material).

Plots of the new estimate for $^{87}Sr/^{86}Sr$ for the lithospheric component were also re-evaluated using the pseudo-binary mixing equations for the $^{87}Sr/^{86}Sr$ vs. $^{206}Pb/^{204}Pb$ system (Figure 4.2c). This results in new estimates of end member contributions of ~20% Afar plume, ~72% DM, and ~8% lithosphere* (Figure 4.2c). These values are now similar to those determined from application of the pseudo-binary mixing equations to the other isotopic systems (Supplemental

material). The new estimate for $^{87}Sr/^{86}Sr$ also now changes the location of the isotopic composition of Pan-African lithosphere in the plot of the $^{87}Sr/^{86}Sr$ vs. $^{143}Nd/^{144}Nd$ isotopic system (Figure 4.2a). This new location now creates an isotopic ternary space between the three end members within which, the Galema Type III samples lie, allowing for re-application of the pseudo-binary mixing equations to this system. The revised estimates of end member contributions for the $^{87}Sr/^{86}Sr$ vs. $^{143}Nd/^{144}Nd$ system are similar to those for the other isotopic systems with ~20% Afar plume, ~72% DM, and ~8% lithosphere* (Figure 4.2a).

4.6 Conclusions

Revised $^{40}Ar/^{39}Ar$ method dating of the Galema magmas indicates an eruptive age range of 2.01-2.51 Ma, placing the magmatism at Galema before that of the WFB and SDFZ, but after the formation of the rift border faults of the CMER. This provides evidence of magmatic strain accommodation within the CMER, prior to that of the WFB, but contemporaneous with other areas of magmatism in the MER. The previous hypotheses of a linear progression from fracturing and faulting of the crust to magmatic intrusion within the rift proper (e.g., Wolfenden et al., 2005) does not account for the timing, and location of magmatic activity and strain accommodation of the Galema Range. Our work indicates that strain accommodation through focused magmatic intrusion can happen over a broader area, to outside of the rift proper, and occur before the process of magmatic strain with the rift. Our work further indicates that magmatic strain accommodation can occur within a relatively thick lithosphere (Chapter 3) , and the timing of the Galema Range indicates that thinning of the lithosphere during continental rifting can occur over short time scales (<~2 Ma).

Our isotopic analysis gives an indication of the lithospheric structure and composition during the magmatism of the Galema Range, and thus indicates how the lithosphere has been modified by rifting processes associated with the Afar plume over the last 2 Ma. Isotopic geochemical analysis of the magmas of the Galema Range indicates they were formed of a source melt composed of mass fractions from multiple mantle end members. Mathematical modeling of isotopic compositions indicates the geochemical reservoir of the Galema magmas contains contributions of ~20% Afar plume, ~70% Depleted mantle, and ~10% Pan-African lithosphere. A subset of Galema magmas indicates a contribution from a fourth end member (G4), which we identify as being Afar plume-like in composition. We attribute the isotopic signature of this G4 end member to areas of sub-continental lithospheric mantle that have been metasomatized by the ascending Afar plume prior to melting.

Our results indicate that while the Galema Range and WFB appear similar within the lithosphere, only the Type III Galema magmas are similar with regard to their isotopic chemistry and geochemical reservoirs. The metasomatic Galema samples display evidence of a fourth mantle end member (G4), which is not present in the isotopic signatures of the WFB or SDFZ magmas. The presence of this G4 end member in the magmas of the Galema Range indicates that this metasomatic material is being melted through processes associated with thermal input from the ascending Afar plume (Chapter 3). As this material is melted, it intrudes the lithosphere to ascend to form the dikes of the Galema Range, actively removing material from the SCLM. This removal of material signifies destruction of the SCLM. Metasomatization and subsequent melting of the lithosphere as indicated at the Galema Range may be one way in which the lithosphere is thinned in the EARS, along with foundering and assimilation of material into the depleted asthenosphere (e.g., Bédard, 2006; Van Wijk et al., 2008; Lee et al., 2011; Rooney et

al., 2012a; Furman et al., 2016; Nelson et al., 2019). This thinning by melting and destruction of the SCLM may allow for subsequent magmatism to occur in different locations, indicating the focusing of magmatic strain accommodation toward the rift axis.

BIBLIOGRAPHY

BIBLIOGRAPHY

Abdelsalam, M.G. and Stern, R.J. (1996) Sutures and shear zones in the Arabian-Nubian Shield. Journal of African Earth Sciences, v. 23, p. 289-310.

Abebe, B., Acocella, V., Korme, T. and Ayalew, D. (2007) Quaternary faulting and volcanism in the Main Ethiopian Rift. Journal of African Earth Sciences, v. 48, p. 115-124 DOI: 10.1016/j.jafrearsci.2006.10.005.

Abebe, T., Balestrieri, M.L. and Bigazzi, G. (2010) The central Main Ethiopian rift is younger than 8 Ma: confirmation through apatite fission-track thermochronology. Terra Nova, v. 22, p. 470-476 DOI: 10.1111/j.1365-3121.2010.00968.x.

Abebe, T., Manetti, P., Bonini, M., Corti, G., Innocenti, F., Mazzarini, F. and Pecskay, Z. (2005) Geological map (scale 1: 200,000) of the northern Main Ethiopian Rift and its implication for the volcano-tectonic evolution of the rift. Geol. Soc. Am. Map Chart Ser., MCH094.

Abebe, T., Mazzarini, F., Innocenti, F. and Manetti, P. (1998) The Yerer-Tullu Wellel volcanotectonic lineament: A transtensional structure in central Ethiopia and the associated magmatic activity. Journal of African Earth Sciences, v. 26, p. 135-150 DOI: 10.1016/S0899-5362(97)00141-3.

Acocella, V. and Korme, T. (2002) Holocene extension direction along the Main Ethiopian Rift, East Africa. Terra Nova, v. 14, p. 191-197 DOI: 10.1046/j.1365-3121.2002.00403.x.

Acocella, V., Korme, T. and Salvini, F. (2003) Formation of normal faults along the axial zone of the Ethiopian Rift. Journal of Structural Geology, v. 25, p. 503-513 DOI: 10.1016/S0191-8141(02)00047-0.

Agostini, A., Bonini, M., Corti, G., Sani, F. and Manetti, P. (2011a) Distribution of Quaternary deformation in the central Main Ethiopian Rift, East Africa. Tectonics, v. 30, DOI: 10.1029/2010TC002833.

Agostini, A., Bonini, M., Corti, G., Sani, F. and Mazzarini, F. (2011b) Fault architecture in the Main Ethiopian Rift and comparison with experimental models: Implications for rift evolution and Nubia–Somalia kinematics. Earth and Planetary Science Letters, v. 301, p. 479-492 DOI: 10.1016/j.epsl.2010.11.024.

Agostini, A., Corti, G., Zeoli, A. and Mulugeta, G. (2009) Evolution, pattern, and partitioning of deformation during oblique continental rifting: Inferences from lithospheric-scale centrifuge models. Geochemistry, Geophysics, Geosystems, v. 10, DOI: 10.1029/2009GC002676.

Ahern, J., Turcotte, D. and Oxburgh, E. (1981) On the upward migration of an intrusion. The Journal of Geology, v. 89, p. 421-432.

Albarede, F. (1992) How deep do common basaltic magmas form and differentiate? Journal of Geophysical Research: Solid Earth, v. 97, p. 10997-11009.

Alene, M., Hart, W.K., Saylor, B.Z., Deino, A., Mertzman, S., Haile-Selassie, Y. and Gibert, L.B. (2017) Geochemistry of Woranso–Mille Pliocene basalts from west-central Afar, Ethiopia: Implications for mantle source characteristics and rift evolution. Lithos, v. 282, p. 187-200.

Anderson, D.L. (2007) New theory of the Earth. Cambridge University Press, Cambridge, UK ; New York. 384 p.

Armitage, J.J., Ferguson, D.J., Goes, S., Hammond, J.O.S., Calais, E., Rychert, C.A. and Harmon, N. (2015) Upper mantle temperature and the onset of extension and break-up in Afar, Africa. Earth and Planetary Science Letters, v. 418, p. 78-90 DOI: 10.1016/j.epsl.2015.02.039.

Arndt, N., Coltice, N., Helmstaedt, H. and Gregoire, M. (2009) Origin of Archean subcontinental lithospheric mantle: Some petrological constraints. Lithos, v. 109, p. 61-71.

Asimow, P.D. and Ghiorso, M.S. (1998) Algorithmic modifications extending MELTS to calculate subsolidus phase relations. American Mineralogist, v. 83, p. 1127-1132 DOI: 10.2138/am-1998-9-1022.

Autin, J., Bellahsen, N., Leroy, S., Husson, L., Beslier, M.-O. and d'Acremont, E. (2013) The role of structural inheritance in oblique rifting: Insights from analogue models and application to the Gulf of Aden. Tectonophysics, v. 607, p. 51-64 DOI: 10.1016/j.tecto.2013.05.041.

Ayalew, D. and Gibson, S.A. (2009) Head-to-tail transition of the Afar mantle plume: Geochemical evidence from a Miocene bimodal basalt–rhyolite succession in the Ethiopian Large Igneous Province. Lithos, v. 112, p. 461-476.

Ayele, A., Keir, D., Ebinger, C., Wright, T.J., Stuart, G.W., Buck, W.R., Jacques, E., Ogubazghi, G. and Sholan, J. (2009) September 2005 mega-dike emplacement in the Manda-Harraro nascent oceanic rift (Afar depression). Geophysical Research Letters, v. 36, DOI: 10.1029/2009GL039605.

Baker, B. (1987) Outline of the petrology of the Kenya rift alkaline province. Geological Society, London, Special Publications, v. 30, p. 293-311 DOI: 10.1144/GSL.SP.1987.030.01.14.

Baker, J., Chazot, G., Menzies, M. and Thirlwall, M. (1998) Metasomatism of the shallow mantle beneath Yemen by the Afar plume—implications for mantle plumes, flood volcanism, and intraplate volcanism. Geology, v. 26, p. 431-434.

Baker, J., Menzies, M., Thirlwall, M. and Macpherson, C. (1997) Petrogenesis of Quaternary intraplate volcanism, Sana'a, Yemen: implications for plume-lithosphere interaction and polybaric melt hybridization. Journal of Petrology, v. 38, p. 1359-1390.

Baker, J., Snee, L. and Menzies, M. (1996) A brief Oligocene period of flood volcanism in Yemen: implications for the duration and rate of continental flood volcanism at the Afro-Arabian triple junction. Earth and Planetary Science Letters, v. 138, p. 39-55 DOI: 10.1016/0012-821X(95)00229-6.

Baker, M.B. and Stolper, E.M. (1994) Determining the composition of high-pressure mantle melts using diamond aggregates. Geochimica et Cosmochimica Acta, v. 58, p. 2811-2827 DOI: 10.1016/0016-7037(94)90116-3.

Balestrieri, M.L., Bonini, M., Corti, G., Sani, F. and Philippon, M. (2016) A refinement of the chronology of rift-related faulting in the Broadly Rifted Zone, southern Ethiopia, through apatite fission-track analysis. Tectonophysics, v. 671, p. 42-55 DOI: 10.1016/j.tecto.2016.01.012.

Barrat, J., Fourcade, S., Jahn, B., Cheminee, J. and Capdevila, R. (1998a) Isotope (Sr, Nd, Pb, O) and trace-element geochemistry of volcanics from the Erta'Ale range (Ethiopia). Journal of Volcanology and Geothermal Research, v. 80, p. 85-100.

Barrat, J.A., Fourcade, S., Jahn, B.M., Cheminée, J.L. and Capdevila, R. (1998b) Isotope (Sr, Nd, Pb, O) and trace-element geochemistry of volcanics from the Erta'Ale range (Ethiopia). Journal of Volcanology and Geothermal Research, v. 80, p. 85-100.

Bastow, I., Pilidou, S., Kendall, J.M. and Stuart, G. (2010) Melt-induced seismic anisotropy and magma assisted rifting in Ethiopia: Evidence from surface waves. Geochemistry, Geophysics, Geosystems, v. 11.

Bastow, I.D. (2012) Relative arrival-time upper-mantle tomography and the elusive background mean. Geophysical Journal International, v. 190, p. 1271-1278.

Bastow, I.D., Booth, A.D., Corti, G., Keir, D., Magee, C., Jackson, C.A.L., Warren, J., Wilkinson, J. and Lascialfari, M. (2018) The Development of Late-Stage Continental Breakup: Seismic Reflection and Borehole Evidence from the Danakil Depression, Ethiopia. Tectonics, v. 37, p. 2848-2862.

Bastow, I.D. and Keir, D. (2011) The protracted development of the continent–ocean transition in Afar. Nature Geoscience, v. 4, p. 248-250 DOI: 10.1038/ngeo1095.

Bastow, I.D., Nyblade, A.A., Stuart, G.W., Rooney, T.O. and Benoit, M.H. (2008) Upper mantle seismic structure beneath the Ethiopian hot spot: Rifting at the edge of the African low-velocity anomaly. Geochemistry, Geophysics, Geosystems, v. 9, DOI: 10.1029/2008GC002107.

Bastow, I.D., Stuart, G.W., Kendall, J.-M. and Ebinger, C.J. (2005) Upper-mantle seismic structure in a region of incipient continental breakup: northern Ethiopian rift. Geophysical Journal International, v. 162, p. 479-493.

Beccaluva, L., Bianchini, G., Natali, C. and Siena, F. (2009) Continental flood basalts and mantle plumes: a case study of the Northern Ethiopian Plateau. Journal of Petrology, v. 50, p. 1377-1403.

Bédard, J.H. (2006) A catalytic delamination-driven model for coupled genesis of Archaean crust and sub-continental lithospheric mantle. Geochimica et Cosmochimica Acta, v. 70, p. 1188-1214.

Bédard, J.H. (2014) Parameterizations of calcic clinopyroxene—Melt trace element partition coefficients. Geochemistry, Geophysics, Geosystems, v. 15, p. 303-336 DOI: 10.1002/2013GC005112.

Behn, M.D., Buck, W.R. and Sacks, I.S. (2006) Topographic controls on dike injection in volcanic rift zones. Earth and Planetary Science Letters, v. 246, p. 188-196 DOI: 10.1016/j.epsl.2006.04.005.

Belachew, M., Ebinger, C., Coté, D., Keir, D., Rowland, J., Hammond, J. and Ayele, A. (2011) Comparison of dike intrusions in an incipient seafloor-spreading segment in Afar, Ethiopia: Seismicity perspectives. Journal of Geophysical Research: Solid Earth, v. 116, DOI: 10.1029/2010JB007908.

Bendick, R., McClusky, S., Bilham, R., Asfaw, L. and Klemperer, S. (2006) Distributed Nubia—Somalia relative motion and dike intrusion in the Main Ethiopian Rift. Geophysical Journal International, v. 165, p. 303-310 DOI: 10.1111/j.1365-246X.2006.02904.x.

Benoit, M.H., Nyblade, A.A., Owens, T.J. and Stuart, G. (2006a) Mantle transition zone structure and upper mantle S velocity variations beneath Ethiopia: Evidence for a broad, deep-seated thermal anomaly. Geochemistry, Geophysics, Geosystems, v. 7.

Benoit, M.H., Nyblade, A.A. and VanDecar, J.C. (2006b) Upper mantle P-wave speed variations beneath Ethiopia and the origin of the Afar hotspot. Geology, v. 34, p. 329-332.

Bialas, R.W., Buck, W.R. and Qin, R. (2010) How much magma is required to rift a continent? Earth and Planetary Science Letters, v. 292, p. 68-78 DOI: 10.1016/j.epsl.2010.01.021.

Biggs, J., Bastow, I.D., Keir, D. and Lewi, E. (2011) Pulses of deformation reveal frequently recurring shallow magmatic activity beneath the Main Ethiopian Rift. Geochemistry, Geophysics, Geosystems, v. 12, DOI: 10.1029/2011GC003662.

Bilham, R., Bendick, R., Larson, K., Mohr, P., Braun, J., Tesfaye, S. and Asfaw, L. (1999) Secular and tidal strain across the Main Ethiopian Rift. Geophysical Research Letters, v. 26, p. 2789-2792 DOI: 10.1029/1998GL005315.

Boccaletti, M., Bonini, M., Mazzuoli, R., Abebe, B., Piccardi, L. and Tortorici, L. (1998) Quaternary oblique extensional tectonics in the Ethiopian Rift (Horn of Africa). Tectonophysics, v. 287, p. 97-116 DOI: 10.1016/S0040-1951(98)80063-2.

Bonini, M., Corti, G., Innocenti, F., Manetti, P., Mazzarini, F., Abebe, T. and Pecskay, Z. (2005) Evolution of the Main Ethiopian Rift in the frame of Afar and Kenya rifts propagation: Evolution of The Main Ethiopian Rift. Tectonics, v. 24, DOI: 10.1029/2004TC001680.

Bosworth, W., Huchon, P. and McClay, K. (2005) The red sea and gulf of aden basins. Journal of African Earth Sciences, v. 43, p. 334-378.

Bown, J.W. and White, R.S. (1995) Effect of finite extension rate on melt generation at rifted continental margins. Journal of Geophysical Research: Solid Earth, v. 100, p. 18011-18029.

Bronner, A., Sauter, D., Manatschal, G., Péron-Pinvidic, G. and Munschy, M. (2011) Magmatic breakup as an explanation for magnetic anomalies at magma-poor rifted margins. Nature Geoscience, v. 4, p. 549-553 DOI: 10.1038/ngeo1201.

Buck, W.R. (2004) Consequences of asthenospheric variability on continental rifting. Rheology and deformation of the lithosphere at continental margins, v. 62, p. 1-30.

Buck, W.R. (2006) The role of magma in the development of the Afro-Arabian Rift System. Geological Society, London, Special Publications, v. 259, p. 43-54 DOI: 10.1144/GSL.SP.2006.259.01.05.

Burke, K. (1996) The African plate. South African Journal of Geology, v. 99, p. 341-409.

Casey, M., Ebinger, C., Keir, D., Gloaguen, R. and Mohamed, F. (2006) Strain accommodation in transitional rifts: extension by magma intrusion and faulting in Ethiopian rift magmatic segments. Special Publication - Geological Society of London, v. 259, p. 143 DOI: 10.1144/GSL.SP.2006.259.01.13.

Chang, S.-J. and Van der Lee, S. (2011) Mantle plumes and associated flow beneath Arabia and East Africa. Earth and Planetary Science Letters, v. 302, p. 448-454.

Chernet, T., Hart, W.K., Aronson, J.L. and Walter, R.C. (1998) New age constraints on the timing of volcanism and tectonism in the northern Main Ethiopian Rift–southern Afar transition zone (Ethiopia). Journal of Volcanology and Geothermal Research, v. 80, p. 267-280.

Chiasera, B., Rooney, T.O., Girard, G., Yirgu, G., Grosfils, E., Ayalew, D., Mohr, P., Zimbelman, J.R. and Ramsey, M.S. (2018) Magmatically assisted off-rift extension—The case for broadly distributed strain accommodation. Geosphere, v. 14, p. 1544-1563.

Chorowicz, J. (2005) The East African rift system. Journal of African Earth Sciences, v. 43, p. 379-410.

Connelly, J.N., Ulfbeck, D.G., Thrane, K., Bizzarro, M. and Housh, T. (2006) A method for purifying Lu and Hf for analyses by MC-ICP-MS using TODGA resin. Chemical Geology, v. 233, p. 126-136.

Cornwell, D.G., Mackenzie, G.D., England, R.W. and Maguire, P.K.H. (2006) Northern Main Ethiopian Rift crustal structure from new high-precision gravity data. The Afar Volcanic Province Within the East African Rift System, p. 307.

Corti, G. (2008) Control of rift obliquity on the evolution and segmentation of the main Ethiopian rift. Nature Geoscience, v. 1, p. 258 DOI: 10.1038/ngeo160.

Corti, G. (2009) Continental rift evolution: From rift initiation to incipient break-up in the Main Ethiopian Rift, East Africa. Earth-Science Reviews, v. 96, p. 1-53 DOI: 10.1016/j.earscirev.2009.06.005.

Corti, G. (2012) Evolution and characteristics of continental rifting: Analog modeling-inspired view and comparison with examples from the East African Rift System. Tectonophysics, v. 522-523, p. 1-33 DOI: 10.1016/j.tecto.2011.06.010.

Corti, G., Bonini, M., Conticelli, S., Innocenti, F., Manetti, P. and Sokoutis, D. (2003) Analogue modelling of continental extension: a review focused on the relations between the patterns of deformation and the presence of magma. Earth-Science Reviews, v. 63, p. 169-247 DOI: 10.1016/S0012-8252(03)00035-7.

Corti, G., Bonini, M., Sokoutis, D., Innocenti, F., Manetti, P., Cloetingh, S. and Mulugeta, G. (2004) Continental rift architecture and patterns of magma migration: A dynamic analysis based on centrifuge models. Tectonics, v. 23, DOI: 10.1029/2003TC001561.

Corti, G., Cioni, R., Franceschini, Z., Sani, F., Scaillet, S., Molin, P., Isola, I., Mazzarini, F., Brune, S. and Keir, D. (2019) Aborted propagation of the Ethiopian rift caused by linkage with the Kenyan rift. Nature communications, v. 10, p. 1309.

Corti, G., Philippon, M., Sani, F., Keir, D. and Kidane, T. (2013) Re-orientation of the extension direction and pure extensional faulting at oblique rift margins: comparison between the Main Ethiopian Rift and laboratory experiments. Terra Nova, v. 25, p. 396-404 DOI: 10.1111/ter.12049.

Corti, G., Sani, F., Agostini, S., Philippon, M., Sokoutis, D. and Willingshofer, E. (2018) Off-axis volcano-tectonic activity during continental rifting: Insights from the transversal Goba-Bonga lineament, Main Ethiopian Rift (East Africa). Tectonophysics, v. 728, p. 75-91.

Cutten, H. (2002) The Mozambique Belt, eastern Africa-tectonic evolution of Gondwanaland amalgamation and (?) Rodinia breakup, GEOLOGICAL SOCIETY OF AUSTRALIA ABSTRACTS. Geological Society of Australia; 1999 p. 109-109.

Daly, E., Keir, D., Ebinger, C.J., Stuart, G.W., Bastow, I.D. and Ayele, A. (2008) Crustal tomographic imaging of a transitional continental rift: the Ethiopian rift. Geophysical Journal International, v. 172, p. 1033-1048 DOI: 10.1111/j.1365-246X.2007.03682.x.

Daniels, K.A., Bastow, I.D., Keir, D., Sparks, R.S.J. and Menand, T. (2014) Thermal models of dyke intrusion during development of continent–ocean transition. Earth and Planetary Science Letters, v. 385, p. 145-153 DOI: 10.1016/j.epsl.2013.09.018.

Danyushevsky, L.V. and Plechov, P. (2011) Petrolog3: Integrated software for modeling crystallization processes. Geochemistry, Geophysics, Geosystems, v. 12.

Darbyshire, F.A. and Eaton, D.W. (2010) The lithospheric root beneath Hudson Bay, Canada from Rayleigh wave dispersion: No clear seismological distinction between Archean and Proterozoic mantle. Lithos, v. 120, p. 144-159.

Dasgupta, R. and Hirschmann, M.M. (2006) Melting in the Earth's deep upper mantle caused by carbon dioxide. Nature, v. 440, p. 659.

Davies, G.F. (1994) Thermomechanical erosion of the lithosphere by mantle plumes. Journal of Geophysical Research: Solid Earth, v. 99, p. 15709-15722.

Deniel, C., Vidal, P., Coulon, C., Vellutini, P.-J. and Piguet, P. (1994) Temporal evolution of mantle sources during continental rifting: the volcanism of Djibouti (Afar). Journal of Geophysical Research: Solid Earth (1978–2012), v. 99, p. 2853-2869.

Djomani, Y.H.P., O'Reilly, S.Y., Griffin, W. and Morgan, P. (2001) The density structure of subcontinental lithosphere through time. Earth and Planetary Science Letters, v. 184, p. 605-621.

Douglass, J. and Schilling, J.-G. (2000) Systematics of three-component, pseudo-binary mixing lines in 2D isotope ratio space representations and implications for mantle plume–ridge interaction. Chemical Geology, v. 163, p. 1-23.

Dugda, M.T. (2005) Crustal structure in Ethiopia and Kenya from receiver function analysis: Implications for rift development in eastern Africa. Journal of Geophysical Research, v. 110, DOI: 10.1029/2004JB003065.

Dugda, M.T., Nyblade, A.A. and Julia, J. (2007) Thin lithosphere beneath the Ethiopian Plateau revealed by a joint inversion of Rayleigh wave group velocities and receiver functions. Journal of Geophysical Research: Solid Earth, v. 112.

Dziewonski, A.M. and Anderson, D.L. (1981) Preliminary reference Earth model. Physics of the earth and planetary interiors, v. 25, p. 297-356.

Eagles, G., Pérez-Díaz, L. and Scarselli, N. (2015) Getting over continent ocean boundaries. Earth-Science Reviews, v. 151, p. 244-265.

Eaton, D.W., Darbyshire, F., Evans, R.L., Grütter, H., Jones, A.G. and Yuan, X. (2009) The elusive lithosphere–asthenosphere boundary (LAB) beneath cratons. Lithos, v. 109, p. 1-22.

Ebinger, C. (1989) Tectonic development of the western branch of the East African rift system. Geological Society of America Bulletin, v. 101, p. 885-903.

Ebinger, C. (2005) Continental break-up: The East African perspective. Astronomy and Geophysics, v. 46, p. 2.16-12.21 DOI: 10.1111/j.1468-4004.2005.46216.x.

Ebinger, C. and Casey, M. (2001a) Continental breakup in magmatic provinces: An Ethiopian example. Geology, v. 29, p. 527-530 DOI: 10.1111/j.1468-4004.2005.46216.x.

Ebinger, C., Yamane, T. and Kelley, S. (1993a) Volcanism and extension between the main Ethiopian and Gregory Rifts. Geoscientific Research in Northeast Africa. Rotterdam, Balkema, p. 301-304.

Ebinger, C., Yemane, T., Woldegabriel, G., Aronson, J. and Walter, R. (1993b) Late Eocene–Recent volcanism and faulting in the southern main Ethiopian rift. Journal of the Geological Society, v. 150, p. 99-108 DOI: 10.1144/gsjgs.150.1.0099.

Ebinger, C.J. and Casey, M. (2001b) Continental breakup in magmatic provinces: An Ethiopian example. Geology, v. 29, p. 527 DOI: 10.1130/0091-7613(2001)029<0527:CBIMPA>2.0.CO;2.

Ebinger, C.J. and Sleep, N. (1998) Cenozoic magmatism throughout east Africa resulting from impact of a single plume. Nature, v. 395, p. 788-791 DOI: 10.1038/27417.

El-Rus, M.M.A. and Rooney, T.O. (2017) Insights into the lithosphere to asthenosphere melting transition in northeast Africa: Evidence from the Tertiary volcanism in middle Egypt. Chemical Geology, v. 455, p. 282-303.

Ferguson, D.J., Maclennan, J., Bastow, I., Pyle, D., Jones, S., Keir, D., Blundy, J., Plank, T. and Yirgu, G. (2013) Melting during late-stage rifting in Afar is hot and deep. Nature, v. 499, p. 70-73.

Feyissa, D., Shinjo, R., Kitagawa, H., Meshesha, D. and Nakamura, E. (2017) Petrologic and geochemical characterization of rift-related magmatism at the northernmost Main Ethiopian Rift: Implications for plume-lithosphere interaction and the evolution of rift mantle sources. Lithos, v. 282, p. 240-261.

Field, L., Blundy, J., Brooker, R., Wright, T. and Yirgu, G. (2012) Magma storage conditions beneath Dabbahu Volcano (Ethiopia) constrained by petrology, seismicity and satellite geodesy. Bulletin of volcanology, v. 74, p. 981-1004 DOI: doi.org/10.1007/s00445-012-0580-6.

Field, L., Blundy, J., Calvert, A. and Yirgu, G. (2013) Magmatic history of Dabbahu, a composite volcano in the Afar Rift, Ethiopia. Geological Society of America Bulletin, v. 125, p. 128-147 DOI: 10.1130/B30560.1.

Finlayson, V., Konter, J., Konrad, K., Koppers, A., Jackson, M. and Rooney, T. (2018) Sr–Pb–Nd–Hf isotopes and 40Ar/39Ar ages reveal a Hawaii–Emperor-style bend in the Rurutu hotspot. Earth and Planetary Science Letters, v. 500, p. 168-179.

Fishwick, S. and Bastow, I.D. (2011) Towards a better understanding of African topography: a review of passive-source seismic studies of the African crust and upper mantle. Geological Society, London, Special Publications, v. 357, p. 343-371.

Furman, T. (1995) Melting of metasomatized subcontinental lithosphere: undersaturated mafic lavas from Rungwe, Tanzania. Contributions to Mineralogy and Petrology, v. 122, p. 97-115.

Furman, T. (2007) Geochemistry of East African Rift basalts: An overview. Journal of African Earth Sciences, v. 48, p. 147-160 DOI: 10.1016/j.jafrearsci.2006.06.009.

Furman, T., Bryce, J., Rooney, T., Hanan, B., Yirgu, G. and Ayalew, D. (2006a) Heads and tails: 30 million years of the Afar plume. Geological Society, London, Special Publications, v. 259, p. 95-119 DOI: 10.1144/GSL.SP.2006.259.01.09.

Furman, T. and Graham, D. (1999) Erosion of lithospheric mantle beneath the East African Rift system: geochemical evidence from the Kivu volcanic province. Lithos, v. 48, p. 237-262.

Furman, T., Kaleta, K.M., Bryce, J.G. and Hanan, B.B. (2006b) Tertiary mafic lavas of Turkana, Kenya: constraints on East African plume structure and the occurrence of high-μ volcanism in Africa. Journal of Petrology, v. 47, p. 1221-1244.

Furman, T., Nelson, W.R. and Elkins-Tanton, L.T. (2016) Evolution of the East African rift: drip magmatism, lithospheric thinning and mafic volcanism. Geochimica et Cosmochimica Acta, v. 185, p. 418-434.

Gallacher, R. and Bastow, I. (2012) The development of magmatism along the Cameroon Volcanic Line: Evidence from teleseismic receiver functions. Tectonics, v. 31.

Gallacher, R.J., Keir, D., Harmon, N., Stuart, G., Leroy, S., Hammond, J.O., Kendall, J.-M., Ayele, A., Goitom, B. and Ogubazghi, G. (2016) The initiation of segmented buoyancy-driven melting during continental breakup. Nature Communications, v. 7, p. 13110.

Garnero, E.J. and McNamara, A.K. (2008) Structure and dynamics of Earth's lower mantle. science, v. 320, p. 626-628.

Gasparon, M., Innocenti, F., Manetti, P., Peccerillo, A. and Tsegaye, A. (1993) Genesis of the Pliocene to Recent bimodal mafic-felsic volcanism in the Debre Zeyt area, central Ethiopia: volcanological and geochemical constraints. Journal of African Earth Sciences (and the Middle East), v. 17, p. 145-165 DOI: 10.1016/0899-5362(93)90032-L.

GeoPRISMS (2013) GeoPRISMS Implementation Plan, Planning Workshop for the East African Rift System Primary Site.

George, R. and Rogers, N. (2002) Plume dynamics beneath the African plate inferred from the geochemistry of the Tertiary basalts of southern Ethiopia. Contributions to Mineralogy and Petrology, v. 144, p. 286-304 DOI: 10.1007/s00410-002-0396-z.

George, R., Rogers, N. and Kelley, S. (1998) Earliest magmatism in Ethiopia: Evidence for two mantle plumes in one flood basalt province. Geology, v. 26, p. 923-926.

Ghiorso, M.S. and Sack, R.O. (1995) Chemical mass transfer in magmatic processes IV. A revised and internally consistent thermodynamic model for the interpolation and extrapolation of liquid-solid equilibria in magmatic systems at elevated temperatures and pressures. Contributions to Mineralogy and Petrology, v. 119, p. 197-212 DOI: 10.1007/BF00307281.

Giordano, F., D'Antonio, M., Civetta, L., Tonarini, S., Orsi, G., Ayalew, D., Yirgu, G., Dell'Erba, F., Di Vito, M.A. and Isaia, R. (2014) Genesis and evolution of mafic and felsic magmas at Quaternary volcanoes within the Main Ethiopian Rift: Insights from Gedemsa and Fanta 'Ale complexes. Lithos, v. 188, p. 130-144 DOI: 10.1016/j.lithos.2013.08.008.

Green, D.H. and Ringwood, A.E. (1967) The genesis of basaltic magmas. Contributions to Mineralogy and Petrology, v. 15, p. 103-190 DOI: 10.1007/bf00372052.

Green, T.H. (1969) High-pressure experimental studies on the origin of anorthosite. Canadian Journal of Earth Sciences, v. 6, p. 427-440 DOI: 10.1139/e69-041.

Gregory, J.W., Baker, E.G., Britten, J., Rendle, A.B., Gepp, A., Smith, A.L., Carruthers, J.B., Clarke, C.B., Thomas, O., R, Clark, R. and John, M. (1896) The Great Rift Valley: being the narrative of a journey to Mount Kenya and Lake Baringo : with some account of the geology, natural history, anthropology and future prospects of British East Africa. John Murray, 405 p.

Gualda, G.A.R. and Ghiorso, M.S. (2015) MELTS_Excel: AMicrosoft Excel-based MELTS interface for research and teaching of magma properties and evolution. Geochemistry, Geophysics, Geosystems, v. 16, p. 315-324 DOI: 10.1002/2014GC005545.

Hammond, J. (2014) Constraining melt geometries beneath the Afar Depression, Ethiopia from teleseismic receiver functions: The anisotropic H-κ stacking technique. Geochemistry, Geophysics, Geosystems, v. 15, p. 1316-1332 DOI: 10.1002/2013GC005186.

Hammond, J.O., Kendall, J.-M., Stuart, G., Ebinger, C., Bastow, I., Keir, D., Ayele, A., Belachew, M., Goitom, B. and Ogubazghi, G. (2013) Mantle upwelling and initiation of rift segmentation beneath the Afar Depression. Geology, v. 41, p. 635-638.

Hanan, B., Kingsley, R. and Schilling, J. (1986) Pb isotope evidence in the South Atlantic for migrating ridge—hotspot interactions. Nature, v. 322, p. 137.

Hanan, B.B., Blichert-Toft, J., Kingsley, R. and Schilling, J.G. (2000) Depleted Iceland mantle plume geochemical signature: artifact of multicomponent mixing? Geochemistry, Geophysics, Geosystems, v. 1.

Hanan, B.B. and Schilling, J.-G. (1997) The dynamic evolution of the Iceland mantle plume: the lead isotope perspective. Earth and Planetary Science Letters, v. 151, p. 43-60.

Hanan, B.B. and Schilling, J.G. (1989) Easter microplate evolution: Pb isotope evidence. Journal of Geophysical Research: Solid Earth, v. 94, p. 7432-7448.

Hart, W.K., Woldegabriel, G., Walter, R.C. and Mertzman, S.A. (1989) Basaltic volcanism in Ethiopia: constraints on continental rifting and mantle interactions. Journal of Geophysical Research: Solid Earth (1978–2012), v. 94, p. 7731-7748.

Hasterok, D. and Chapman, D. (2011) Heat production and geotherms for the continental lithosphere. Earth and Planetary Science Letters, v. 307, p. 59-70 DOI: 10.1016/j.epsl.2011.04.034.

Havlin, C., Parmentier, E.M. and Hirth, G. (2013) Dike propagation driven by melt accumulation at the lithosphere–asthenosphere boundary. Earth and Planetary Science Letters, v. 376, p. 20-28 DOI: 10.1016/j.epsl.2013.06.010.

Herzberg, C. and Asimow, P.D. (2008) Petrology of some oceanic island basalts: PRIMELT2. XLS software for primary magma calculation. Geochemistry, Geophysics, Geosystems, v. 9.

Herzberg, C. and Asimow, P.D. (2015) PRIMELT3 MEGA.XLSM software for primary magma calculation: Peridotite primary magma MgO contents from the liquidus to the solidus. Geochemistry, Geophysics, Geosystems, v. 16, p. 563-578 DOI: 10.1002/2014GC005631.

Herzberg, C. and O'Hara, M. (2002) Plume-associated ultramafic magmas of Phanerozoic age. Journal of Petrology, v. 43, p. 1857-1883.

Hirose, K. and Kushiro, I. (1993) Partial melting of dry peridotites at high pressures: determination of compositions of melts segregated from peridotite using aggregates of diamond. Earth and Planetary Science Letters, v. 114, p. 477-489 DOI: 10.1016/0012-821X(93)90077-M.

Hofmann, C., Courtillot, V., Feraud, G., Rochette, P., Yirgu, G., Ketefo, E. and Pik, R. (1997) Timing of the Ethiopian flood basalt event and implications for plume birth and global change. Nature, v. 389, p. 838-841 DOI: 10.1038/39853.

Holtzman, B.K. and Kendall, J.-M. (2010) Organized melt, seismic anisotropy, and plate boundary lubrication: PLATE BOUNDARY LUBRICATION. Geochemistry, Geophysics, Geosystems, v. 11, p. n/a-n/a DOI: 10.1029/2010GC003296.

Horwitz, E.P., Chiarizia, R., Dietz, M.L., Diamond, H. and Nelson, D.M. (1993) Separation and preconcentration of actinides from acidic media by extraction chromatography. Analytica Chimica Acta, v. 281, p. 361-372.

Isola, I., Mazzarini, F., Bonini, M. and Corti, G. (2014) Spatial variability of volcanic features in early-stage rift settings: the case of the Tanzania Divergence, East African rift system. Terra Nova, v. 26, p. 461-468 DOI: 10.1111/ter.12121.

Kampunzu, A., Caron, J. and Lubala, R. (1986) The East-African Rift, magma genesis and astheno-lithospheric dynamics. Episodes, v. 9, p. 211-216.

Keir, D., Bastow, I.D., Corti, G., Mazzarini, F. and Rooney, T.O. (2015) The origin of along-rift variations in faulting and magmatism in the Ethiopian Rift. Tectonics, v. 34, p. 464-477 DOI: 10.1002/2014TC003698.

Keir, D., Bastow, I.D., Pagli, C. and Chambers, E.L. (2013) The development of extension and magmatism in the Red Sea rift of Afar. Tectonophysics, v. 607, p. 98-114 DOI: 10.1016/j.tecto.2012.10.015.

Keir, D., Kendall, J.M., Ebinger, C. and Stuart, G. (2005) Variations in late syn-rift melt alignment inferred from shear-wave splitting in crustal earthquakes beneath the Ethiopian rift. Geophysical Research Letters, v. 32, DOI: 10.1029/2005GL024150.

Keir, D., Pagli, C., Bastow, I.D. and Ayele, A. (2011) The magma-assisted removal of Arabia in Afar: Evidence from dike injection in the Ethiopian rift captured using InSAR and seismicity: Magma-Assisted Removal of Arabia in Afar. Tectonics, v. 30, DOI: 10.1029/2010TC002785.

Kendall, J.-M., Stuart, G.W., Ebinger, C.J., Bastow, I.D. and Keir, D. (2005) Magma-assisted rifting in Ethiopia. Nature, v. 433, p. 146-148.

Kendall, J., Pilidou, S., Keir, D., Bastow, I.D., Stuart, G.W. and Ayele, A. (2006) Mantle upwellings, melt migration and the rifting of Africa: Insights from seismic anisotropy. Special Publication - Geological Society of London, v. 259, p. 55.

Kennan, P., Mitchell, J. and Mohr, P. (1990) The Sagatu ridge dyke swarm, Ethiopian rift margin: Revised age and new Sr-isotopic data. Journal of African Earth Sciences (and the Middle East), v. 11, p. 39-42 DOI: 10.1016/0899-5362(90)90075-P.

Keranen, K. and Klemperer, S.L. (2008) Discontinuous and diachronous evolution of the Main Ethiopian Rift: Implications for development of continental rifts. Earth and Planetary Science Letters, v. 265, p. 96-111 DOI: 10.1016/j.epsl.2007.09.038.

Keranen, K., Klemperer, S.L., Gloaguen, R. and Group, E.W. (2004) Three-dimensional seismic imaging of a protoridge axis in the Main Ethiopian rift. Geology, v. 32, p. 949 DOI: 10.1130/G20737.1.

Keranen, K.M., Klemperer, S.L., Julia, J., Lawrence, J.F. and Nyblade, A.A. (2009) Low lower crustal velocity across Ethiopia: Is the Main Ethiopian Rift a narrow rift in a hot craton? Geochemistry, Geophysics, Geosystems, v. 10, DOI: 10.1029/2008GC002293.

Kieffer, B. (2004) Flood and Shield Basalts from Ethiopia: Magmas from the African Superswell. Journal of Petrology, v. 45, p. 793-834 DOI: 10.1093/petrology/egg112.

Kim, S., Nyblade, A.A., Rhie, J., Baag, C.-E. and Kang, T.-S. (2012) Crustal S-wave velocity structure of the Main Ethiopian Rift from ambient noise tomography. Geophysical Journal International, v. 191, p. 865-878 DOI: 10.1111/j.1365-246X.2012.05664.x.

Kimura, J.-I. and Kawabata, H. (2014) Trace element mass balance in hydrous adiabatic mantle melting: The Hydrous Adiabatic Mantle Melting Simulator version 1 (HAMMS1). Geochemistry, Geophysics, Geosystems, v. 15, p. 2467-2493 DOI: 10.1002/2014GC005333.

Kimura, J.I. and Ariskin, A.A. (2014) Calculation of water-bearing primary basalt and estimation of source mantle conditions beneath arcs: PRIMACALC2 model for WINDOWS. Geochemistry, Geophysics, Geosystems, v. 15, p. 1494-1514.

Konter, J.G. and Storm, L.P. (2014) High precision 87Sr/86Sr measurements by MC-ICP-MS, simultaneously solving for Kr interferences and mass-based fractionation. Chemical Geology, v. 385, p. 26-34.

Koppers, A.A., Staudigel, H., Pringle, M.S. and Wijbrans, J.R. (2003) Short-lived and discontinuous intraplate volcanism in the South Pacific: Hot spots or extensional volcanism? Geochemistry, Geophysics, Geosystems, v. 4.

Korme, T., Acocella, V. and Abebe, B. (2004) The role of pre-existing structures in the origin, propagation and architecture of faults in the Main Ethiopian Rift. Gondwana Research, v. 7, p. 467-479.

Korme, T., Chorowicz, J., Collet, B. and Bonavia, F.F. (1997) Volcanic vents rooted on extension fractures and their geodynamic implications in the Ethiopian Rift. Journal of Volcanology and Geothermal Research, v. 79, p. 205-222 DOI: 10.1016/S0377-0273(97)00034-6.

Kurz, T., Gloaguen, R., Ebinger, C., Casey, M. and Abebe, B. (2007) Deformation distribution and type in the Main Ethiopian Rift (MER): A remote sensing study. Journal of African Earth Sciences, v. 48, p. 100-114 DOI: 10.1016/j.jafrearsci.2006.10.008.

Kushiro, I. (1996) Partial melting of a fertile mantle peridotite at high pressures: an experimental study using aggregates of diamond. Earth processes: Reading the isotopic code, p. 109-122 DOI: 10.1029/GM095p0109.

Langmuir, C.H. and Forsyth, D.W. (2007) Mantle melting beneath mid-ocean ridges. Oceanography, v. 20, p. 78-89.

Lavayssière, A., Rychert, C., Harmon, N., Keir, D., Hammond, J.O., Kendall, J.M., Doubre, C. and Leroy, S. (2018) Imaging lithospheric discontinuities beneath the northern East African Rift using S-to-P receiver functions. Geochemistry, Geophysics, Geosystems.

Le Corvec, N., Menand, T. and Lindsay, J. (2013) Interaction of ascending magma with pre-existing crustal fractures in monogenetic basaltic volcanism: an experimental approach. Journal of Geophysical Research: Solid Earth, v. 118, p. 968-984 DOI: 10.1002/jgrb.50142.

Lee, C.-T.A., Luffi, P. and Chin, E.J. (2011) Building and destroying continental mantle. Annual Review of Earth and Planetary Sciences, v. 39, p. 59-90.

Lee, C.-T.A., Luffi, P., Plank, T., Dalton, H. and Leeman, W.P. (2009) Constraints on the depths and temperatures of basaltic magma generation on Earth and other terrestrial planets using new thermobarometers for mafic magmas. Earth and Planetary Science Letters, v. 279, p. 20-33.

Leeman, W. and Hawkesworth, C. (1986) Open magma systems: trace element and isotopic constraints. Journal of Geophysical Research: Solid Earth, v. 91, p. 5901-5912.

LeMaitre, R. (2002) Igneous Rocks: IUGS classification and glossary. Cambridge University Press.

Maccaferri, F., Rivalta, E., Keir, D. and Acocella, V. (2014) Off-rift volcanism in rift zones determined by crustal unloading. Nature Geoscience, v. 7, p. 297-300 DOI: 10.1038/ngeo2110.

Macgregor, D. (2015) History of the development of the East African Rift System: A series of interpreted maps through time. Journal of African Earth Sciences, v. 101, p. 232-252.

Mackenzie, G.D., Thybo, H. and Maguire, P.K.H. (2005) Crustal velocity structure across the Main Ethiopian Rift: results from two-dimensional wide-angle seismic modelling. Geophysical Journal International, v. 162, p. 994-1006 DOI: 10.1111/j.1365-246X.2005.02710.x.

Maguire, P.K.H., Keller, G.R., Klemperer, S.L., Mackenzie, G.D., Keranen, K., Harder, S., O Reilly, B., Thybo, H., Asfaw, L. and Khan, M.A. (2006) Crustal structure of the northern Main Ethiopian Rift from the EAGLE controlled-source survey; a snapshot of incipient lithospheric break-up. SPECIAL PUBLICATION-GEOLOGICAL SOCIETY OF LONDON, v. 259, p. 269.

Mahatsente, R., Jentzsch, G. and Jahr, T. (1999) Crustal structure of the Main Ethiopian Rift from gravity data: 3-dimensional modeling. Tectonophysics, v. 313, p. 363-382 DOI: 10.1016/S0040-1951(99)00213-9.

Mazzarini, F., Keir, D. and Isola, I. (2013a) Spatial relationship between earthquakes and volcanic vents in the central-northern Main Ethiopian Rift. Journal of Volcanology and Geothermal Research, v. 262, p. 123-133.

Mazzarini, F., Le Corvec, N., Isola, I. and Favalli, M. (2016) Volcanic field elongation, vent distribution, and tectonic evolution of a continental rift: The Main Ethiopian Rift example. Geosphere, v. 12, p. 706-720 DOI: 10.1130/GES01193.1.

Mazzarini, F., Rooney, T.O. and Isola, I. (2013b) The intimate relationship between strain and magmatism: A numerical treatment of clustered monogenetic fields in the Main Ethiopian Rift. Tectonics, v. 32, p. 49-64 DOI: 10.1029/2012TC003146.

McKenzie, D. (1978) Some remarks on the development of sedimentary basins. Earth and Planetary science letters, v. 40, p. 25-32.

McKenzie, D. (1989) Some remarks on the movement of small melt fractions in the mantle. Earth and planetary science letters, v. 95, p. 53-72.

McKenzie, D. and Bickle, M. (1988) The volume and composition of melt generated by extension of the lithosphere. Journal of petrology, v. 29, p. 625-679 DOI: 10.1093/petrology/29.3.625.

McKenzie, D.A.N. and O'Nions, R.K. (1991) Partial Melt Distributions from Inversion of Rare Earth Element Concentrations. Journal of Petrology, v. 32, p. 1021-1091 DOI: 10.1093/petrology/32.5.1021.

McWilliams, M. (1981) Palaeomagnetism and Precambrian tectonic evolution of Gondwana. Developments in Precambrian Geology, v. 4, p. 649-687.

Medynski, S., Pik, R., Burnard, P., Vye-Brown, C., France, L., Schimmelpfennig, I., Whaler, K., Johnson, N., Benedetti, L. and Ayelew, D. (2015) Stability of rift axis magma reservoirs: Spatial and temporal evolution of magma supply in the Dabbahu rift segment (Afar, Ethiopia) over the past 30 kyr. Earth and Planetary Science Letters, v. 409, p. 278-289 DOI: 10.1016/j.epsl.2014.11.002.

Mège, D., Purcell, P., Bézos, A., Jourdan, F. and La, C. (2016) A major dyke swarm in the Ogaden region south of Afar and the early evolution of the Afar triple junction. Geological Society, London, Special Publications, v. 420, p. 221-248.

Menand, T. (2011) Physical controls and depth of emplacement of igneous bodies: A review. Tectonophysics, v. 500, p. 11-19 DOI: 10.1016/j.tecto.2009.10.016.

Meshesha, D. and Shinjo, R. (2007) Crustal contamination and diversity of magma sources in the northwestern Ethiopian volcanic province. Journal of Mineralogical and Petrological Sciences, v. 102, p. 272-290 DOI: 10.2465/jmps.061129.

Meshesha, D. and Shinjo, R. (2010) Hafnium isotope variations in Bure volcanic rocks from the northwestern Ethiopian volcanic province: a new insight for mantle source diversity. Journal of Mineralogical and Petrological Sciences, v. 105, p. 101-111.

Mohr, P. (1967) Major volcano-tectonic lineament in the Ethiopian rift system. Nature, v. 213, p. 664-665 DOI: 10.1038/213664a0.

Mohr, P. (1980) Geochemical aspects of the Sagatu ridge dike swarm, Ethiopian rift margin. Geodynamic Evolution of the Afro Arabian Rift System. Acad. Nat. Lincei, Atti Convegni Lincei, v. 47, p. 384-406.

Mohr, P., Mitchell, J. and Raynolds, R. (1980) Quaternary volcanism and faulting at O'a Caldera, Central Ethiopian Rift. Bulletin Volcanologique, v. 43, p. 173 DOI: 10.1007/BF02597619.

Mohr, P.A. (1962) Surface cauldron subsidence with associated faulting and fissure basalt eruptions at Gariboldi Pass, Shoa, Ethiopia. Bulletin Volcanologique, v. 24, p. 421-428 DOI: 10.1007/BF02599358.

Mohr, P.A. and Potter, E.C. (1976) The sagatu ridge dike swarm, ethiopian rift margin. Journal of Volcanology and Geothermal Research, v. 1, p. 55-71 DOI: 10.1016/0377-0273(76)90018-4.

Molin, P. and Corti, G. (2015) Topography, river network and recent fault activity at the margins of the Central Main Ethiopian Rift (East Africa). Tectonophysics, v. 664, p. 67-82 DOI: 10.1016/j.tecto.2015.08.045.

Montelli, R., Nolet, G., Dahlen, F. and Masters, G. (2006) A catalogue of deep mantle plumes: New results from finite-frequency tomography. Geochemistry, Geophysics, Geosystems, v. 7.

Montelli, R., Nolet, G., Dahlen, F., Masters, G., Engdahl, E.R. and Hung, S.-H. (2004) Finite-frequency tomography reveals a variety of plumes in the mantle. Science, v. 303, p. 338-343.

Morley, C. (1994) Interaction of deep and shallow processes in the evolution of the Kenya rift. Tectonophysics, v. 236, p. 81-91.

Morse, S. (1980) Basalts and phase diagrams: an introduction to the quantitative use of phase diagrams in igneous petrology, 493 pp. Springer, New York.

Morton, W.H., Rex, D.C., Mitchell, J.G. and Mohr, P. (1979) Riftward younging of volcanic units in the Addis Ababa region, Ethiopian rift valley. Nature, v. 280, p. 284-288 DOI: 10.1038/280284a0.

Nelson, W.R., Hanan, B., Graham, D.W., Shirey, S.B., Yirgu, G., Ayalew, D. and Furman, T. (2019) Distinguishing plume and metasomatized lithospheric mantle contributions to post-flood basalt volcanism on the southeastern Ethiopian Plateau. Journal of Petrology.

Nimis, P. (1995) A clinopyroxene geobarometer for basaltic systems based on crystal-structure modeling. Contributions to Mineralogy and Petrology, v. 121, p. 115-125 DOI: 10.1007/s004100050093.

Nimis, P. and Taylor, W.R. (2000) Single clinopyroxene thermobarometry for garnet peridotites. Part I. Calibration and testing of a Cr-in-Cpx barometer and an enstatite-in-Cpx thermometer. Contributions to Mineralogy and Petrology, v. 139, p. 541-554 DOI: 10.1007/s004100000156.

Nyblade, A.A. and Robinson, S.W. (1994) The African superswell. Geophysical Research Letters, v. 21, p. 765-768.

O'Hara, M. (1968) The bearing of phase equilibria studies in synthetic and natural systems on the origin and evolution of basic and ultrabasic rocks. Earth-Science Reviews, v. 4, p. 69-133 DOI: 10.1016/0012-8252(68)90147-5.

Pallister, J.S., McCausland, W.A., Jónsson, S., Lu, Z., Zahran, H.M., Hadidy, S.E., Aburukbah, A., Stewart, I.C.F., Lundgren, P.R., White, R.A. and Moufti, M.R.H. (2010) Broad accommodation of rift-related extension recorded by dyke intrusion in Saudi Arabia. Nature Geoscience, v. 3, p. 705-712 DOI: 10.1038/ngeo966.

Parsons, T. and Thompson, G.A. (1991) The role of magma overpressure in suppressing earthquakes and topography: Worldwide examples. Science, v. 253, p. 1399-1402 DOI: 10.1126/science.253.5026.1399

Pasteels, P., Villeneuve, M., De Paepe, P. and Klerkx, J. (1989) Timing of the volcanism of the southern Kivu province: implications for the evolution of the western branch of the East African Rift system. Earth and Planetary Science Letters, v. 94, p. 353-363.

Peccerillo, A., Barberio, M.R., Yirgu, G., Ayalew, D., Barbieri, M. and Wu, T.U. (2003) Relationships between Mafic and Peralkaline Silicic Magmatism in Continental Rift Settings: a Petrological, Geochemical and Isotopic Study of the Gedemsa Volcano, Central Ethiopian Rift. Journal of Petrology, v. 44, p. 2003-2032 DOI: 10.1093/petrology/egg068.

Peccerillo, A., Donati, C., Santo, A.P., Orlando, A., Yirgu, G. and Ayalew, D. (2007) Petrogenesis of silicic peralkaline rocks in the Ethiopian rift: Geochemical evidence and volcanological implications. Journal of African Earth Sciences, v. 48, p. 161-173 DOI: 10.1016/j.jafrearsci.2006.06.010.

Philippon, M., Willingshofer, E., Sokoutis, D., Corti, G., Sani, F., Bonini, M. and Cloetingh, S. (2015) Slip re-orientation in oblique rifts. Geology, v. 43, p. 147-150 DOI: 10.1130/G36208.1.

Pik, R., Deniel, C., Coulon, C., Yirgu, G. and Marty, B. (1999) Isotopic and trace element signatures of Ethiopian flood basalts: evidence for plume–lithosphere interactions. Geochimica et Cosmochimica Acta, v. 63, p. 2263-2279 DOI: 10.1016/S0016-7037(99)00141-6.

Pilet, S., Baker, M.B., Müntener, O. and Stolper, E.M. (2011) Monte Carlo simulations of metasomatic enrichment in the lithosphere and implications for the source of alkaline basalts. Journal of Petrology, v. 52, p. 1415-1442.

Pilet, S., Baker, M.B. and Stolper, E.M. (2008) Metasomatized lithosphere and the origin of alkaline lavas. Science, v. 320, p. 916-919.

Pin, C. and Zalduegui, J.S. (1997) Sequential separation of light rare-earth elements, thorium and uranium by miniaturized extraction chromatography: application to isotopic analyses of silicate rocks. Analytica Chimica Acta, v. 339, p. 79-89.

Pizzi, A., Coltorti, M., Abebe, B., Disperati, L., Sacchi, G. and Salvini, R. (2006) The Wonji fault belt (Main Ethiopian Rift): structural and geomorphological constraints and GPS monitoring. Geological Society, London, Special Publications, v. 259, p. 191-207 DOI: 10.1144/GSL.SP.2006.259.01.16.

Purcell, P. (2018) Re-imagining and re-imaging the development of the East African Rift. Petroleum Geoscience, v. 24, p. 21-40.

Putirka, K.D. (2008) Thermometers and barometers for volcanic systems. Reviews in Mineralogy and Geochemistry, v. 69, p. 61-120 DOI: 10.2138/rmg.2008.69.3.

Putirka, K.D., Mikaelian, H., Ryerson, F. and Shaw, H. (2003) New clinopyroxene-liquid thermobarometers for mafic, evolved, and volatile-bearing lava compositions, with applications to lavas from Tibet and the Snake River Plain, Idaho. American Mineralogist, v. 88, p. 1542-1554 DOI: 10.2138/am-2003-1017.

Renne, P.R., Swisher, C.C., Deino, A.L., Karner, D.B., Owens, T.L. and DePaolo, D.J. (1998) Intercalibration of standards, absolute ages and uncertainties in 40Ar/39Ar dating. Chemical Geology, v. 145, p. 117-152.

Ritsema, J., van Heijst, H.J. and Woodhouse, J.H. (1999) Complex shear wave velocity structure imaged beneath Africa and Iceland. Science, v. 286, p. 1925-1928.

Robertson, E., Biggs, J., Cashman, K., Floyd, M. and Vye-Brown, C. (2016) Influence of regional tectonics and pre-existing structures on the formation of elliptical calderas in the Kenyan Rift. Geological Society, London, Special Publications, v. 420, p. 43-67 DOI: 10.1144/SP420.12.

Rochette, P., Tamrat, E., Féraud, G., Pik, R., Courtillot, V., Ketefo, E., Coulon, C., Hoffmann, C., Vandamme, D. and Yirgu, G. (1998) Magnetostratigraphy and timing of the Oligocene Ethiopian traps. Earth and Planetary Science Letters, v. 164, p. 497-510 DOI: 10.1016/S0012-821X(98)00241-6.

Rogers, N., James, D., Kelley, S. and De Mulder, M. (1998a) The generation of potassic lavas from the eastern Virunga province, Rwanda. Journal of Petrology, v. 39, p. 1223-1247.

Rogers, N., Macdonald, R., Fitton, J.G., George, R., Smith, M. and Barreiro, B. (2000) Two mantle plumes beneath the East African rift system: Sr, Nd and Pb isotope evidence from Kenya Rift basalts. Earth and Planetary Science Letters, v. 176, p. 387-400.

Rogers, N.W., James, D., Kelley, S.P. and De Mulder, M. (1998b) The generation of potassic lavas from the eastern Virunga province, Rwanda. Journal of Petrology, v. 39, p. 1223-1247.

Rooney, T., Furman, T., Bastow, I., Ayalew, D. and Yirgu, G. (2007) Lithospheric modification during crustal extension in the Main Ethiopian Rift. Journal of Geophysical Research, v. 112, DOI: 10.1029/2006JB004916.

Rooney, T.O. (2010) Geochemical evidence of lithospheric thinning in the southern Main Ethiopian Rift. Lithos, v. 117, p. 33-48 DOI: 10.1016/j.lithos.2010.02.002.

Rooney, T.O. (2017) The Cenozoic magmatism of East-Africa: Part I–Flood basalts and pulsed magmatism. Lithos, DOI: 10.1016/j.lithos.2017.05.014.

Rooney, T.O. (2019) The Cenozoic Magmatism of East Africa: Part II–Rifting of the mobile belt. Lithos, p. 105291.

Rooney, T.O., Bastow, I.D. and Keir, D. (2011) Insights into extensional processes during magma assisted rifting: Evidence from aligned scoria cones. Journal of Volcanology and Geothermal Research, v. 201, p. 83-96 DOI: 10.1016/j.jvolgeores.2010.07.019.

Rooney, T.O., Bastow, I.D., Keir, D., Mazzarini, F., Movsesian, E., Grosfils, E.B., Zimbelman, J.R., Ramsey, M.S., Ayalew, D. and Yirgu, G. (2014a) The protracted development of focused magmatic intrusion during continental rifting: focused magma intrusion during rifting. Tectonics, v. 33, p. 875-897 DOI: 10.1002/2013TC003514.

Rooney, T.O., Furman, T., Yirgu, G. and Ayalew, D. (2005) Structure of the Ethiopian lithosphere: Xenolith evidence in the Main Ethiopian Rift. Geochimica et Cosmochimica Acta, v. 69, p. 3889-3910 DOI: 10.1016/j.gca.2005.03.043.

Rooney, T.O., Hanan, B.B., Graham, D.W., Furman, T., Blichert-Toft, J. and Schilling, J.-G. (2012a) Upper Mantle Pollution during Afar Plume-Continental Rift Interaction. Journal of Petrology, v. 53, p. 365-389 DOI: 10.1093/petrology/egr065.

Rooney, T.O., Hart, W.K., Hall, C.M., Ayalew, D., Ghiorso, M.S., Hidalgo, P. and Yirgu, G. (2012b) Peralkaline magma evolution and the tephra record in the Ethiopian Rift. Contributions to Mineralogy and Petrology, v. 164, p. 407-426 DOI: 10.1007/s00410-012-0744-6.

Rooney, T.O., Herzberg, C. and Bastow, I.D. (2012c) Elevated mantle temperature beneath East Africa. Geology, v. 40, p. 27-30 DOI: 10.1130/G32382.1.

Rooney, T.O., Krans, S.R., Mège, D., Arnaud, N., Korme, T., Kappelman, J. and Yirgu, G. (2018) Constraining the Magmatic Plumbing System in a Zoned Continental Flood Basalt Province. Geochemistry, Geophysics, Geosystems, v. 19, p. 3917-3944.

Rooney, T.O., Lavigne, A., Svoboda, C., Girard, G., Yirgu, G., Ayalew, D. and Kappelman, J. (2016) The making of an underplate: Pyroxenites from the Ethiopian lithosphere. Chemical Geology, DOI: 10.1016/j.chemgeo.2016.09.011.

Rooney, T.O., Mohr, P., Dosso, L. and Hall, C. (2013) Geochemical evidence of mantle reservoir evolution during progressive rifting along the western Afar margin. Geochimica et Cosmochimica Acta, v. 102, p. 65-88 DOI: 10.1016/j.gca.2012.08.019.

Rooney, T.O., Morell, K.D., Hidalgo, P. and Fraceschi, P. (2015) Magmatic consequences of the transition from orthogonal to oblique subduction in Panama. Geochemistry, Geophysics, Geosystems, v. 16, p. 4178-4208.

Rooney, T.O., Nelson, W.R., Ayalew, D., Hanan, B., Yirgu, G. and Kappelman, J. (2017) Melting the lithosphere: Metasomes as a source for mantle-derived magmas. Earth and Planetary Science Letters, v. 461, p. 105-118.

Rooney, T.O., Nelson, W.R., Dosso, L., Furman, T. and Hanan, B. (2014b) The role of continental lithosphere metasomes in the production of HIMU-like magmatism on the northeast African and Arabian plates. Geology, v. 42, p. 419-422 DOI: 10.1130/G35216.1.

Rubin, A.M. and Pollard, D.D. (1988) Dike-induced faulting in rift zones of Iceland and Afar. Geology, v. 16, p. 413-417 DOI: 10.1130/0091-7613(1988)016<0413:DIFIRZ>2.3.CO;2.

Rychert, C.A., Hammond, J.O., Harmon, N., Kendall, J.M., Keir, D., Ebinger, C., Bastow, I.D., Ayele, A., Belachew, M. and Stuart, G. (2012) Volcanism in the Afar Rift sustained by decompression melting with minimal plume influence. Nature Geoscience, v. 5, p. 406.

Schilling, J.G., Kingsley, R.H., Hanan, B.B. and McCully, B.L. (1992) Nd-Sr-Pb isotopic variations along the Gulf of Aden: Evidence for Afar mantle plume-continental lithosphere interaction. Journal of Geophysical Research: Solid Earth, v. 97, p. 10927-10966.

Spohn, T. and Schubert, G. (1982) Convective thinning of the lithosphere: a mechanism for the initiation of continental rifting. Journal of Geophysical Research: Solid Earth, v. 87, p. 4669-4681.

Stab, M., Bellahsen, N., Pik, R., Quidelleur, X., Ayalew, D. and Leroy, S. (2015) Modes of rifting in magma-rich settings: Tectono-magmatic evolution of Central Afar. Tectonics, DOI: 10.1002/2015TC003893.

Staudacher, T., Jessberger, E., Dorflinger, D. and Kiko, J. (1978) A refined ultrahigh-vacuum furnace for rare gas analysis. Journal of Physics E: Scientific Instruments, v. 11, p. 781.

Stern, R.J. (1994) Arc-assembly and continental collision in the Neoproterozoic African orogen: implications for the consolidation of Gondwanaland. Annual Review of Earth and Planetary Sciences, v. 22, p. 319-351.

Stuart, G., Bastow, I. and Ebinger, C. (2006) Crustal structure of the northern Main Ethiopian Rift from receiver function studies. Geological Society, London, Special Publications, v. 259, p. 253-267.

Sun, S.-S. and McDonough, W.-s. (1989) Chemical and isotopic systematics of oceanic basalts: implications for mantle composition and processes. Geological Society, London, Special Publications, v. 42, p. 313-345.

Thompson, R. (1972) Melting behavior of two Snake River lavas at pressures up to 35 kb. Carnegie Institute of Washington Yearbook, v. 71, p. 406-410.

Tommasini, S., Manetti, P., Innocenti, F., Abebe, T., Sintoni, M. and Conticelli, S. (2005) The Ethiopian subcontinental mantle domains: geochemical evidence from Cenozoic mafic lavas. Mineralogy and Petrology, v. 84, p. 259-281 DOI: 10.1007/s00710-005-0081-9.

Trestrail, K.R., Rooney, T.O., Girard, G., Svoboda, C., Yirgu, G., Ayalew, D. and Keppelman, J. (2016) Sub-continental lithospheric mantle deformation in the Yerer-Tullu Wellel Volcanotectonic Lineament: A study of peridotite xenoliths. Chemical Geology, DOI: 10.1016/j.chemgeo.2016.10.013.

Trestrail, K.R., Rooney, T.O., Girard, G., Svoboda, C., Yirgu, G., Ayalew, D. and Keppelman, J. (2017) Sub-continental lithospheric mantle deformation in the Yerer-Tullu Wellel Volcanotectonic Lineament: A study of peridotite xenoliths. Chemical Geology, v. 455, p. 249-263.

Trua, T., Deniel, C. and Mazzuoli, R. (1999) Crustal control in the genesis of Plio-Quaternary bimodal magmatism of the Main Ethiopian Rift (MER): geochemical and isotopic (Sr, Nd, Pb) evidence. Chemical Geology, v. 155, p. 201-231 DOI: 10.1016/S0009-2541(98)00174-0.

Turner, S. and Hawkesworth, C. (1995) The nature of the sub-continental mantle: constraints from the major-element composition of continental flood basalts. Chemical Geology, v. 120, p. 295-314.

Van Calsteren, P., Harris, N., Hawkesworth, C., Menzies, M. and Rogers, N. (1986) Xenoliths from southern Africa: a perspective on the lower crust. Geological Society, London, Special Publications, v. 24, p. 351-362.

Van Wijk, J., Van Hunen, J. and Goes, S. (2008) Small-scale convection during continental rifting: Evidence from the Rio Grande rift. Geology, v. 36, p. 575-578.

Walker, D., Shibata, T. and DeLong, S.E. (1979) Abyssal tholeiites from the Oceanographer fracture zone. Contributions to mineralogy and petrology, v. 70, p. 111-125 DOI: 10.1007/BF00374440.

Wang, K., Plank, T., Walker, J.D. and Smith, E. (2002) A mantle melting profile across the Basin and Range, SW USA. Journal of Geophysical Research: Solid Earth, v. 107, DOI: 10.1029/2001JB000209.

Wendt, I. and Carl, C. (1991) The statistical distribution of the mean squared weighted deviation. Chemical Geology: Isotope Geoscience Section, v. 86, p. 275-285.

White, R. and McKenzie, D. (1989) Magmatism at rift zones: the generation of volcanic continental margins and flood basalts. Journal of Geophysical Research: Solid Earth, v. 94, p. 7685-7729.

Wilson, M. (1994) Igneous petrogenesis. Chapman & Hall, London; New York.

Winter, J.D. (2001) An introduction to igneous and metamorphic petrology. Prentice Hall, Upper Saddle River, NJ. 697 p.

Woldegabriel, G., Aronson, J.L. and Walter, R.C. (1990) Geology, geochronology, and rift basin development in the central sector of the Main Ethiopia Rift. Geological Society of America Bulletin, v. 102, p. 439-458 DOI: 10.1130/0016-7606(1990)102<0439:GGARBD>2.3.CO;2.

Wolfenden, E., Ebinger, C., Yirgu, G., Deino, A. and Ayalew, D. (2004) Evolution of the northern Main Ethiopian rift: birth of a triple junction. Earth and Planetary Science Letters, v. 224, p. 213-228 DOI: 10.1016/j.epsl.2004.04.022.

Wolfenden, E., Ebinger, C., Yirgu, G., Renne, P.R. and Kelley, S.P. (2005) Evolution of a volcanic rifted margin: Southern Red Sea, Ethiopia. Geological Society of America Bulletin, v. 117, p. 846-864 DOI: 10.1130/B25516.1.

Workman, R.K. and Hart, S.R. (2005) Major and trace element composition of the depleted MORB mantle (DMM). Earth and Planetary Science Letters, v. 231, p. 53-72.

Wright, T.J., Sigmundsson, F., Pagli, C., Belachew, M., Hamling, I.J., Brandsdóttir, B., Keir, D., Pedersen, R., Ayele, A. and Ebinger, C. (2012) Geophysical constraints on the dynamics of spreading centres from rifting episodes on land. Nature Geoscience, v. 5, p. 242-250 DOI: 10.1038/ngeo1428.

Wyllie, P.J. (1979) Magmas and volatile components. American Mineralogist, v. 64, p. 469-500.

Yirgu, G., Ebinger, C.J. and Maguire, P.K.H. (2006) The afar volcanic province within the East African Rift System: introduction. Geological Society, London, Special Publications, v. 259, p. 1-6.

Zindler, A. and Hart, S. (1986) Chemical geodynamics. Annual review of earth and planetary sciences, v. 14, p. 493-571.